Dissertation zur Erlangung des Doktorgrades

der Fakultät für Chemie und Pharmazie

der Ludwig-Maximilians-Universität München

Surface modification
of metal-organic framework nanoparticles
for biomedical applications

Andreas Zimpel

aus

Rosenheim, Deutschland

2018

Erklärung

Diese Dissertation wurde im Sinne von § 7 der Promotionsordnung vom 28. November 2011 von Herrn Prof. Dr. Thomas Bein betreut.

Eidesstattliche Versicherung

Diese Dissertation wurde eigenständig und ohne unerlaubte Hilfe bearbeitet.

München, den 03. August 2018

_____

Andreas Zimpel

Dissertation eingereicht am 28.06.2018

1. Gutachter: Prof. Dr. Thomas Bein

2. Gutachter: Dr. Stefan Wuttke

Mündliche Prüfung am 24.07.2018

Danksagung

Zu Beginn meiner Dissertation möchte ich einigen Leuten danken, ohne die das Erlangen meines Doktorgrades niemals zu Stande gekommen wäre.

Als erstes möchte ich mich bei meinem Chef, Mentor und Freund Dr. Stefan Wuttke bedanken, ohne den ich ziemlich sicher nie zu diesem, sehr interessanten Forschungsgebiet der „Metall-organischen Gerüstverbindungen" gekommen wäre. Danke, dass du mich auf meinem wissenschaftlichen Weg, von unserer ersten Begegnung und Zusammenarbeit als F-Praktikant von Christian Dietl in der organischen Chemie, über das PC-F-Praktikum und die Masterarbeit bis hin zu meiner Doktorarbeit, immer angetrieben und unterstützt hast.

Besonders herzlicher Dank gilt meinem Doktorvater, Prof. Dr. Thomas Bein für die Möglichkeit meine Dissertation in seiner Arbeitsgruppe anfertigen zu dürfen, für all die finanzielle und wissenschaftliche Unterstützung über die Jahre meiner Promotion, sowie bereits während meiner Masterarbeit.

Bei beiden möchte ich mich auch speziell für die Chancen bedanken, meine Forschungsarbeiten auf diversen nationalen und internationalen Konferenzen präsentieren zu dürfen. Diese haben mich nicht nur durch interessante Diskussionen mit anderen Doktoranden wissenschaftlich neu inspiriert, sondern auch menschlich gefestigt, indem ich gezwungen war dadurch meine Kontaktscheu Fremden gegenüber abzulegen.

Vielen Dank auch an meine diversen Kooperationspartner, besonders an Ulrich Lächelt, Hanna Engelke und Michael Peller. Ohne eurer Engagement und wissenschaftlichen Input zu den gemeinsamen Projekten wäre diese Arbeit in ihrer jetzigen Form nie zustande gekommen. Dafür möchte ich mich auch speziell bei meinen Kollegen in den verschiedenen Forschungslaboren bedanken, die zusammen mit mir die Vielzahl an Experimenten durchgeführt haben (u.a. Tobias Preiß, Ruth Röder, Konstantin Böll, Miriam Höhn, Nader Danaf, Simone Braig, Michael Ingrisch, Waldemar Schrimpf,...). Danke auch an die Gruppenleiter und Professoren Ernst Wagner, Joachim Rädler, Angelika Vollmar, Don Lamb und Silke Meiners für ihre Ideen, Kommentare und Korrekturen an den gemeinsamen Publikationen.

Ein großer Dank gilt auch allen jetzigen und ehemaligen Mitgliedern der MOF/COF- und Mesobio-Subgroups für ihre Kommentare und Anregungen während der vielen Meetings.

All meinen Praktikanten (namentlich Linda, Aylin, Nadine, Luca, Kate und Marina) möchte ich an dieser Stelle für die gute und erfolgreiche Zusammenarbeit bedanken. Durch eure Betreuung habe ich viel für eine spätere Position mit Führungsverantwortung gelernt.

Danke an all meine Bürokollegen (Alesja, Andi, Andre, Noggi, Patrick, Sabrina, Stefan und Tina) für die angenehme Büroatmosphäre. Ganz besonderer Dank gilt dabei Noggi, Stefan und Sabrina, welche im Laufe meiner Promotion zu sehr guten Freunden geworden sind. Außerdem danke ich Hans, Mona und Fabi für ihr „Mentoring" auf den unterschiedlichsten Gebieten während meiner Promotion.

Für alles Organisatorische möchte ich mich ganz herzlich bei Tina, Regina und Corinna bedanken.

Mein besonderer Dank gilt natürlich auch allen anderen Personen im Arbeitskreis Bein, welche hier nicht namentlich erwähnt worden sind. Ein großes Dankeschön an alle jetzigen und ehemaligen Kollegen und Kolleginnen mit denen ich diese interessanten und spaßigen Jahre verbringen konnte.

Meiner Ehefrau Marion danke ich ganz herzlich für all die bisherigen gemeinsamen Jahre, für die aufbauenden Worte und die volle Unterstützung während meiner Promotion. Danke für dein Verständnis für meine schlechte Laune wenn es mal nicht so gut lief (eher selten) und für späteres Heimkommen wenn es mal wieder was zu feiern gab (häufiger). Ich liebe dich!

In diesem Zuge möchte ich mich auch bei meiner Schwägerin Andrea bedanken, die durch das mehrmalige Bereitstellen eines Schlafplatzes in ihrer Wohnung in Großhadern auch sehr viel zum Erfolg von Einstands-, Doktor-, Weihnachts- und sonstigen Feiern beigetragen hat.

Weiterhin möchte ich mich noch bei meinen Schwiegereltern Renate und Reiner für die nette Aufnahme in die Familie bedanken. Danke vor allem für die mentale Unterstützung in Prüfungszeiten und an „Kapuzentagen".

Meinen beiden Brüdern Fredi und Stefan danke ich für den tollen geschwisterlichen Zusammenhalt, der sehr viel dazu beiträgt, dass ich mich zu Hause sehr wohl fühle und eine sehr große Heimatverbundenheit spüre. In diesem Zusammenhang auch danke an all meine Freunde in Rott am Inn!

Der größte Dank gilt meinen Eltern. Ohne die finanzielle und geistige Unterstützung, sowie euer Talent mir das Gefühl zu geben, alles richtig und euch stolz zu machen, hätte ich keinesfalls diesen erfolgreichen akademischen Weg eingeschlagen.

Abstract

Nowadays, cancer is one of the most challenging diseases on earth. Since the 1970s, the number of patients almost doubled, due to the demographic development of mankind. Cancer researcher Robert A. Weinberg put it in a nutshell by claiming, "If we lived long enough, sooner or later we all would get cancer." Therefore, effective and targeted treatment of affected tissue is of immense interest as common chemotherapy suffers from severe side effects. One way towards selective cancer treatment is the implementation of porous nanocarrier systems for the targeted delivery of chemotherapeutics into tumor tissue to minimize side effects. To fulfil all of its ambitious tasks, the nanocarrier has to provide several different properties such as long circulation lifetimes in the bloodstream, a stimuli-responsive capping system which allows drug release at the desired location or targeting ligands on their external surface to enhance preferential uptake in cancer cells. All these properties can be addressed by the functionalization of the external surface of the designated nanocarrier system. In recent years, metal-organic frameworks (MOFs) have attracted great interest in the field of drug delivery. The ability to adjust their pore sizes and to implement functionalities within the pores as well as on their external surface makes this material class a promising candidate.

This thesis focuses on the surface modification of MOF nanoparticles (NPs) with regard to prospective biomedical applications. In this context, the uptake potential of porous MOF NPs for guest molecules and the *in vitro* toxicity of the MOF NPs used in this study are investigated in detail. Further, the possibility for external surface functionalization using different approaches is an important focus of this work. The resulting MOF NPs were fully characterized by various methods to ensure their expected morphology, composition and structure. The final achievement of the work is to evaluate the MOF NPs in the biological context. The work aims at determining how the MOF NP structure and their responsiveness to the surrounding biological environment are related to each other and how this behaviour can be correlated to their toxicity.

The first main part (Chapter 3 and 4) demonstrates that the outer surface of MOF NPs can be specifically functionalized with biocompatible polymers to control the interface between colloidally stable MOF NPs and their environment. Chapter 3 is focused on the covalent attachment of different functional polymers on the external surface of the biologically well-tolerated iron based MOF NPs (MIL-100(Fe)). With this approach, it is possible to increase

the chemical and colloidal stability and to provide fluorescence properties by using dye-labeled polymers. The functionalization of the MOF NPs with fluorescent-labeled polymers enables the investigation by fluorescence-based techniques, as demonstrated by fluorescence correlation spectroscopy (FCS) and confocal fluorescence microscopy. Furthermore, the influence of the polymer shell on the intrinsic magnetic resonance imaging (MRI) activity of MIL-100(Fe) is investigated in detail.

As already demonstrated in the third chapter, the effective bio-application of MOF NPs is still hampered by limited control of their surface chemistry and insuffucient understanding of their interactions at the biointerface. Using a self-assembly approach, the fourth chapter of the thesis shows that coating of MOF NPs (Zr-*fum*) with polymers, frequently used for biomedical applications, is a convenient way for peripheral surface functionalization. Detailed investigation of the binding reveals the mechanism to be a self-assembly modulator replacement by the coordinating group-containing polymers. This strong coordinative binding is further used to attach the shielding polymer polysarcosine onto the MOF surface, which results in an exceptionally high colloidal stability of the NPs. The effect of the polymer coatings on the biointerface is investigated with regard to cell interactions and protein binding.

An important feature of MOF NPs for their use as nanocarriers is the high loading capacity for cargo molecules in their porous scaffold. Therefore, the molecular transport of the model-cargo fluorescein into two MOF NPs, MIL-100(Fe) and MIL-101(Cr) is studied in detail in the second main part (Chapter 5). The equilibrium dissociation constants and maximum number of adsorbed molecules per NP are determined via fluorescence spectroscopy. The resulting maximum payload capacity of 65 wt% MIL-100(Fe) and 41 wt% MIL-101(Cr) is shown to be in agreement with the internal area estimated from nitrogen sorption measurements. Kinetic studies show that release and loading rates are pH dependent. Theoretical modeling of diffusion to target, slowed internal diffusion and equilibrium binding reproduce the observed loading and release times. This study helps to optimize payload and release rates of MOF NPs under varying pH conditions as for example encountered in medical drug delivery applications.

The third main part of the thesis (Chapter 6, 7 and 8) is focused on the use of lipids for external surface functionalization of MOF NPs. Two different approaches were thereby applied for the creation of MOF-lipid NPs. The study in chapter six focuses on the synthesis of MOF@Lipid NPs as a versatile and powerful novel class of nanocarriers based on MOF

NPs (MIL-100(Fe) and MIL-101(Cr)). It is shown that the created MOF@Lipid system can effectively store dye molecules inside the porous scaffold of the MOF while the lipid bilayer prevents the premature release. Efficient uptake of the MOF@Lipid NPs by cancer cells makes these nanocarriers promising for drug delivery and diagnostic purposes.

The study presented in chapter seven comprehensively analyzes the nanosafety of different MOF NPs used so far in this thesis, namely bare Zr-*fum* NPs, MIL-100(Fe) NPs and MIL-101(Cr) NPs as well as their MOF@DOPC NP analogs (see chapter six) with regard to diverse medical applications such as drug delivery via blood or lung to multifunctional surface coatings of medical implants. For that purpose, biocompatibility of the MOF NPs on different effector cells (e.g., primary human gingiva fibroblasts) which are defined as those cells that directly interact with NPs when these are introduced into the biological system are tested. Nanosafety of tested MOF NPs strongly varies with the effector cell types revealing their differential suitability as nanomedical agents for drug delivery and implant coatings. These results thus demonstrate the requirement for thorough testing of nanomaterials for their nanosafety with respect to their particular medical application and their interacting primary cell type, respectively.

Finally, chapter eight deals with a modified lipid-coating procedure for MIL-100(Fe) NPs using the same lipid (DOPC). It shows the applicability of such Lip-MOF NPs as effective anti-cancer agents, without loading of any toxic chemotherapeutics into the framework. The toxicity of the particles is thereby triggered by a slightly acidic pH of the extracellular medium (pH = 7.2). These results are promising for a selective treatment of tumor tissue, which provides lower extracellular pH due to an increased lactic acid fermentation of cancer cells (Warburg effect).

In summary, the thesis discusses different MOF NPs systems for their use in biomedical applications. It covers the highly relevant challenges of MOF nanocarriers with respect to a better understanding of drug loading, external surface functionalization and nanosafety. Furthermore, a novel Lipid-MOF nanocarrier system is examined regarding its prospective application as a pH-selective chemotherapeutic. The obtained results highlight MOF NPs as a promising platform for targeted tumor theranostics.

Table of contents

1. Introduction

This chapter is based on the following book chapter:

Beetz, M.; <u>Zimpel, A.</u>; Wuttke, S. (August 2016); *Nanoparticles*. In: Kaskel, S. (Ed.); *The Chemistry of Metal-Organic Frameworks: Synthesis, Characterization, and Applications.* Weinheim: Wiley-VCH

1.1. Metal-organic frameworks (MOFs)

Metal-organic frameworks are a class of materials, which came up by the end of the 20th century. They consist of organic linker molecules and inorganic metal clusters acting as nodes in between. The two different building blocks are connected via coordinative bonds forming a rigid porous scaffold which is accessible e.g. for small molecules. Both, the choice of organic linker and metal strongly determine the properties of the resulting framework (structure, pore size, pore environment…). Due to the variety of possible combinations of metal and linker, the material class of MOFs offers a nearly endless number of different compounds.

1.2. Nanoparticles

Introduction into the nanoworld

The term "nano" (Greek for dwarf) became an important notion in science and technology in the last two decades. The prefix "nano" stands for the order of magnitude of 10^{-9}. On a scale of length one nanometer correspond to $0.000,000,001 \, m = 1 \cdot 10^{-9} \, m$. In a vivid size comparison, a bacterium, one of the smallest forms of life on earth, is thousand times larger than a nanometer. A human hair in average has a diameter of around 50,000 nm.

The so-called nanoparticles assign small particles with a diameter of $1-100$ nm in size in at least one dimension. Today, these types of particles are technically and commonly used and can be found everywhere in daily life. Man-made nanoparticles are produced by various combustion processes or domestic activities like material fabrication and transportation utilizing.[1] Carbon nanoparticles, for example, are mostly produced due to incomplete combustion processes like in wax candles or petrol engines and are commercially available as carbon black from the furnace process.[2] The production of other particles is mainly due to attrition on friction-processes. Natural nanoparticles form during volcanic eruptions or forest

fires.[3] Furthermore, virus particles are naturally nanostructured particles, consisting of nucleic acids and a protein shell.[4]

There are different ways in which nanomaterials can be classified. The degree of structural order in nanoparticles can be either crystalline or amorphous. The crystalline nanoparticles are referred to as nanocrystals. They are mostly single-crystalline and hence, have different optical and electrical properties compared to them polycrystalline or bulk form.[5] They can be composed of either one material or distinctly different components, the latter are denoted as nanocomposites. Another class of nanoparticles is found in so-called nanostructured materials. The main focus of such materials lies on the shape, surface structure or the superstructure, which give them characteristic abilities with respect to nano-properties. The structure of these particles causes them to have different properties compared to the bulk material due to nano-relevant effects. It is important to say that strong agglomeration or aggregation of this kind of particles mostly leads to a loss of their specific nano-properties and they act like the macroscopic bulk material.[5] Nevertheless, sometimes agglomeration is intentionally used to adjust particles sizes and surface-structures. Colloidal nanoclusters and nanoparticle aerogels, for example, have interesting optical and magnetic properties, and are used as catalysts.

Size depending forces between particles

Nanoparticles are so tiny that some effects and forces vanish while others strongly increase. This leads to a shift in the balance of forces influencing the nanoparticle itself. The impact of gravitational force on nanoparticles is strongly reduced due to their lower weight per particle, leading to a more flexible particles' behavior: they act like molecules. With smaller particle sizes, the influence of the force of surface charges increases, resulting in strong interactions (Coulomb-attraction/repulsion) between the particles themselves or towards counter ions. Another dominant effect is the strong increase of the surface energy. Reducing the particle size, the surface area to volume ratio increases drastically, leading to a high surface energy. Therefore, nanoparticles have a strong tendency to agglomerate between each other, as it is energetically favored.

The effect of size-dependency on properties and their macroscopic consequences can be illustrated by the example of silicon dioxide SiO_2 (Fig. 1-1).
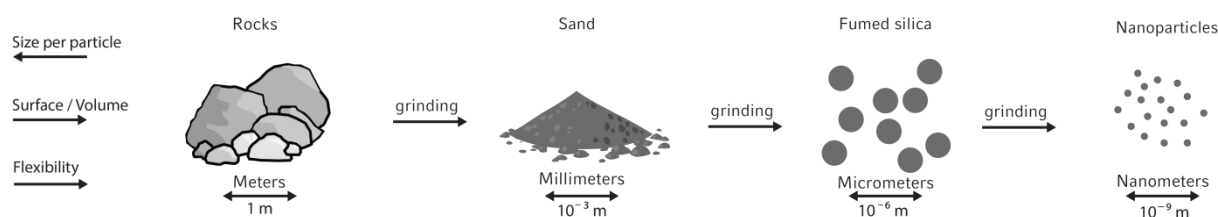
Figure 1-1. Different size-depending properties of silicon dioxide.

As a rock, silicon dioxide is hard and brittle. The smaller the particles of silicon dioxide are, for example like in sand, the softer and more flexible the material gets, and it acts rather like a fluid than a rock. Very small SiO_2 particles like fumed silica have a very fluffy appearance. They are soft and can be fluidized due to the increasing impact of electrostatic repulsion and the very low effect that the gravitational force has on the particles. This trend continues towards silicon dioxide nanoparticles, where the influence of electrostatic and gravitational forces further increases.

Nanoscale-effects

The importance of size-relevant effects increases with decreasing particle sizes. Especially when particles are observed in the dimensions of about 1–100 nm (nanometer-scale) the properties of the material change significantly. In this scale, properties like melting point,[6] color,[7] electrical conductivity,[8] magnetic permeability,[9] catalytic activity[10] and chemical reactivity[11] are a function of both particle size and shape.

Effects that play a role in nanoparticles or nanostructures are mostly surface-,[12] optical-[13] or quantum-effects[14]. One well-known example for a surface effect is the Lotus-effect.[15] Materials using the Lotus-effect are commonly used as self-cleaning surfaces due to their highly hydrophobic properties. On normal surfaces, adhesive effects ensure water droplets to cover the whole surface-area. Superhydrophobic-Lotus-like materials have a nanostructured surface that minimizes the contact area of the droplets. This causes the droplet to form its most stable form, the sphere. Due to the strong surface curvature of a sphere, there is almost no contact area and hence very little adhesive force of the material. This causes the water droplet to roll down along this surface until it falls off.[16]

Another effect derived from the specific properties of nanomaterials is the surface-plasmon-resonance. Plasmons are fluctuations in the electron density against the restoring force of the positive atomic cores. With the limited size of these materials in all three dimensions, the wave function of this electron gas can be excited in its eigenstates. Therefore, nanoparticle

composition, size and shape, specific resonant wavelengths resulting in a color or other optical properties differ from those of the bulk-material.[17] A commercial example for such materials are the so-called quantum dots. These are semiconductor-nanoparticles, whose properties can be adjusted to a high degree by composition, doping, size distribution or interactions with each other.[14]

Another interesting example, where optical properties can be adjusted by nanoscaled structures, is the so-called Vantablack-material (Vanta stands for Vertically Aligned Nano Tube Arrays). It is absorbing 99.965% of the radiation in the visible spectrum and appears therefore as the blackest substance known at the moment. This material has vertically aligned nano-tubes on its surface which scatter the light very effectively between one another and the energy of light is finally converted to heat.[18]

Synthesis

For synthesis, processing and analytics, it is important to obtain and manipulate nanostructures at the nanometer-scale. In general, the used methods can be classified in the so-called bottom-up and top-down approaches. Examples for bottom-up methods are the liquid phase synthesis (hydrothermal/solvothermal synthesis, the sol-gel processing, etc.) or gas phase methods (chemical vapor deposition, laser ablation deposition, sputtering techniques, etc.). Most top-down methods are based on milling or grinding processes.

In order to achieve high quality nanoparticles regarding size distribution, agglomeration, stabilization and specific properties, different parameters have to be controlled during the synthesizing process (Fig. 1-2).
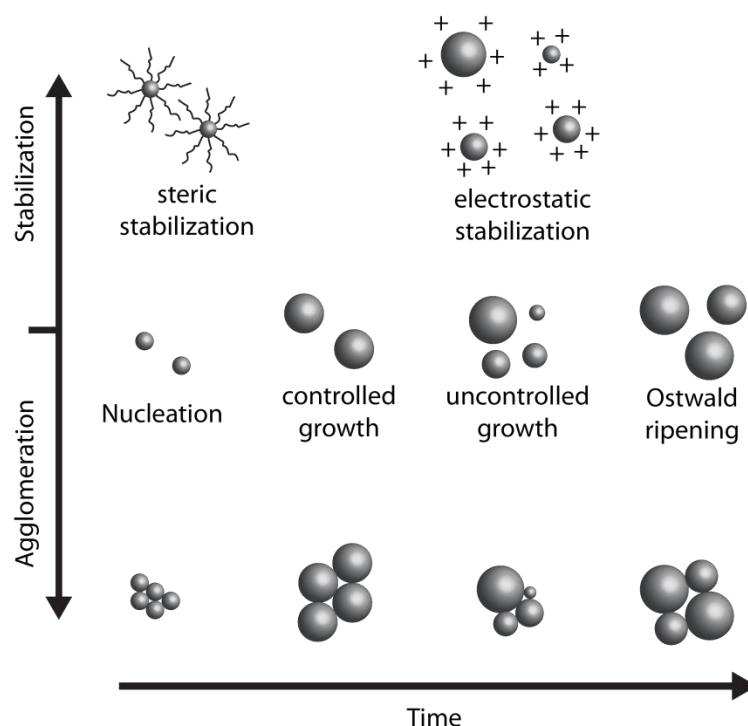
Figure 1-2. Time-dependence of nanoparticle growth and agglomeration/Ostwald-ripening.

To form nanoparticles with a narrow size distribution, the nucleation and growth should be controlled precisely and adjusted as accurately as possible. However, some MOFs preferentially form nanoparticles in the regular synthesis. Another important aspect is the suppression of agglomeration processes. Nanomaterials lose or change their very specific properties when they agglomerate. Additionally, most agglomerated particle-clusters cannot be separated into single particles. The agglomeration behavior in liquid-phase synthesis can be controlled by functionalizing the surface of the nanoparticles immediately after nucleation. Typically, steric demanding organic molecules like long-chain alkyl compounds, surfactants or polymers are used. These can influence the growth direction of the particle and can prevent particles from interacting with each other. Another way of stabilizing single particles is the electrostatic stabilization, where polar molecules on the particle surface prevent agglomeration through electrostatic repulsion. Both strategies prevent also the Ostwald ripening – the process where small particles are merged into larger ones.

In general, nanomaterials open the world to novel advanced material properties. To get such properties it is important to have highly reproducible and adjustable synthesis routes. In recent years, MOF syntheses were mostly optimized for single crystal growth to elucidate the structures. In future a high potential in the field of MOF chemistry will develop by working towards nanostructured MOF materials.

1.3. Metal-organic framework nanoparticles (MOF NPs)

Metal-organic framework materials stand for crystalline materials, a huge number of inorganic building blocks combined with almost endless organic linkers, a tunable pore structure, ultrahigh porosity and different functionalization concepts. The combination of these properties with the nano-world offers manifold perspectives for the synthesis of well-defined multifunctional nanoparticles with novel properties. Operating at a length scale of one-billionth of a meter, the properties of MOF nanoparticles differ significantly from their bulk substances due to the high surface-to-volume ratio and quantum size effects. By combining the inorganic and organic chemistry worlds, MOF nanoparticles will possibly display novel and enhanced properties compared to the already established nanomaterials such as gold nanoparticles, iron oxide nanoparticles, quantum dots, polymers, carbon nanotubes, liposomes, mesoporous silica etc. Further, they could be integrated in well-established systems for enhancing diffusion paths in catalysis[19] or as MOF membrane[20].

Establishing synthesis protocols for precisely tuning the composition, morphology and the physical properties of MOF nanoparticles (Fig. 1-3) is a huge task but at the same time a chance for synthesis chemists to develop new creative ideas.
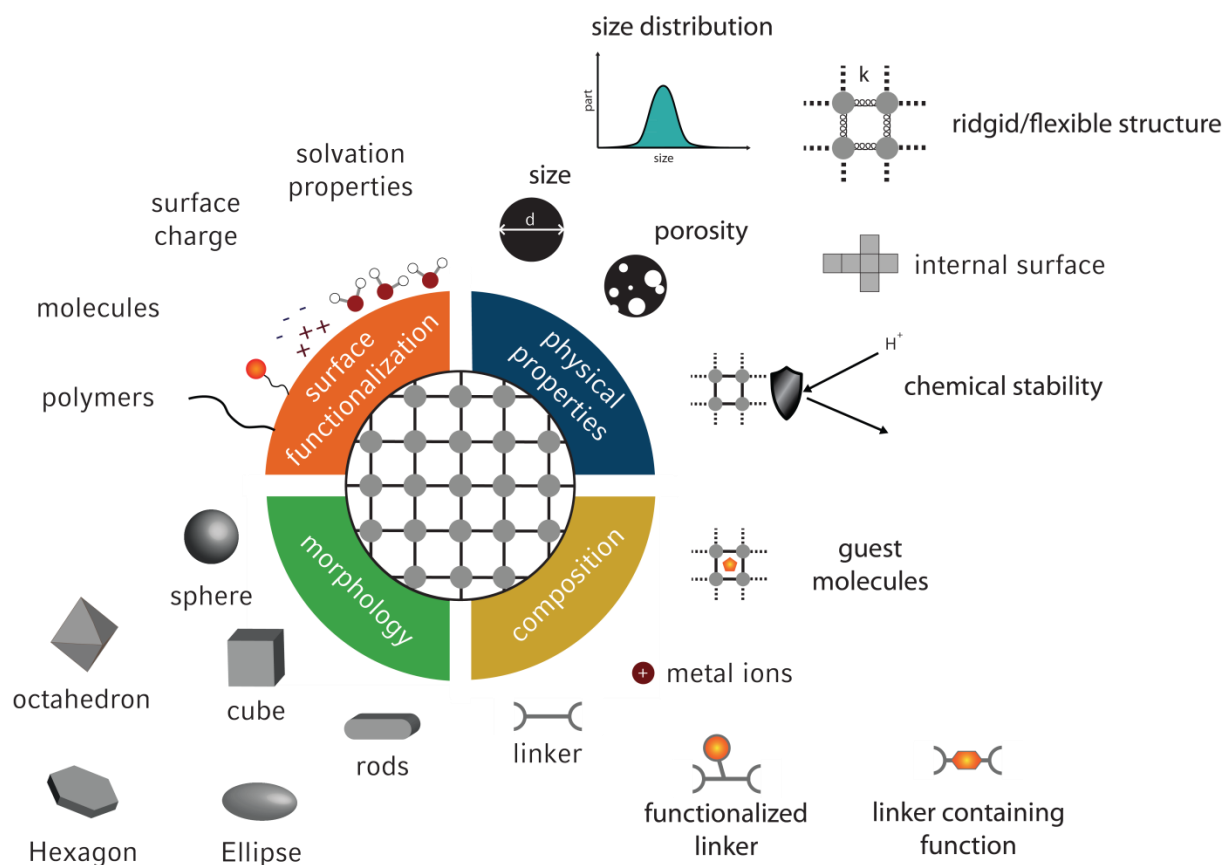

Figure 1-3. Overview of the most important design parameters for the synthesis of MOF NPs.

In addition, for different applications the internal and external surface can be functionalized with MOF specific functionalization concepts. However, the appropriate characterization and evaluation of the MOF nanoparticle properties are a tremendous challenge as it requires different and very expensive analytic instruments. Here, the MOF community is confronted with the challenge to prove the crystallinity of a MOF nanoparticle and with this the underlying MOF structure. Due to peak broadening in powder X-ray diffraction analysis and MOFs being beam sensitive for transmission electron microscopy (TEM) this challenge can hopefully be solved with the new versions of TEM instruments operating at low voltage. Once all the issues mentioned above have being met, well-defined and precisely functionalized MOF nanoparticles can possibly bring new fundamental understanding for the nanoscience area.

1.4. Synthesis of MOF NPs

Nanoparticles made of metal-organic frameworks (NMOFs) can have versatile applications. In general, these applications require narrow particle size distributions and uniformly shaped crystallites. Therefore, the controlled synthesis of well-defined MOF nanoparticles is of huge interest. Several techniques have been developed in recent years - this chapter deals with procedures which are most commonly applied in chemistry laboratories.

Overall, the shape of the NMOFs is determined by two important factors: The intrinsic structure of the resulting material, which - if predominant - leads to a huge variety of non-spherical NMOF morphologies and further, causes interactions with solvent molecules, which forces the crystals to a more spherical appearance.[21] In most cases, crystal lattice energy tends to overcome the particle/solvent interactions leading to polyhedral NMOFs morphologies such as spheres, cubes, octahedra, hexagonal prisms, etc. (Fig. 1-1). The particle size can mainly be controlled by adjusting the reaction time and temperature.[22] Further improvements in the synthesis of nanoscaled MOFs has been done in recent years. Adding modulator molecules or by carrying out the NMOF synthesis in nano-reactors, the morphologies and particle size can be tuned. The different approaches, which will be described in the following chapters, are summarized in Figure 1-4.
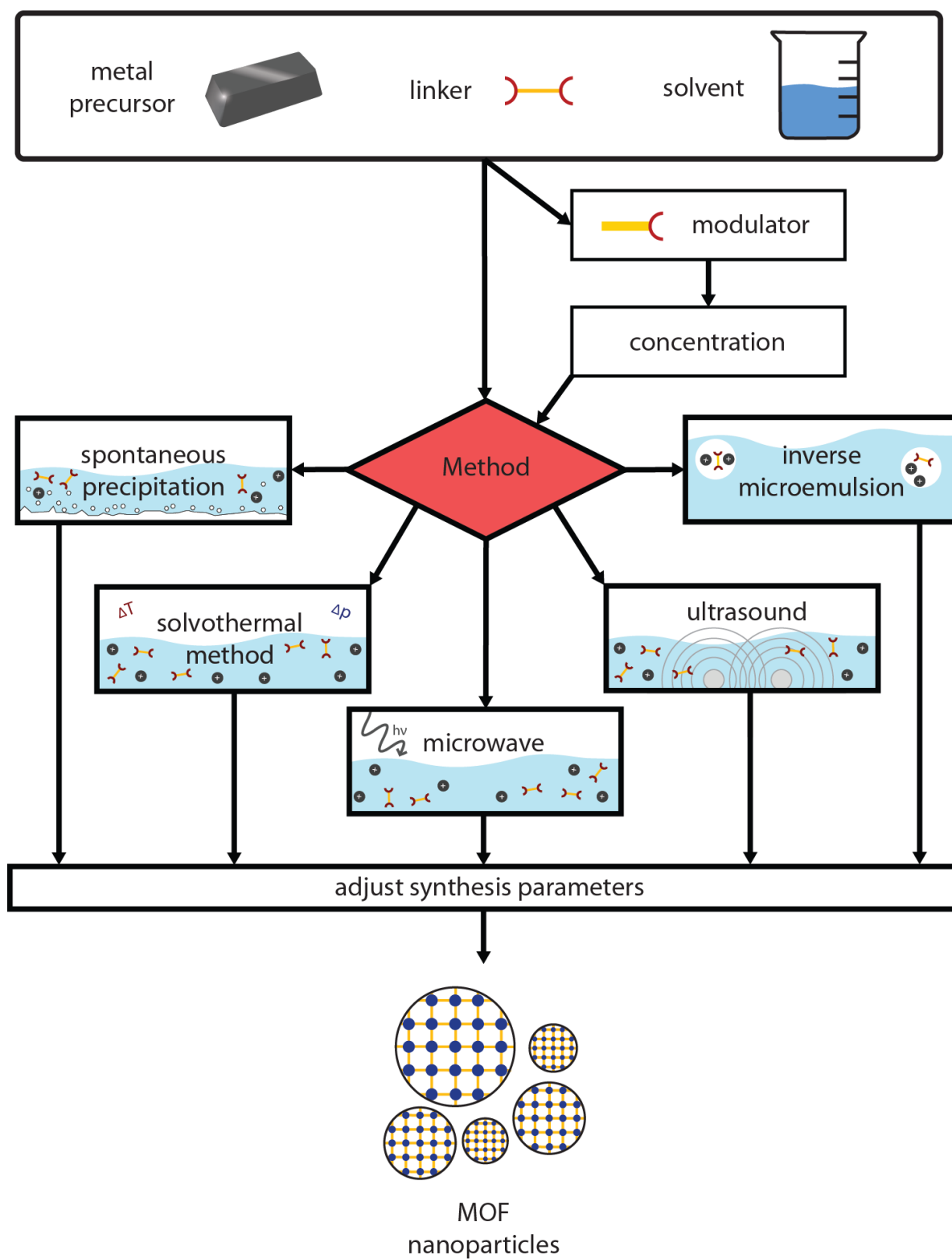
Figure 1-4. Overview over the different techniques for the synthesis of MOF NPs.

Spontaneous precipitation method

The simplest way to synthesize MOF NPs is their precipitation after mixing metal and linker in a stirring solution. The spontaneous assembly of linker and metal clusters can lead, if controlled by time, temperature and concentration of the precursors, to the formation of NMOFs. Two different techniques have been applied for amorphous coordination polymers first and then have found their way into the synthesis of crystalline MOF NPs. The first one was published by Sun *et al.* in 2005, where they showed a successful preparation of amorphous spherical colloids, consisting of coordinatively bounded *p*-phenylenediamine (PPD) and platinum ions, by combining H_2PtCl_6 and PPD in aqueous solution.[23] The second technique was introduced by the group of Chad A. Mirkin also for amorphous particles. A solution of $M(OAc)_2$ (M = Cu, Zn, Ni) and carboxylate-functionalized binaphthyl bis-metallotridentate Schiff base (BMSB) in pyridine was diluted with diethylether to induce the precipitation of nanospheres. They also showed the reversibility of this system by dissolving the particles in an excess of pyridine.[24] Due to the versatility of these methods, the techniques have been extended to a wide range of coordination particles as well as NMOFs. HKUST-1 nanoparticles, for instance, have been synthesized by pouring an aqueous solution of copper nitrate into a preliminary prepared aqueous solution of trimesic acid.[25-26] Further, Pan *et al.* showed a precipitation of a zeolitic imidazolate framework (ZIF-8) out of an aqueous solution of $Zn(NO_3)_2 \cdot 6\,H_2O$ and 2-methylimidazole at ambient temperature.[27]

Solvo-thermal method

A frequently used route for the formation of MOFs is solvo-thermal synthesis, where the reaction mixture is heated up in a sealed autoclave, which can be made of glass, teflon or high-grade steel. It is well known, that the solubility of precursors and products is increased at high temperatures, preferentially leading to crystallization vs. a rapid precipitation of amorphous material. Control over precursor ratio and concentration, pressure, time and temperature can allow the formation of homogeneous nanoparticles. Furthermore, the choice of solvent is very crucial for the formation and co-determines the resulting MOF structure. Horcajada *et al.* prepared a variety of iron based NMOFs of the MIL (Materials of Institut Lavoisier) family by solvo-thermal synthesis in DMF, ethanol, methanol or water, respectively.[28] Furthermore, it was possible to expand the pore size of MIL-100/101 topologies, using extended bi- or tricarboxylic linker molecules under solvo-thermal conditions.[29-30]

Microwave synthesis

Using microwave irradiation for the production of nano-scaled MOFs turned out to be a useful type of solvo-thermal synthesis. Compared to the classical route, microwave synthesis provides the advantages of fast heating within the reaction mixture. Local superheating provides a huge amount of hot spots which can serve as nucleation seeds for crystal growth.[31] This allows short reaction times towards other techniques and narrow particle size distributions. Various MOF NPs have been synthesized by microwave synthesis.[32] Jhung *et al.*, for instance, were able to produce very homogeneous MIL-101(Cr) nanoparticles in high yield and uniform shape.[33]

Preparation by ultrasonic sound

This approach is based on the interaction of high-energetic ultrasonic sound with the reaction solvent, which is followed by cyclic alternating areas of compression and rarefaction. In rarefaction areas, occurring pressures below the vapor pressure of the solvent lead to cavitation. After reaching a maximum size, the cavitation collapses under rapid release of energy, leading to so-called hot spots were MOF formation can take place.[34]

The ultrasonic method was established for MOF nanoparticle synthesis in 2008, when Qui *et al.* investigated the formation of $Zn_3(BTC)_2 \cdot 12\ H_2O$ by combining zinc acetate dihydrate and trimesic acid in an ethanol/water mixture. Spontaneous precipitation did not occur by just mixing the precursors at room temperature, but sonochemical synthesis resulted in MOF nanoparticles with approx. 100 nm in diameter in a high yield.[35] A few month later, Son *et al.* successfully prepared MOF-5 particles at least at the micrometer scale by applying ultrasonic sound. They were able to significantly reduce the reaction time compared to conventional solvothermal synthesis from 24 hours to about 30 minutes.[36]

Reverse microemulsion method

Another widely approved road to the production of homogeneous nanoparticles is the reverse microemulsion technique. It has successfully been used for a broad range of other nanomaterials and was applied for coordination polymer particles for the first time by the group of Mann in 2000.[37] As the name already suggests, an emulsion of the precursor solution in a second liquid solvent is used for the creation of nanosized reactors. In these tiny droplets MOF formation occurs and the particle growth is limited by the border of the two liquids. Tuning the droplet size leads directly to a control over the size of the nanoparticles. Different solvent mixtures have already been applied for this method, such as water/oil, which was used

by Mann for the synthesis of Prussian Blue nanoparticles[37] or an isooctane/1-hexanol/water mixture, which was applied by the group of Lin for the formation of $[Gd(1,2,4-BTC)(H_2O)_3] \cdot H_2O$ nanocrystals.[38]

Morphology modulation using additives

Furthermore, addition of modulators to the reaction medium can lead to an improved crystal shape as well as to a narrow size distribution. The idea behind this approach is to limit the particle growth by adding capping molecules to the reaction media. Different types of additives have been approved in literature and showed a confinement effect leading to homogeneously shaped MOF nanocrystals.

One possibility is the usage of small molecules with the same chemical functionality as the linker molecule. In contrast to the linker, these molecules possess only one coordinating functional group and which allow for the coordination to metal centers of the framework, but do not provide a chemical functionality for a further crystal growth. The group of Kitagawa originally introduced the modulation approach, using acetic acid as a monovalent modulator molecule. By taking advantage of the competitive interaction between modulator and linker molecules, they were able to obtain small and homogeneous $[\{Cu_2(ndc)_2\text{-}(dabco)\}_n]$ nanoparticles [39] as well as bigger, heterogeneous $[Cu_3(btc)_2]$ nanoparticles[40]. Further investigations on this synthesis approach have been performed by Behrens and co-workers, focusing on benzoic acid, acetic acid or formic acid as modulator for the synthesis of Zr-based metal-organic frameworks. They provided control over the nucleation rate of the nanocrystals by changing the concentration of the modulator molecule.[41-42]

Kitagawa's group also used the confinement effect of polyvinyl- pyrrolidine (PVP) for the synthesis of MOF nanoparticles for the first time.[43] Prussian Blue nanoparticles were synthesized in an aqueous solution of $FeCl_3$ and $K_3Fe(CN)_6$ in the presence of PVP. Without PVP, large particles (>300 nm) with a broad size distribution were formed. They attributed the latter to a steric stabilization effect of the PVP due to a weak coordination of its amide moiety to the Fe ions during the nucleation and growth process of the particles. Using the same technique, Kerbellec *et al.* stabilized ultra-small luminescent $Tb_2(bdc)_3(H_2O)_4$ nanoparticles with sizes below 10 nm.[44]

Another approach is the addition of a surfactant in order to stabilize the particles during their formation. Taylor *et al.* reported a CTAB (cetyltrimethylammonium bromide) supported formation of $[Gd_2(bhc)(H_2O)_6]$ and $[Gd_2(bhc)(H_2O)_8](H_2O)_2$ nanoparticles in a 1-hexanol/n-

heptane/water microemulsion.[45] They showed that microemulsion synthesis without addition of surfactant resulted in an amorphous material.

Top down processing and combination of different techniques

The synthesis of high-quality nanoparticles, namely those with a defined diameter, almost monodispersed size distribution, and small degree of agglomeration, is often realized by starting from a homogeneous liquid phase solution. Especially in MOF chemistry downsizing by milling is detrimental causing often surface area loss and amorphization. However, some elaborations have recently focused on the formation of superstructures made of MOF nanoparticles [46] (see chapter "Engineering MOF NPss"). Disassembly of these hierarchical structured architectures can lead to nanoparticles. Maspoch and co-workers, for instance, developed a spray-drying strategy to build up MOF hollow spheres. After sonication in methanol, they obtained a colloidal dispersion of homogeneous HKUST-1 nanoparticles.[47]

Due to the diversity of different synthetic methods towards MOF nanoparticles, researchers started to combine those methods for a further improved control over size and shape of the particles. As an example, Tanaka *et al.* used reversed microemulsion technique in combination with ultrasonic sound for the preparation of $\{[Zn(ip)(bpy)]\}_n$ (ip = isophthalate, bpy = 4,4′-bipyridyl; CID-1) nanoparticles.[48]

1.5. Engineering MOF NPs

External surface functionalization of MOF NPs

The functionalization of MOF NPs on their external surface (Fig. 1-1) is of immense interest, especially with regard to their possible application as drug delivery vehicle (see chapter "Applications of MOF NPs"). Towards an explicit attachment of molecules on the particle shell, depending on the surface appearance, functionalization can be done effectively in different ways.

Addressing coordinatively unsaturated metal centers on the particle surface has been attempted by Rowe *et al.* in 2009. They reported the attachment of RAFT copolymers containing thiolate functionality on vacant orbitals on Gd^{3+} ions at the surface of Gd MOF NPs.[49] Alternatively, postsynthetic modification on pre-functionalized organic linker molecules on the external surface is a known procedure in literature. Liu *et al.* were able to cover a copper MOF selectively with an amino-functionalized isoreticular MOF (terephthalic acid was replaced by 2-aminoterephthalic acid) using copper acetate as a connector. The amino group was further functionalized with a fluorescent dye and could be observed via

fluorescence microscopy.[50] This method might as well be a promising approach for the functionalization of MOF NPs. Furthermore, the linking groups of MOFs can also be used as anchoring point for modifications on the outer surface of nanoparticles. In fact, typical organic linkers of the MOFs contain carboxylate groups, for instance. Park and co-workers assumed that a certain amount of carboxylate groups is exposed on the surface and they confirmed this assumption by covalent attachment of enhanced green fluorescent protein (EGFP). They demonstrated their results on a one- dimensional indium-based coordination polymer, the two dimensional $[Zn(bpydc)(H_2O)]\cdot(H_2O)_n$, and IRMOF-3 as a model system of a three dimensional MOF. Activation of the carboxylates was achieved with 1-ethyl-3-(3-dimethylaminopropyl) carbodiimide (EDC) or dicyclohexyl carbodiimide (DCC), respectively.[51]

Structuring MOF NPs at the macroscopic scale

In order to enrich the overall performance of MOF NPs, researchers started to focus on the construction of hierarchical MOF superstructures. The specific arrangement can have versatile advantages, considering the desired application. In general, there are four different possibilities for the structuring at the macroscopic scale (Fig. 1-5).
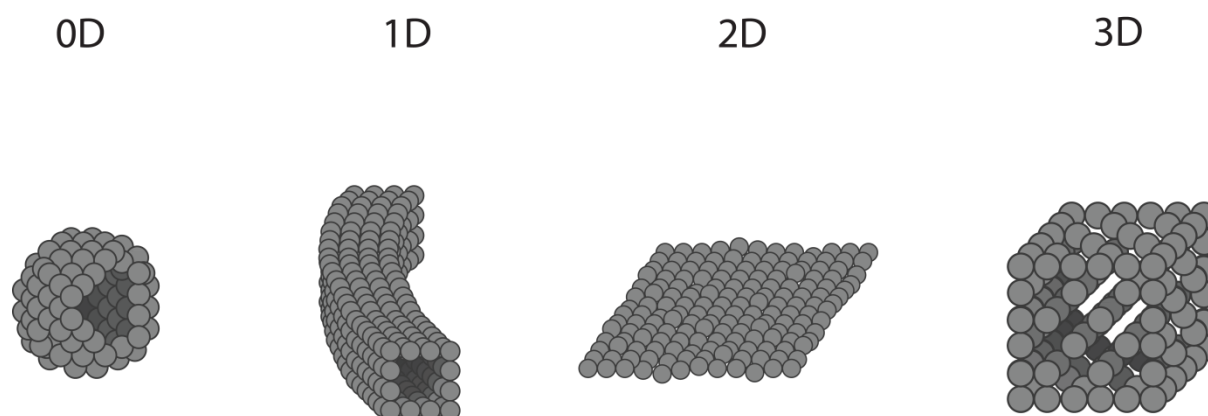

Figure 1-5. Illustration of the different types of MOF superstructures made of nanoparticles.

Zero-dimensional (0D) objects like hollow spheres can serve as shell to compartmentalize space. Those voids can have possible applications in energy storage,[52] chemical catalysis,[53] photonics,[54] etc. One-dimensional (1D) architectures, like MOF nanorods or MOF nanofibers, are promising candidates for sensing, optoelectronics, or magnetic devices, for instance.[46] Thin films, membranes or patterns can be created by an assembly of MOF NPs in a two-dimensional (2D) MOF superstructure. They provide potential as photonic crystal for sensing

applications,[55] as membrane for gas separation [56] or proton and electronic conduction.[57] The advantage of a MOF nanoparticle arrangement in three dimensional (3D) frameworks is mainly its contribution to an increased diffusion rate of the guest molecules into the nanoparticle pores, compared to a packed bed system.[58] Fast diffusion rates can be crucial in applications such as gas sorption, gas separation or chemical sensing.

The assembly of these superstructures is based on two general methods, "top-down" and "bottom-up" approaches. "Top-down" means the pre-synthesis of MOF NPs and their further structuring by coating, etching or aligning techniques. As an example, the rearrangement of a dispersion of ZIF-8 crystals into a one-dimensional superstructure by applying an electric field was investigated.[59-60] Ostermann *et al.* obtained MOF nanofibers with an adjustable diameter between 150 nm and 300 nm, adding PVP to a dispersion of ZIF-8 in methanol and injecting the mixture into a reaction chamber, where a voltage of 5 kV was applied.[59, 61]

"Bottom-up" means the direct synthesis of MOF NPs in an oriented superstructure. Therefore, different strategies have been developed in recent years. Adding a pre-shaped macrostructural (hard) template or a molecular (soft) template to the reaction, can lead to controlled particle crystallization on the template surface. Subsequent removal of the structure directing material provides hierarchical architectures of the metal organic framework. Common hard templates which have already found their way into the synthesis of MOF superstructures, are e.g. carbons [62], silica [63] or organic polymers [64-65].

Cao *et al.* showed the use of block-copolymers as soft template for the formation of three-dimensional superstructures of ZIF-8 and HKUST-1 nanoparticles.[66]

Interfacial reactions provide another possibility for the formation of hierarchically structured metal-organic frameworks. An important feature of this technique is the confinement of metal and precursor at different compartments of the reaction mixture. Thus, MOF formation can only occur at the border between those compartments.

In literature, liquid-solid interfacial reactions and liquid-liquid interfacial reactions are well known. The former method is, in a way, similar to macrostructural templates. The solid compartment serves as template as well as a reservoir for metal ions. The linker molecule is simply dissolved in the liquid phase. Using this technique, Zheng and co-workers coated zinc oxide nanorods with ZIF-8 nanoparticles, immersing the Zn-containing nanorods in a solution of 2-methylimidazole in DMF/water and heating it in an autoclave at 70 °C.[67] Only one year before, the group of Kitagawa successfully performed a variation of this method, called coordination replication.[68] They converted a hexagonal alumina "parent phase" into a

hierarchical structure of MOF NPs with same architecture, reacting the alumina in an aqueous solution of 1,4-naphtalenedicarboxylic acid.

A liquid-liquid interfacial reaction for the generation of hollow spheres, consisting of [$Cu_3(BTC)_2$] nanocrystals was published by Ameloot *et al.* in 2011.[69] Injecting droplets of an aqueous cupper acetate solution in a flow of trimesic acid in 1-octanol yielded homogenous MOF capsules in a range of 300–400 μm in size.

Reaction confinement by evaporation has already been explored in recent years for the structuring of MOF NPs. Thereby, metal source and organic linker have been well stabilized in the reaction medium, so that reaction cannot take place spontaneously. The formation of the MOF is induced by the evaporation of the solvent. This strategy opens the possibility to "print" MOF particles on desired surfaces, which was published by de Vos and co-workers.[70] A stable solution of copper nitrate trihydrate and trimesic acid in DMSO was patterned by a stamp onto a glass substrate. After solvent evaporation, they obtained micro-sized MOF crystals in an ordered manner. A route towards zero-dimensional MOF hollow spheres by a reaction confinement approach was shown by Carné-Sánchez *et al.* in 2013.[47] Spray-drying of the precursor solution of different MOFs resulted in spherical capsules, consisting of highly crystalline and homogenous nanoparticles.

Core-shell MOF NPs

The fascination of polyfunctional nanoparticles and their use in different fields of application leads to the synthesis of core-shell particles, which exhibit new or enhanced properties in comparison to individual units. However, rising the degree of functionality goes along with an increased level of synthesis complexity. Controlling the size of the core and shell, the composition, the dispersed nature, the colloidal stability, the spatial distribution as well as confinement of the core-shell nanoparticles is a huge and exciting challenge.[71]

In general, core-shell nanoparticles are made from two or more materials. Normally, core-shell nanoparticles are synthesized using a two-step process: the synthesis of the core and the synthesis of the shell. However, the uniform pore structures of MOF materials can be utilized as nanoreactor for the synthesis of metal nanoparticles ensuring controlled particle sizes inside the MOF pores (Fig. 1-6).
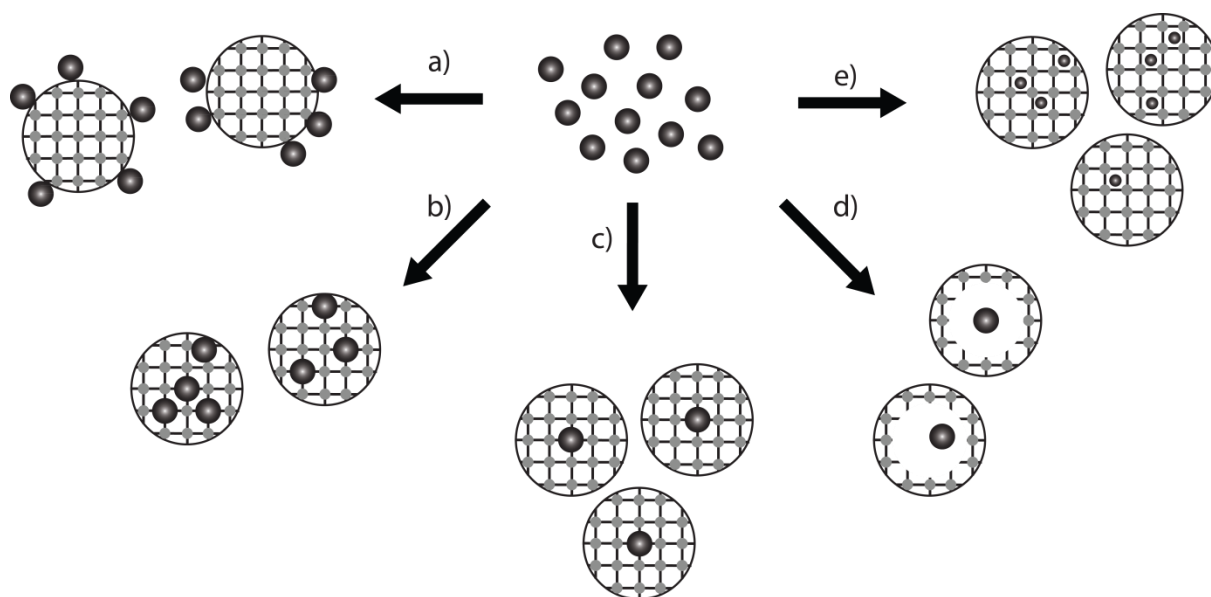
Figure 1-6. Synthesis of different core-shell MOF NPs: a) metal nanoparticles attached on the external surface of a MOF nanoparticle; b) multiple metal core materials covered by a MOF shell; c) one core metal material covered by a MOF shell; d) metal nanoparticle yolk and MOF shell nanoparticle; e) small metal core nanoparticles synthesized inside the pores of the MOF.

This synthesis concept is known as "ship-in-bottle" approach.[72] The MOF scaffold is loaded with a metal precursor solution in a first step, followed by a reduction step. In this way, different metals, *e.g.* Pd, Au, Pt, could be synthesized inside the MOF pores.[73-79] Another synthesis approach was developed by Fischer and co-workers based on metal organic chemical vapor deposition (MOCVD).[80-85] The main challenge of these core-shell synthesis approaches is the formation step in the pores of MOF NPs, which tend to agglomerate during this step.[72]

A better control of the synthesis obtaining well-defined core-shell nanoparticles can be realized by the separate synthesis of the core metal nanoparticles, followed by coating with the MOF shell material (Fig. 1-6).[86-90] Here the challenge is to provoke a heterogeneous nucleation of the MOF shell specifically on the core material. To address this challenge, the surface of the core material must be functionalized with linkers that can serve as anchoring point for the MOF crystallization. One interesting example reported by Furukawa and co-workers is the surface modification of gold nanorods with PEG-chains, followed by the coating of amorphous alumina and finally the synthesis of the MOF shell.[91] Another approach is the mercapto acetic acid (MAA)-functionalization of the metal core, joined by the step-by-step assembly [92-94] of the MOF shell [95-98]. The growth of the MOF shell is achieved through repeated growth cycles; immersion of the metal nanoparticle in the MOF metal precursor solution is followed by the organic linker solution. In this way, the MOF shell thickness can be controlled by the growth cycles. In terms of incorporating more than one core material and

controlling the spatial distribution of the core nanoparticles Hupp, Huo and co-workers reported an interesting work.[99] They achieved the spatial distribution of polyvinylpyrrolidone (PVP) modified metal nanoparticles within the MOF matrix by simply controlling the moment of addition. Tsung and co-workers could even demonstrate the synthesis of yolk-shell nanoparticles (Fig. 1-6).[100] Last but not least, MOFs and metal nanoparticles can be synthesized both separately and the metal nanoparticles can be attached to the MOF nanoparticle surface (Fig. 1-6).[72]

1.6. Biomedical application of MOF NPs

MOFs NPs as drug carrier

The delivery of drugs is an area of immense importance for human health. Main challenges in drug delivery include: low drug solubility, drug stability and toxicity, rapid metabolism and clearance, and most importantly a lack of selectivity. Nanocarriers hold the key to addressing these challenges. Incorporating drugs into nanoparticles offers exciting opportunities to redefine the pharmacokinetic properties, improving therapeutic efficiency and reducing side effects.[101-103] However, the key challenge to realize this potential is to advance the methodologies for the enhanced design of nanoparticles with the following prerequisites:[104]

- Biocombatibility
- High loading and protection of the drug molecules
- Zero premature release before reaching the target
- Efficient cellular uptake
- Efficient endosomal escape
- Controllable rate of release to achieve an effective local concentration
- Cell targeting

In the past decades, several strategies have been developed to design drug delivery materials to accomplish the above mentioned goals. Several drug delivery nanocarriers based on organic platforms such as liposomes, polymers, and dendrimers have been used as "smart" systems, capable of releasing therapeutic agents under physiological conditions.[105-107] In addition, recent discoveries are based on inorganic nanoparticles such as gold, iron oxide or mesoporous silica.[107] Each of these classes of nanomaterials has its own strengths and drawbacks. However, it can be stated that although significant progress has been made in the

synthesis of functional nanocarriers, the goals for the targeted release of drugs in the context of treating severe diseases with nanomaterials are still far from being met.

In this respect, MOFs are a unique class of porous hybrid solids with a wide range of compositions, structures, tunable pore sizes, and pore volumes. Their ability to combine both organic and inorganic design principles is one key advantage. Therefore, they could bridge the gap of purely inorganic and organic nanocarriers. The challenging task is the design of site-specific, stimuli-responsive controlled MOF drug delivery systems that - in addition - are biocompatible. Their successful application for medical purposes requires the development of MOF NPs with inner pore functionalization for controlled interaction with biologically active molecules as well as outer functionality for targeted cell uptake, triggered drug release, and with surface shielding against unwanted interactions inside the physiological environment (Fig. 1-7).
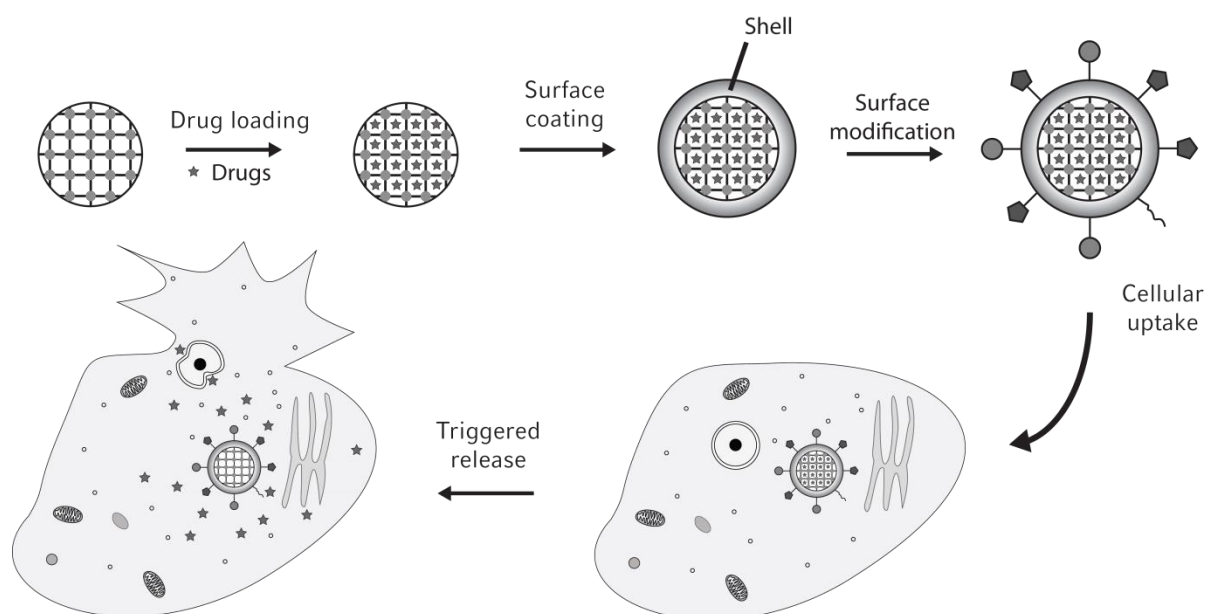

Figure 1-7. Synthesis path of a multifunctional MOF nanocarrier as well as the cell uptake of the nanocarrier and triggered drug release inside the cell.

In 2006, Horcajada *et al.* reported the first example of using MOF NPs as drug carrier system. Here, Ibuprofen has been encapsulated by simple adsorption into the mesoporous structures of MIL-100(Cr) and MIL-101(Cr).[108] Utilizing non-covalent drug delivery, where MOF NPs are loaded through the suspension with the drug, has several unique advantages. First of all, non-covalent drug delivery systems can be designed without direct modification of the drug, retaining its therapeutic efficiency. Secondly, optimizing the non-covalent drug transport for one drug can be applied to other drugs with similar properties, allowing for a broader assessment of how nanoparticles function *in vitro* and *in vivo*. Finally, non-covalently bound

drugs do not require additional external stimuli escape from the nanocarrier, but are rather released from the nanoparticle based on a triggered opening mechanism.

This approach has been extended in the following years by different researchers. Horcajada and co-workers tested different carboxylate-linked MOF NPs for their loading capacities of drugs as well as the release kinetics.[109] They could demonstrate that especially iron carboxylate MOF NPs are suitable for encapsulation and controlled delivery of a large number of drugs, such as busulfan, cidofovir, doxorubicin or azidothymidine triphosphate, but being at the same time biocompatible.[28, 110-111] Due to the high surface area of MOF NPs, new records of loading capacity for certain drugs in comparison to other nanosystems could be found.

Lin and co-workers reported an approach based on MOF decomposition behavior in physiological medium.[112-113]

Silica has been used to cover and to control the MOF NP degradation and the core-shell nanoparticle could further be functionalized by postsynthetic covalent attachment of targeting ligands.[113] The same group recently published their results of using UiO MOF NPs for the co-delivery of cisplatin and pooled siRNAs.[114] The interior of the particles was loaded with cisplatin and afterwards the external surface with siRNA. The efficiency of this multi-functionalized system compared to the individual compartments could be demonstrated.

Another functional system was reported by Zhang and co-workers using magnetic porous MOF for drug delivery.[115] A core-shell system was synthesized with a Fe_3O_4 nanorod core and HKUST-1. The shell material could be loaded with the anticancer drug Nimesulide.

One challenge by encapsulating sophisticated drugs into MOF NP structures is the small window size of the pores. Normally, MOF pores are like a space with a small entrance (pore window diameter) in comparison to the void itself (pore diameter). Weerapana, Tsung and co-workers proposed a ship-in-the-bottle strategy to address this challenge by simply forming the MOF structure around the drug.[116] This trapping strategy was demonstrated for ZIF-8 nanoparticles by encapsulating fluorescein or the anticancer drug campthothecin. The drawback of the ship-in-the-bottle strategy is that the stability of many drugs does not match with the condition of the MOF synthesis.

Another way of encapsulating a drug inside the MOF is to build up the network from bioactive linkers. The decomposition of the framework in the body leads to a release of the drug. This strategy was first proposed by the Serre group of Versailles, which constructs Bio-MIL-1, and afterwards many other examples, from nicotinic acid and iron as a metal source.[109, 117-118] The challenge of this strategy is the necessity of a bioactive linker, that is

suitable for the MOF synthesis and, at the same time, does not change its bioactivity. Since the contergan-scandal we know that even two enantiomers can have totally different biological effects and we should keep this in mind when changing the structure of bioactive molecules.

Recently, Lin's group could report the synthesis of Hf-porphyrin MOF NPs (named as DBP-UiO) being able to generate cytotoxic reactive oxygen species.[119] Instead of encapsulating a drug, a photosensitizer was used as linker molecule for the MOF NPs, which can be applied for photodynamic therapy. The high *in vivo* efficacy could be demonstrated by 50-fold tumor volume reduction in half of the mice and complete tumor eradication in the other half of the mice that were treated with the Hf-porphyrin MOF NPs.

The same group lately reported the *in vivo* performance of so-called nanoscale coordination polymers (NCPs).[120] They are built up from metal ions and organic bridging ligands – same design principle like MOFs - but in contrast to MOFs they are not crystalline. However, using cisplatin and oxaliplatin as linkers for NCPs and applying them against different cancer tumors, reveal, that NCPs could be a new promising nanocarrier class and should therefore be mentioned here.

Last but not least, MOF NPs can be used to transport gasotransmitters such as nitric oxide (NO) or hydrogen sulfide (H_2S). Morris' group of St. Andrews is the leading group for storing and release gasotransmitter molecules inside MOFs.[121, 109] The occurrence of coordinatively unsaturated metal sites (CUSs) and the high surface area of MOFs ensure a high uptake of the various gases. First results show promising bioactivity of such systems, which will be further improved and biologically tested in the future [109]. In this respect, Furukawa and co-workers recently reported a strategy for controllable NO release based on photoactive MOFs.[122]

MOF NPs for Diagnostics

Employing MOF NPs with diagnostic capabilities have the long-term objective to combine them with drug delivery properties in order to design theranostic MOF NPs (Fig. 1-8).
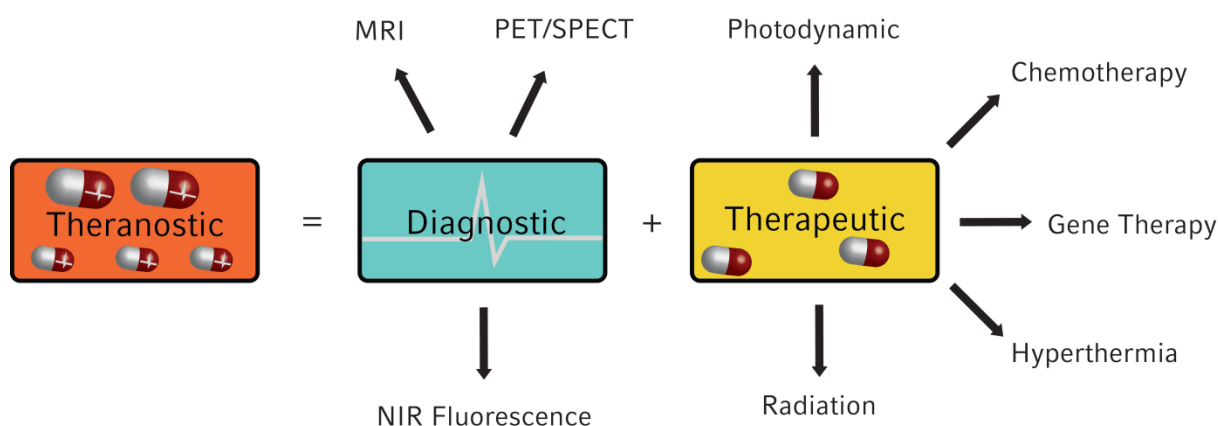
Figure 1-8. Schematic illustration of the theranostic idea (MRI = magnetic resonance imaging, PET = positron emission tomography, SPECT = single-photon emission computed tomography, NIR = near-infrared).

Magnetic resonance imaging (MRI) is a non-invasive method of mapping the internal structure and certain aspects of function within the body. It is based on the detection of nuclear spin reorientations in a magnetic field. To improve the visibility and with this the clinical diagnostics MRI contrast agents are used. They can be classified into two groups: (*i*) MRI contrast agents with positive signal enhancement by shortening the value of the T1 relaxation time or (*ii*) MRI contrast agents with negative signal enhancement by reducing the T2 signals.

The most commonly used compounds for contrast enhancement are Gadolinium-based contrast agents for positive signal enhancement. Lin and co-workers reported first the effectiveness of Gd^{3+}-based MOF NPs as T1-weighted contrast agents.[38] Other MOFs based on Gd^{3+} or even on Mn^{2+} have been published afterwards.[45, 49, 123-124] The main problem of these materials for their practical use is the poor chemical stability resulting in toxicity.

Another approach was proposed by Horcajada and co-workers by using iron-based MOF NPs as a negative signal enhancement contrast agent.[28] The key advantage of this strategy is, that the combination of the MRI diagnostic capability with drug delivery properties is straightforward.[28] The disadvantage of the lower visibility of these MRIs in comparison with gadolinium-based contrast agent images should be improved in the future.

Crystalline MOF NPs, which are used for optical imaging purposes are surprisingly rare.[109, 124] Optical imaging is widely used for *in vitro* and *in vivo* monitoring. For *in vivo* imaging near-infrared (NIR) dyes must be used because of the low absorption of biological tissues in this region. However, until now there is no example published so far. The straightforward way to functionalize a MOF with fluorescence properties is the covalent attachment of the dye. However, the fluorescence of the dye can be completely quenched after

incorporation into the MOF.[125-127] Such an example was reported by Lin and co-workers who functionalized MIL-101(Fe)-NH$_2$ with a BODIPY dye.[128]

The dye was not fluorescent due to quenching but exhibited strong turn-on fluorescence based on the decomposition of the MOF NPs in the cells, which induces the release of the BODIPY dyes. If this degradation of the MOF is specific to one analyte, the development of a sensitive optical MOF sensor is possible.[125] Lin and co-workers reported the design of a real-time pH MOF sensor for cells by covalent attachment of fluorescein isothiocyanate (FITC) to a UiO NMOF.[114] 4 wt% of FITC loading was chosen for the calibration curve due to the absence of FITC self-quenching at such amount. Incubation of fixed cells with these functionalized NPs revealed a pH change over time from 6.4 to 5.6, showing the intracellular endocytosis of the nanoparticles.

1.7. Toxicology of MOF NPs

Nanotoxicology refers to the toxicity of nanomaterials and is a very important but at the same time a complex research field. Health effects of nanoparticles have attracted considerable and increasing concern of the public society. With nanomaterials offering completely different properties than the bulk-material, the toxicity of these materials cannot be broken down to the chemical composition. They can be easily incorporated into organisms due to their small diameter and taken up by our smallest building block unit of life – the cell.[129] But not only direct incorporation is a problem since plants can take up nanoparticles from the soil and translocate them to organisms by the food chain.[130]

Nanotoxicology is a relative new field of interest. There are no results from long-term studies about the toxicology of materials in the nanometer scale. Long-term studies are needed especially for cancerogenious and statistically relevant investigations. There are short-term investigations which show that even inert materials like gold can have toxic effects on cells in the nanometer scale.[130] This compels us to handle each material in different nanometer-size and shape as a new material with unknown effects on living tissue. Furthermore, it has to be distinguished between acute and chronic exposure of the nanoparticles.

The toxicity of nanoparticles is depending on their size [131], shape [132], surface-area [133], material [134] and amount [135]. Because the dose is directly related to exposure time and the concentration of the substance, it is expected that a higher dose causes a higher toxicity of the particles. But generally it could be shown that the effects on the organism do not correlate with the mass dose but rather with the surface area of the particles.[136] For example, nanoparticles can adsorb proteins or other substances in the cell and cause changes in their structure, transforming

proteins to work unspecifically or inhibit their function.[137] This can cause irreversible damages to cells or tissues. Another important factor is the size depending toxicity of the particles, which determines the distribution of them in the human body. It could be shown that ultra-fine titanium dioxide particles were taken up significantly faster and had a faster clearance rate than fine titanium dioxide particles in the lung. Moreover, the shape of these materials can have an important influence in their toxicological effect.

Shape depending toxicology is already known from asbestos which then was a commonly used thermal insulator and robust material. Its dangers were not taken seriously first, due to its long-term cancer hazard. The long and very thin fibers of which asbestos is built up, can find their way into the alveoli of the lung and cause a chronic inflammatory. The lung's alveolar macrophages (dust cells) have the task to wrap around external particles like dust or soot and remove them from the very sensitive alveoli. In the case of asbestos fibers, it is not possible for these macrophages to remove the fibers if they have a width/length ratio larger than 3:1. This leads to the chronic inflammatory of the lung's tissue which can result in lung cancer for the long term. Similar size and shape depending effects can be expected for a variety of nanomaterials. Further, with nanomaterials having very active structured surfaces their influence on special tissues is widely unknown.

For investigation of the toxicological potential of these kinds of materials, it is important to have reliable and systematic methods which give information about the destination and influence on the surrounding tissue. At the moment the toxicological potential of a substance is determined by toxicokinetics, which describe the absorption of the substance by the skin or other organs, its distribution in the bloodstream, metabolism and its excretion. Both acute and chronical toxicities are also very important parameters for the toxicological potential of a substance. Further, long-term effects like cancerogenous, genotoxicity or neurotoxicity have to be well known until a substance can be introduced. All these studies are very expensive and take a long time until statistically relevant and reliable results can be received. With respect to MOF NPs, many used metal salts and linkers are toxic and not biocompatible. But the versatility of the MOFs also gives the chance to build up a whole new set of biocompatible MOFs. It is worth to note that the composition of MOF NPs is not the only important aspect which has to be considered in terms of toxicology (see above). Furthermore toxicology has to be determined in dependence of shape, size and solubility of these MOFs in tissues. This requires adjustment of the well-established toxicological studies and should be done in the future.

All in all, until now nanomaterials and their general effect on organisms has not yet been well investigated and understood. Each nanomaterial has to be examined like a new material in dependence of its physical and chemical properties. Further, with MOF nanomaterials often consisting of toxic or carcinogenic metal ions and linker substances, even their composition for biological applications is an important issue. At the moment, there are a few MOF NPs which are claimed to be biocompatible proven by the use of harmless metal salts and biologically used linkers [109]. Thereby, it has not been taken into account what these particles' shapes and nanostructured surfaces can cause in organisms. Hence, deeper standardized toxicological studies developed by medical scientists and pharmacist should be introduced and used.

1.8. References

[1]   J. F. Gomes, R. M. Miranda, T. J. Santos, P. A. Carvalho, *Journal of toxicology and environmental health. Part A* **2014**, *77*, 924-930.

[2]   B. M. Simonet, M. Valcárcel, *Anal Bioanal Chem* **2009**, *393*, 17-21.

[3]   N. Tepe, M. Bau, *The Science of the total environment* **2014**, *488-489*, 243-251.

[4]   J. E. Johnson, W. Chiu, *Current Opinion in Structural Biology* **2000**, *10*, 229-235.

[5]   G. Nichols, S. Byard, M. J. Bloxham, J. Botterill, N. J. Dawson, A. Dennis, V. Diart, N. C. North, J. D. Sherwood, *Journal of Pharmaceutical Sciences* **2002**, *91*, 2103-2109.

[6]   K. Dick, T. Dhanasekaran, Z. Zhang, D. Meisel, *Journal of the American Chemical Society* **2002**, *124*, 2312-2317.

[7]   W. L. Barnes, A. Dereux, T. W. Ebbesen, *Nature* **2003**, *424*, 824-830.

[8]   S. Makhlouf, M. Kassem, M. A. Abdel-Rahim, *J Mater Sci* **2009**, *44*, 3438-3444.

[9]   H. Yun, X. Liu, T. Paik, D. Palanisamy, J. Kim, W. D. Vogel, A. J. Viescas, J. Chen, G. C. Papaefthymiou, J. M. Kikkawa, M. G. Allen, C. B. Murray, *ACS nano* **2014**, *8*, 12323-12337.

[10]   X. Zhou, W. Xu, G. Liu, D. Panda, P. Chen, *Journal of the American Chemical Society* **2010**, *132*, 138-146.

[11]   C. Carlson, S. M. Hussain, A. M. Schrand, L. K. Braydich-Stolle, K. L. Hess, R. L. Jones, J. J. Schlager, *The Journal of Physical Chemistry B* **2008**, *112*, 13608-13619.

[12]   A. Albanese, P. S. Tang, W. C. Chan, *Annual Review of Biomedical Engineering* **2012**, *14*, 1-16.

[13]   C. C. D. Wang, W. C. H. Choy, C. Duan, D. D. S. Fung, W. E. I. Sha, F.-X. Xie, F. Huang, Y. Cao, *Journal of Materials Chemistry* **2012**, *22*, 1206-1211.

[14]   A. P. Alivisatos, *Science* **1996**, *271*, 933-937.

[15]   H. J. Ensikat, P. Ditsche-Kuru, C. Neinhuis, W. Barthlott, *Beilstein Journal of Nanotechnology* **2011**, *2*, 152-161.

[16]   A. Marmur, *Langmuir* **2004**, *20*, 3517-3519.

[17]   S. Link, M. A. El-Sayed, *The Journal of Physical Chemistry B* **1999**, *103*, 8410-8426.

[18]   E. Theocharous, R. Deshpande, A. C. Dillon, J. Lehman, *Appl. Opt.* **2006**, *45*, 1093-1097.

[19]   J. Liu, L. Chen, H. Cui, J. Zhang, L. Zhang, C.-Y. Su, *Chemical Society Reviews* **2014**, *43*, 6011-6061.

[20]   Y. Liu, N. Wang, J. H. Pan, F. Steinbach, J. Caro, *Journal of the American Chemical Society* **2014**, *136*, 14353-14356.

[21]   W. Lin, W. J. Rieter, K. M. L. Taylor, *Angewandte Chemie (International ed. in English)* **2009**, *48*, 650-658.

[22]   T. Chalati, P. Horcajada, R. Gref, P. Couvreur, C. Serre, *Journal of Materials Chemistry* **2011**, *21*, 2220-2227.

[23]   X. Sun, S. Dong, E. Wang, *Journal of the American Chemical Society* **2005**, *127*, 13102-13103.

[24]   M. Oh, C. A. Mirkin, *Nature* **2005**, *438*, 651-654.

[25]   J. Huo, M. Brightwell, S. El Hankari, A. Garai, D. Bradshaw, *Journal of Materials Chemistry A* **2013**, *1*, 15220-15223.

[26]   L. H. Wee, M. R. Lohe, N. Janssens, S. Kaskel, J. A. Martens, *Journal of Materials Chemistry* **2012**, *22*, 13742-13746.

[27]   Y. Pan, Y. Liu, G. Zeng, L. Zhao, Z. Lai, *Chemical Communications* **2011**, *47*, 2071-2073.

[28]   P. Horcajada, T. Chalati, C. Serre, B. Gillet, C. Sebrie, T. Baati, J. F. Eubank, D. Heurtaux, P. Clayette, C. Kreuz, J.-S. Chang, Y. K. Hwang, V. Marsaud, P.-N. Bories, L. Cynober, S. Gil, G. Ferey, P. Couvreur, R. Gref, *Nat Mater* **2010**, *9*, 172-178.

[29]   A. Sonnauer, F. Hoffmann, M. Fröba, L. Kienle, V. Duppel, M. Thommes, C. Serre, G. Férey, N. Stock, *Angewandte Chemie International Edition* **2009**, *48*, 3791-3794.

[30]   P. Horcajada, H. Chevreau, D. Heurtaux, F. Benyettou, F. Salles, T. Devic, A. Garcia-Marquez, C. Yu, H. Lavrard, C. L. Dutson, E. Magnier, G. Maurin, E. Elkaim, C. Serre, *Chemical Communications* **2014**, *50*, 6872-6874.

[31]   Z. Ni, R. I. Masel, *Journal of the American Chemical Society* **2006**, *128*, 12394-12395.

[32]   A. García Márquez, A. Demessence, A. E. Platero-Prats, D. Heurtaux, P. Horcajada, C. Serre, J.-S. Chang, G. Férey, V. A. de la Peña-O'Shea, C. Boissière, D. Grosso, C. Sanchez, *European Journal of Inorganic Chemistry* **2012**, *2012*, 5165-5174.

[33]   S. H. Jhung, J. H. Lee, J. W. Yoon, C. Serre, G. Férey, J. S. Chang, *Advanced Materials* **2007**, *19*, 121-124.

[34]   N. Stock, S. Biswas, *Chemical Reviews* **2011**, *112*, 933-969.

[35]   L.-G. Qiu, Z.-Q. Li, Y. Wu, W. Wang, T. Xu, X. Jiang, *Chemical Communications* **2008**, 3642-3644.

[36]   W.-J. Son, J. Kim, J. Kim, W.-S. Ahn, *Chemical Communications* **2008**, 6336-6338.

[37] S. Vaucher, M. Li, S. Mann, *Angewandte Chemie International Edition* **2000**, *39*, 1793-1796.

[38] W. J. Rieter, K. M. L. Taylor, H. An, W. Lin, W. Lin, *Journal of the American Chemical Society* **2006**, *128*, 9024-9025.

[39] T. Tsuruoka, S. Furukawa, Y. Takashima, K. Yoshida, S. Isoda, S. Kitagawa, *Angewandte Chemie International Edition* **2009**, *48*, 4739-4743.

[40] S. Diring, S. Furukawa, Y. Takashima, T. Tsuruoka, S. Kitagawa, *Chemistry of Materials* **2010**, *22*, 4531-4538.

[41] A. Schaate, P. Roy, A. Godt, J. Lippke, F. Waltz, M. Wiebcke, P. Behrens, *Chemistry – A European Journal* **2011**, *17*, 6643-6651.

[42] G. Wißmann, A. Schaate, S. Lilienthal, I. Bremer, A. M. Schneider, P. Behrens, *Microporous and Mesoporous Materials* **2012**, *152*, 64-70.

[43] T. Uemura, S. Kitagawa, *Journal of the American Chemical Society* **2003**, *125*, 7814-7815.

[44] N. Kerbellec, L. Catala, C. Daiguebonne, A. Gloter, O. Stephan, J.-C. Bunzli, O. Guillou, T. Mallah, *New Journal of Chemistry* **2008**, *32*, 584-587.

[45] K. M. L. Taylor, A. Jin, W. Lin, *Angewandte Chemie International Edition* **2008**, *47*, 7722-7725.

[46] S. Furukawa, J. Reboul, S. Diring, K. Sumida, S. Kitagawa, *Chemical Society Reviews* **2014**.

[47] A. Carné-Sánchez, I. Imaz, M. Cano-Sarabia, D. Maspoch, *Nat Chem* **2013**, *5*, 203-211.

[48] D. Tanaka, A. Henke, K. Albrecht, M. Moeller, K. Nakagawa, S. Kitagawa, J. Groll, *Nat Chem* **2010**, *2*, 410-416.

[49] M. D. Rowe, D. H. Thamm, S. L. Kraft, S. G. Boyes, *Biomacromolecules* **2009**, *10*, 983-993.

[50] B. Liu, M. Ma, D. Zacher, A. Bétard, K. Yusenko, N. Metzler-Nolte, C. Wöll, R. A. Fischer, *Journal of the American Chemical Society* **2011**, *133*, 1734-1737.

[51] S. Jung, Y. Kim, S.-J. Kim, T.-H. Kwon, S. Huh, S. Park, *Chemical Communications* **2011**, *47*, 2904-2906.

[52] X. W. Lou, Y. Wang, C. Yuan, J. Y. Lee, L. A. Archer, *Advanced Materials* **2006**, *18*, 2325-2329.

[53] J. Yu, H. Yu, H. Guo, M. Li, S. Mann, *Small* **2008**, *4*, 87-91.

[54]   S. E. Skrabalak, J. Chen, Y. Sun, X. Lu, L. Au, L. M. Cobley, Y. Xia, *Accounts of chemical research* **2008**, *41*, 1587-1595.

[55]   F. M. Hinterholzinger, A. Ranft, J. M. Feckl, B. Ruhle, T. Bein, B. V. Lotsch, *Journal of Materials Chemistry* **2012**, *22*, 10356-10362.

[56]   A. Huang, N. Wang, C. Kong, J. Caro, *Angewandte Chemie International Edition* **2012**, *51*, 10551-10555.

[57]   G. Xu, K. Otsubo, T. Yamada, S. Sakaida, H. Kitagawa, *Journal of the American Chemical Society* **2013**, *135*, 7438-7441.

[58]   R. Krishna, J. R. Long, *The Journal of Physical Chemistry C* **2011**, *115*, 12941-12950.

[59]   R. Ostermann, J. Cravillon, C. Weidmann, M. Wiebcke, B. M. Smarsly, *Chemical Communications* **2011**, *47*, 442-444.

[60]   N. Yanai, M. Sindoro, J. Yan, S. Granick, *Journal of the American Chemical Society* **2012**, *135*, 34-37.

[61]   M. Rose, B. Böhringer, M. Jolly, R. Fischer, S. Kaskel, *Advanced Engineering Materials* **2011**, *13*, 356-360.

[62]   P. Pachfule, B. K. Balan, S. Kurungot, R. Banerjee, *Chemical Communications* **2012**, *48*, 2009-2011.

[63]   N. Liu, Y. Yao, J. Cha, M. McDowell, Y. Han, Y. Cui, *Nano Res.* **2012**, *5*, 109-116.

[64]   H. J. Lee, W. Cho, M. Oh, *Chemical Communications* **2012**, *48*, 221-223.

[65]   T. Ben, C. Lu, C. Pei, S. Xu, S. Qiu, *Chemistry – A European Journal* **2012**, *18*, 10250-10253.

[66]   S. Cao, G. Gody, W. Zhao, S. Perrier, X. Peng, C. Ducati, D. Zhao, A. K. Cheetham, *Chemical Science* **2013**, *4*, 3573-3577.

[67]   W.-w. Zhan, Q. Kuang, J.-z. Zhou, X.-j. Kong, Z.-x. Xie, L.-s. Zheng, *Journal of the American Chemical Society* **2013**, *135*, 1926-1933.

[68]   J. Reboul, S. Furukawa, N. Horike, M. Tsotsalas, K. Hirai, H. Uehara, M. Kondo, N. Louvain, O. Sakata, S. Kitagawa, *Nat Mater* **2012**, *11*, 717-723.

[69]   R. Ameloot, F. Vermoortele, W. Vanhove, M. B. J. Roeffaers, B. F. Sels, D. E. De Vos, *Nat Chem* **2011**, *3*, 382-387.

[70]   R. Ameloot, E. Gobechiya, H. Uji-i, J. A. Martens, J. Hofkens, L. Alaerts, B. F. Sels, D. E. De Vos, *Advanced Materials* **2010**, *22*, 2685-2688.

[71]   R. Ghosh Chaudhuri, S. Paria, *Chemical Reviews* **2011**, *112*, 2373-2433.

[72]   Q.-L. Zhu, Q. Xu, *Chemical Society Reviews* **2014**, *43*, 5468-5512.

[73]   Y. K. Hwang, D.-Y. Hong, J.-S. Chang, S. H. Jhung, Y.-K. Seo, J. Kim, A. Vimont, M. Daturi, C. Serre, G. Férey, *Angewandte Chemie International Edition* **2008**, *47*, 4144-4148.

[74]   D. Esken, X. Zhang, O. I. Lebedev, F. Schroder, R. A. Fischer, *Journal of Materials Chemistry* **2009**, *19*, 1314-1319.

[75]   A. Aijaz, T. Akita, N. Tsumori, Q. Xu, *Journal of the American Chemical Society* **2013**, *135*, 16356-16359.

[76]   A. Aijaz, A. Karkamkar, Y. J. Choi, N. Tsumori, E. Rönnebro, T. Autrey, H. Shioyama, Q. Xu, *Journal of the American Chemical Society* **2012**, *134*, 13926-13929.

[77]   Q.-L. Zhu, J. Li, Q. Xu, *Journal of the American Chemical Society* **2013**, *135*, 10210-10213.

[78]   M. Sabo, A. Henschel, H. Frode, E. Klemm, S. Kaskel, *Journal of Materials Chemistry* **2007**, *17*, 3827-3832.

[79]   S. Opelt, S. Türk, E. Dietzsch, A. Henschel, S. Kaskel, E. Klemm, *Catalysis Communications* **2008**, *9*, 1286-1290.

[80]   S. Hermes, M.-K. Schröter, R. Schmid, L. Khodeir, M. Muhler, A. Tissler, R. W. Fischer, R. A. Fischer, *Angewandte Chemie International Edition* **2005**, *44*, 6237-6241.

[81]   M. Muller, O. I. Lebedev, R. A. Fischer, *Journal of Materials Chemistry* **2008**, *18*, 5274-5281.

[82]   F. Schröder, D. Esken, M. Cokoja, M. W. E. van den Berg, O. I. Lebedev, G. Van Tendeloo, B. Walaszek, G. Buntkowsky, H.-H. Limbach, B. Chaudret, R. A. Fischer, *Journal of the American Chemical Society* **2008**, *130*, 6119-6130.

[83]   F. Schröder, S. Henke, X. Zhang, R. A. Fischer, *European Journal of Inorganic Chemistry* **2009**, *2009*, 3131-3140.

[84]   M. Meilikhov, K. Yusenko, A. Torrisi, B. Jee, C. Mellot-Draznieks, A. Pöppl, R. A. Fischer, *Angewandte Chemie International Edition* **2010**, *49*, 6212-6215.

[85]   D. Esken, S. Turner, O. I. Lebedev, G. Van Tendeloo, R. A. Fischer, *Chemistry of Materials* **2010**, *22*, 6393-6401.

[86]   J. H. Cavka, S. Jakobsen, U. Olsbye, N. Guillou, C. Lamberti, S. Bordiga, K. P. Lillerud, *Journal of the American Chemical Society* **2008**, *130*, 13850-13851.

[87]   H. Furukawa, F. Gándara, Y.-B. Zhang, J. Jiang, W. L. Queen, M. R. Hudson, O. M. Yaghi, *Journal of the American Chemical Society* **2014**, *136*, 4369-4381.

[88]   K. Na, K. M. Choi, O. M. Yaghi, G. A. Somorjai, *Nano Letters* **2014**, *14*, 5979-5983.

[89]   P. Hu, J. Zhuang, L.-Y. Chou, H. K. Lee, X. Y. Ling, Y.-C. Chuang, C.-K. Tsung, *Journal of the American Chemical Society* **2014**, *136*, 10561-10564.

[90]   R. Pérez, B. Albero, J. Tadeo, E. Molero, C. Sánchez-Brunete, *Anal Bioanal Chem* **2015**, 1-12.

[91]   K. Khaletskaya, J. Reboul, M. Meilikhov, M. Nakahama, S. Diring, M. Tsujimoto, S. Isoda, F. Kim, K.-i. Kamei, R. A. Fischer, S. Kitagawa, S. Furukawa, *Journal of the American Chemical Society* **2013**, *135*, 10998-11005.

[92]   O. Shekhah, H. Wang, S. Kowarik, F. Schreiber, M. Paulus, M. Tolan, C. Sternemann, F. Evers, D. Zacher, R. A. Fischer, C. Wöll, *Journal of the American Chemical Society* **2007**, *129*, 15118-15119.

[93]   O. Shekhah, H. Wang, D. Zacher, R. A. Fischer, C. Wöll, *Angewandte Chemie International Edition* **2009**, *48*, 5038-5041.

[94]   O. Shekhah, H. Wang, M. Paradinas, C. Ocal, B. Schupbach, A. Terfort, D. Zacher, R. A. Fischer, C. Woll, *Nat Mater* **2009**, *8*, 481-484.

[95]   F. Ke, L.-G. Qiu, Y.-P. Yuan, X. Jiang, J.-F. Zhu, *Journal of Materials Chemistry* **2012**, *22*, 9497-9500.

[96]   F. Ke, J. Zhu, L.-G. Qiu, X. Jiang, *Chemical Communications* **2013**, *49*, 1267-1269.

[97]   T.-H. Park, K. J. Lee, S. Hwang, J. Yoon, C. Woell, J. Lahann, *Advanced Materials* **2014**, *26*, 2883-2888.

[98]   M. E. Silvestre, M. Franzreb, P. G. Weidler, O. Shekhah, C. Wöll, *Advanced Functional Materials* **2013**, *23*, 1210-1213.

[99]   G. Lu, S. Li, Z. Guo, O. K. Farha, B. G. Hauser, X. Qi, Y. Wang, X. Wang, S. Han, X. Liu, J. S. DuChene, H. Zhang, Q. Zhang, X. Chen, J. Ma, S. C. J. Loo, W. D. Wei, Y. Yang, J. T. Hupp, F. Huo, *Nat Chem* **2012**, *4*, 310-316.

[100]   C.-H. Kuo, Y. Tang, L.-Y. Chou, B. T. Sneed, C. N. Brodsky, Z. Zhao, C.-K. Tsung, *Journal of the American Chemical Society* **2012**, *134*, 14345-14348.

[101]   M. Ferrari, *Nat Rev Cancer* **2005**, *5*, 161-171.

[102]   D. Peer, J. M. Karp, S. Hong, O. C. Farokhzad, R. Margalit, R. Langer, *Nat Nano* **2007**, *2*, 751-760.

[103]   M. E. Davis, Z. Chen, D. M. Shin, *Nat Rev Drug Discov* **2008**, *7*, 771-782.

[104]   J. L. Vivero-Escoto, I. I. Slowing, B. G. Trewyn, V. S. Y. Lin, *Small* **2010**, *6*, 1952-1967.

[105]   X. Chen, S. S. Gambhir, J. Cheon, *Accounts of Chemical Research* **2011**, *44*, 841-841.

[106]   *Chemical Society Reviews* **2012**, *41*, 2521-2521.

[107] Z. Li, J. C. Barnes, A. Bosoy, J. F. Stoddart, J. I. Zink, *Chemical Society Reviews* **2012**, *41*, 2590-2605.

[108] P. Horcajada, C. Serre, M. Vallet-Regí, M. Sebban, F. Taulelle, G. Férey, *Angewandte Chemie International Edition* **2006**, *45*, 5974-5978.

[109] P. Horcajada, R. Gref, T. Baati, P. K. Allan, G. Maurin, P. Couvreur, G. Férey, R. E. Morris, C. Serre, *Chemical Reviews* **2011**, *112*, 1232-1268.

[110] T. Baati, L. Njim, F. Neffati, A. Kerkeni, M. Bouttemi, R. Gref, M. F. Najjar, A. Zakhama, P. Couvreur, C. Serre, P. Horcajada, *Chemical Science* **2013**, *4*, 1597-1607.

[111] C. Tamames-Tabar, D. Cunha, E. Imbuluzqueta, F. Ragon, C. Serre, M. J. Blanco-Prieto, P. Horcajada, *Journal of Materials Chemistry B* **2014**, *2*, 262-271.

[112] R. C. Huxford, J. D. Rocca, W. Lin, *Current opinion in chemical biology* **2010**, *14*, 262-268.

[113] W. J. Rieter, K. M. Pott, K. M. L. Taylor, W. Lin, *Journal of the American Chemical Society* **2008**, *130*, 11584-11585.

[114] C. He, K. Lu, D. Liu, W. Lin, *Journal of the American Chemical Society* **2014**, *136*, 5181-5184.

[115] F. Ke, Y.-P. Yuan, L.-G. Qiu, Y.-H. Shen, A.-J. Xie, J.-F. Zhu, X.-Y. Tian, L.-D. Zhang, *Journal of Materials Chemistry* **2011**, *21*, 3843-3848.

[116] J. Zhuang, C.-H. Kuo, L.-Y. Chou, D.-Y. Liu, E. Weerapana, C.-K. Tsung, *ACS nano* **2014**, *8*, 2812-2819.

[117] S. R. Miller, D. Heurtaux, T. Baati, P. Horcajada, J.-M. Greneche, C. Serre, *Chemical Communications* **2010**, *46*, 4526-4528.

[118] S. R. Miller, E. Alvarez, L. Fradcourt, T. Devic, S. Wuttke, P. S. Wheatley, N. Steunou, C. Bonhomme, C. Gervais, D. Laurencin, R. E. Morris, A. Vimont, M. Daturi, P. Horcajada, C. Serre, *Chemical Communications* **2013**, *49*, 7773-7775.

[119] K. Lu, C. He, W. Lin, *Journal of the American Chemical Society* **2014**, *136*, 16712-16715.

[120] D. Liu, C. Poon, K. Lu, C. He, W. Lin, *Nature communications* **2014**, *5*, 4182.

[121] B. Xiao, P. S. Wheatley, X. Zhao, A. J. Fletcher, S. Fox, A. G. Rossi, I. L. Megson, S. Bordiga, L. Regli, K. M. Thomas, R. E. Morris, *Journal of the American Chemical Society* **2007**, *129*, 1203-1209.

[122] S. Diring, D. O. Wang, C. Kim, M. Kondo, Y. Chen, S. Kitagawa, K.-i. Kamei, S. Furukawa, *Nature communications* **2013**, *4*.

[123] K. M. L. Taylor, W. J. Rieter, W. Lin, *Journal of the American Chemical Society* **2008**, *130*, 14358-14359.

[124] J. Della Rocca, D. Liu, W. Lin, *Accounts of Chemical Research* **2011**, *44*, 957-968.

[125] F. M. Hinterholzinger, B. Rühle, S. Wuttke, K. Karaghiosoff, T. Bein, *Sci. Rep.* **2013**, *3*.

[126] S. Wuttke, C. Dietl, F. M. Hinterholzinger, H. Hintz, H. Langhals, T. Bein, *Chemical Communications* **2014**, *50*, 3599-3601.

[127] H. H. C. Dietl, B. Rühle, J. S. Günne, H. Langhals, S. Wuttke, *Chem. Eur. J.* **2015**.

[128] K. M. L. Taylor-Pashow, J. D. Rocca, Z. Xie, S. Tran, W. Lin, *Journal of the American Chemical Society* **2009**, *131*, 14261-14263.

[129] H. Zhu, J. Han, J. Q. Xiao, Y. Jin, *Journal of Environmental Monitoring* **2008**, *10*, 713-717.

[130] U. Taylor, A. Barchanski, W. Garrels, S. Klein, W. Kues, S. Barcikowski, D. Rath, in *Nano-Biotechnology for Biomedical and Diagnostic Research, Vol. 733* (Eds.: E. Zahavy, A. Ordentlich, S. Yitzhaki, A. Shafferman), Springer Netherlands, **2012**, pp. 125-133.

[131] A. Ivask, I. Kurvet, K. Kasemets, I. Blinova, V. Aruoja, S. Suppi, H. Vija, A. Käkinen, T. Titma, M. Heinlaan, M. Visnapuu, D. Koller, V. Kisand, A. Kahru, *PLoS ONE* **2014**, *9*, e102108.

[132] A. Magrez, S. Kasas, V. Salicio, N. Pasquier, J. W. Seo, M. Celio, S. Catsicas, B. Schwaller, L. Forró, *Nano Letters* **2006**, *6*, 1121-1125.

[133] W. Wallace, M. Keane, D. Murray, W. Chisholm, A. Maynard, T.-m. Ong, in *Nanotechnology and Occupational Health* (Eds.: A. Maynard, D. H. Pui), Springer Netherlands, **2007**, pp. 23-38.

[134] C. Beer, R. Foldbjerg, Y. Hayashi, D. S. Sutherland, H. Autrup, *Toxicology Letters* **2012**, *208*, 286-292.

[135] C. Buzea, I. Pacheco, K. Robbie, *Biointerphases* **2007**, *2*, MR17-MR71.

[136] K. Donaldson, V. Stone, *Annali dell'Istituto superiore di sanita* **2003**, *39*, 405-410.

[137] S. R. Saptarshi, A. Duschl, A. L. Lopata, *Journal of Nanobiotechnology* **2013**, *11*, 26.

2. Characterization techniques

A complete and detailed characterization of the produced materials, composites and their effects and possible applications has to be part of any scientific work or publication. The different characterization techniques and their theoretical background are shown in this chapter.

Investigations on the crystallinity of modified and unmodified nanoparticles were done using X-ray diffractometry (XRD). Infrared (IR) and Raman vibrational spectroscopy as well as nuclear magnetic resonance (NMR) spectroscopy was used to examine the composition of synthesized materials. UV-vis and Fluorescence spectroscopy (FS) revealed information about optical properties and was used further to determine loading and release behavior of dye molecules on- or into the MOF nanoparticles. Nitrogen sorption measurements were used to gain information about the porous structure (surface area, pore size, pore volume…) and electron microscopy (TEM/SEM) provided images of the particles and gave further evidence of morphology and structural details. Thermogravimetric analysis (TGA) was used to show the behavior under thermal treatment. The surface charge was investigated by using zeta potential measurement and the particle size was determined by means of dynamic light scattering (DLS) and/or fluorescence cross correlation spectroscopy (FCS), respectively. Additionally, confocal laser scanning microscopy (CLSM) and magnetic resonance imaging (MRI) was performed for investigations on particle-cell interactions and imaging properties.

2.1. X-ray diffraction (XRD)

XRD is a standard non-destructive technique to identify crystalline material. The distance between the lattice planes of these materials is in the same order of magnitude as the wavelength of X-rays (10^{-8} to 10^{-12} m), which is required for constructive or destructive interference, respectively. Therby, structural information as well as crystallite sizes can be gained from the occurring diffraction pattern.

The technique is based on monochromatic X-radiation, which is usually generated in a cathode ray tube. By heating a filament electrons are emitted and are accelerated towards a target anode (typically Cu, Mo or Co) using high voltage. The collision of the accelerated electrons with the anode material leads to the emission of a continuous radiation (Bremsstrahlung) and characteristic X-ray radiation. After filtering by a monochromator, the X-ray beam is focused on the sample and scattered by the regular array of atoms within the crystal lattice, creating a specific diffraction pattern for each material (Figure 2-1).
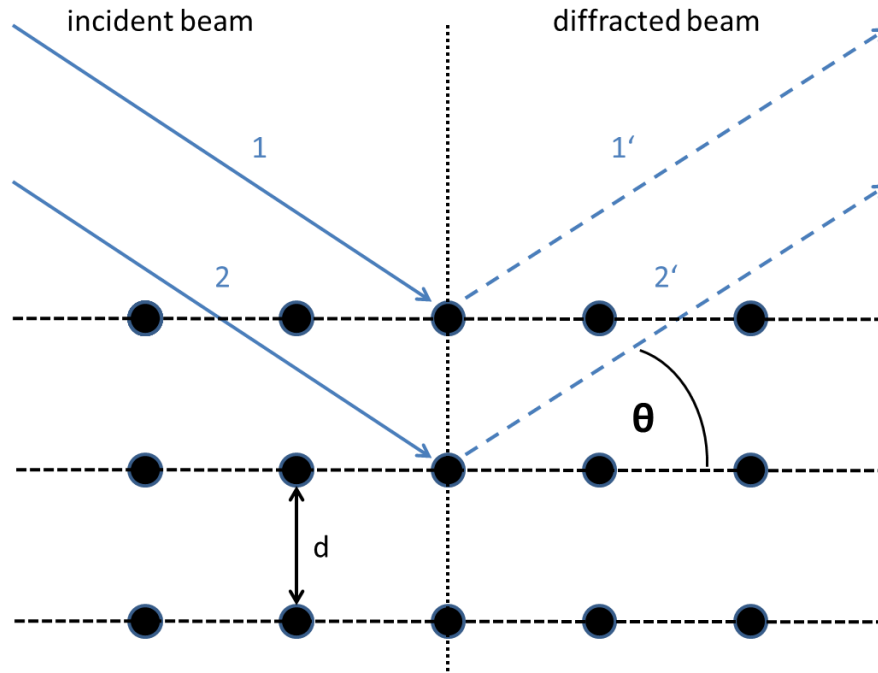
Figure 2-1. Schematic illustration of X-ray diffraction at a crystal lattice plane according to Bragg's relation; d: lattice plane spacing; θ: angle of incidence.

The incident beam hits the parallel crystal lattice planes under the Bragg angle θ. Interference of the scattered waves occurs either in a constructive or destructive way. Constructive wave interference appears only if the path length difference equals an integer multiple of the wavelength. Thus in many directions, the waves are cancelled out due destructive interference, but in some directions the Bragg law is satisfied:

$$n \cdot \lambda = 2d \; sin\theta \qquad\qquad (2\text{-}1)$$

Equation 2-1. Bragg's law; *n*: order of interference; *λ*: wavelength of X-rays; *d*: lattice plane spacing; θ: angle of incidence

Considering a perfect orientated crystalline sample, the diffraction pattern will show reflexes in exact intervals corresponding to the staggered lattice planes. Thus, structure determination is possible with single-crystal XRD measurement. The crystal is gradually rotated in the beam such that Bragg's law is fulfilled for every orientation. The occurring regular pattern exhibits full structural information about the sample.

In powders, every possible crystallographic orientation is represented in a statistic manner which leads to a disordered but characteristic diffraction pattern. Therefore, powder diffraction can be used to determine the crystallinity of the material as well as to analyze a crystalline sample by comparison to literature data. Furthermore, it is a worthy method in

structure determination of metal-organic frameworks via AASBU (automated assembly of secondary building units).[1]

As mentioned above, it is further possible to gain information about the crystallite size, which can be equated to particle size in the case of MOF NPs. It can be calculated by using the broadening of the reflections in the diffraction pattern. For this purpose, the Scherrer equation is used:

$$D = \frac{K\lambda}{\beta cos\theta}$$ (2-2)

Equation 2-2. Scherrer equation; D: mean size of the crystalline domains, K: dimensionless shape factor, β: full width at half maximum (FWHM) of the reflection corrected for the intrinsic instrumental broadening, λ: wavelength, θ: diffraction angle.

In this thesis, X-ray diffraction was measured with the STOE transmission diffractometer system Stadi MP with Cu Kα_1 radiation ($\lambda = 1.54060$ Å) and Ge(111) single crystal monochromator. Diffraction patterns were recorded with a DECTRIS solid state strip detector MYTHEN 1K in an omega-2-theta scan mode using a step size of 4.71° and a counting time of 80 s per step.

2.2. Dynamic light scattering (DLS)

Size determination of particles in suspension is possible with DLS.[2] Reliable values of measured hydrodynamic diameters of colloidal nanoparticles are thereby in the range between 1 and 1000 nm. As DLS measurements are based on the Brownian motion of the particles, the important feature is the size dependent diffusion behavior of particles in solution, which is defined in the Stokes-Einstein equation (2-3):

$$D = \frac{kT}{6\pi\eta R}$$ (2-3)

Equation 2-3. Stokes-Einstein equation; D: diffusion coefficient; T: temperature; η: viscosity; R: hydrodynamic radius; k: Boltzmann constant

Temperature T and viscosity of the solvent η are known parameter, an therefore, the hydrodynamic radius of the particles R only depends on their diffusion coefficient D. It depends on several parameters, including the ionic strength of the suspension, the texture of the particle surface, and the shape of the particles. Determination of the diffusion coefficient is done by interpreting the scattering intensity fluctuation data. Monochromatic visible light ($\lambda = 633$ nm) is focused on a sample loaded cuvette. The beam is scattered by the dispersed

particles and con- or destructive interference occurs after penetration of the cuvette. Brownian motion of the particles leads to fluent intensity changes in the diffraction pattern. The Zetasizer Nano system measures the rate of fluctuation and uses this to evaluate the hydrodynamic radius/diameter of the particles. The particle size distribution which is obtained by DLS measurements is based on intensity. This intensity-derived size distribution is suitable for small particles (size smaller than one-tenth of the wavelength of the illuminating light) in a suspension featuring monodispersity, and is well described by Rayleigh scattering. The Rayleigh approximation (2-4) presents the relation between the light scattering intensity I and the particle diameter $d = 2R$.

$$I \propto d^6 \qquad\qquad (2\text{-}4)$$

Equation 2-4. Rayleigh approximation, I: intensity of scattered light, d: particle diameter.

As the scattering intensity is proportional to d^6 (Equation 2-4), the contribution of huge particles to the scattering intensity is much higher as compared to small ones. This leads to an over-estimation of the size in polydisperse samples and thus needs to be considered in data evaluation. To solve this issue, the intensity-based measurement data of the DLS can also be presented as volume-weighted (d^3) or number-weighted (d) distributions.

DLS measurements in this work were performed on diluted suspensions using a Malvern Zetasizer-Nano instrument with a 4 mW He-Ne laser ($\lambda = 633$ nm) and an avalanche photo detector.

2.3. Zeta potential measurement

Zeta potential provides information about the external surface charge of particles in dispersion. The value is depending on the pH value and composition of medium as well as on the nature of the nanoparticles' external surface. Therefore, it is an important tool for the detection of modifications on the external surface of the nanoparticles.

The technique is based on the attraction of ions from the charged particles which form a surrounding dens ion layer (Stern layer). This is followed by a second layer built up from loosely attached ions of both charges (Figure 2-2). Within this "diffuse layer" an imaginary boundary occurs, which is called "slipping plane". The slipping plane is defined as the spherical barrier, where everything which is inside will move with the particle. Everything outside this barrier will be no influence the movement of the particle. The potential which occurs between stationary solution and mobile particle is known as the Zeta Potential ζ.[2, 3]
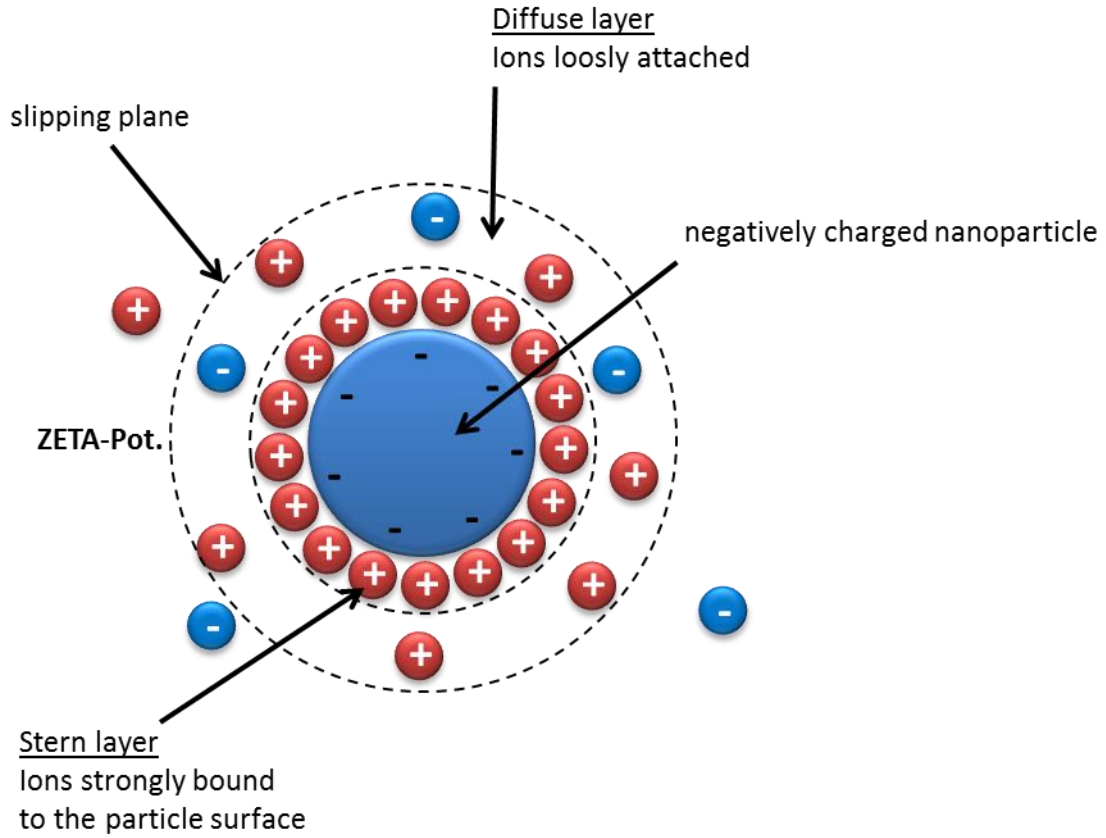
Figure 2-2. Schematic illustration of the spherical arrangement of ions around charged nanoparticles

The Zeta Potential is calculated by determining the electrophoretic mobility U_e of the particles and then applying the Henry equation:

$$U_e = \frac{2\varepsilon\zeta \cdot f(ka)}{3\eta}$$

(2-5)

Equation 2-5. Henry equation; U_e: electrophoretic mobility; ε: dielectric constant; $f(ka)$: Henry function; η: viscosity; ζ: zeta potential

Applying the Hückel approximation to the Henry equation which assumes small particles and low dielectric constant media, $f(ka)$ becomes 1 and can be removed from the equation. Thus, the Zeta Potential is only dependent of the electrophoretic mobility, which can be calculated from the velocity of the nanoparticles at known electric field.

$$U_e = \frac{v}{E}$$

(2-6)

Equation 2-6. Definition of the electrophoretic mobility μ_e; v: particle velocity; E: electric field

The measurement of the velocity is done using Laser Dopler Velocimetry (LDV). An electric field of known strength is applied to a capillary cell containing the particle suspension. The frequency shift of the laser light passing through the suspension is used to determine the velocity of the nanoparticles.

In this work, zeta potential is determained in specific biological relevant media or is plotted against the set pH value. In the latter case, the isoelectric point of the nanoparticles is a characteristic value, which is determined by the crossing of the X-axis (zeta potential equals zero). Zeta potential measurements were carried out on diluted suspensions (0.1 mg/mL) using a Malvern Zetasizer-Nano instrument with a 4 mW He-Ne laser (λ = 633 nm), an avalanche photo detector and an MPT-2 titration system.

2.4. Sorption measurement

Sorption measurements are a common tool to observe the properties of porous materials in matters of surface area, pore size and pore volume.[4] Reversible interactions between the surface area and inert gas molecules (physisorption) at a known partial pressure lead to characteristic isotherms which are classified according IUPAC.[5] All measurements of mesoporous MOF materials in this work were performed with nitrogen as an adsorptive.

In principle, a sample of the porous material is placed into a tube with known volume. The tube is evacuated and heated for a few hours to clean the nanoparticle surface from adsorbed molecules. Afterwards the measuring cell is cooled down to the temperature of liquid nitrogen (T = 77 K). Small amounts of nitrogen gas are injected stepwise. The gas is adsorbed by the pores and until equilibrium pressure occurs. Those pressures (expressed as partial pressure p/p_0) and the corresponding amounts of adsorbed gas are recorded. This is done until the value for the partial pressure reaches 1. That means that the equilibrium pressure p has reached the vapor pressure of the adsorptive p_0. The similar procedure is performed for desorption, with decreasing the partial pressure until 0.

The resulting isotherms are plotted as the amount of adsorbed nitrogen is a function of the relative pressure (Figure 2-3). The different types (I-VI) distinguish porous materials regarding pore structure and size, and the interactions of the adsorbed gas molecules with the adsorbent.
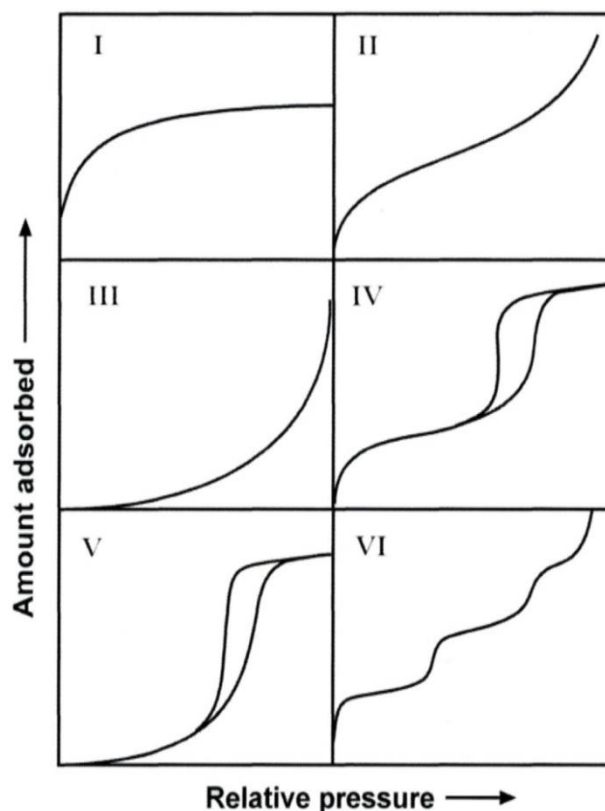
Figure 2-3. Types of sorption isotherms according to IUPAC classification.[6]

Type I isotherm shows a typical curve for microporous materials with a small external surface area. The curve reaches a maximum when the micropores are filled. Nonporous and macroporous solids with high energies of adsorption result in a type II isotherm. The first part of the isotherm represents the creation of a monolayer of the absorbed molecules. With increasing pressure multilayer are formed. Type III also shows nonporous and macroporous solids, but the weak surface-adsorptive interactions prevent the prior building of a monolayer. Type IV and V are reflecting mesoporous materials with strong (IV) and weak (V) surface-adsorptive interactions. The hysteresis loop is a result of the capillary condensation which takes place in mesoporous materials. Type VI shows the gradual formation of individual adsorbate layers, which is due to a multimodal pore distribution.

The specific surface area of metal-organic frameworks can be determined with the Brunnauer-Emmert-Teller theory which was developed in 1938.[7] It is a further development of the Langmuir models, in which exclusively monolayers are allowed.[8] Walton *et al*. showed in 2007 that the BET theory can be used for the evaluation of MOF surfaces by comparing the geometric surface area calculated from the crystal structure with the simulated adsorption isotherm.[9]

The BET isotherm model assumes multilayer adsorption, neglecting interactions of the adsorbates among each other. The initial monolayer serves as a substrate for further adsorption processes, and consequently a change in adsorption enthalpy between the first and the subsequent layers occurs. The model is mathematically given by Equation 2-7, with n_a being the amount of adsorbate, n_m the specific monolayer capacity and C the BET constant being exponentially related to the monolayer adsorption.

$$\frac{n_a}{n_m} = \frac{C \cdot \frac{p}{p_0}}{\left(1 - \frac{p}{p_0}\right)\left(1 + C - \frac{p}{p_0}\right)} \tag{2-7}$$

Equation 2-7. BET equation; n_a:amount of the adsorbate at pressure p, n_m:capacity of one monolayer, C: BET constant; p: equilibrium pressure; p_0: saturation vapor pressure of the adsorbate.

The BET method is the most widely used procedure for evaluating surface areas. To determine n_m only the linear form of the BET equation is valid, which is typically the case for low $\frac{p}{p_0}$ (0.0-0.3). Considering the linear form and taking into account the molecular cross-sectional area (σ_m), the BET surface area (A_s) can be calculated by Equation 2-8.

$$A_S = n_m N_A \sigma_m \tag{2-8}$$

Equation 2-8. Calculation of the BET surface are (A_S); N_A: Avogadro constant; σ_m: molecular cross-sectional area

Further, isotherms can be used to calculate the pore size distribution. Density functional theory (DFT) and Monte Carlo simulations are nowadays reliable tools for pore size analysis.[10] Based on fundamental principles of statistical mechanics they are able to describe the distribution of adsorbed materials and provide information on the local fluid structure at curved solid surface. Hence, different models for various pore shapes (slit, cylindrical and spherical) and material classes (such as zeolites, carbons and silicas) exist to determine the pore size and pore volume of porous materials.

Nitrogen sorption measurements in this work were either performed on Quantachrome Instruments NOVA 4000e or Autosorb at 77 K. For the measurements approximately 10 mg of a sample were outgassed at 120 °C and 10 mTorr for approximately 16 hours.

2.5. Thermogravimetric analysis (TGA)

Thermal stability of MOFs can be investigated by TGA.[11, 12] Furthermore it is a useful technique to evaluate the content of organic substance within a hybrid material. The sample is placed onto a thermo-balance in an electrically heated oven. A constant heating rate ($\beta = dT/dt$) is applied and the behavior of the sample up to 900 °C can be investigated under desired atmosphere such as nitrogen or synthetic air. A steady laminar flow of the chosen gas passes the sample and volatile components are removed from the heating chamber. The weight loss can be caused by evaporation of volatile molecules, desorption of incorporated molecules and the decomposition of the sample, respectively.

Thermogravimetric analysis was performed in this work with a thermo-microbalance (Netzsch, STA 449 C Jupiter) with a heating rate of 10 °C/min. Approximately 10 mg of the material were heated under synthetic air conditions with a flow rate of 25 mL/min.

2.6. Infrared spectroscopy (IR)

IR spectroscopy is based on absorption of electromagnetic waves in the infrared area. In this area molecule vibrations and/or rotations are encouraged depending on length and strength of the covalent bonds. The whole scope of infrared irradiation ranges over wave numbers from 10 cm^{-1} to 14000 cm^{-1}. It can be divided into three regions; near-infrared (14000 cm^{-1} - 4000 cm^{-1}), mid-infrared (4000 cm^{-1} - 400 cm^{-1}) and far-infrared (400 cm^{-1} - 10 cm^{-1}). Characteristic infrared absorption bands of the materials, studied in this thesis appear in the mid-infrared area. Due to the typical stimulation energies, it is possible to determine different functional groups in molecules. To describe the transitions between different vibrational states, the quantum mechanical model of the anharmonic oscillator is applied (Figure 2-4).
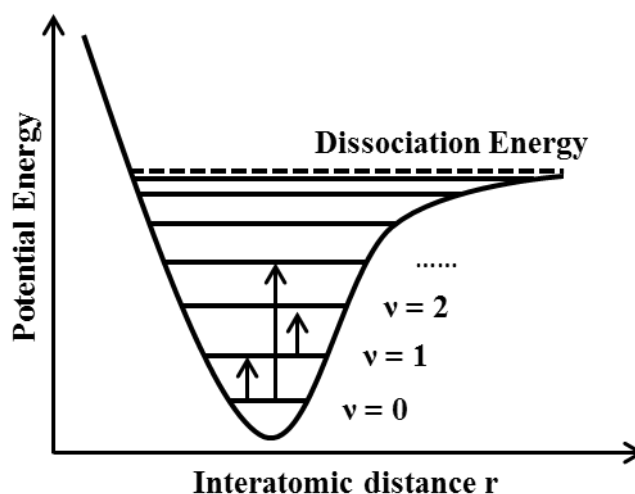
Figure 2-4. Potential of the anharmoic oscillator

If the wavelength of the infrared light fits the energy between different vibrational states it is absorbed, resulting in characteristic vibrational bands in the IR spectrum of the analyzed molecule or material, respectively.

Nowadays IR spectroscopy is performed by a Fourier-Transform-IR (FTIR) spectrometer. In contrast to a classical scanning IR spectrometer using monochromatic irradiation, polychromatic light is guided through a Michelson interferometer. The resulting time-depending data is translated via Fourier-Transformation into the common infrared spectrum which is a function of the wave number.

FTIR spectroscopy has three major advantages compared to classical spectroscopy:[13]

- time saving aspect (multiplex of Fellgett's advantage)
- better signal to noise ratio (Jacquinot advantage)
- better wavelength accuracy (Cones advantage)

However, IR spectroscopy is only applicable if a vibration is accompanied with a change of the dipole moment. Complementary to IR, Raman spectroscopy can be used to analyze molecules missing vibrational modes with change in dipole moment.

IR spectroscopy was performed on an FT-IR spectrometer (Thermo Scientific, NICOLET 6700) in transmission mode. Transparent potassium bromide pellets (150 mg) served as matrix for 1 mg MOF nanoparticles.

2.7. Raman spectroscopy

Raman spectroscopy is based on sample irradiation by monochromatic light, usually generated by a laser. Due to scattering of the light by interaction with the electron shells of the material/molecules, the composition can be analyzed (see Figure 2-5). In contrast to IR spectroscopy, requirement for molecules to be Raman active is the polarizability (deformation of the electron cloud) of the excited vibrational mode.
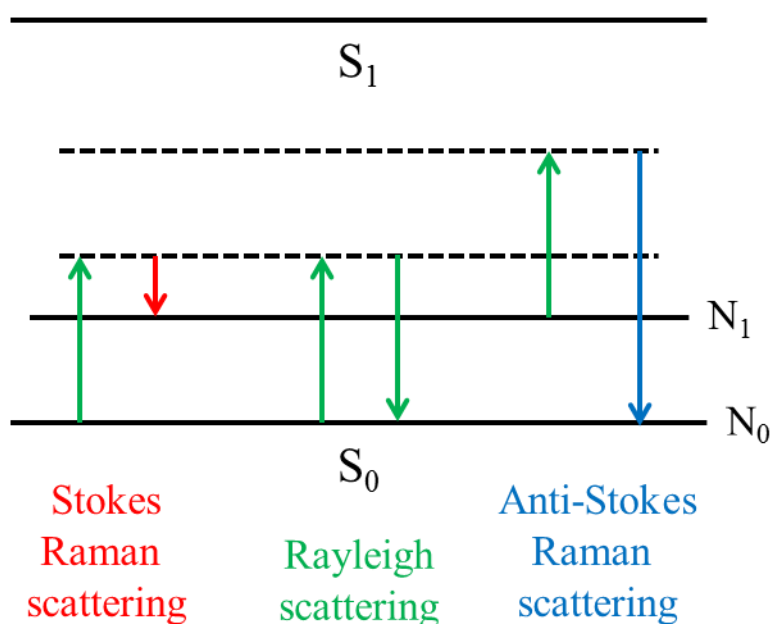
Figure 2-5. Raman excitation and relaxation processes.

Electrons are exited in virtual energy states (dashed lines) and by an elastic scattering process they can relax back to the ground state, emitting light with the same wavelength as the incident beam (Rayleigh scattering). However, a small fraction of light (approximately 1 in 10^7 photons) is inelastically scattered, leading to the Raman effect (Stokes or Anti-Stokes Raman scattering, respectively). The scattered light is either shifted to higher frequencies if electrons are exited from N_1 and are relaxing to the ground state N_0 (Anti-Stokes scattering) or shifted to lower frequencies if the electrons are exited from N_0 and are remaining in an exited state after relaxation from the virtual energy state (Stokes scattering). Those changes in frequency are characteristic for different functional groups within the material and can therefore be used to identify its chemical composition.

Raman spectra were in this thesis were measured on a Bruker Equinox 55 FTIR/FTNIR, set in Raman mode. Laser power was adjusted to the material properties (50 - 100 mW).

2.8.   Ultraviolet-Visible spectroscopy (UV-Vis)

UV-Vis spectroscopy is a common method to record absorption of electromagnetic waves in the ultraviolet and optical range. The energy of the irradiation in this spectral scope corresponds to the energy gap between highest unoccupied molecule orbital (HOMO) and the lowest unoccupied molecule orbital (LUMO) Thus, incoming photons are able to excite electrons from the ground state into a higher energetic level. Afterwards, the ground state is re-established by relaxation processes.[14]

UV-Vis spectroscopy can give information about the electronical properties of the analyzed sample. Further, the amount of analyte can be quantified using the Lambert-Beer law (Equation 2-9).

$$A = log\frac{I}{I_0} = \varepsilon_\lambda \cdot d \cdot c \tag{2-9}$$

Equation 2-9. Lambert-Beer law; A: Absoption; I: intensity of transmitted light; I_0: intensity of incident light; ε_λ: extinction coefficient; d: absorption path length of light; c: concentration of analyte

UV-Vis measurements were carried out using a Perkin Elmer Lambda 1050 UV-Vis-NIR spectrometer equipped with a 150 mm InGaAs integrating sphere. The UV-Vis light range is scanned in a desired step size and the transmitted light is detected. Absorption is plotted against wavelength, resulting in a typical UV-Vis spectrum.

2.9. Fluorescence spectroscopy (FS)

FS is another type of electromagnetic spectroscopy and a useful method to quantify an amount of fluorescent molecules in solution. The emission of fluorescence light is based on induced photon absorption according to UV-Vis spectroscopy (Figure 2-6).
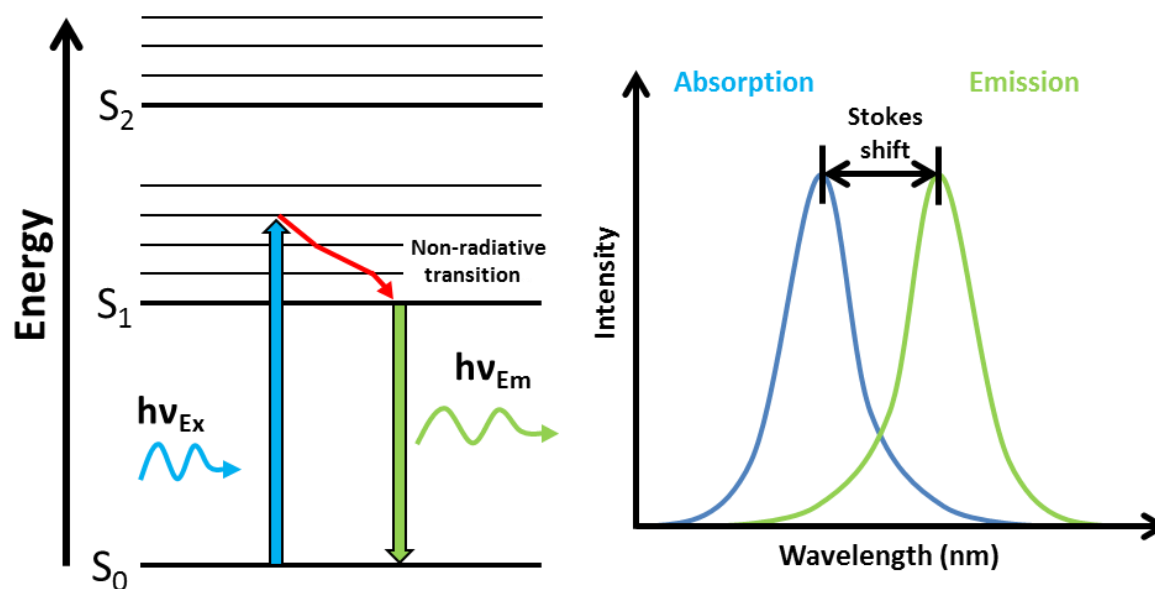
Figure 2-6. (left) Jablonski diagram illustrating the absorption of light, the non-radiative deactivation and the relaxation to the ground state causing the emission of fluorescence light. (right) schematic absorption and emission spectra of a fluorescent dye.

The excitation energy $h\nu_{Ex}$ lifts the molecule in an electronically exited state. The electron relaxes to the vibrational ground state of the excited elcetronic state by non radiative transition. Relaxation to the electronical ground state S_0 is accompanied with the emission of

light with lower energy ($h\nu_{Ex} \gg h\nu_{Em}$). The energy difference between excitation and emission wavelength is called "Stokes-shift" and is due to the energy loss by radiationless transition to the vibrational ground state S_1.[14]

Fluorescence spectra in this work were recorded on a PTI spectrofluorometer with a xenon short arc lamp (UXL-75XE USHIO) and a photomultiplier detection system (model 810/814).

2.10. Fluorescence correlation spectroscopy (FCS)

FCS is a powerful single-molecule detection technique to characterize interactions and dynamics of fluorescent particles or molecules by correlating fluctuations in fluorescence intensity over time. This method was introduced by Magde, Elson and Webb in 1972. In 1993, Rigler *et al.* introduced a confocal microscope to confine data gathering to a small volume of known size while reducing background noise. A laser of suitable wavelength excites the fluorophores inside the confocal volume. The intensity of the emitted light is measured continuously over a fixed period of time. Based upon the assumption of a high probability of chronologically close subsequent signals to have been emitted by the same particle inside the confocal volume, a so called autocorrelation function (Equation 2-10):

$$G(\tau) = \frac{\langle F(t)F(t+\tau)\rangle}{\langle F\rangle^2} \tag{2-10}$$

can be formulated that yields information about diffusion time τ_D and total particle number N inside the confocal volume.
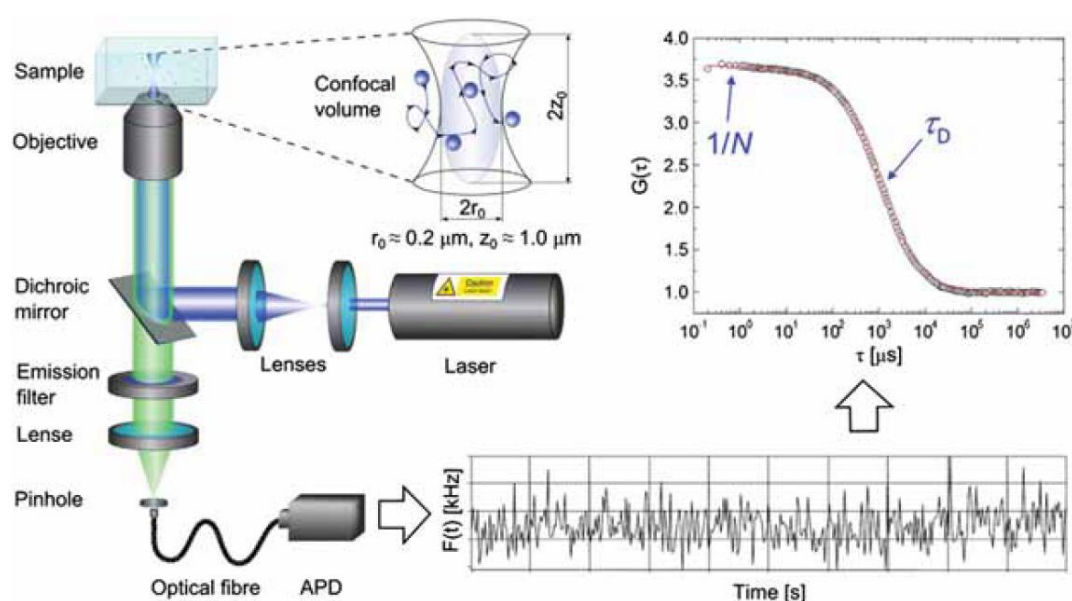
Figure 2-7. Schematic view of a FCS setup.[15] A laser excites the fluorophores in a liquid sample inside a confocal volume, the fluorescence intensity is measured by an APDs capable of detecting single photons. The resulting intensities are correlated over time using the correlation function.

Assuming Brownian motion causing the concentration fluctuations and therefore fluorescence fluctuations, these sample properties are accessible by fitting the correlation curves according to equation 2-11.

$$G(\tau) = \frac{1}{N} \frac{1}{1+\frac{\tau}{\tau_D}} \frac{1}{\sqrt{1+\frac{\tau}{S^2\tau_D}}}$$ (2-11)

S is the structure parameter, the ratio between the lateral and the axial confocal volume radius, while τ_D is the mean time a particle needs to cross the focal volume.[16] The amplitude $G(0)$ contains the mean particle count $N = \frac{1}{G(0)}$ within the focal volume of the autocorrelations.

The measurement of a reference dye with known hydrodynamic Radius yields the extent of the confocal volume ω_0. Knowing that it is possible to calculate the hydrodynamic radius R_H of the sample of interest with the Stokes-Einstein equation $D = \frac{k_B T}{6\pi\eta R_H}$ and $D = \frac{\omega_0^2}{4\tau_D}$.

A poly-disperse system, e.g. free dye with labeled nanoparticles shows additional shoulders which have their own diffusion time. The relative height of the Shoulders provides the ratio of the different components.

The FCS measurements were carried out on a ConfoCor2 (Zeiss, Jena) setup with a 40x NA1.2 water immersion objective employing a red 633 nm HeNe-Laser for excitation of Cy5 fluorophore or on a home-built microscope as described elsewhere.[17]

2.11. Fluorescence microscopy

Fluorescence microscopy is a non-invasive technique frequently used in biophysics to investigate interactions of nanoparticles with cells. The method is based on detection of fluorescent light emitted by fluorescently-labeled nanoparticles and/or specific stained structures within the cells. Thereby, the nanoparticles can be localized within different compartements of living cells.

To get the required spatial resolution in 3 dimensions, confocal microscopy is employed for routine investigations on molecules, cells, and living tissues. The basic concept was originally developed by Marvin Minsky in the mid-1950s and advances in computer and laser technology, coupled to new algorithms for digital manipulation of images, led to a growing interest in confocal microscopy in the 1980s.[18] A schematic view of a confocal laser scanning microscope is presented in Figure 2-8.
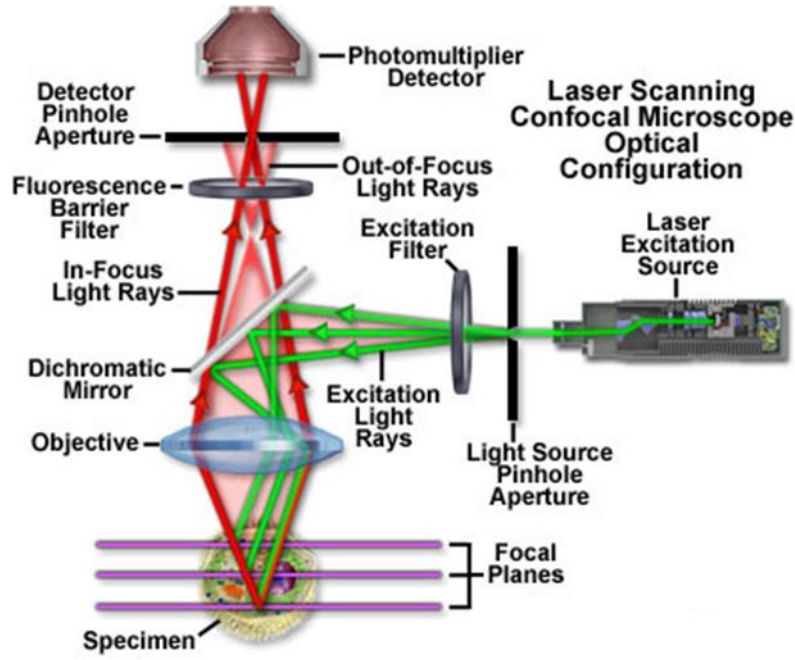
Figure 2-8. Schematic view of a confocal laser scanning microscope setup.[18]

A confocal microscope is improved in comparison to a simple fluorescence microscope by introducing pinholes in the excitation and detection pathway to block the out-of-focus fluorescence. Thereby, especially the axial resolution is increased, which is given by the Rayleigh criterion.

$$d_{axial} = \frac{2n\lambda}{N.A.} \qquad (2\text{-}12)$$

Equation 2-12. Rayleigh criterion; d_{axial}: axial resolution of confocal microscope, n: refractive index, λ: wavelength, $N.A.$: numerical aperture.

However, convential confocal microscopy is limited in temporal resolution due to the need of rastering the sample with the confocal spot. Further improvement was made with the development of spinning disc confocal microscopes. The pinholes are substituted with a spinning disk unit which consists of two fast rotating discs. In one disc, multiple lenses are concentrically arranged, while the other disc contains pinholes that allow for multiple simultaneous scans. With the combination of these fast rotating discs many confocal spots can be screened over the sample at the same time. Hence, this leads to a faster imaging compared to a scanning confocal microscope and to a significant increase in temporal resolution.

In this work, confocal microscopy for live-cell imaging was performed on a Leica-TCS-SP8 confocal laser scanning microscope fitted with an HC PL APO 63x 1.4 objective or on a setup based on the Zeiss Cell Observer SD utilizing a Yokogawa spinning disk unit CSU-X1, equipped with a 1.40 NA 100x Plan apochromat oil immersion objective or a 0.45 NA 10x air objective from Zeiss or a 63x Plan apochromat oil immersion objective.

2.12. Electron microscopy

As optical microscopy is limited by the Abbe restriction (maximal resolution of approximately 250 nm) nano-sized structures can only be imaged by different techniques of electron microscopy.[19] Therby, free electrons are focused on the specimen by an array of magnetic lenses. Acceleration voltage varies from 1 kV to 300 kV depending on the method and desired resolution, which is proportional to the wavelength of the high energetic electrons (Equation 2-13).

$$\lambda = \frac{h}{\sqrt{2m_e E_{kin}}} \qquad (2\text{-}13)$$

Equation 2-13: λ: wavelength of electrons; h: Planck constant; m_e: electron mass; E_{kin}: acceleration energy

The created high energetic electrons show very strong interactions with matter which makes it is necessary to avoid interruptions caused by foreign molecule within the electron beam. Therefore, ultra-high vacuum is applied in the measurement chamber. The interaction of the accelerated electron beam with the sample causes several effects (Figure 2-9), which provide information about morphology, structure and composition of the investigated material.
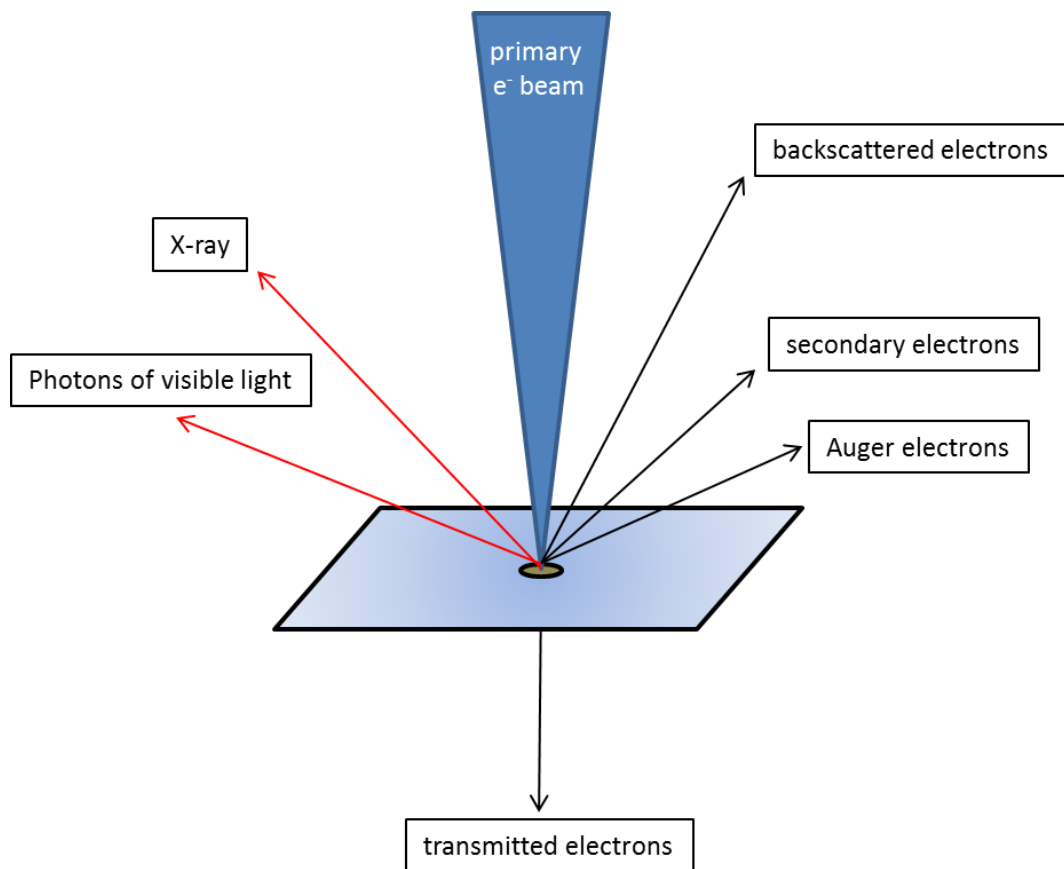
Figure 2-9. Schematic illustration of the occuring effects under electron irradiation of a sample.

(In-)elastically scattered electrons from the primary beam are called backscattered electrons. Furthermore, secondary electrons are generated by inelastic scattering of high energetic electrons with loosely bound outer-shell electrons. They gain enough energy to overcome the work function, can propagate through the sample and can be emitted into the vacuum. Their limited kinetic energy allows short diffusion pathways and therefore presence only close to the sample surface is detectable. Additionally, high energetic electrons can cause inner shell electron displacement, which is followed by filling the holes with electrons from outer shells. The excess of energy is emitted by light, X-ray or Auger electrons, respectively.

Scanning electron microscopy (SEM) uses the information of secondary electrons (SE), back-scattered electrons (BSE) and emitted X-rays to visualize the sample morphology. The image of the topology is built up by raster scanning of the surface. In most cases secondary electrons are detected as imaging signal. Therby, a resolution up to a few nanometer is possible. Further, back-scattered electrons (BSE) can provide information about element distribution in the sample because the intensity of BSE is strongly related to the atomic number of the chemical elements. X-ray can be used to determine the elemental composition of the surface as the emitted frequencies are element dependent (EDX).

SEM measurement were carried out using a FEI HELIOS NANOLAB G3 UC microscope equipped with a field emission gun and operated at acceleration voltages between 2 and 20 kV.

Transmission electron microscopy (TEM) is a common method to image structural details of crystalline materials. After penetration of the sample, transmitted electrons are detected with a fluorescence screen or a CCD camera. The resulting pattern provides information about cell parameters, pore dimensions and wall thicknesses with resolutions up to 0.1 nm, depending on the electron energy. Since the sample has to be penetrated, the applied acceleration voltage (80 kV to 300 kV) is higher than required for REM measurements (1 kV to 30 kV). As electron radiation is ionizing and therefore can interact in many different ways with the analyzed sample, it can lead to radiolysis where chemical bonds within the sample structure are destroyed. Other limiting factors for high resolution are spherical aberrations, chromatic aberrations, and astigmatism.[20]

If not stated otherwise, all samples were investigated with an FEI Titan Themis equipped with an extreme field emission gun (X-FEG). A 4k × 4k Ceta 16M™ camera detected bright field and high-resolution TEM images.

2.13. Nuclear molecular resonance (NMR)
Magnetic resonance imaging (MRI)

NMR and MRI are two techniques based on the same principle of electromagnetic radiation absorption by magnetic nuclei in a static magnetic field. The magnetic field influences the energy states of isotopes with an intrinisic nuclear spin unequal to zero and hence containing a permanent magnetic moment $\vec{\mu}$. (e.g. ^{1}H, ^{13}C, etc.).[21]

$$\vec{\mu} = \gamma\vec{s} \tag{2-14}$$

Equation 2-14: Magnetic moment; γ: gyromagnetic constant; $\vec{s}$: nuclear spin

Applying external magnetic field results in a differentiation of the energy levels into distinct energy states $(2\vec{s}+1)$, each associated with a magnetic quantum number m (e.g. $\vec{s} = \frac{1}{2}$; $m = +\frac{1}{2}$ or $m = -\frac{1}{2}$ for ^{1}H). Usually the z-axis is chosen to be along with B_0, resulting in an effective magnetic moment μ_z:

$$\mu_z = \gamma s_z = \gamma m \frac{h}{2\pi} \tag{2-15}$$

Equation 2-15: *z*-component of the magnetic moment

The difference between the generated energetic states can be calculated by:

$$\Delta E = \Delta\mu_z B_0 = \gamma\Delta m \frac{h}{2\pi} B_0 = \gamma \frac{h}{2\pi} B_0 \tag{2-16}$$

Equation 2-16: Difference in energy levels

If electromagnetic radiation of the corresponding energy or frequency ω (Larmor frequency, typically ranging from a few kHz to several hundred MHz) is focused on the sample, transition between these quantum states can be induced.

NMR spectroscopy uses differences in the effective external magnetic field, which is dependent on the chemical surrounding, for fast and precise analysis of organic reaction products and determination of molecular structures. ^{1}H-NMR spectroscopy in this thesis was performed on a Bruker 400 or a Bruker 400 TR NMR spectrometer, respectively.

MRI is a medical imaging technique, which uses the detection of water protons by electromagnetic radiation for the visualization of the anatomy and physiological process *in vivo*. MRI in this thesis was performed with a 1.5 T clinical MRI system (Magnetom Aera, Siemens Health Care, Germany).

2.14. References

[1]   C. Mellot-Draznieks, J. Dutour, G. Ferey, *Angew. Chem. Int. Ed.* **2004**, *43*, 6290.

[2]   Malvern Instruments Ltd., *Zetasizer Nano Series User Manual*, Worcestershire, **2003.**

[3]   H. Butt, K. Graf, M. Kappl, *Physics and Chemistry of Interfaces, Wiley VCH,* **2003**.

[4]   S. Lowell, J. E. Shields, M. A. Thomas, M. Thommes, *Characterization of Porous Solids and Powders: Surface Area, Pore Size and Density.*, Springer, **2006**.

[5]   K. S. W. Sing, D. H. Everett, R. A. W. Haul, L. Moscou, R. A. Pierotti, J. Rouquérol, T. Siemieniewska, *Pure Appl. Chem.* **1985**, *57*, 603–619.

[6]   Z. A. ALOthman, *Materials* **2012**, *5*(12), 2874-2902.

[7]   S. Brunauer, P. H. Emmett, E. Teller, *J. Am. Chem. Soc.* **1938**, *60*, 309.

[8]   I. Langmuir, *J. Am. Chem. Soc.* **1916**, *38*, 2221–2295.

[9]   K. S. Walton, R. Q. Snurr, *J. Am. Chem. Soc.* **2007**, *129*, 8552–8556.

[10]   M. Thommes, K. Kaneko, A. V. Neimark, J. P. Olivier, F. Rodriguez-Reinoso, J. Rouquerol, K. S. W. Sing, *Pure Appl. Chem.* **2015**, *87*, 1051–1069.

[11]   L. S. K. Pang, J. D. Saxby, S. P. Chatfield, *J. Phys. Chem.* **1993**, *97*, 6941.

[12]   M. P. Sepe, *Thermal Analysis of Polymers*, Rapra Technology Limited, **1997**.

[13]   M. Hesse, H. Meier, B. Zeeh, *Spectroscopic Methods in Organic Chemistry*, Thieme Verlag, New York, **2008**.

[14]   P. W. Atkins, *Physikalische Chemie*, Wiley-VCH, Weinheim, **2001**.

[15]   K. Koynov, H.-J. Butt, *Curr. Opin. Colloid Interface Sci.* **2012**, *17*, 377-387.

[16]   P. Schwille, E. Haustein, *Spectroscopy* **2009**, *22*, 1-33.

[17]   J. Hendrix, V. Baumgartel, W. Schrimpf, S. Ivanchenko, M. A. Digman, E. Gratton, H. G. Krausslich, B. Muller and D. C. Lamb, *J Cell Biol*, **2015**, *210*, 629-646.

[18]   https://www.olympuslifescience.com/en/microscoperesource/primer/techniques/ confocal/confocalintro/ (28.05.2018)

[19]   C. R. Brundle, C. A. E. Jr. and S. Wilson, *Encyclopedia of materials characterization: Surfaces, interfaces, thin films*, Butterworth-Heinemann Limited, **1992**.

[20]   B. Fultz, J. Howe, *Transmission Electron Microscopy and Diffractometry of Materials*, Springer, **2008**.

[21]   N. Shah, A. Sattar, M. Benanti, S. Hollander, L. Cheuck, **2006**, *The Journal of the American Osteopathic Association. 106 (1),* 23–27.

3. Imparting functionality to MOF nanoparticles by external surface selective covalent attachment of polymers

This chapter is based on the following publication:

Andreas Zimpel*, Tobias Preiß*, Ruth Röder, Hanna Engelke, Michael Ingrisch, Michael Peller, Joachim O. Rädler, Ernst Wagner, Thomas Bein, Ulrich Lächelt, and Stefan Wuttke, *Chemistry of Materials* **2016**, *28*, 3318–3326.

* These authors contributed equally to this work
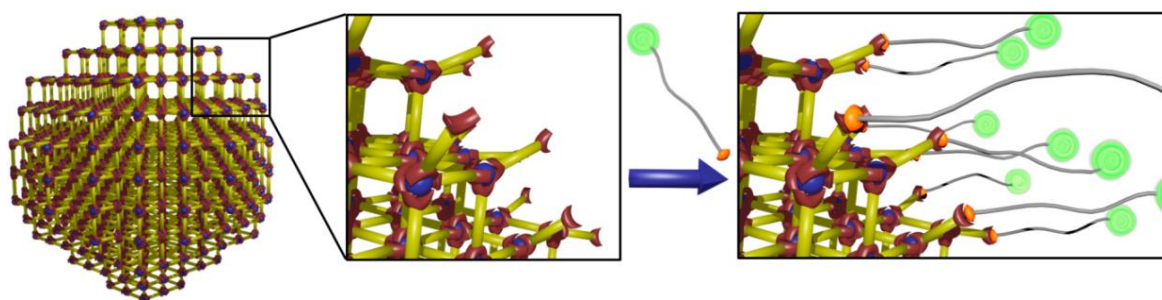
3.1. Introduction

Manipulating the surface of nanoparticles (NPs) has been a prominent research topic in recent years.[1-3] The nanoparticle surface is defined as the interface between the nanoparticle and its surroundings and determines the interactions with the environment.[4] In addition, particle surface properties become dominant in the nanometer range due to the high surface-to-volume ratio. Therefore, the controlled surface functionalization is of great importance for nanoparticle applications in fields like sensing, imaging, or drug delivery.[5-7]

Surface functionalization has been adapted to many different nanoparticles such as gold, metal oxides, carbon, polymers or mesoporous silica.[8, 9] Metal-organic framework nanoparticles (MOF NPs), consisting of metal clusters and organic linker molecules, are a relatively new class of nanomaterials.[10-12] Besides their unique properties such as structural diversity, crystalline structure, tunable porosity and high surface area, they further provide great potential for functionalization on their internal as well as on their external surface.[13-17] In particular, the use of MOF nanoparticles in biomedical applications requires that the external-

surface functionalization fulfills different tasks varying from inhibiting agglomeration within the bloodstream to the specific recognition of cancer cells.[18] Attachment of biocompatible polymeric structures or proteins is a common method to achieve those functionalities.[19]

Two different general strategies have been proposed so far, regarding the attachment of molecules onto the external surface of MOFs: "functionalization during synthesis", also known as coordination modulation approach, and "postsynthetic modification" (PSM).[20] According to literature, PSM is the most common way to achieve core-shell MOF nanoparticles. With this approach, four different ways of external surface functionalization of MOFs have been already mentioned and discussed.

Firstly, one possibility consists of grafting, through coordinative bonds, polymeric structures on the coordinatively unsaturated metal sites (CUS) present on the external surface of MOF particles (Fig. 3-1a). This was reported for the first time by Rowe *et al.*[21] and was adopted by other groups to create core-shell functionalized MOF nanoparticles in recent years.[22, 23] However, due to the potential presence of CUS on the MOF particle internal surface, the latter can also be potentially functionalized, especially if the functional unit is smaller than the pore aperture. Consequently, this undesired inner functionalization, added to the weak interaction between the functional unit and CUS,[24] restricts the implementation of this approach.
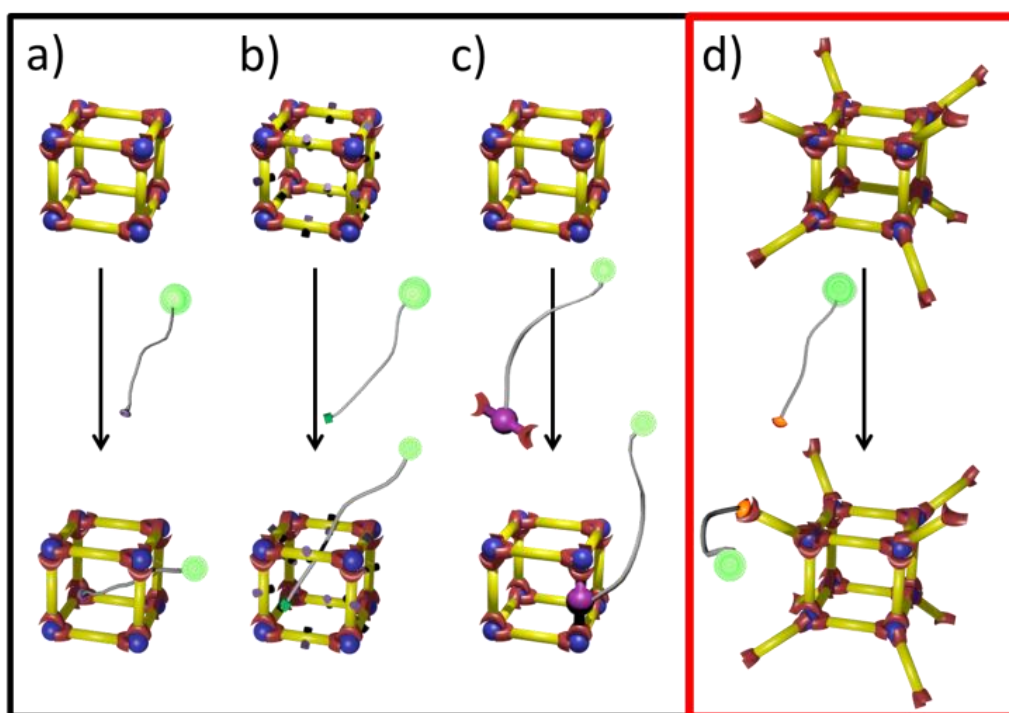
Figure 3-1. Schematic illustration of the different postsynthetic functionalization possibilities for MOFs: coordinative binding on CUS (a), covalent binding to pre-functionalized linkers (b), ligand exchange (c), and covalent binding to the linking group (d, red box), which was applied in this work.

Secondly, covalent postsynthetic modification of MOFs, a well-known method, using linker molecules with functional groups to functionalize the internal surface of MOF bulk material, can also be implemented to functionalize the MOF NP's external surface (Fig. 3-1b). Once more, the selectivity of this functionalization towards the MOF NP's external surface is only achieved as long as functional units are large enough not to access the internal surface of the framework. To overcome this limitation, an improved method was developed by Fischer, Wöll and co-workers.[25] Their approach consisted of the selective anchoring of functional groups on the external surface of the metal-organic framework only (surface-attached metal-organic framework multilayers, SURMOFs).[26] These groups were subsequently functionalized with a fluorescent dye, which was detected *via* fluorescence microscopy. Recently, a similar approach was reported for the preparation of MOF core-shell bulk structures, as demonstrated by Matzger *et al.*.[27]

Thirdly, the group of Kitagawa demonstrated that postsynthetic ligand exchange with functional linker molecules only occurs on the first external monolayer of MOF microcrystals (Fig. 3-1c). The authors pointed out that the key point for this functionalization strategy was the dynamic nature of the underlying MOF scaffold along with the chemical properties of the functional ligand, which somehow limits the broad applicability of this strategy to MOF NP surface functionalization.[28]

Finally, unsaturated functional groups of the organic linker can be used for covalent attachment of functional molecules. This approach allows for the selective functionalization of the MOF NP external surface without further restrictions, since the functional groups are used within the framework for coordinative bonding to metal ions and are not addressable for covalent bonding (Fig. 3-1d, Fig. 3-2). It was first presented by Jung *et al.*, who anticipated the presence of externally exposed carboxyl groups of the linker and addressed them by attachment of enhanced green fluorescent protein (eGFP) on bulk MOF material.[29] In a water-based carbodiimide-mediated amidation, they successfully functionalized aliphatic carboxylates but faced issues with aromatic carboxylic linkers, because of their reduced reactivity. They were able to overcome this only by changing the reaction medium to an organic solvent (dichloromethane). Shih *et al.* used a similar way to immobilize trypsin on the external surface and transferred this functionalization approach to the field of nanoparticles.[30] To the best of our knowledge, no further work was published on this interesting concept of MOF NPs external surface functionalization and hence it has not yet been investigated in greater detail.

In our work, we explicitly focus on the latter functionalization approach, which provides the advantage of covalent bonding in combination with a high selectivity for the external surface of the MOF nanoparticle. This allows precise control over the external nanoparticle interface while retaining the porous MOF scaffold. We show successful covalent surface coating of MOF nanoparticles containing aromatic linkers by a water-based "green" carbodiimide mediated reaction (Fig. 3-2). We chose MIL-100(Fe) nanoparticles (MIL: Materials of Institute Lavoisier) as MOF platform because of their biocompatibility[31] and chemical stability in aqueous environments,[32, 33] which is required for the chosen reaction conditions. Further, MIL-100(Fe) NPs already showed high potential for applications in biomedicine.[34-37] The framework consists of iron clusters acting as nodes and trimesic acid serving as linker molecules, which are expected to provide free aromatic carboxylic acid groups at the particle external surface.[38] We show the covalent nature of the bonding to polymers and estimate the achievable amount of functionalization. For surface modification we chose two different kinds of polymer (shown in Fig. 3-2): i) commercially available amino-polyethylene glycol (PEG5000), a hydrophilic polymer, frequently used to increase colloidal stability and to mediate surface shielding of nanoparticles[39-41] and ii) Stp10-C, a solid-phase synthesis-derived oligoamino amide serving as bi-functional linking polymer, providing a primary amine for conjugation with the nanoparticle surface groups and a thiol for fluorescent labeling or additional functionalization. The two terminal groups of Stp10-C are connected via a repetitive diaminoethane motif with proton-sponge characteristics, which can be utilized for electrostatic binding of nucleic acids, enhancement of cellular uptake and improvement of endosomal escape.[42-44] By means of a covalent Stp10-C attachment, we combine the high precision of crystalline MOF nanoparticles with the sequence-definition of solid-phase derived polymers and thus generate a controlled interface towards solution. In addition, the two polymers, PEG and Stp10-C, were chosen as representative compounds because of the potential prospective use of the resulting MOF@Polymer core-shell nanoparticles in biomedical applications and for multi-imaging purposes.[45] We demonstrate first promising results of that kind of hybrid nanoparticles by fluorescence microscopy and magnetic resonance imaging (MRI).
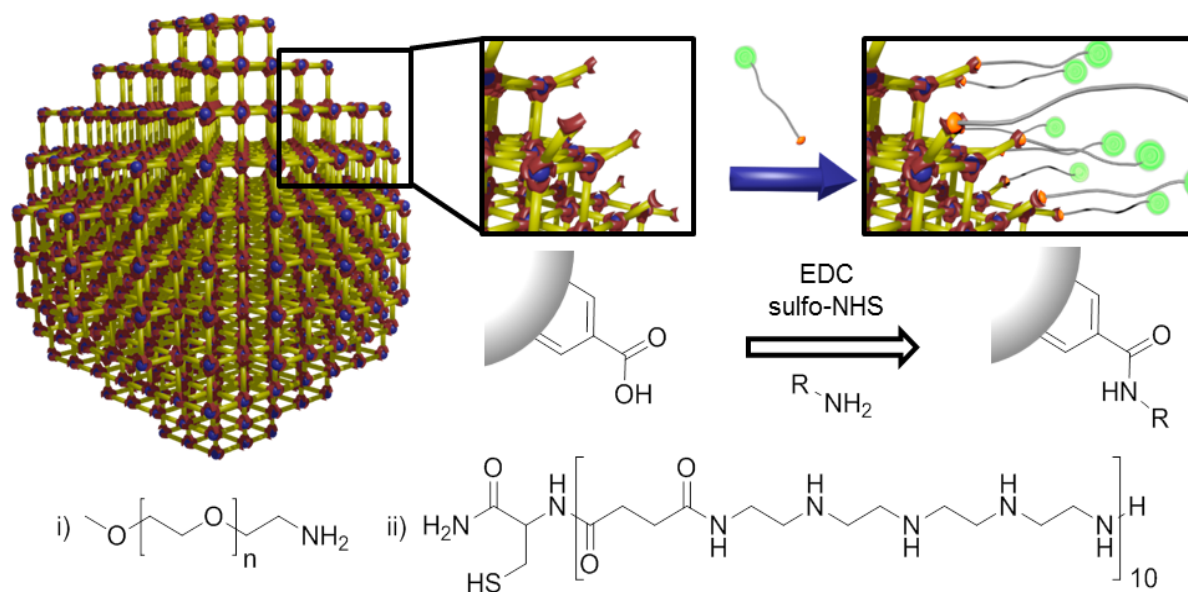
Figure 3-2. Schematic illustration of the polymer coating and reaction scheme of the amidation by EDC hydrochloride and sulfo-NHS mediation. Chemical structures of the polymers used this work: i) PEG and ii) Stp10-C.

3.2. Results and Discussion

Synthesis, Functionalization and Characterization of MOF@Polymer nanoparticles. The nanoparticles were synthesized following a slightly modified procedure developed by Agostoni *et al.*.[46] Iron (III) chloride hexahydrate was dissolved in bi-distilled water and trimesic acid was added to the solution. The mixture was sealed in a Teflon autoclave and heated to 130 °C by microwave irradiation, yielding a homogenous dispersion of MIL-100(Fe) nanoparticles. The particles were filtered and washed with ethanol. For the functionalization process, the nanoparticles were dispersed in ethanol and 1-ethyl-3-(3-dimethylaminopropyl) carbodiimide (EDC) hydrochloride was added. PEG5000 or Stp10-C was dissolved in water, hydroxy-2,5-dioxopyrrolidine-3-sulfonic acid sodium salt (sulfo-NHS) was added and the solution was pipetted to the MOF suspension. After a reaction time of 30 min, the functionalized nanoparticles were washed with water or ethanol, respectively (for further details see Supporting Information).

Functionalized as well as unfunctionalized MIL-100(Fe) nanoparticles showed characteristic X-ray diffraction (XRD) reflections, which indicate retained crystallinity after functionalization (see also Fig. S3-2). This was further confirmed by transmission electron microscopy (TEM), where the crystalline arrangement of the MOF could be visualized (see also Fig. S3-3, S3-4 and S3-5). Particle sizes measured by dynamic light scattering (DLS) in colloidal ethanolic dispersion revealed a hydrodynamic diameter of 130 ± 45 nm (see also Fig. S3-6). DLS measurements in aqueous nanoparticle dispersions showed an increased colloidal stability of the functionalized particles in comparison to unfunctionalized ones. After 3 weeks in water, pure MIL-100(Fe) nanoparticles tend to form agglomerates, while polymer-shielded particles retained their colloidal stability (see also Table S3-1, Fig. S3-7). Furthermore, functionalized particles provided increased stability in 10% fetal bovine serum (Fig. 3-3, Table S3-2). While unfunctionalized particles formed large agglomerates within minutes after dispersion, the functionalized ones stayed in dispersion over a time period of at least 72 h. This behavior can be explained by the shielding ability of the polymers and demonstrates the change in the physicochemical behavior of the MOF NPs by external surface modification. These results are promising with regard to later applications, e.g. in drug delivery, where colloidal stability in aqueous media is mandatory. The change of the external surface of the MOF NP can also be observed with zeta-potential measurements, revealing an increased pH value of the isoelectric point for functionalized particles (see also Fig. S3-8). We attribute this shift (pH 4.1 for unfunctionalized particles to pH 5.6 for PEG, and to pH 5.8 for Stp10-C) to the changes on the particle surface resulting from polymer

attachment. The acidic carboxy-groups were chemically changed and covered by the polymer, resulting in reduced influence of the negative charges of these groups and therefore, leading to an increased zeta-potential of the particles. Moreover, both polymers additionally impact zeta-potential by shielding the surface charge or even introducing positive charges in case of the amine-rich Stp10-C. The calculations of the BET specific surface area based on nitrogen sorption measurements gave a value of 1905 m^2/g for unfunctionalized MIL-100(Fe) nanoparticles. For functionalized particles, the surface areas decreased moderately to 1338 m^2/g or 1432 m^2/g, for the PEG and Stp10-C treated nanoparticles, respectively (see also Fig. S3-9). This can be attributed to the attached amount of nonporous organic material on the external surface as well as to partial pore blocking under the dry and cold measurement conditions, where the polymer chains collapse and freeze on the external surface of the nanoparticles. An increase of the organic fraction after functionalization could be detected by thermogravimetric analysis (TGA). Heating the samples stepwise to 900 °C in synthetic air, a lower percentage of inorganic mass (iron oxides) remained for functionalized compared to unfunctionalized particles after combustion of the material (see also Fig. S3-10).
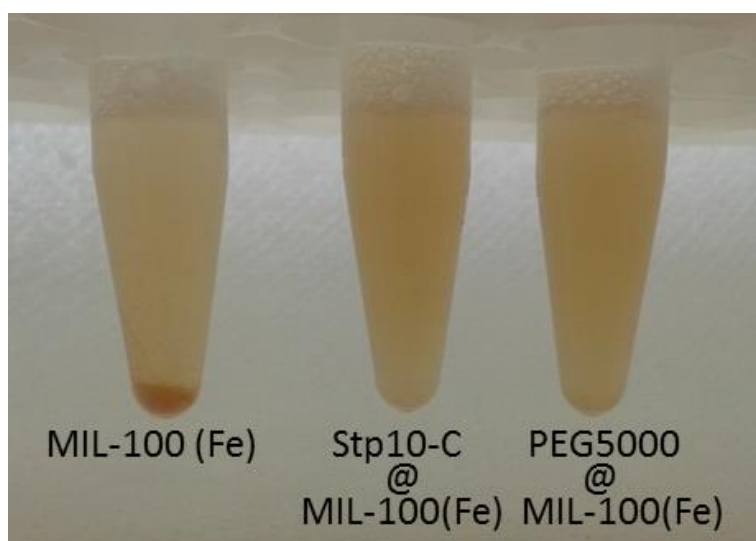
Figure 3-3. Particles dispersion of functionalized and unfunctionalized MIL-100(Fe) nanoparticles after 3 h in 10% FBS in water. Unfunctionalized particles start to agglomerate immediately, while polymer-functionalized particles retain their colloidal stability.
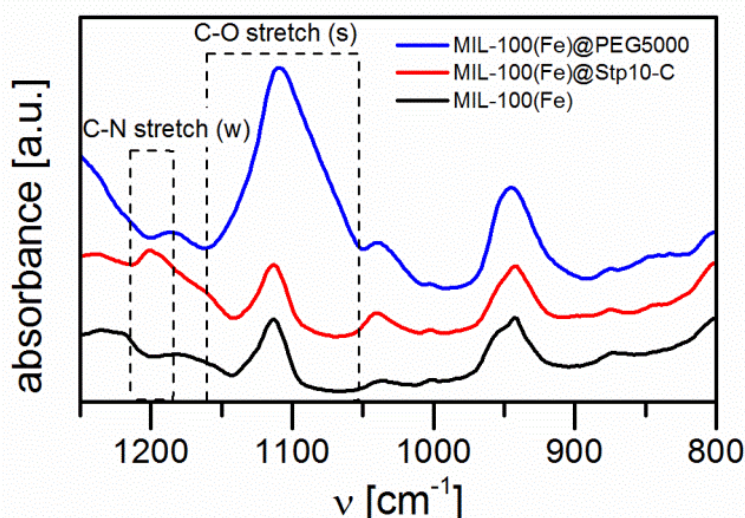
Figure 3-4. IR spectra of functionalized and unfunctionalized MIL-100(Fe) nanoparticles (offset to show differences): dashed lines frame the specific vibrations resulting from attached polymer, increased C-O stretching vibration for PEG5000 (blue line) or increased C-N stretching vibration for Stp10-C (red line).47 (full IR spectra are provided in the Supporting Information; Figure S3-11).

A further confirmation of successful functionalization was given by IR spectroscopy, which revealed the appearance of bands of the C-O or C-N stretching vibrations of the polymeric backbone for MIL-100(Fe)@PEG5000 and MIL-100(Fe)@Stp10-C, respectively (Fig. 3-4).

We further performed fluorescence correlation spectroscopy (FCS), a single molecule technique, which is able to measure the diffusion coefficient and the concentration of fluorescently labeled particles.[48-50] In order to probe the binding of the functional polymer to MOF nanoparticles, Cy5 was attached on the free thiol group of the Stp10-C polymer tail by a maleimide-thiol coupling reaction. A sample of Stp10-C*Cy5 as well as a suspension of MIL-100(Fe)@Stp10-C*Cy5 nanoparticles (50% labeled, 50% unlabeled Stp10-C) in water were measured. The normalized autocorrelation curve of Stp10-C*Cy5 exhibited diffusion corresponding to an effective hydrodynamic radius of 1.1 nm (Fig. 3-5).
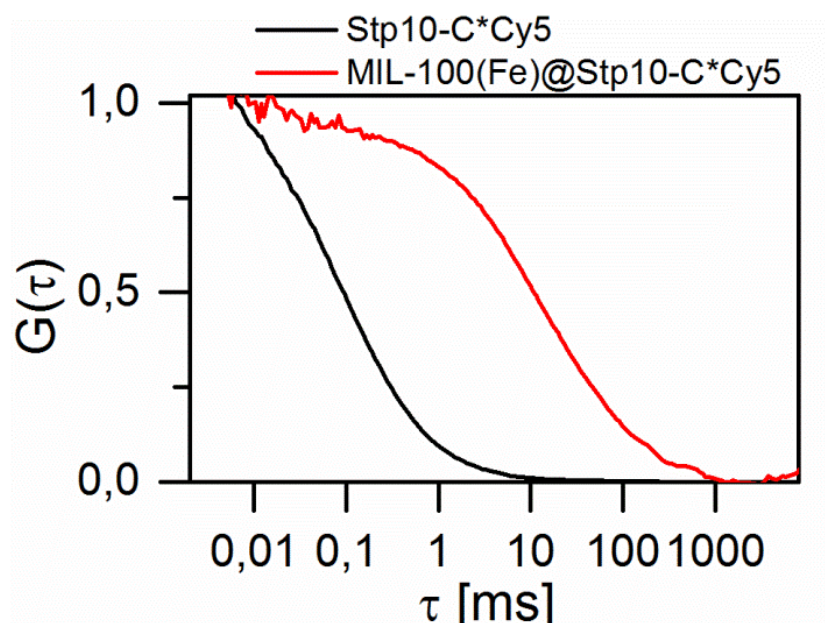
Figure 3-5. Normalized autocorrelation curves of Stp10-C*Cy5 (black) and MIL-100(Fe)@Stp10-C*Cy5 nanoparticles (red). The shift to higher lag-times τ of nanoparticles' correlation curve confirms the successful attachment of polymer molecules to nanoparticles.

In contrast, the FCS signal of the nanoparticle samples showed a distinct increase in the diffusion time (t=4.8 ms), which corresponds to a hydrodynamic radius of 56 nm. As the measured hydrodynamic radius agrees well to the size of the particles determined by DLS (see supporting information), we conclude that labeled polymer molecules are attached to the non-fluorescing nanoparticles. This indicates a successful polymer coating of MIL-100(Fe) particles. A variation of the amount of labeled Stp10-C in the nanoparticle coating process showed no difference in the normalized autocorrelation curves (see SI, Fig. S3-12), indicating that the fluorescent label Cy5 has no effect on the functionalization process with Stp10-C.

Examination of the covalent bonding and estimation of polymer amount. The above results confirm the formation of MOF@Polymer core-shell nanoparticles but do not reveal the nature of the connection. Using UV-Vis spectroscopy, we gained first indications concerning the expected covalent bonding. After the conventional functionalization reaction, the supernatant after centrifugation of the nanoparticles was analyzed and revealed no residue of dye-labeled polymer, which indicated a successful attachment to the MOF. When omitting sulfo-NHS in the reaction mixture, which is essential for the activation of the carboxylic group in aqueous media, almost all initial dye-labeled polymer was still detected in the supernatant (see also Fig. S3-13). This led to the conclusion that the MOF-polymer bonding is of covalent nature, as sulfo-NHS is required for the attachment. Furthermore, for postsynthetic modification of the internal surface, liquid NMR analysis after digestion of the functionalized MOF but without destroying the newly formed bonds is a common method to verify the covalent attachment of molecules.[51]

Therefore, we dissolved the functionalized nanoparticles in a gentle way by adding ethylenediaminetetraacetic acid (EDTA).[52] Due to its chelate effect, EDTA is able to strongly bind the iron(III) ions. When performing the dissolution of the MOF NPs, we found an

increased stability for the PEG-functionalized particles compared to unfunctionalized ones. This was reflected by a prolonged dissolution time and prevention of crystallinity (see also Fig. S3-14). After digestion of the MOF, the aqueous solution was extracted with dichloromethane (DCM) for separation of the functionalized trimesic acid from the pure organic linker. ^{1}H-NMR spectroscopy exhibited peaks in the aliphatic region for the polymeric part as well as an aromatic signal resulting from the trimesic acid (Fig. 3-6). Splitting of the aromatic peak indicates the covalent nature of the bonding, since the aromatic protons lose their chemical equivalence after functionalization of one carboxylic group (inset in Fig. 3-6). After having shown the covalent nature of the bonding, we further estimated the amount of anchored polymer on the NPs surface. This was again determined by UV-Vis measurements of unbound Stp10-C*Cy5 left in the supernatant after EDC-reaction and centrifugation.
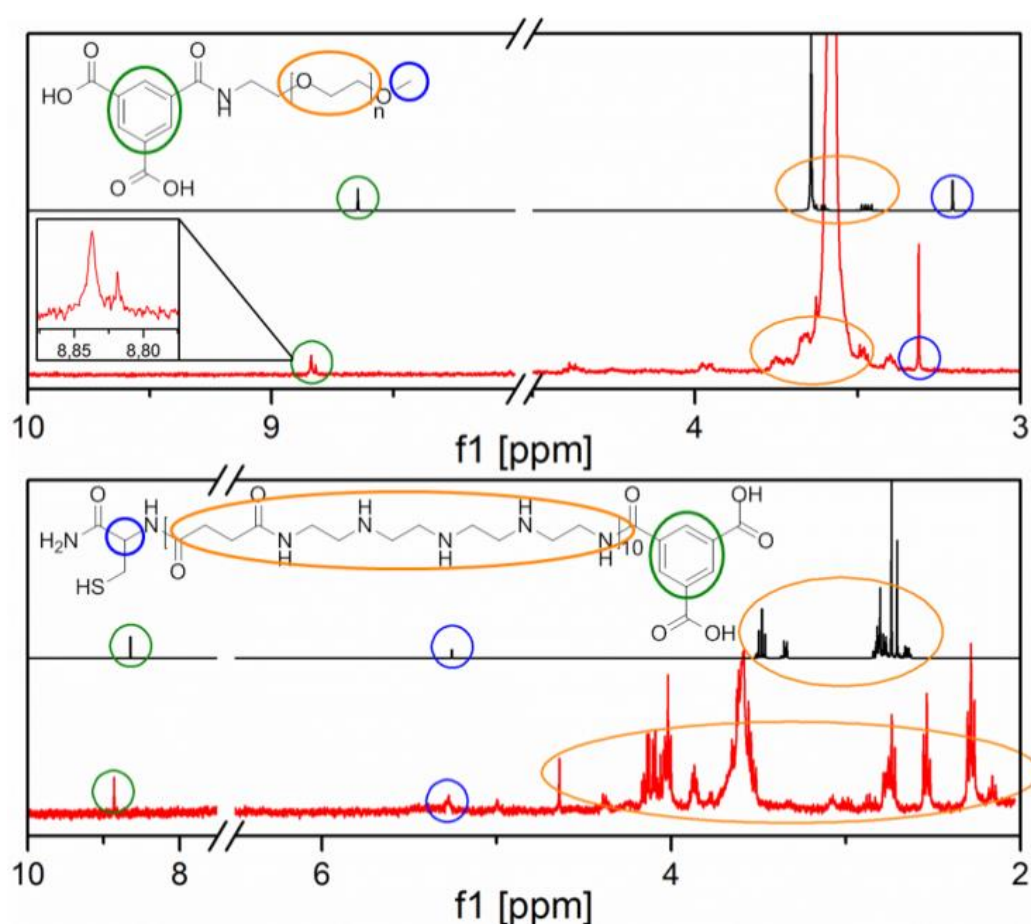
Figure 3-6. NMR spectra of functionalized trimesic acid after dissolution of the MIL-100(Fe) nanoparticles and extraction in DCM in comparison to calculated spectra;[53] TrimesicAcid@PEG (top) and TrimesicAcid@Stp10-C (bottom). Colored lines encircle the aliphatic proton signals of the polymeric backbone (orange), the aromatic proton signals of the trimesic acid (green) and the tertiary proton of the cysteine or the methyl protons for Stp10-C or PEG5000, respectively (blue).

Assuming that all polymer molecules that are covalently bound to the MOF nanoparticles can be removed from the supernatant, we estimated the attached amount of Stp10-C to approx. 10 – 20 nmol per milligram MIL-100(Fe) nanoparticles (see also Fig. S3-15). This amount corresponds to approx. 460 – 920 polymer molecules per MIL-100(Fe) nanoparticle or an external surface coverage of 9 – 17 pmol/cm^2. These values were calculated from geometry and mass density of the NPs ($\rho = 0.98$ g/mL[38]; r = 26.5 nm; for further details see Supporting Information). Furthermore, the results are in good agreement with TGA data, which provided an increased mass loss of 2.7% for PEG5000 and 1% for Stp10-C functionalized nanoparticles, respectively (see also Fig. S3-10). Regarding the rather low functionalization degree, which is at the border of the brush regime,[54] the amount of free carboxylic acid functions on the nanoparticles external surface is considered to be the major limiting factor.

Towards application in theranostics. As we had altered the external surface of the MOF nanoparticles and functionalized them with fluorescent moieties, we were interested in the cellular uptake and toxicity of these particles. Cellular biocompatibility and the interactions between nanoparticles and cells were studied since they are fundamental prerequisites for biomedical applications. The particles were incubated with murine neuroblastoma N2A cells. Cell membranes were stained with WGA 488, and all non-absorbed particles were removed from cells by washing with buffer solution. Fluorescence microscopy revealed successful uptake of particles after 7 h, which can be seen in Figure 3-7a.
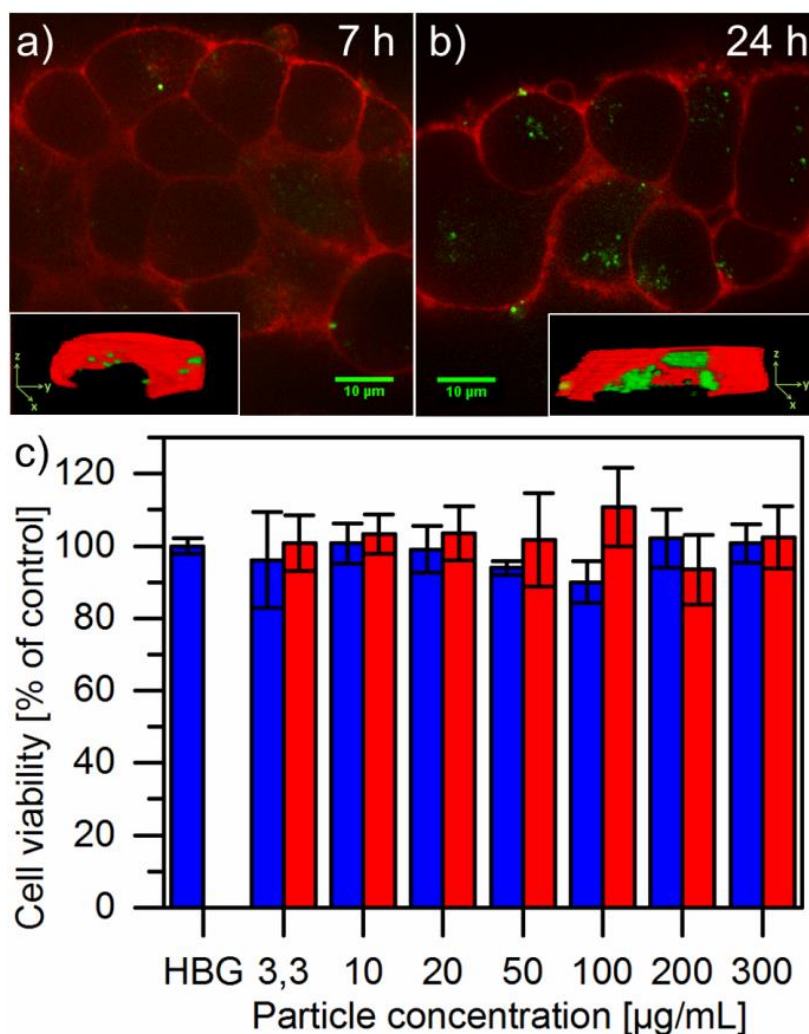
Figure 3-7. Fluorescence microscope images of N2A cells after 7 h (a) and 24 h (b) incubation with MIL-100(Fe)@Stp10-C nanoparticles under standard cell culture conditions in serum-containing medium (insets: 3D images of single cells calculated from stacked confocal fluorescence microscope images55); MTT-plot of N2A cells after 24 h incubation of MIL-100(Fe)@Stp10-C (red) and MIL-100(Fe) (blue) nanoparticles (c).

After 24 h of incubation (Fig. 3-7b), cell images showed a significantly increased uptake of the functionalized nanoparticles, while further incubation showed no additional effect. Hence, this time period was chosen for the investigation of the influence of nanoparticle exposure and up take on cell viability. MTT-assays with N2A cells were carried out after 24 h incubation with unmodified MIL-100(Fe) and MIL-100(Fe)@Stp10-C*Cy5 in a dosing range between 3.3 and 300 µg/mL (Fig. 3-7c). In all investigated concentrations no significant effect on the metabolic activity of N2A cells could be observed, indicating the good cellular tolerance towards the bare as well as the functionalized MOF nanoparticles. In addition, the influence of the polymer shell on the MRI activity of MIL-100(Fe) was investigated. As MIL-100(Fe) is known to be MR active,[34] we studied the change of the MRI signal in order to ensure that magnetic resonance imaging is still possible with polymer attached at the external surface.

Magnetic resonance imaging is a particularly attractive modality for clinical and preclinical imaging, e.g. in cancer research. As MIL-100(Fe) may serve either as drug carrier or as potentially highly selective contrast agent, we studied the visualization of both uncoated and coated nanoparticles and the effect of surface functionalization on longitudinal and transversal relaxivities of MIL-100(Fe).
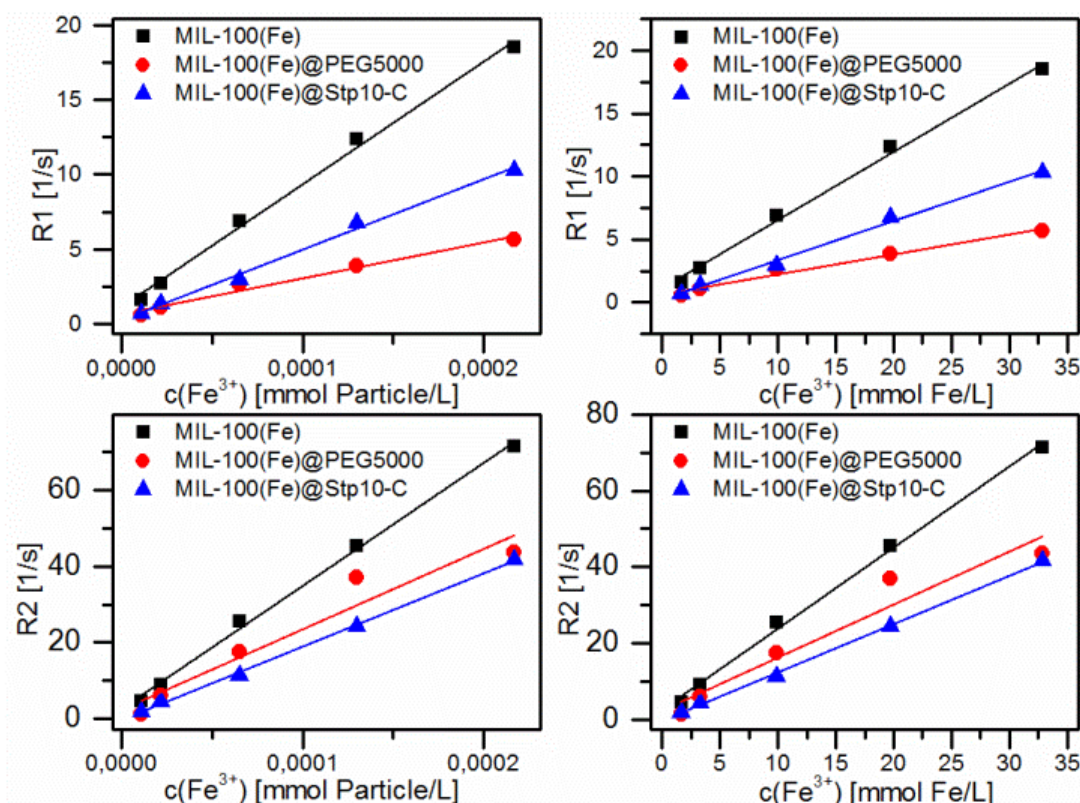
Figure 3-8. Plots of longitudinal and transverse relaxation rates R1 (top) and R2 (bottom) of coated and uncoated MOF particles for "per particle" (left) and "per Fe^{3+}" (right).

Here, the relaxivity is the property of a substance to alter the relaxation rate of the water protons in the aquaeous solution, in which the substance is dissolved. Two independent sets of samples (MIL-100(Fe), MIL-100(Fe)@PEG5000 and MIL-100(Fe)@Stp10-C) were prepared in concentrations up to 10 mg/mL in water, and underwent imaging at a clinical 1.5 T MRI system (Magnetom Aera, Siemens Healthcare) using T1-weighted saturation recovery sequences and T2-weighted multi-echo sequences. Longitudinal (T1) and transverse (T2) relaxation times and relaxation rates (R1 and R2) were calculated in region of interests (ROI) in each sample as described. Longitudinal and transversal relaxivities of each sample were estimated assuming a linear relation between concentration and relaxation time, as shown in Figure 3-8. Relaxivities were calculated for mmol of entire nanoparticles as well as for mmol Fe^{3+} ions, to ensure comparability to existing contrast agents in clinical use (Tab. 3-1).

Table 3-1. Relaxivities (L s^{-1} mmol^{-1}) calculated from the linear slopes of Figure 8.

	Calculations per mmol particles		Calculations per mmol Fe^{3+}	
	Relaxivity r_1	Relaxivity r_2	Relaxivity r_1	Relaxivity r_2
MIL-100(Fe)	$8.21 \cdot 10^4$	$3.22 \cdot 10^5$	0.54	2.12
MIL-100(Fe)@Stp10-C	$4.72 \cdot 10^4$	$1.92 \cdot 10^5$	0.31	1.27
MIL-100(Fe)@PEG5000	$2.40 \cdot 10^4$	$2.10 \cdot 10^5$	0.16	1.36

All samples could be visualized in a clinical MRI setting (see Fig. 3-9). Longitudinal and transversal relaxation rates showed a linear dependence on the MOF NP concentration (see Fig. 3-8). T1 relaxivity, i.e. the slope of the relaxation rate, was highest for uncoated MIL-100(Fe) and somewhat reduced for coated NPs (top of Fig. 3-8). In T2 (bottom of Fig. 3-8), this difference was less obvious, but a difference still remains between coated and uncoated MIL-100(Fe). As a reference, samples with clinically used Gd-DTPA-BMA (0-2.5 mM; Omniscan, GE) diluted in water have been examined. r_1 relaxivity of 3.33 s^{-1} mM^{-1} at 35.7 °C or for r_2 3.55 s^{-1} mM^{-1} at 35 °C which is according to literature.[56] Based on these results and using the same methods, the observed relaxivities of MOF preparations were considered valid.

Overall, the r_2 relaxivity of the MIL-100(Fe) samples is higher than the r_1 relaxivity, showing that the T2 relaxation process is more effective. Calculated per mmol Fe^{3+} ions, both relaxivities were lower than for commercially available superparamagnetic iron-based contrast agents (e.g. Feridex, $r_1 = 4.7$ L s^{-1} mmol^{-1}, $r_2 = 41$ L s^{-1} mmol^{-1}).[56] We assume that the coating of the MOF NPs reduces water exchange between the NP pores and its surroundings as seen before using thermosensitive liposomes.[57] Since T1 relaxation is a short-range effect, this would account for the reduced relaxivity of coated MOF NPs. T2 relaxation, on the other hand, is a long-range effect, which is less affected by reduced water exchange between pores and the surroundings.
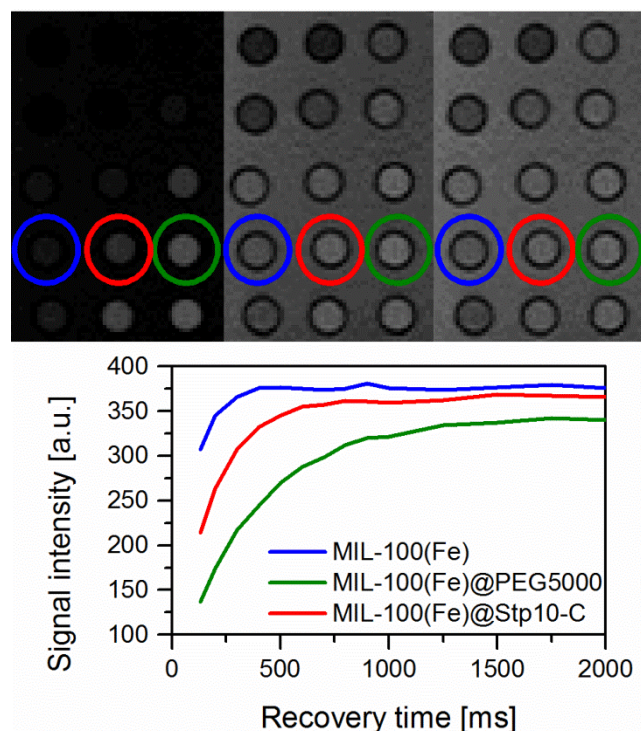
Figure 3-9. Top: MR images of MIL-100(Fe) samples (left column), MIL-100(Fe)@Stp10-C samples (center column) and MIL-100(Fe)@PEG5000 samples (right column), at concentrations of 0.5, 1, 3, 6 and 10 mg/mL from top to bottom. Images are shown with recovery times of 130 ms (left), 800 ms (center) and 1250 ms (right). Bottom: Signal intensity curves of the three indicated samples with a concentration of 6 mg/mL. Uncoated MOF NP show the fastest T1 relaxation (blue), the T1 relaxation of both coated MOFs (red and green) is slower.

Contrary to our results, previous reports about gadolinium based MOF nanoparticles have shown that surface modification can even enhance MRI properties.[58] We point out that the iron-based MOF nanoparticles used in our study exhibit different MRI properties which can be attributed to differences in size, shape and composition.[59] Further, the polymer nature as well as the way of functionalization were different from previous publications. Despite the reduced MR-activity of coated MOF NPs, relaxivities were still high enough to allow visualization by means of MR imaging. This highlights the potential of such core-shell particles as smart theranostic system with a wide range of possible functionalities and applications.

3.3. Conclusion

In summary, we successfully report the selective covalent external surface functionalization of MIL-100(Fe) nanoparticles with two different polymeric structures. Using the mild reaction conditions of peptide coupling chemistry to attach the polymer at the MOF NP surface revealed unchanged crystallinity of the MOF scaffold, proven by XRD and TEM. The attachment of polymer and covalent nature of the bonding was investigated and proven by several techniques, e.g. IR, Zeta-Potential measurements and liquid NMR. Further, the amount of polymer attachable to the external surface was estimated by UV-Vis spectroscopy. The functionalized MOF nanoparticles showed increased colloidal stability in aqueous media and in initial cell studies, and they revealed potential for biomedical applications, displaying good uptake by cells but no cytotoxic effects up to rather high nanoparticle concentrations over 24 h. Furthermore, the influence of the surface coating on MIL-100(Fe) nanoparticles regarding their magnetic resonance imaging properties was investigated and evaluated in detail. Although the coating affected the MRI signal, visualization of functionalized particles was still possible. This allows for the modification of the coating according to the scientific and clinical needs and, at the same time, *in vivo* investigation of MOF nanoparticle distributions such as accumulation in a tumor. The work presented here opens the door for the precise functionalization of the external surface of MOF NPs and hence, defined control over the nanoparticle/environment interface. Furthermore, this functionalization approach provides the potential to be extended to a large variety of MOF-polymer combinations and thus is a versatile tool for the design of multifunctional nanoparticle systems.

3.4. Materials and Methods

Chemicals. Iron (III) chloride hexahydrate (Grüssing GmbH), trimesic acid (BTC, Aldrich), 1-ethyl-3-(3-dimethylaminopropyl)carbodiimide (EDC hydrochloride, Aldrich, crystalline), hydroxy-2,5-dioxopyrrolidine-3-sulfonic acid sodium salt (sulfo-NHS, Aldrich) sodium sulfate (Grüssing GmbH, water-free), 2-[4-(2-hydroxyethyl)piperazine-1-yl]ethanesulfonic acid (HEPES, Biomol GmbH), Glucose (Applichem), α-methoxy-ω-amino poly(ethylene glycol) (PEG5000 amine, Rapp Polymere, PEG-MW: 5000 g/mol), Tentagel S RAM resin (Rapp Polymere), Nα-Fmoc-S-trityl-L-cysteine (Fmoc-Cys(Trt)-OH, Iris Biotech), N-methyl-2-pyrrolidone (NMP, Iris Biotech), 1-hydroxybenzotriazole (HOBt, Aldrich), 2-(1H-benzotriazol-1-yl)-1,1,3,3-tetramethyluronium hexafluorophosphate (HBTU, Multisyntech), N,N-diisopropylethylamine (DIPEA, Iris Biotech), piperidine (Iris Biotech), trifluoroacetic acid (TFA, Iris Biotech), triisopropylsilane (TIS, Aldrich), acetonitrile (HPLC grade, VWR), tris(2-carboxyethyl)phosphine hydrochloride solution (TCEP, 0.5 M, pH 7.0, Aldrich), Cyanine5 maleimide (Lumiprobe) were used as received. The solvents ethanol (EtOH, Aldrich, absolute), N-N,-dimethylformamide (DMF, Iris Biotech) and deuterated trichloromethane (CDCl$_3$, Euriso-top, 99.8 % D) were used without further purification. Dichloromethane (DCM) and methyl-tert-butyl ether (MTBE, Brenntag) were distilled before use. Cell culture media, antibiotics and fetal bovine serum (FBS) were purchased from Life Technologies or Sigma-Aldrich, respectively. As a reference in MRI Gd-DTPA-BMA (Omniscan, GE Healthcare) diluted in water (0-2.5 mM) have been examined.

Synthesis of MIL-100(Fe) nanoparticles. MIL-100(Fe) nanoparticles were prepared in a procedure similar to a literature method.[60] For the microwave synthesis of MIL-100 (Fe) nanoparticles, iron(III) chloride hexahydrate (2.43 g, 9.00 mmol) and trimesic acid (0.84 g, 4.00 mmol) in 30 ml H$_2$O was put into a Teflon tube, sealed and placed in the microwave reactor (Microwave: Synthos3000, *Anton Paar*). The mixture was heated to 130 °C under solvothermal conditions (p = 2.5 bar) within 30 seconds, kept at 130 °C for 4 minutes and 30 seconds, and the resulting solid was cooled down to room temperature. For the purification of the solid, the reaction mixture was centrifuged (Sorvall Evolution RC, *Thermo Scientific*, 47808 rcf / 20000 rpm, 20 min), the solvent was removed and the pellet was redispersed in EtOH. This cycle was repeated two times and the dispersed solid was allowed to sediment overnight. The supernatant was filtrated three times (filter discs grade: 391; Sartorius Stedim Biotech), yielding MIL-100(Fe) nanoparticles, which are left in the filtrate. Afterwards the

material was characterized by DLS, XRD, IR, TGA, TEM, N_2 sorption and zeta-potential measurements.

External surface coating of MIL-100(Fe) nanoparticles with PEG5000. In a standard reaction, MIL-100(Fe) nanoparticles (1.0 mg) were dispersed in ethanol (100 µL). EDC hydrochloride (approx. 1 mg) and a catalytic amount of sulfo-NHS were added to the suspension and stirred for a few minutes. Afterwards, PEG5000amine (100 µg, 20.0 nmol) dissolved in bi-distilled H_2O (100 µL) was poured into the MOF dispersion and the mixture was stirred for 30 min. The functionalized nanoparticles were centrifuged (Eppendorf 5418/5418R, 16873 rcf / 14000 rpm; 10 min), the supernatant was removed and the pellet was washed three times with water by the centrifugation and redispersion technique.

Synthesis of Stp10-C. The oligoamino amide Stp10-C was synthesized on solid-phase using the artificial oligoamino acid Fmoc-Stp(Boc$_3$)-OH[61] and conventional Fmoc solid-phase peptide synthesis conditions. 416.6 mg Tentagel S RAM resin (0.24 mmol/g loading; 100 µmol scale size) were weighed into a 10 mL syringe microrector with PTFE frit (Mutltisyntech). The syringe was put on a vacuum manifold (Promega) and 5 mL DCM were added for resin swelling. After 30 min the DCM was discarded. The resin was washe0d once with 5 mL DMF and the reactor was put in the microwave reactor block of a Biotage Syro Wave automated peptide synthesizer. Fmoc deprotection was carried out by 5-fold incubation with 3 mL 20 % piperidine in DMF for 10 min under shaking. The resin was washed 5 times with 3.2 mL DMF after Fmoc deprotection. Coupling of the C-terminal cysteine was initiated by addition of 1.2 mL of a solution containing 0.33 M Fmoc-Cys(Trt)-OH and HOBt in NMP (400 µmol, 4 eq), 1.26 mL of 0.32 M HBTU in DMF (400 µmol, 4 eq) and 0.6 mL of 1.33 M DIPEA in NMP (800 µmol, 8 eq). The mixture was incubated for 60 min at room temperature under shaking. Subsequently, the solution was removed and the resin was washed twice with 3.2 mL DMF. The coupling step was repeated followed by 5-fold resin washing with 3.2 mL DMF. Fmoc deprotection was carried out as described above followed by 5-fold resin wash with 3.2 mL DMF. The subsequent Stp units were coupled using the same stoichiometry under microwave irradiation. For this, the resin was incubated with 1.2 mL of a solution containing 0.33 M Fmoc-Stp(Boc$_3$)-OH and HOBt in NMP (400 µmol, 4 eq), 1.26 mL of 0.32 M HBTU in DMF (400 µmol, 4 eq) and 0.6 mL of 1.33 M DIPEA in NMP (800 µmol, 8 eq) at 60 °C for 10 min. After removal of the coupling solution and twofold resin wash with 3.2 mL DMF, the coupling step was repeated. The solution was removed and the resin was

washed 5-fold with 3.2 mL DMF. The following Fmoc deprotection, washing and coupling steps were carried out and repeated as described above to assemble the final sequence $H_2NCO-C(Trt)-[Stp(Boc_3)]_{10}-NH_2$. The resin was washed once with 5 mL DCM and dried in vacuo. Cleavage was carried by incubation with 5 mL TFA/TIS/H_2O (95/2.5/2.5, v/v/v) for 90 min at room temperature. The mixture was collected and the resin was washed twice with 2 mL of TFA. The combined solutions were concentrated under reduced pressure and the product was precipitated in 50 mL of cold MTBE/n-Hexan (25/25, v/v). The supernatant was discarded, the pellet was dried under a nitrogen stream. The compound was purified by size exclusion chromatography using the ÄKTApurifier 10 system (GE Healthcare). Sephadex G-10 (GE Healthcare) was used as gel filtration medium and 10 mM hydrochloric acid solution/acetonitrile (7/3, v/v) as eluent. The absorption at 214, 260 and 280 nm was monitored and the fractions corresponding to the high-molecular weight oligomer were pooled, snap-frozen and freeze-dried. As a result of the eluent used, the HCl salt of the multiple amino groups was formed after purification. Stp10-C was analyzed by ^{1}H-NMR (Fig. S3-17), MALDI-MS (Fig. S3-18) and RP-HPLC.

Synthesis of Stp10-C*Cy5. 24.1 mg of Stp10-C (6.1 µmol) were dissolved in 1000 µL HEPES buffer (10 mM, pH 7.4). 122 µL of 0.5 M TCEP solution (61 µmol, 10 eq) were added and the solution was incubated for 30 min under shaking. 5.85 mg of Cyanine5 maleimide (9.1 µmol, 1.5 eq) were dissolved in 200 µL DMF and added to the Stp10-C solution. The reaction tube was flushed with nitrogen and incubated for 4 hours at room temperature under shaking in the dark. The compound was purified by size exclusion chromatography as described above using the ÄKTA purifier 10 system (GE Healthcare), Sephadex G-10 (GE Healthcare) as gel filtration medium and 10 mM hydrochloric acid solution/acetonitrile (7/3, v/v) as eluent. The absorption at 214, 280 and 646 nm was monitored, and the fractions corresponding to the high-molecular weight oligomer were pooled, snap-frozen and freeze-dried.

External surface coating of MIL-100(Fe) nanoparticles with Stp10-C. In a standard reaction, MIL-100(Fe) nanoparticles (1.0 mg) were dispersed in ethanol (100 µL). EDC hydrochloride (approx. 1 mg) and a catalytic amount of sulfo-NHS were added to the suspension and stirred for a few minutes. Afterwards, Stp10-C (79.3 µg, 20.0 nmol) dissolved in bi-distilled H_2O (100 µL) was poured into the MOF dispersion and the mixture was stirred for 30 min. The functionalized nanoparticles were centrifuged (14000 rpm; 10 min), the

supernatant was removed and the pellet was washed three times with water by the centrifugation and redispersion technique.

Dissolution of MOF particles in EDTA solution and extraction of functionalized linker.
Functionalized MIL-100(Fe) particles were dispersed in an EDTA solution (0.1 mM) to result in a 2 mg/mL concentration. The dispersion was stirred for approx. 24 h until complete dissolution had occurred. Afterwards, the aqueous phase was extracted three times with equal amounts of DCM (20 mL). The organic phases were combined and dried over sodium sulfate for 1 h. After removal of the solvent, the product was dried under high vacuum. NMR spectroscopy was performed in $CDCl_3$.

Cell Culture. Murine neuroblastoma (N2A) were cultured in Dulbecco's modified Eagle's medium (DMEM), supplemented with 1 g/L glucose, 10% FBS, 100 U/mL penicillin, 100 μg/mL streptomycin and 4 mM stable glutamine.

Preparation of HEPES-buffered glucose (HBG). In an aqueous solution of HEPES (20 mM), 5% glucose was added and the pH was adjusted to 7.4 by addition of hydrochloric acid.

Metabolic activity assay of MIL-100(Fe) and MIL-100(Fe)@Stp10-C*Cy5 (MTT assay).
Murine neuroblastoma (N2A) cells were seeded in 96-well plates at a density of 10.000 cells/well 24 h prior to incubation with the different particle concentrations. Before incubation with the particles, medium was replaced with 80 μL fresh medium containing 10% FBS. Particles diluted in 20 μL HBG were added to each well and incubated on cells for 24 h at 37°C and 5% CO_2. 10 μL of MTT (3-(4,5-dimethylthia-zol-2-yl)-2,5-diphenyltetrazolium bromide) (5 mg/mL) were added to each well reaching a final concentration of 0.5 mg/mL. After an incubation time of 2 h, unreacted dye and medium were removed and the 96-well plates were frozen at −80°C for at least one hour. The purple formazan product was then dissolved in 100 μL DMSO (dimethyl sulfoxide) per well and quantified measuring absorbance using microplate reader (TecanSpectrafluor Plus, Tecan, Switzerland) at 590 nm with background correction at 630 nm. All studies were performed in quintuplicate. The relative cell viability (%) related to control wells treated only with 20 μL HBG was calculated as ([A] test/[A] control) × 100%.

Magnetic Resonance Imaging (MRI). Imaging was performed with a 1.5 T clinical MRI system (Magnetom Aera, Siemens Health Care, Germany). Samples were filled into 2 mL Eppendorf tubes that were imaged in parallel rows of 5 samples. A PMMA sample holder fixed the tubes submersed in a basin filled with 650 mL water and 0.4 mL Gd-DTPA (0.5 mmol/mL) at 24 °C. As a reference sample tubes with Gd-DTPA-BMA (Omniscan, GE Healthcare) diluted in water (0-2.5 mM) have been examined. This setup was placed in a standard MRI head coil for imaging. After using standard MRI pulse sequences for orientation, a gradient echo sequence with a nonselective saturation recovery (SR) preparation pulse was applied for calculation of T1 parameter maps varying the saturation recovery time from 130 – 3000 ms in 17 steps. T2-weighted multi contrast 2D spin echo sequences (SE MC) were repeated varying the echo time 16 times in steps of 15 ms starting with 15 ms and ending with 240 ms for T2 parameter map calculation. Other imaging parameters for SR were as follows: echo time = 1.71 ms, repetition time = 747 ms; matrix = 128 x 128; in plane resolution = 1 mm; slice thickness = 6 mm; α = 15°; parallel imaging acceleration factor = 2. Slice thickness, FOV and the parallel imaging acceleration factor were the same for SE MC. However, here the repetition time was 3 s; the in plane resolution was 0.5 mm; the echo train length was 16; and the matrix was 256 x 256.All data were transferred in DICOM format and processed off-line using the software PMI 0.3, written in-house using IDL 6.4 (ITT Visual Information Systems, Boulder, CO). Calculations were done using mean signal intensity values that were determined in region of interests (ROI). ROIs were placed in the center of each sample tube as displayed in Fig. S3-1. Least-squares fitting was done using the Levenberg-Marquardt-algorithm.

Fluorescence Microscopy. Murine neuroblastoma (N2A) cells were seeded in Nunc chamber slides (Thermo Scientific, Germany) at a density of 30.000 cells/ well 24h prior to incubation with different particle concentrations. Before incubation with the particles, medium was replaced with 80µL fresh medium containing 10% fetal bovine serum (FBS). Particles diluted in 60µL HEPES-buffered glucose (HBG) were added to each well and incubated for 7 h and 24 h at 37°C and 5% CO_2. Cell membranes were stained with wheat germ agglutinin Alexa Fluor 488 conjugate (Life Technologies) at a final concentration of 5 µg/mL prior to imaging. Live cells were imaged using spinning disc microscopy (Zeiss Cell Observer SD utilizing a Yokogawa spinning disk unit CSU-X1). The objective was a 1.40 NA 63x Plan apochromat oil immersion objective (Zeiss). Cy5 was imaged with 639 nm and WGA 488 with 488 nm laser excitation, respectively. For two color detection a dichroic mirror (560 nm, Semrock)

and band-pass filters 525/50 and 690/60 (both Semrock) were used in the detection path. Separate images for each fluorescence channel were acquired using two separate electron multiplier charge coupled device (EMCCD) cameras (PhotometricsEvolve^{TM}).

3.5. References

[1]   Zhang, F.; Lees, E.; Amin, F.; Rivera Gil, P.; Yang, F.; Mulvaney, P.; Parak, W. J., *Small* **2011,** 7, (22), 3113-3127.

[2]   Goesmann, H.; Feldmann, C., *Angewandte Chemie International Edition* **2010,** 49, (8), 1362-1395.

[3]   Choi, K. M.; Jeong, H. M.; Park, J. H.; Zhang, Y.-B.; Kang, J. K.; Yaghi, O. M., *ACS Nano* **2014,** 8, (7), 7451-7457.

[4]   Tay, C. Y.; Setyawati, M. I.; Xie, J.; Parak, W. J.; Leong, D. T., *Advanced Functional Materials* **2014,** 24, (38), 5936-5955.

[5]   Nel, A. E.; Madler, L.; Velegol, D.; Xia, T.; Hoek, E. M. V.; Somasundaran, P.; Klaessig, F.; Castranova, V.; Thompson, M., *Nature Materials* **2009,** 8, (7), 543-557.

[6]   Bogart, L. K.; Pourroy, G.; Murphy, C. J.; Puntes, V.; Pellegrino, T.; Rosenblum, D.; Peer, D.; Lévy, R., *ACS Nano* **2014,** 8, (4), 3107-3122.

[7]   Falcaro, P.; Ricco, R.; Doherty, C. M.; Liang, K.; Hill, A. J.; Styles, M. J., *Chemical Society Reviews* **2014,** 43, (16), 5513-5560.

[8]   Biju, V., *Chemical Society Reviews* **2014,** 43, (3), 744-764.

[9]   Li, Z.; Barnes, J. C.; Bosoy, A.; Stoddart, J. F.; Zink, J. I., *Chemical Society Reviews* **2012,** 41, (7), 2590-2605.

[10]   Cohen, S. M., *Chemical Science* **2010,** 1, (1), 32-36.

[11]   Horcajada, P.; Gref, R.; Baati, T.; Allan, P. K.; Maurin, G.; Couvreur, P.; Férey, G.; Morris, R. E.; Serre, C., *Chemical Reviews* **2012,** 112, (2), 1232-1268.

[12]   Hirschle, P.; Prei; Auras, F.; Pick, A.; Volkner, J.; Valdeperez, D.; Witte, G.; Parak, W. J.; Radler, J. O.; Wuttke, S., *CrystEngComm* **2016**, *18*, 4359–4368.

[13]   Cohen, S. M., *Chemical Reviews* **2012,** 112, (2), 970-1000.

[14]   Furukawa, H.; Cordova, K. E.; O'Keeffe, M.; Yaghi, O. M., *Science* **2013,** 341, (6149), 974.

[15]   Furukawa, H.; Müller, U.; Yaghi, O. M., *Angewandte Chemie International Edition* **2015,** 54, (11), 3417-3430.

[16]   Guillerm, V.; Kim, D.; Eubank, J. F.; Luebke, R.; Liu, X.; Adil, K.; Lah, M. S.; Eddaoudi, M., *Chemical Society Reviews* **2014,** 43, (16), 6141-6172.

[17]   Doherty, C. M.; Grenci, G.; Riccò, R.; Mardel, J. I.; Reboul, J.; Furukawa, S.; Kitagawa, S.; Hill, A. J.; Falcaro, P., *Advanced Materials* **2013,** 25, (34), 4701-4705.

[18]   Alexis, F.; Pridgen, E.; Molnar, L. K.; Farokhzad, O. C., *Molecular Pharmaceutics* **2008,** 5, (4), 505-515.

[19]   Monopoli, M. P.; Aberg, C.; Salvati, A.; Dawson, K. A., *Nature Nanotechnology* **2012,** 7, (12), 779-786.

[20]   McGuire, C. V.; Forgan, R. S., *Chemical Communications* **2015,** 51, 5199-5217.

[21]   Rowe, M. D.; Thamm, D. H.; Kraft, S. L.; Boyes, S. G., *Biomacromolecules* **2009,** 10, (4), 983-993.

[22]   Bellido, E.; Hidalgo, T.; Lozano, M. V.; Guillevic, M.; Simón-Vázquez, R.; Santander-Ortega, M. J.; González-Fernández, Á.; Serre, C.; Alonso, M. J.; Horcajada, P., *Advanced Healthcare Materials* **2015,** 4, (8), 1246-1257.

[23]   Wang, S.; Morris, W.; Liu, Y.; McGuirk, C. M.; Zhou, Y.; Hupp, J. T.; Farha, O. K.; Mirkin, C. A., *Angewandte Chemie International Edition* **2015,** 54, 14738–14742.

[24]   Wuttke, S.; Dietl, C.; Hinterholzinger, F. M.; Hintz, H.; Langhals, H.; Bein, T., *Chemical Communications* **2014,** 50, (27), 3599-3601.

[25]   Liu, B.; Ma, M.; Zacher, D.; Bétard, A.; Yusenko, K.; Metzler-Nolte, N.; Wöll, C.; Fischer, R. A., *Journal of the American Chemical Society* **2011,** 133, (6), 1734-1737.

[26]   Liu, B.; Fischer, R., *Sci. China Chem.* **2011,** 54, (12), 1851-1866.

[27]   Matzger, A.; McDonald, K. A.; Feldblyum, J.; Koh, K.; Wong-Foy, A., *Chemical Communications* **2015,** 51, (60), 11994-11996.

[28]   Kondo, M.; Furukawa, S.; Hirai, K.; Kitagawa, S., *Angewandte Chemie International Edition* **2010,** 49, (31), 5327-5330.

[29]   Jung, S.; Kim, Y.; Kim, S.-J.; Kwon, T.-H.; Huh, S.; Park, S., *Chemical Communications* **2011,** 47, (10), 2904-2906.

[30]   Shih, Y.-H.; Lo, S.-H.; Yang, N.-S.; Singco, B.; Cheng, Y.-J.; Wu, C.-Y.; Chang, I. H.; Huang, H.-Y.; Lin, C.-H., *ChemPlusChem* **2012,** 77, (11), 982-986.

[31]   Baati, T.; Njim, L.; Neffati, F.; Kerkeni, A.; Bouttemi, M.; Gref, R.; Najjar, M. F.; Zakhama, A.; Couvreur, P.; Serre, C.; Horcajada, P., *Chemical Science* **2013,** 4, (4), 1597-1607.

[32]   Bezverkhyy, I.; Weber, G.; Bellat, J.-P., *Microporous and Mesoporous Materials* **2016,** 219, 117-124.

[33]   Bellido, E.; Guillevic, M.; Hidalgo, T.; Santander-Ortega, M. J.; Serre, C.; Horcajada, P., *Langmuir* **2014,** 30, (20), 5911-5920.

[34]   Horcajada, P.; Chalati, T.; Serre, C.; Gillet, B.; Sebrie, C.; Baati, T.; Eubank, J. F.; Heurtaux, D.; Clayette, P.; Kreuz, C.; Chang, J.-S.; Hwang, Y. K.; Marsaud, V.; Bories, P.-N.; Cynober, L.; Gil, S.; Ferey, G.; Couvreur, P.; Gref, R., *Nature Materials* **2010,** 9, (2), 172-178.

[35] Wuttke, S.; Braig, S.; Preiß, T.; Zimpel, A.; Sicklinger, J.; Bellomo, C.; Radler, J. O.; Vollmar, A. M.; Bein, T., *Chemical Communications* **2015,** 51, (87), 15752-15755.

[36] He, C.; Liu, D.; Lin, W., *ACS Nano* **2015,** 9, (1), 991-1003.

[37] Huxford-Phillips, R. C.; Russell, S. R.; Liu, D.; Lin, W., *RSC advances* **2013,** 3, (34), 14438-14443.

[38] Horcajada, P.; Surble, S.; Serre, C.; Hong, D.-Y.; Seo, Y.-K.; Chang, J.-S.; Greneche, J.-M.; Margiolaki, I.; Ferey, G., *Chemical Communications* **2007**, (27), 2820-2822.

[39] Cauda, V.; Argyo, C.; Bein, T., *Journal of Materials Chemistry* **2010,** 20, (39), 8693-8699.

[40] Gref, R.; Domb, A.; Quellec, P.; Blunk, T.; Müller, R. H.; Verbavatz, J. M.; Langer, R., *Advanced drug delivery reviews* **1995,** 16, (2-3), 215-233.

[41] Mori, Y.; Nagaoka, S.; Takiuchi, H.; Kikuchi, T.; Noguchi, N.; Tanzawa, H.; Noishiki, Y., *ASAIO Journal* **1982,** 28, (1), 459-463.

[42] Schaffert, D.; Troiber, C.; Salcher, E. E.; Fröhlich, T.; Martin, I.; Badgujar, N.; Dohmen, C.; Edinger, D.; Kläger, R.; Maiwald, G.; Farkasova, K.; Seeber, S.; Jahn-Hofmann, K.; Hadwiger, P.; Wagner, E., *Angewandte Chemie International Edition* **2011,** 50, (38), 8986-8989.

[43] Lächelt, U.; Kos, P.; Mickler, F. M.; Herrmann, A.; Salcher, E. E.; Rödl, W.; Badgujar, N.; Bräuchle, C.; Wagner, E., *Nanomedicine: Nanotechnology, Biology and Medicine* **2014,** 10, (1), 35-44.

[44] Scholz, C.; Kos, P.; Leclercq, L.; Jin, X.; Cottet, H.; Wagner, E., *ChemMedChem* **2014,** 9, (9), 2104-2110.

[45] Ali, Z.; Abbasi, A. Z.; Zhang, F.; Arosio, P.; Lascialfari, A.; Casula, M. F.; Wenk, A.; Kreyling, W.; Plapper, R.; Seidel, M.; Niessner, R.; Knöll, J.; Seubert, A.; Parak, W. J., *Analytical Chemistry* **2011,** 83, (8), 2877-2882.

[46] Agostoni, V.; Horcajada, P.; Noiray, M.; Malanga, M.; Aykaç, A.; Jicsinszky, L.; Vargas-Berenguel, A.; Semiramoth, N.; Daoud-Mahammed, S.; Nicolas, V.; Martineau, C.; Taulelle, F.; Vigneron, J.; Etcheberry, A.; Serre, C.; Gref, R., *Scientific Reports* **2015,** 5.

[47] Socrates, G., *Infrared and Raman Characteristic Group Frequencies: Tables and Charts*. 3rd Edition ed.; John Wiley and Sons, Ltd.: Chichester, 2001.

[48] Rusu, L.; Gambhir, A.; McLaughlin, S.; Rädler, J., *Biophysical Journal* **2004,** 87, (2), 1044-1053.

[49]   Rigler, R.; Mets, Ü.; Widengren, J.; Kask, P., *European Biophysics Journal* 22, (3), 169-175.

[50]   Elson, E. L.; Magde, D., *Biopolymers* **1974,** 13, (1), 1-27.

[51]   Wang, Z.; Tanabe, K. K.; Cohen, S. M., *Inorganic Chemistry* **2009,** 48, (1), 296-306.

[52]   Ikezoe, Y.; Washino, G.; Uemura, T.; Kitagawa, S.; Matsui, H., *Nature Materials* **2012,** 11, (12), 1081-1085.

[53]   Banfi, D.; Patiny, L., *CHIMIA International Journal for Chemistry* **2008,** 62, (4), 280-281.

[54]   Brittain, W. J.; Minko, S., *Journal of Polymer Science Part A: Polymer Chemistry* **2007,** 45, (16), 3505-3512.

[55]   Torrano, A. A.; Blechinger, J.; Osseforth, C.; Argyo, C.; Reller, A.; Bein, T.; Michaelis, J.; Brauchle, C., *Nanomedicine (London, England)* **2013,** 8, (11), 1815-28.

[56]   Rohrer, M.; Bauer, H.; Mintorovitch, J.; Requardt, M.; Weinmann, H. J., *Investigative Radiology* **2005,** 40, (11), 715-24.

[57]   Hossann, M.; Wang, T.; Syunyaeva, Z.; Wiggenhorn, M.; Zengerle, A.; Issels, R. D.; Reiser, M.; Lindner, L. H.; Peller, M., *Journal of Controlled Release* **2013,** 166, (1), 22-29.

[58]   Rowe, M. D.; Chang, C.-C.; Thamm, D. H.; Kraft, S. L.; Harmon, J. F.; Vogt, A. P.; Sumerlin, B. S.; Boyes, S. G., *Langmuir* **2009,** 25, (16), 9487-9499.

[59]   Hatakeyama, W.; Sanchez, T. J.; Rowe, M. D.; Serkova, N. J.; Liberatore, M. W.; Boyes, S. G., *ACS Applied Materials & Interfaces* **2011,** 3, (5), 1502-1510.

[60]   García Márquez, A.; Demessence, A.; Platero-Prats, A. E.; Heurtaux, D.; Horcajada, P.; Serre, C.; Chang, J.-S.; Férey, G.; de la Peña-O'Shea, V. A.; Boissière, C.; Grosso, D.; Sanchez, C., *European Journal of Inorganic Chemistry* **2012**, *2012*, 5165-5174.

[61]   Schaffert, D.; Badgujar, N.; Wagner, E., *Organic Letters* **2011**, *13*, 1586-1589.

3.6. Appendix
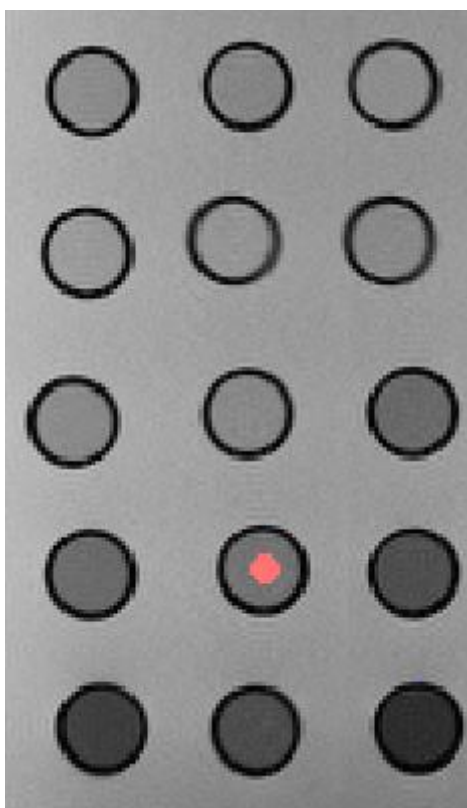
Figure S3-1. Image of axial cross section of sample tubes acquired with SE MC (TE = 15 ms). ROI (red region of interest) used for calculation of T2 using mean signal intensities determined in these ROIs. As the samples comprise a wide range of T2 times it was not possible to set the window in such a way that all samples appear differently.
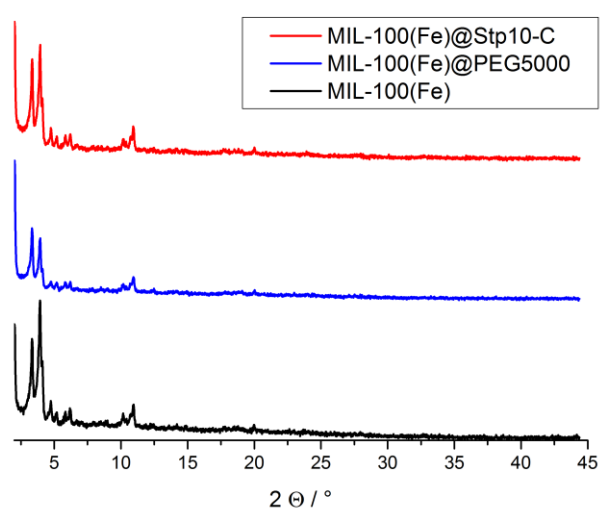
Figure S3-2. XRD pattern of functionalized and unfunctionalized MIL-100(Fe) nanoparticles.
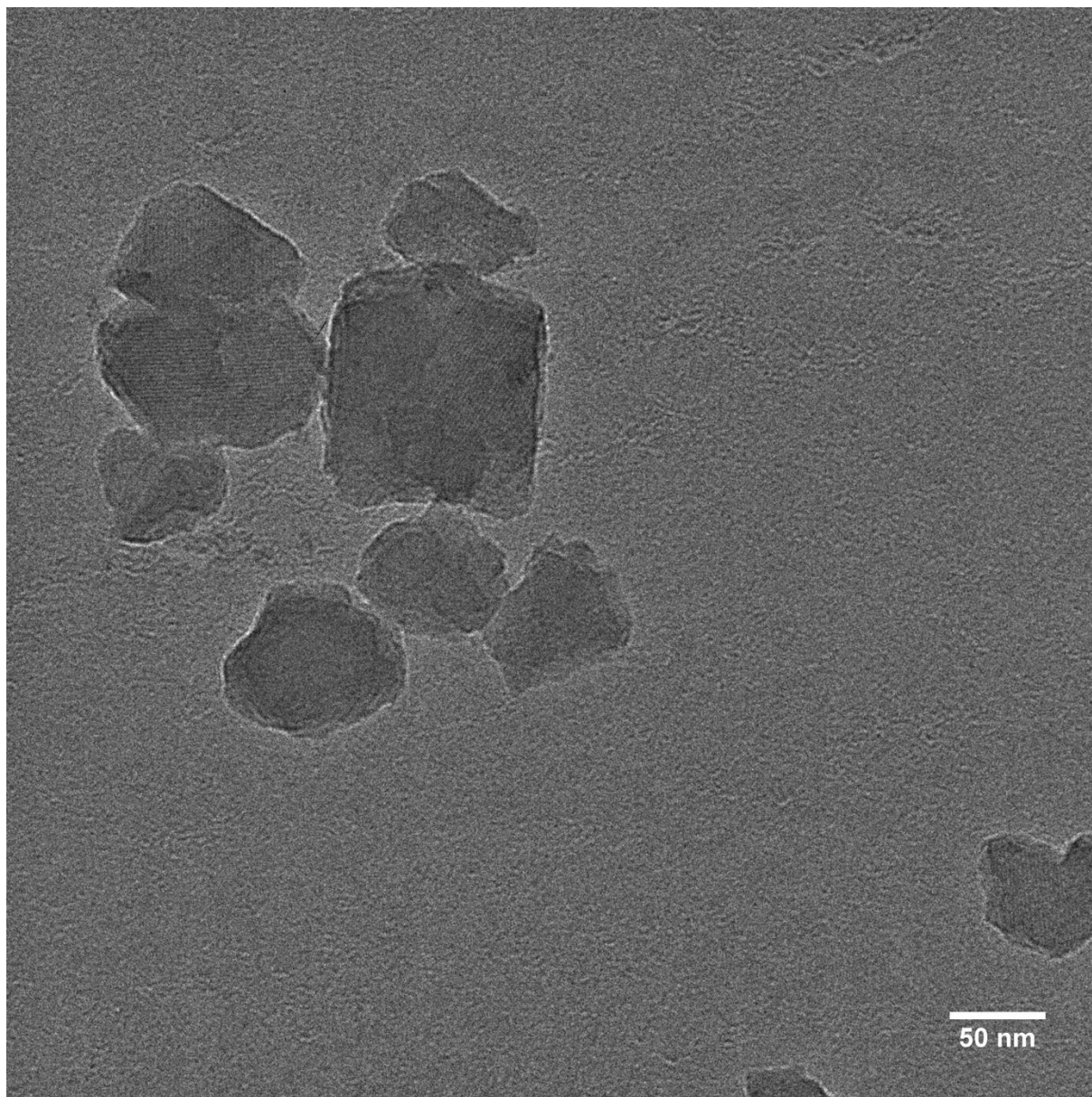
Figure S3-3. TEM image of unfunctionalized MIL-100(Fe) nanoparticles.
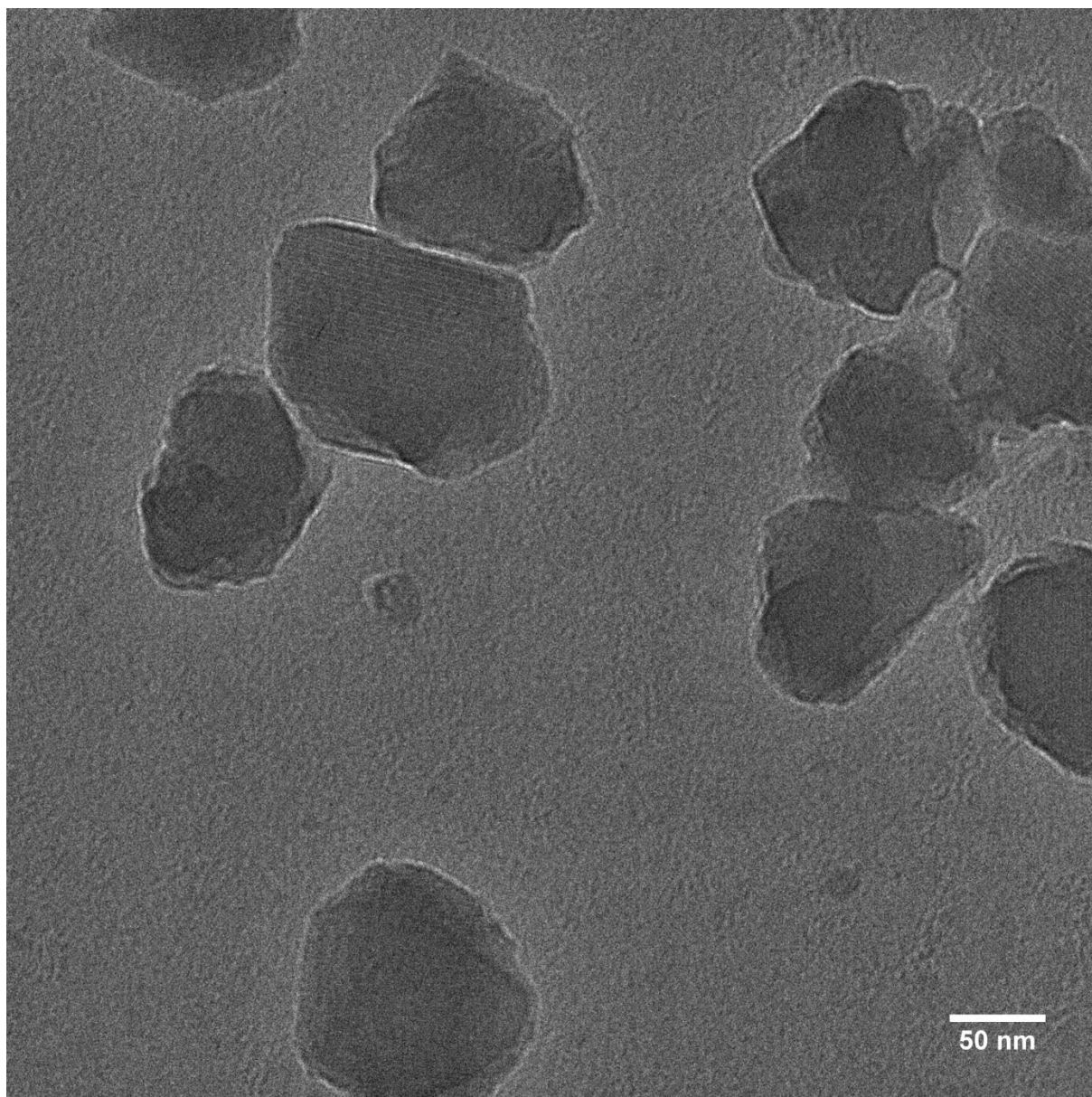
Figure S3-4. TEM image of MIL-100(Fe)@Stp10-C nanoparticles.
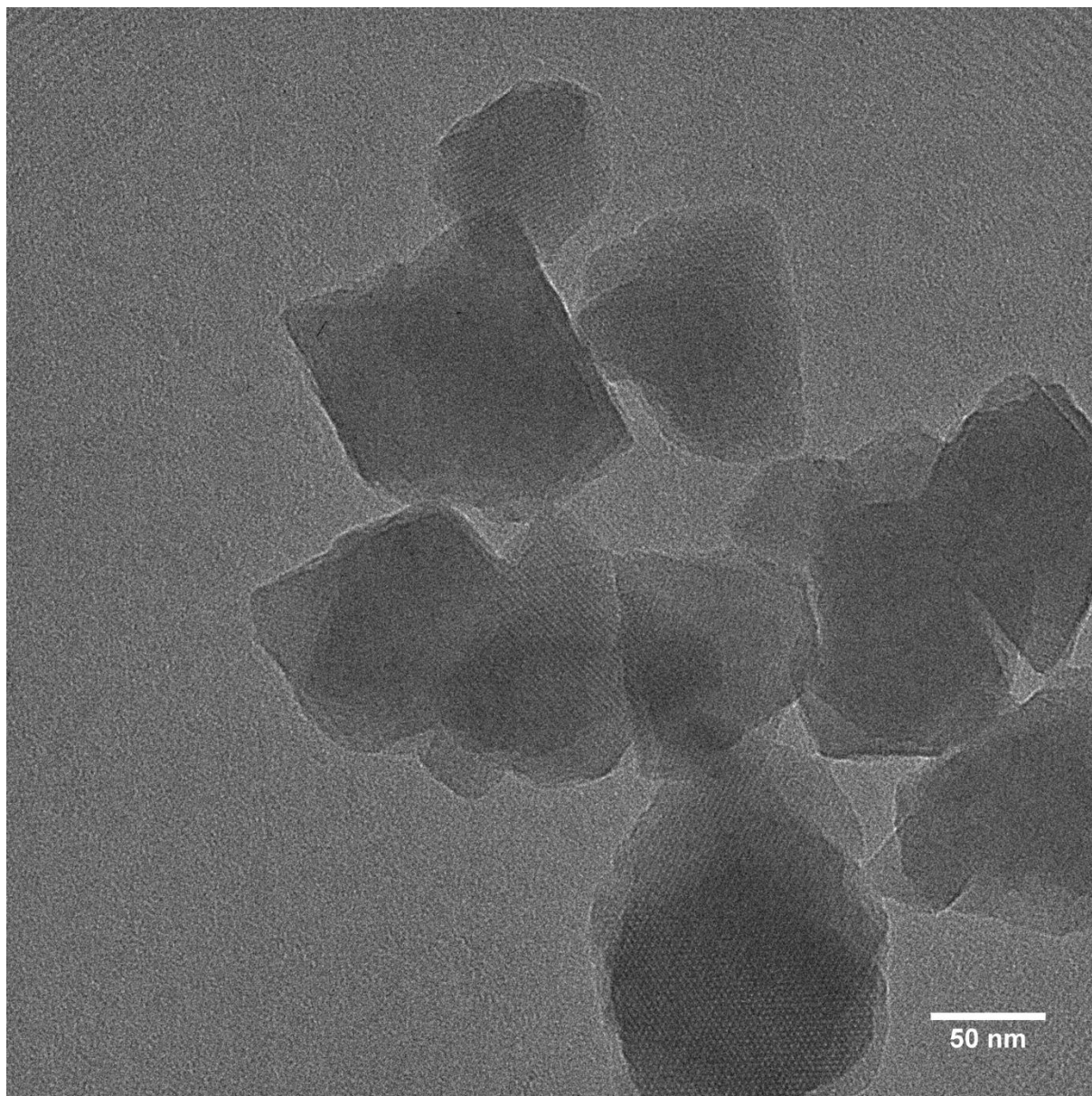
Figure S3-5. TEM image of MIL-100(Fe)@PEG5000 nanoparticles.
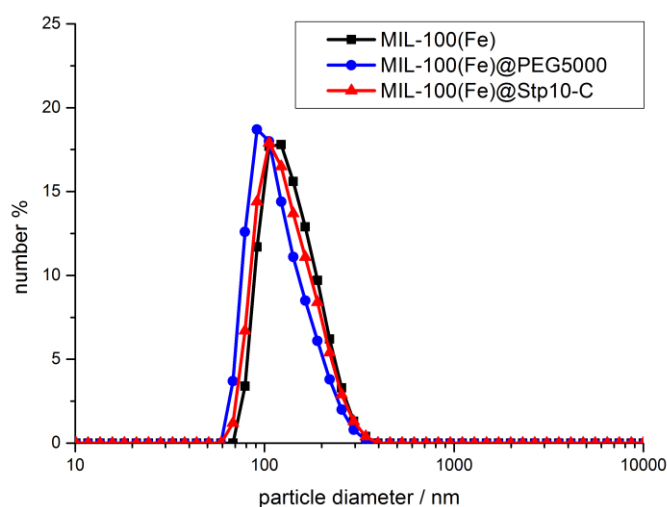
Figure S3-6. DLS measurements of functionalized and unfunctionalized MIL-100(Fe) nanoparticles in EtOH.

Table S3-1. DLS (Z-Average) data of functionalized and unfunctionlized MIL-100(Fe) nanoparticles dispersed in bi-distilled water . After 3 weeks, MIL-100(Fe) particles start to agglomerate, while the functionalized particles retain their colloidal stability.

Sample	MIL-100(Fe)	MIL-100(Fe)@Stp10-C	MIL-100(Fe)@PEG5000
after dispersion	159 nm	156 nm	154 nm
after 3h	153 nm	156 nm	150 nm
after 24h	157 nm	156 nm	150 nm
after 72h	156 nm	154 nm	147 nm
after 1 week	158 nm	155 nm	148 nm
after 3 weeks	**213 nm**	152 nm	146 nm
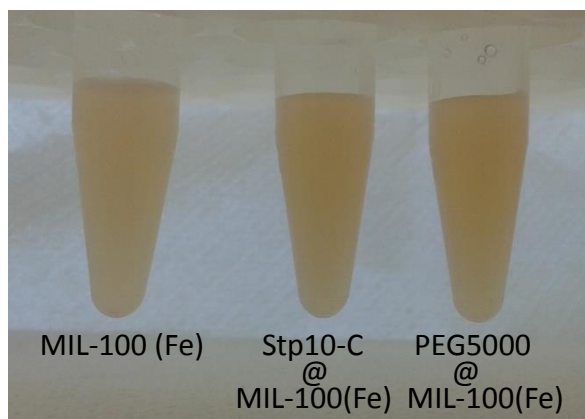
Figure S3-7. Particles dispersion of functionalized and unfunctionalized MIL-100(Fe) nanoparticles after 3h in H$_2$O

Table S3-2. DLS (Z-Average) data of functionalized and unfunctionlized MIL-100(Fe) nanoparticles dispersed in 10% fetal bovine serum (FBS) within 3 weeks. Unfunctionalized particles start to agglomerate immediately, while polymer-functionalized particles retain their colloidal stability for 72 h.

Sample	MIL-100(Fe)	MIL-100(Fe)@Stp10-C	MIL-100(Fe)@PEG5000
after dispersion	> 1000 nm	376 nm	600 nm
after 3h	> 1000 nm	429 nm	669 nm
after 24h	> 1000 nm	432 nm	695 nm
after 72h	> 1000 nm	489 nm	715 nm
after 1 week	> 1000 nm	721 nm	> 1000 nm
after 3 weeks	> 1000 nm	879 nm	958 nm
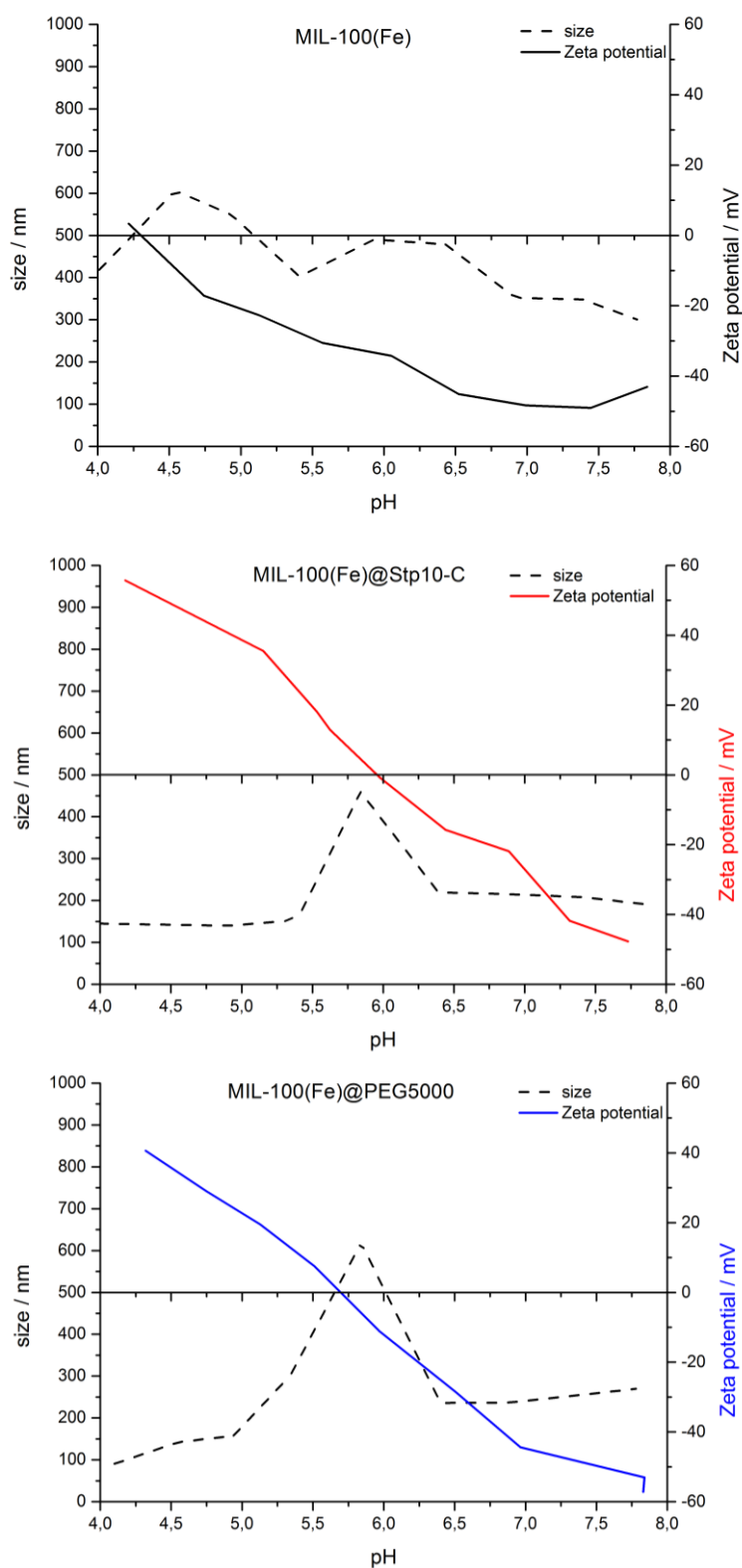
Figure S3-8. Zeta-potential compared to particle size in the pH range from 4 to 8 for functionalized and unfunctionalized MIL-100(Fe) nanoparticles.
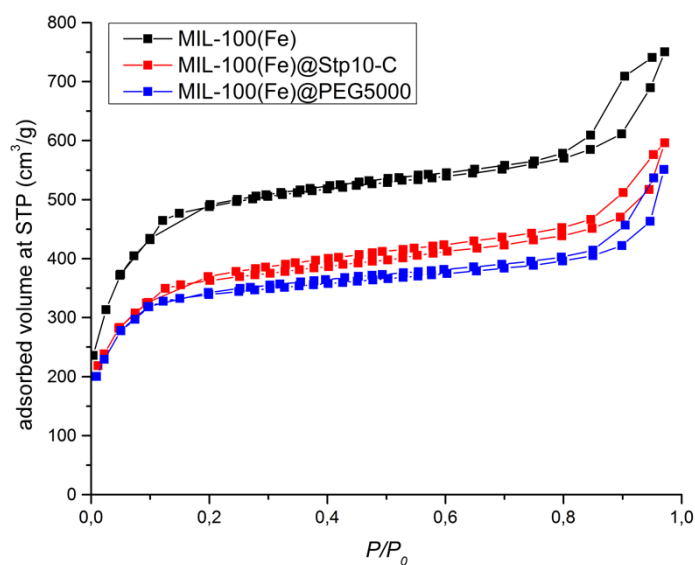
Figure S3-9. Nitrogen sorption isotherms of functionalized and unfunctionalized MIL-100(Fe) nanoparticles.

Table S3-3. Pore volume and BET surface areas of MIL-100(Fe) and functionalized MIL-100(Fe) nanoparticles calculated from N2 sorption isothermes of Figure S-9

MOF	pore volume (cm³/g)	BET surface area (m²/g)
MIL-100(Fe)	1.057	1905
MIL-100(Fe)@PEG5000	0.750	1338
MIL-100(Fe)@Stp10-C	0.823	1432
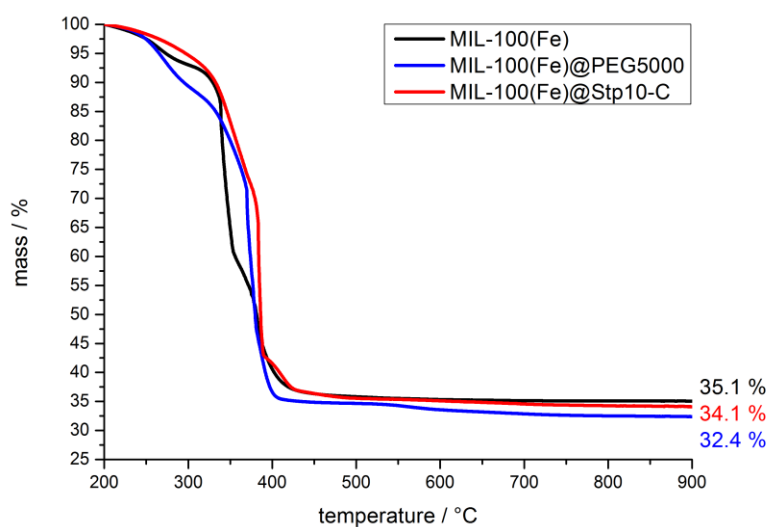
Figure S3-10. TGA of functionalized and unfunctionalized MIL-100(Fe) nanoparticles.
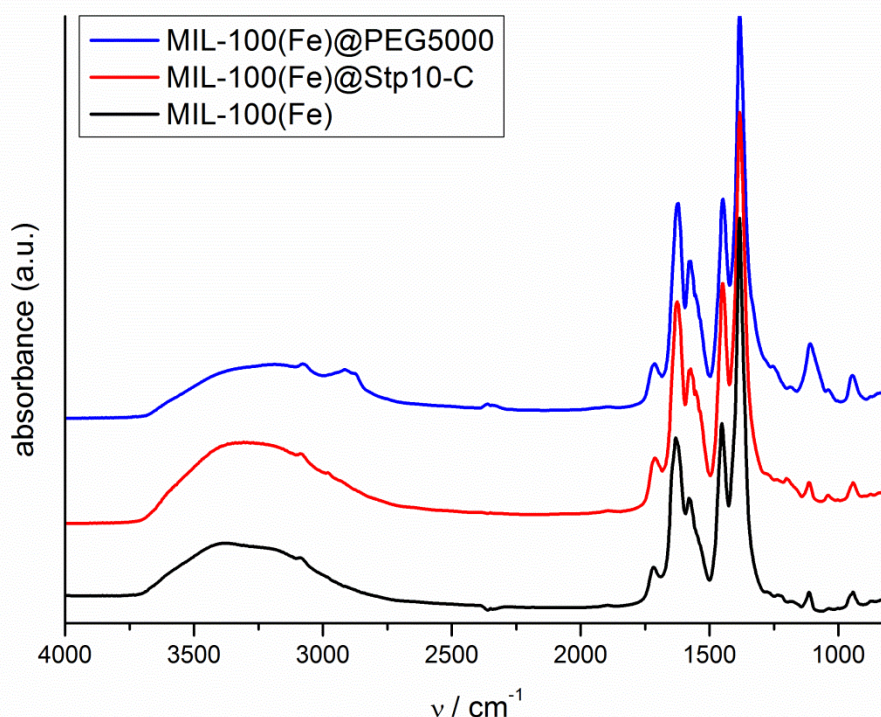
Figure S3-11. IR spectra of functionalized and unfunctionalized MIL-100(Fe) nanoparticles.
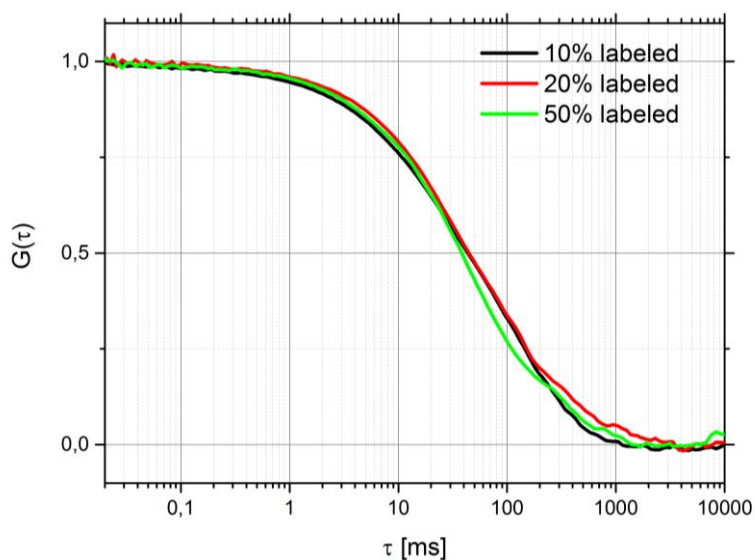
Figure S3-12. Normalized FCS curves of MIL-100(Fe)@Stp10-C*Cy5 nanoparticles with varied amount of labelled Stp10-C. As the curves show no significant deviation we conclude that the fluorescent label has no effect on the function of Stp10-C.
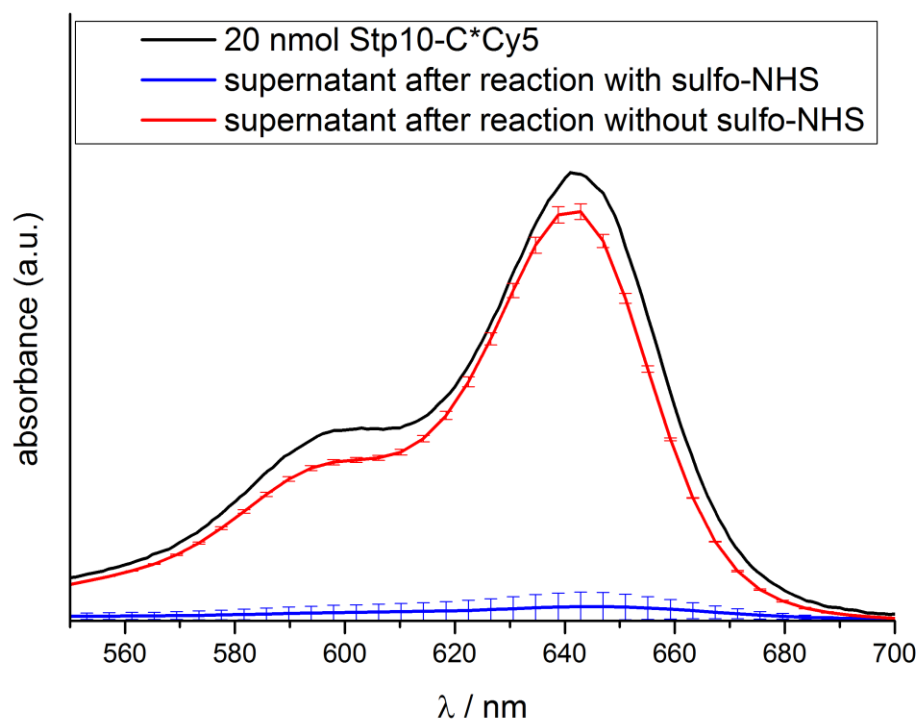
Figure S3-13. UV-Vis spectra of supernatant with and without addition of sulfo-NHS to the reaction mixture.
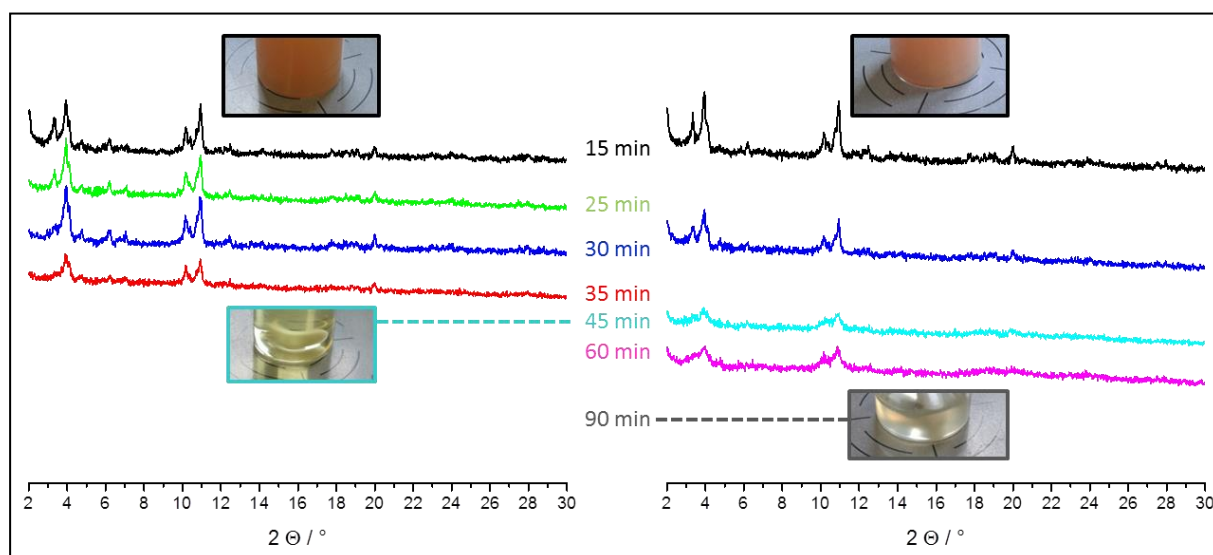
Figure S3-14. XRD spectra of PEG-functionalized (right) and unfunctionalized (left) MOF nanoparticles in comparison; time-based dissolution behaviour in EDTA-solution (0.1 mM; 2.0 mg (MOF)/mL). After 45 minutes, the unfunctionalized particles are completely dissolved. PEG-functionalized nanoparticles are stable up to 90 minutes.
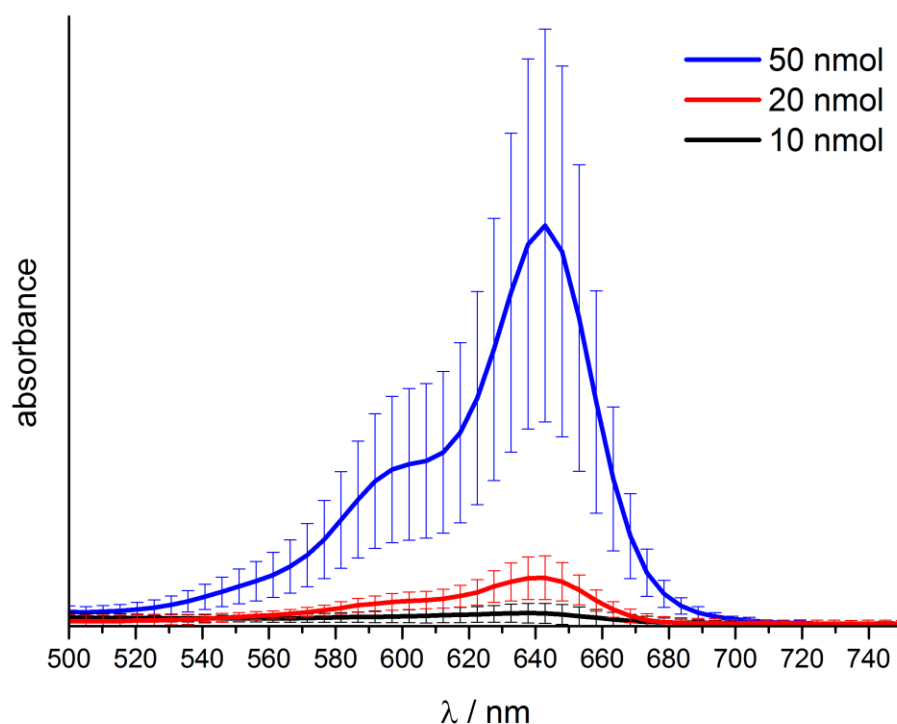
Figure S3-15. Averaged UV-Vis data with standard deviations (error bars indicate the deviation of three individual measurements) of supernatant after coating reactions of Stp10-C; for 10 nmol polymer, the whole amount of polymer was attached to the MOF while there is some residue for 20 nmol. Therefore the covalent attachable amount was estimated to be between 10 and 20 nmol.
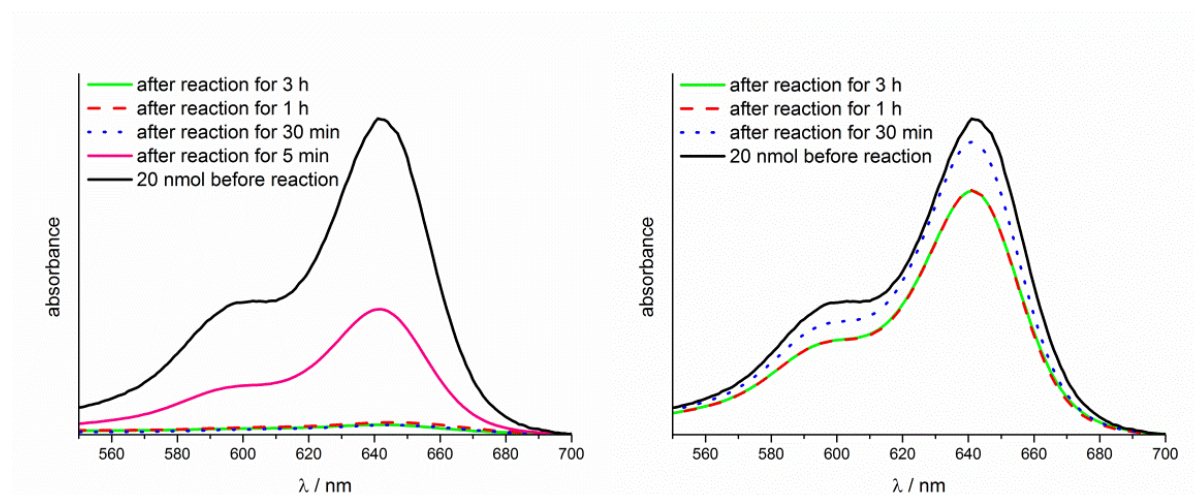
Figure S3-16. Time-dependent amount of polymer left in the supernatant after reaction with (left) and without sulfo-NHS added to the reaction mixture. After 30 minutes with sulfo-NHS the reaction is already completed. During the same period of time almost no dye was adsorbed unspecifically to the particles, as there is no decrease of polymer visible after 30 minutes reaction without sulfo-NHS.

Figure S3-17. ^{1}H-NMR (400 MHz, deuterium oxide) δ = 4.39 (t, 1H), 3.55 – 3.12 (m, 162H), 2.50 (s, 40H).

Figure S3-18. MALDI-MS spectrum of C-Stp10. Mass calculated for $[M+H]^+$ 2833.1, mass found 2835.2; mass calculated for $[M+Na]^+$ 2855.0, mass found 2859.9.
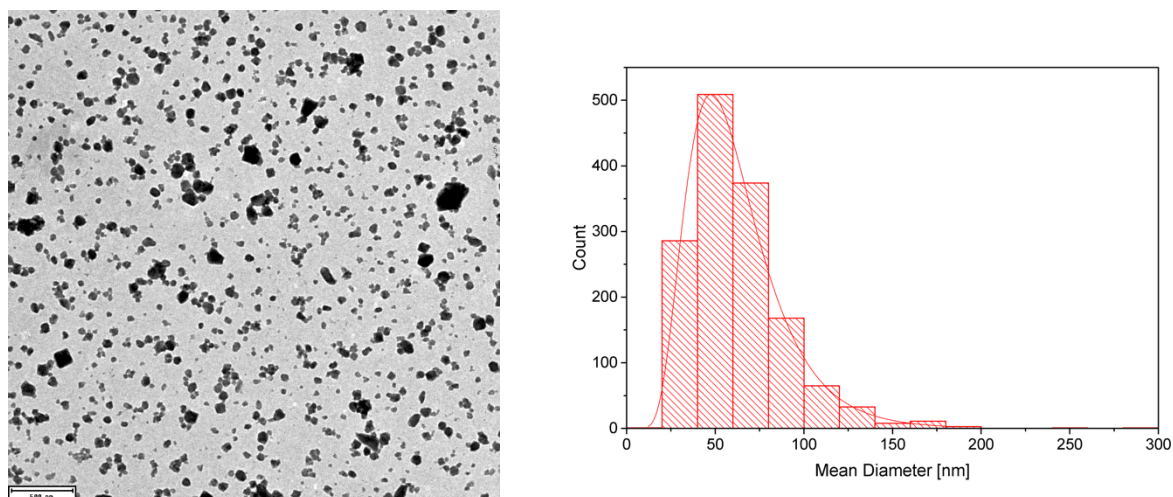
Figure S3-19. Representative transmission electron micrograph of MIL-100(Fe) nanoparticles (left). Size distribution of more than 1500 analyzed MIL-100(Fe) nanoparticles acquired from TEM pictures via image analysis (right). The mean radius was determined to be 26.5 nm.

Calculations on the amount of attachable polymer

The mass density of MIL-100(Fe), determined by structure refinement of XRD pattern, is $\rho = 0.98 \frac{g}{mL}$.[1] Using a mass of $m = 1\,mg$, and a mean radius for the nanoparticles of $r = 26.5\,nm$ taken from TEM-analysis (see Figure S3-19), one derives a **number of particles per mg** of

$$N = \frac{V_{overall}}{V_{NP}} = \mathbf{1.309 \cdot 10^{13}}$$

with

$$V_{overall} = m/\rho = 1.020\ \mu L = 1.020\ mm^3$$

as the volume taken up by one mg of material, and

$$V_{NP} = \frac{4}{3}\pi r^3 = \frac{4}{3}\pi\,(26.5\ nm)^3 = 77951.8\ nm^3 = 7.795 \cdot 10^{-14}\ mm^3,$$

the volume of a sphere with the size of one nanoparticle.

The amount of polymer used per mg nanoparticles was 10 nmol and 20 nmol. With the Avogadro constant the respective number of polymer molecules is

$$10\ nmol = 6.022 \cdot 10^{15}\ \text{and}\ 20\ nmol = 1.204 \cdot 10^{16}.$$

Assuming a full uptake of polymer, the **number of polymer molecules per particle** is

$$\frac{10\ nmol}{N} = \frac{6.022 \cdot 10^{15}}{1.309 \cdot 10^{13}} = 460\ \text{in the case of 10 nmol}$$

and

$$\frac{20\ nmol}{N} = \frac{6.022 \cdot 10^{15}}{1.204 \cdot 10^{16}} = 920\ \text{in the case of 20 nmol.}$$

3. Imparting functionality to MOF nanoparticles by external surface selective covalent attachment of polymers

To estimate the mean area one polymer molecule could occupy on the nanoparticle surface we evaluate the **surface area** of a sphere with the size **of a nanoparticle** to

$$S \ = \ 4 \ \pi \ r^2 \ = \ 8.825 \cdot 10^3 \ nm^2.$$

By dividing this number with the number of polymer molecules per nanoparticle we get the **surface space per polymer molecule**:

$$\frac{8.825 \cdot 10^3 nm^2}{460} \ = \ 19.2 \ nm^2 \ \text{in the case of 10 nmol}$$

and

$$\frac{8.825 \cdot 10^3 nm^2}{920} \ = \ 9.59 \ nm^2 \ \text{in the case of 20 nmol.}$$

This corresponds to a surface coverage of:

$$8.65 \ pmol/cm^2 \ \text{ in the case of 10 nmol}$$

and

$$17.3 \ pmol/cm^2 \ \text{in the case of 20 nmol}$$

Compared to the size of the polymer molecules (hydrodynamic radius determined by FCS: 1.1 nm) the surface of one nanoparticle is loosely occupied by polymer molecules.

Mass % of polymer per MOF nanoparticles was calculated to allow comparison to TGA (see Fig. S3-10).
Using a molecular mass of 5000 g/mol for PEG5000 and assuming 20 -10 nmol of PEG5000 attached to 1 mg MOF, the mass % is

$$\frac{20 \ nmol \cdot 5000 \frac{g}{mol}}{20 \ nmol \cdot 5000 \frac{g}{mol} + 1 \ mg} \ = \ 9.1 \ \% \ \text{in the case of 20 nmol}$$

and

$$\frac{10\ nmol \cdot 5000\frac{g}{mol}}{10\ nmol \cdot 5000\frac{g}{mol}+1\ mg} = 4.8\ \% \text{ in the case of 10 nmol}$$

Using a molecular mass of 2800 g/mol for Stp10-C (free base) and assuming 20 -10 nmol of Stp10-C attached to 1 mg MOF, the mass % is

$$\frac{20\ nmol \cdot 2800\frac{g}{mol}}{20\ nmol \cdot 2800\frac{g}{mol}+1\ mg} = 5.3\ \% \text{ in the case of 20 nmol}$$

and

$$\frac{10\ nmol \cdot 2800\frac{g}{mol}}{10\ nmol \cdot 2800\frac{g}{mol}+1\ mg} = 2.7\ \% \text{ in the case of 10 nmol}$$

This is in good agreement with TGA data (2,7% and 1%, respectively; see Fig. S3-10), considering the accuracy of TGA.

Reference

[1]   Horcajada, P.; Surble, S.; Serre, C.; Hong, D.-Y.; Seo, Y.-K.; Chang, J.-S.; Greneche, J.-M.; Margiolaki, I.; Ferey, G., *Chemical Communications* **2007**, 2820-2822.

4. Self-assembly of different polymers on MOF nanoparticles for better control of interactions at the biointerface

This chapter is based on the following work:

Andreas Zimpel, Nader Danaf, Benjamin Steinborn, Miriam Höhn, Waldemar Schrimpf, Hanna Engelke, Ernst Wagner, Thomas Bein, Matthias Barz, Don C. Lamb, Ulrich Lächelt, and Stefan Wuttke; **2018**, *in preparation*
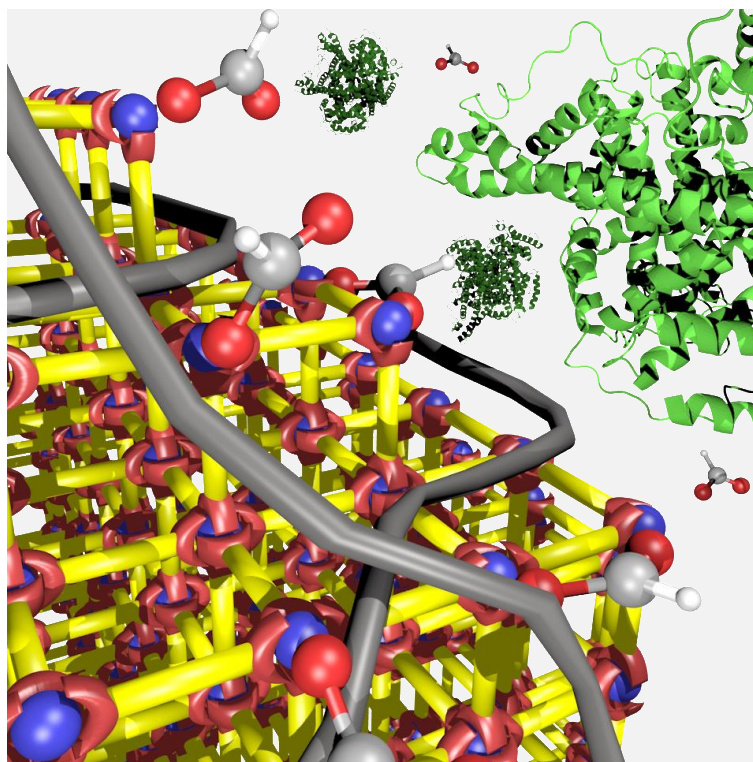
4.1. Introduction
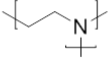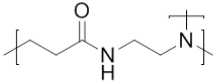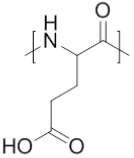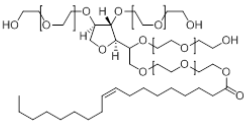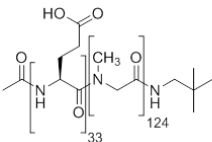
The chemistry of metal-organic frameworks (MOFs) provides great flexibility for the generation of crystalline inorganic-organic hybrid materials spanning an enormous chemical compound space for these materials.[1] By selection of appropriate inorganic building units (metal ions, or metal oxide clusters) and organic linker molecules, a huge number of MOFs

with tailored properties can be produced in simple, scalable and cost-effective reactions driven by self-organizing processes.[1-5] Beside industrial applications, such as catalysis,[6-9] gas storage,[10] separation[11-12] or sensing,[13-15] the materials class of MOFs is also being explored for biomedical purposes.[16-22] MOF nanoparticles (NPs) have already been used as carriers for drugs[18, 23-26], nucleic acids[27], peptides and proteins[28-29] as well as biofunctional materials on their own, such as MRI contrast agents[30-33] or photosensitizers[34]. Considering the unique characteristics and tunable properties of MOFs, it is expected that other biomedical applications will follow.[18-20] As with other classes of nanomaterials, the interaction of the MOF NP surface with their environment critically impacts the behavior in biological systems.[35-37] Functionalization of the MOF outer surface is a rational approach to control interactions at the MOF-biointerface and thereby increases the potential for biomedical applications. Several post-synthetic modification procedures have been reported, such as surface adsorption[38-40], lipid coating[41-43], covalent conjugation[32, 44] or coordinative binding of functional units[28]. Here, we systematically investigated Zr-*fum* MOF NP surface coating with polymers by simply mixing them in an aqueous medium. Zr-*fum* MOF NPs were selected because of their favorable size distribution[45], colloidal stability[45], nanosafety profile[46] and favorable cellular uptake[28]. Self-assembly of polymers at MOF NPs appears as a powerful concept as it could potentially ensure a defined arrangement of these units at the outer surface without any guidance from external forces. This kind of process is ubiquitous in chemistry and biology and is increasingly used in industry as it simplifies processes, lowers costs, offers molecular control, and generates structures in three dimensions and on curved surfaces.[47] Since the feasibility of the NP-polymer functionalization based on surface adsorption depends on the individual nature of the coating material, we selected representative polymers with relevance in the biomedical field but with different physicochemical properties (Table 4-1). The set contained two positively charged (branched polyethylene imine, BPEI and PAMAM dendrimer G4), two negatively charged (polyglutamic acid, PGA and polyacrylic acid, PAA) and two uncharged (polyethylene glycol, PEG and polysorbate 20, Tween®) polymers. BPEI and PAMAM dendrimers are frequently used for nucleic acid transfections as well as for intracellular transport of other materials.[48-49] Due to their cationic nature, these polymers bind nucleic acids by electrostatic interaction and mediate cellular uptake of the resulting complexes.[50-51] BPEI can be considered to be an archetype of transfecting agents. Its beneficial buffer capacity in the acidic environment of endo- and lysosomes promotes cargo release into the cytosol due to the so called 'proton-sponge effect'[52-53].

Table 4-1. Summary of selected polymers used in this work. 'Polymer' defines abbreviations used in this work (BPEI, branched polyethylene imine; PAMAM, polyamidoamine dendrimer generation 4; PGA, polyglutamic acid; PAA, polyacrylic acid; PEG, polyethylene glycole; Tween®, Polysorbate 20; PGA-PS, polyglutamate-*b*-polysarcosine block-co-polymer); 'Charge' indicates positive (+) or negative (-) netto charge at pH 7; 'Structure' shows simplified molecular structure or repeating units of selected polymers; 'Properties' exemplifies characteristics and biomedical applications.

Polymer	Charge at pH 7	Structure	Properties
BPEI	+		basic; high buffer capacity at endosomal pH; → intracellular drug delivery, non-viral nucleic acid transfections
PAMAM	+		basic; high buffer capacity at endosomal pH; → intracellular drug delivery, non-viral nucleic acid transfections
PGA	-		acidic, polypeptide, natural monomer sub-unit → polymer scaffold for drug delivery systems, drug packaging and delivery applications
PAA	-		acidic → polymer scaffold for drug delivery systems, binding agent for drug formulations
PEG	0		neutral, hydrophilic → shielding polymer, extends plasma half lives of drugs and drug carriers
Tween®	0		neutral, amphiphilic, nonionic surfactant → solubilizer, additive in drug formulations
PGA-PS	0/-		Block-co-polymer PGA: acidic, binding domain; PS: neutral, shielding domain → MOF surface functionalization polymer with separate assembly and shielding domains

In contrast to the statistical polymerization product BPEI, PAMAM dendrimers represent perfectly defined monodisperse compounds. The anionic polymers PGA, PAA and corresponding block-co-polymers have been widely used as polymer scaffolds for drug conjugation, NP functionalization and hydrogel or micelle formation[54-58]. The neutral polymer PEG is the most prominent agent used for shielding and colloidal stabilization of nanoparticles or biopharmaceuticals; 'PEGylation' is even considered a generally accepted technical term in pharmaceutical sciences[59]. PEG is a polyether with amphiphilic character, it is able to form multiple hydrogen bonds generating a hydrophilic layer in an aqueous environment. It also reduces adsorption or aggregation at surfaces due to sterical hindrance. Polysorbate 20 is a neutral surfactant which also contains PEG-like structural parts and is used in pharmaceutical products as solubilizer or emulsifier. In addition, a co-polymer (PGA-PS) composed of a polyglutamate and a polysarcosine block was used as an example for MOF

surface functionalization with more sophisticated and advanced polymer architecture.[60] Here, the PGA block was expected to show binding properties similar to the bare PGA. The polypeptoid polysarcosine (or poly(N-methyl glycine))[61] is highly hydrophilic and exhibits a very low interaction potential with biomolecules.[62] Therefore, polysarcosine is considered as promising alternative to the most frequently used shielding agent PEG.[63-64]

In this work, we study the binding of the different polymers by simple mixing in biological buffer and at room temperature in order to identify the most facile, reproducible and scalable functionalization processes under mild and biocompatible conditions (Figure 4-1a).[19] We screened the selected polymers with regard to their ability to bind to Zr-*fum* NPs, effects on physicochemical properties and interactions at the MOF-biointerface. Evaluated key parameters were change of zeta-potential, colloidal stabilization, protein binding and cellular interactions (Figure 4-1b). It is worth stressing that the functionalization concept and polymers used can be applied to any other MOF NP. Thus the study is considered to be fundamental, as we established the efficient generation of MOF NPs with various surface properties. Moreover, our study identified relationships between functionalized MOF NPs and the biointerface, which will help to guide the rational design of hybrid nanomaterials.
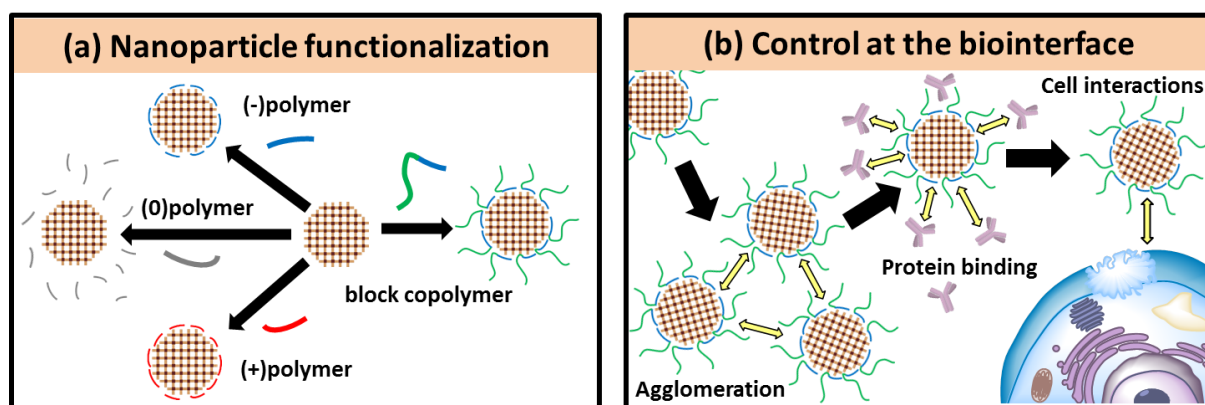
Figure 4-1. Schematic illustration of the coating procedures using the four different polymer groups (negatively charged, neutral, positively charged, block copolymer) (**a**), and of the investigations performed with the functionalized MOF NPs biointerface (agglomeration, protein binding and cell interactions) (**b**).

4.2 Results and Discussion

Synthesis and Characterization of Zr-*fum* NPs

Zr-*fum* NPs were prepared according to *Zahn et al.*[65] under formic acid mediated hydrothermal conditions. The resulting NPs were dispersed in ethanol and characterized by dynamic light scattering (DLS), revealing Zr-*fum* NPs with uniform size distribution (72 ± 16 nm, see supporting information (SI), Figure S4-1). A spherical shape of the particles and a homogenous size distribution was confirmed by scanning electron microscopy (SEM; see SI, Figure S4-2). Evaluation of the particle size from SEM showed slightly smaller diameters (46 ± 8 nm), which is agreement with literature.[45] For Zeta-potential measurements, HEPES buffered glucose (HBG) was chosen as medium with physiological pH and tonicity. Therein, bare Zr-*fum* NPs showed a negative value of approximately -27 mV. Finally, the powder X-ray diffraction (PXRD) pattern of the Zr-*fum* MOF NPs (SI, Figure S4-3) featured well-defined reflections across the entire measurement range, indicating the formation of the expected framework.

Nanoparticle functionalization

For the assessment of polymer binding to bare Zr-*fum* NPs, a coating procedure was adopted from *Bellido et al.*.[40] A Zr-*fum* NP suspension was added dropwisely to an aqueous polymer solution under vigorous stirring. The resulting NP suspension was treated by sonication and stirred for three minutes. The obtained NPs were washed with bi-distilled H_2O and stored as an aqueous suspension.

All Zr-*fum*@polymer NPs were characterized by PXRD to prove their retained crystallinity after the coating procedure (see SI, Figure S4-4). SEM images of the different Zr-*fum*@polymer NPs showed no change in their morphology (see SI, Figure S4-5). Raman spectroscopy of the different Zr-*fum*@polymer NPs was performed to confirm successful coating by detection of additional vibrational bonds introduced by the respective polymer (Figure 4-2).
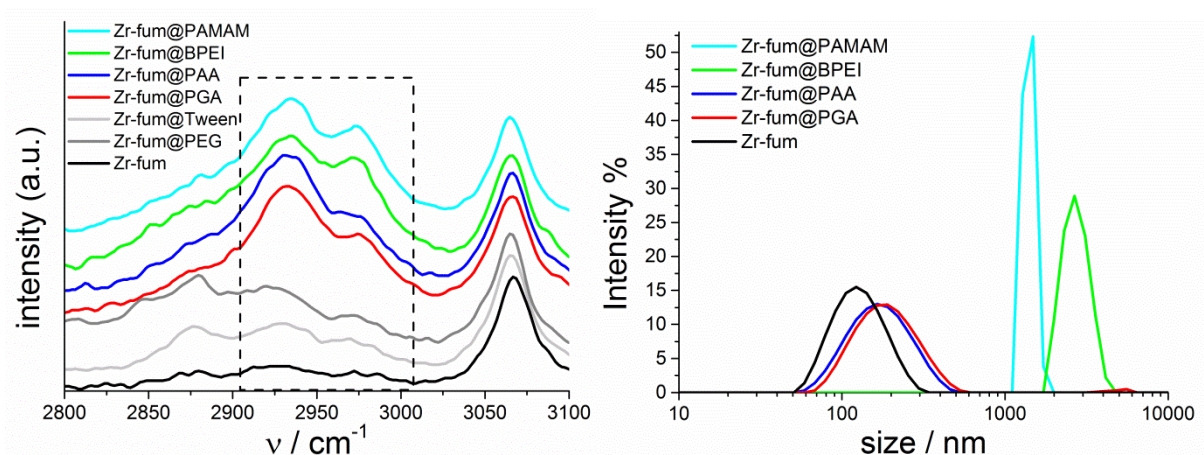
Figure 4-2. (left) Raman spectra (normalized to internal Zr-*fum* reference at 3065 cm^{-1}) of unfunctionalized Zr-*fum* NPs in comparison to Zr-*fum*@polymer NPs in the region of interest (2700 – 3100 cm^{-1}). For full spectra see SI, Figure S4-6. (right) DLS plot (by intensity) of Zr-*fum* NPs in comparison to Zr-*fum*@polymer NPs in HBG.

An increase of the CH$_2$ vibrational bands (asym. stretch 2934 cm^{-1}, sym. stretch 2975 cm^{-1}) of the aliphatic backbone, which is included in all polymers, indicated a successful attachment for cationic ((+)-polymer, BPEI and PAMAM) as well as anionic polymers ((-)-polymer, PGA and PAA). Neutral polymers (PEG and Tween®) showed a significantly lower intensity of the characteristic vibrations. The vibration triplet (approximately at 2875 cm^{-1}, 2925 cm^{-1} and 2975 cm^{-1}) which is slightly visible for Zr-*fum* as well as for Zr-*fum*@PEG and Zr-*fum*@Tween is attributed to ethanol and is covered by the more intense signals of polymer backbone modes in the case of successful coating (see SI; Figure S4-7). Therefore, both neutral polymers were considered to be not able to coat Zr-*fum* NPs and were not considered for further studies on biophysical properties.

For DLS investigations, HEPES buffered glucose (HBG) solution was chosen as medium to simulate physiological conditions. The measurements further confirmed successful attachment of cationic and anionic polymers (Figure 4-2). For anionic polymer coated Zr-*fum* NPs, a significant shift of the peak maximum (≈ 125 nm for uncoated Zr-*fum* NPs to 170 nm for Zr-*fum*@(-)polymer) could be detected. Cationic polymer coated Zr-*fum* NPs showed much higher values due to agglomeration of the NPs. Furthermore, investigations by zeta-potential measurements showed a significant shift of the Zr-*fum*@polymer NPs' surface charge depending on the nature of the polymer. While anionic polymers revealed a more negative zeta-potential compared to unfunctionalized Zr-*fum* (Table 4-2) leading to an increased electrostatic repulsion and high colloidal stability, cationic polymers showed a shift towards neutrality resulting in NP agglomeration.

Table 4-2. Zeta-potential values of different coated Zr-*fum* NPs in HBG.

MOF	Zr-*fum*@PAA	Zr-*fum*@PGA	Zr-*fum*	Zr-*fum*@PAMAM	Zr-*fum*@BPEI
Zeta-pot. in mV	≈-30.2	≈-29.1	≈-25	≈-16.1	≈-11.6

Infrared (IR) spectroscopy was performed in addition to Raman spectroscopy but produced no further information, as all significant organic vibrational bands from the polymer coating overlapped with the organic linker vibrational bands of fumaric acid (see SI, Figure S4-8). Nitrogen sorption measurements revealed a BET surface area for uncoated particles of 736 m^2/g and, as expected, a moderate decrease of BET surface for Zr-*fum*@polymer NPs ($\Delta \approx 200$ - 350 m^2/g see SI, Figure S4-9). This can be attributed to the attached amount of nonporous organic material on the external surface as well as to partial pore blocking by polymer chains during nitrogen sorption measurements.

Nature of binding

Thermogravimetric analysis (TGA) provided hints on the nature of the polymer binding to Zr-*fum*. As expected, (-)-polymer coated Zr-*fum* NPs showed increased weight loss after combustion in comparison to unfunctionalized particles, indicating the increased content of organic material. (see SI, Figure S4-10). In contrast, (+)-polymer coated NPs surprisingly showed lower weight loss which cannot be explained by a simple polymer attachment process since obviously organic content can also be lost during functionalization. A possible explanation is an exchange of formic acid molecules covering the external surface of Zr-*fum* NPs with the polymers. Due to the modulation synthesis approach, unsaturated Zr-ions at the external surface are covered coordinatively by carboxyl-groups of formic acid. The polymers contain coordinating groups as well (carboxylates + amines) and should therefore be able to replace formic acid by an entropically favored linker exchange reaction.[66] Depending on the molecular mass and the attached amount of polymer, the organic content of the MOF@polymer nanocomposites can increase or decrease.

A detailed look at BET surface areas suggests a higher degree of attachment for PGA and PAA as their surface areas decreased in a more significant way (736 m^2/g to 413 m^2/g and 400 m^2/g, respectively) than observed for BPEI and PAMAM (736 m^2/g to 472 m^2/g and 543 m^2/g, respectively). This is in agreement with the obtained higher organic content for Zr-*fum*@(-)-polymer measured by TGA, and the lower weight loss of Zr-*fum*@(+)-polymer NPs may be the result of formic acid depletion but a comparably low degree of polymer attachment (see SI, Figures S4-9 – S4-11).

The postulated exchange mechanism was further confirmed by quantification of released formic acid after polymer coating. An assay kit (K-FORM, Megazyme) was used to specifically quantify formic acid by conversion to carbon dioxide with formate dehydrogenase (Scheme 4-1). The molar amount of generated NADH (abs. 340 nm) is equal to the amount of formic acid present in the supernatant.

Scheme 4-1. Reaction of the formic acid assay for its quantitative detection by UV-VIS (NADH at $\lambda = 340$ nm).

$$\text{HCOOH} + \text{NAD}^+ \xrightarrow{\text{formate dehydrogenase}} \text{CO}_2 + \text{NADH} + \text{H}^+$$
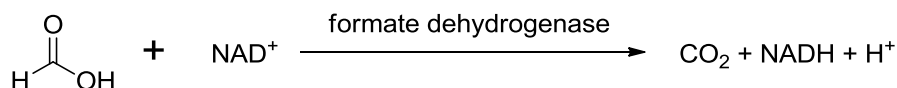
As a control experiment, the reaction was performed without adding polymer to the solution and the supernatant was tested for free residual formic acid left in the MOF pores after synthesis and workup. Here, only a small amount of formic acid was detectable (Figure 3, left, "Zr-*fum*"). After coating with (-)- and (+)-polymers, a significantly higher amount of formic acid was present in the supernatant compared to the control experiment, which supports the assumption of an exchange between formic acid and polymer on the external MOF NP surface (Figure 4-3, left). Additionally, pure polymer solutions (50 µg/mL ≡ ¼ of $c_{max.}$) were tested to identify assay interference and false-positive effects. This control experiment showed a significant absorption only for PAA control (Figure 4-3, right), which explains the steady increase and higher absorption of Zr-*fum*@PAA supernatant.
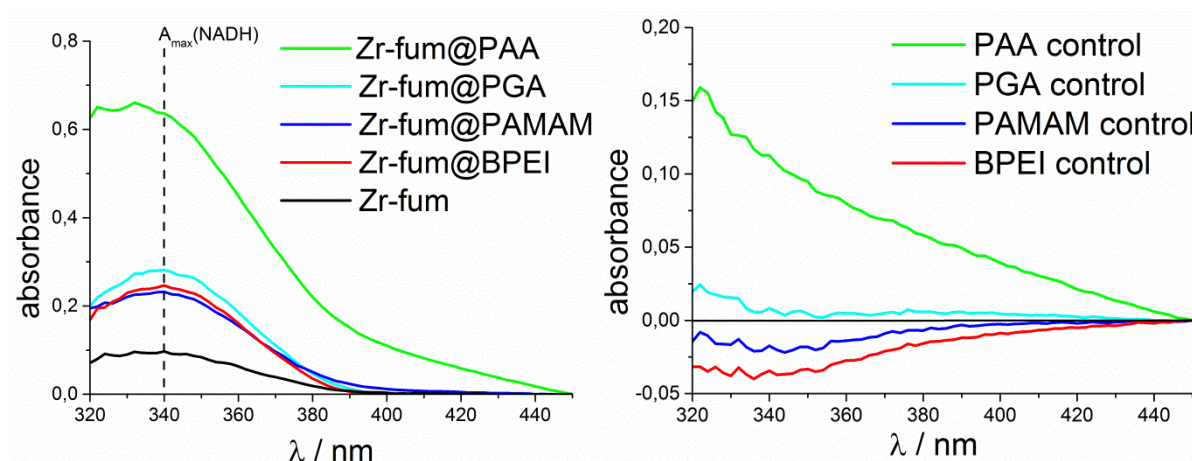
Figure 4-3. (left) UV-VIS spectroscopic determination of NADH from the supernatant after coating reactions. Absorption at 340 nm was used for the determination of the formic acid release (see SI, Table S1). (right) Control experiments of pure polymer solutions (c = 50µg/mL), showing a steady increase for PAA control which indicates assay interference (same assay with a 70:30 ethanol/water mixture was used for background substraction)

Therefore, Zr-*fum*@PAA was excluded from the calculations of the exchanged amount of formic acid from experimental data. The calculations resulted in approx. 10 µg formic acid per 1 mg provided Zr-*fum* NPs (≈ 1 w%; see SI, Table S4-1). This value is in very good agreement with a theoretical estimate of a maximum amount of formic acid present on the external surface of Zr-*fum* NPs (≈ 0.8 w%; see SI, *"Theoretical Estimate"*).

Considering all the above results, we propose the nature of binding to be coordinative self-assembly, accompanied by an exchange of formic acid by the polymers' coordinative groups, similar to functionalization mechanisms published in the literature.[67-68]

Block copolymer

Based on the above results, the effective binding of PGA was used as molecular adapter for surface attachment and functionalization of MOF NPs with other moieties. To this end, the block-copolymer PGA-PS[60] (see Table 4-1) was attached to the Zr-*fum* NPs. The polymer consists of polysarcosine (PS), a biopolymer based on the natural subunit sarcosine (N-methyl glycine) which is known to provide a remarkable shielding effect,[62-64] and polyglutamic acid, which is working as a biocompatible assembly domain. Preparation of Zr-*fum*@PGA-PS NPs was performed according to the procedure presented above.

Raman spectroscopy provided information about a significant attachment of the polymer onto Zr-*fum* NPs (Figure 4-4, left), and XRD measurements confirmed the retained crystallinity of the Zr-*fum* core (Figure 4-4, right) as expected from previous polymer coatings. Furthermore, no change in morphology could be detected by SEM (see SI, Figure S4-12).
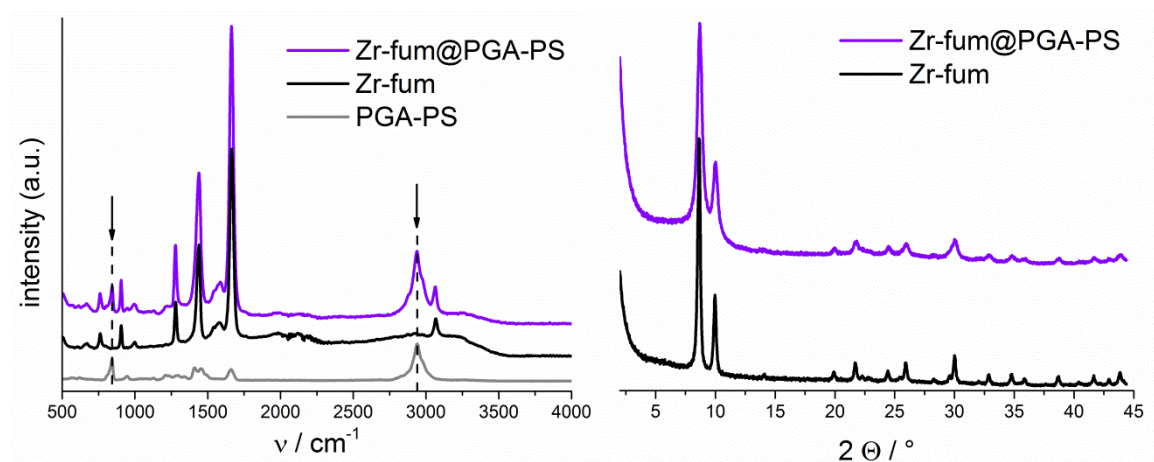
Figure 4-4. Raman (left) and XRD (right) pattern of Zr-*fum*@PGA-PS NPs compared to unfunctionalized Zr-*fum*. Black arrows highlight the characteristic polymer vibrational bands.

Agglomeration

Simultaneous measurements of zeta-potential and size at different pH revealed remarkable results concerning the agglomeration behavior of the NP dispersion in aqueous solution at biologically relevant pH (pH=4 to pH=8). The pH range was chosen in view of prospective biomedical applications of the Zr-*fum*@polymer NPs (pH 7.4 within the bloodstream to approx. pH 4.5 in cell lysosomes).[69] As expected, the measurements revealed a shift of isoelectric point (IEP, determined by interpolation of zeta-potential values) of the different formulations depending on the ionic nature (+ or -) of the polymer. The NP dispersions of bare Zr-*fum* as well as of (-)- and (+)-polymer coated Zr-*fum* tended to agglomerate at pH values close to the IEP (see SI, Figure S4-13) where electrostatic repulsion is minimal.[70] For illustration, the titration curve of bare Zr-*fum* is shown in Figure 5, left. In contrast, PGA-PS coated NPs showed completely different behavior. Although the zeta-potential drops from approx. +25 mV at pH 4 to -12 mV at pH 8, resulting in an isoelectric point at pH 5.8, the NPs remain nanodispersed with constant size of approximately 130 nm within the entire pH range (Figure 4-5, right). We note that to the best of our knowledge this impressive colloidal stabilization is by far the best example within the MOF NP field.
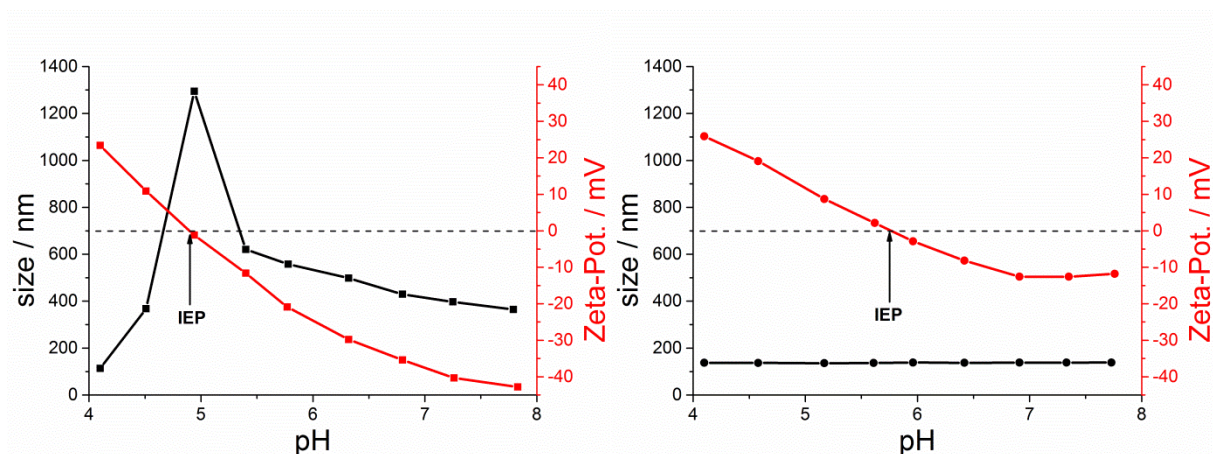
Figure 4-5. Nanoparticle size (Z-average, black) and zeta-potential measurements (red) of Zr-*fum* NPs (left) compared to Zr-*fum*@PGA-PS NPs (right). Bare Zr-*fum* NPs show strong agglomeration at pH 5 (≈ IEP) while Zr-*fum*@PGA-PS NPs remain colloidal over the whole pH range.

Protein binding experiments

In view of the encouraging previous results, protein binding to Zr-*fum* NPs was investigated by fluorescence correlation spectroscopy (FCS). FCS provides opportunity to look at the interaction of labeled-proteins with the differently coated Zr-*fum* NPs with very high sensitivity. In principle, the diffusion of fluorescing molecules into and out of a small confined volume results in a certain fluctuating fluorescence intensity, which is recorded for that single observation volume. The recorded intensity fluctuations of the diffusing-fluorescing particles through the observation volume constitute the basis for a temporal autocorrelation analysis. Hence, FCS is established by an autocorrelation function (ACF) of the temporal autocorrelation provided by the fluorescence intensity fluctuations. The fraction of several diffusing labeled particles and their respective diffusion coefficients can be deduced from the temporal information of the ACF.[71-72] The number of diffusing particles and their rate of diffusion are the main criteria that determine the shape of an ACF. Fast diffusing particles will show a quick temporal fluctuation and thus quickly diffuse out of the observation volume. The fast diffusion of such particles is represented in a quick temporal decay of the ACF. In contrast, big particles that diffuse slowly would show a slow temporal fluctuation, which is represented in a slow temporal decay of the ACF. Moreover, FCS is a sensitive tool to investigate the interactions of different particles. Once a fraction of labeled fast diffusing particles interacts with bigger slowly diffusing particles, the fraction of interacting particles can be monitored with FCS, which would be indicated in the ACF.

Here, Zr-*fum* NPs were incubated with two different fluorescein isothiocyanate (FITC)-labeled proteins, i.e. FITC-immunoglobulin G (FITC-IgG) and FITC-albumin (FITC-alb), respectively. Albumin was chosen as it presents the most prominent protein in the human blood plasma (up to 60 %), IgG as it mediates an immune response by activating the complement system of the human body and thus leading to rapid particle clearance from the bloodstream.[73-74] FITC-IgG and FITC-alb, respectively, were provided in HBG and Zr-*fum* as well as all Zr-*fum*@polymer NPs preparations were added to the solution. As shown in Figure 6 (top, left), FITC-IgG alone shows a quick decay of the ACF that corresponds to its fast diffusion out of the observation volume, which is to be expected for the IgG alone without the bigger slowly diffusing NPs. The slower decay of the FITC-IgG ACF in the presence of all nanocomposites but Zr-*fum*@PGA-PS in Figure 4-6 (top, right) shows the interaction between the two partners. The slower decay indicates the slower diffusion of the FITC-IgG upon binding to all the NPs but Zr-*fum*@PGA-PS. The minimal change of the ACF of FITC-IgG in the presence of Zr-*fum*@PGA-PS underlines the exceptional high shielding capability of the

polysarcosin. In contrast to FITC-IgG no binding of albumin onto all the kinds of NPs studied here could be observed, as the ACF of FITC-alb remains unchanged in the presence of the different Zr-*fum* NPs. Furthermore, investigations on the protein binding experiments were performed by fluorescence cross-correlation spectroscopy (FCCS). FCCS, similar to FCS, is established by a cross-correlation function (CCF) of the temporal cross-correlation provided by the fluorescence intensity fluctuations of dually-labeled particles.[75-76] Therefore, with FCCS we investigated two-colored fluorescently interacting particles, in which the Zr-*fum* NP was labeled with Atto 647N and contacted with FITC-albumin and FITC-IgG, respectively. FCCS allows us to look at the interaction of the Zr-*fum* with the two proteins of interest, albumin and IgG, respectively. Indeed, the absence of FITC-alb binding but strong association of FITC-IgG with Atto 647N-Zr-*fum* NPs can be validated by looking at the CCF, Figure 4-6 (bottom, right). A cross-correlation amplitude was only observed once FITC-IgG and Atto 647N-Zr-*fum* were present together. In contrast, the absence of any cross-correlation amplitude in the presence of FITC-alb and Atto 647N-Zr-*fum* indicated that labeled albumin and Zr-*fum* do not happen to temporally diffuse together, i.e. no interaction between them is present. The corresponding fluorescence fluctuation intensity traces from which the ACFs are deduced are reported in the SI, Figure S4-14, which shows the interaction of the FITC-IgG with the NPs, depicted in the different peaks. These peaks represent the high fluorescence intensity of several FITC-IgG bound to the bigger NPs upon diffusing into the confined observation volume. The lack of the high fluorescence intensity peaks in the fluorescence intensity traces of FITC-alb is a further validation that no interaction between FITC-alb and the NPs is observed.

Furthermore, we report the fraction of interacting FITC-IgG with the Zr-*fum* as well as for all Zr-*fum*@polymer NPs, see SI (FCS section and Table S4-2). Analysis of the ACFs allows for a quantitative determination of the interaction between the FITC-IgG and the different NPs. The fraction of the FITC-IgG binding to the NPs can be observed and the interaction was thus described. Summarizing, the protein interaction with the Zr-*fum* NPs investigated by FCS and FCCS shows that the coating is a determining factor for the interaction with certain proteins, such as IgG. The interaction between IgG and Zr-*fum* NPs can be tuned based on the NP surface coating. On the other hand, some other important proteins like albumin showed to be inert regarding binding to the differently coated Zr-*fum* NPs.
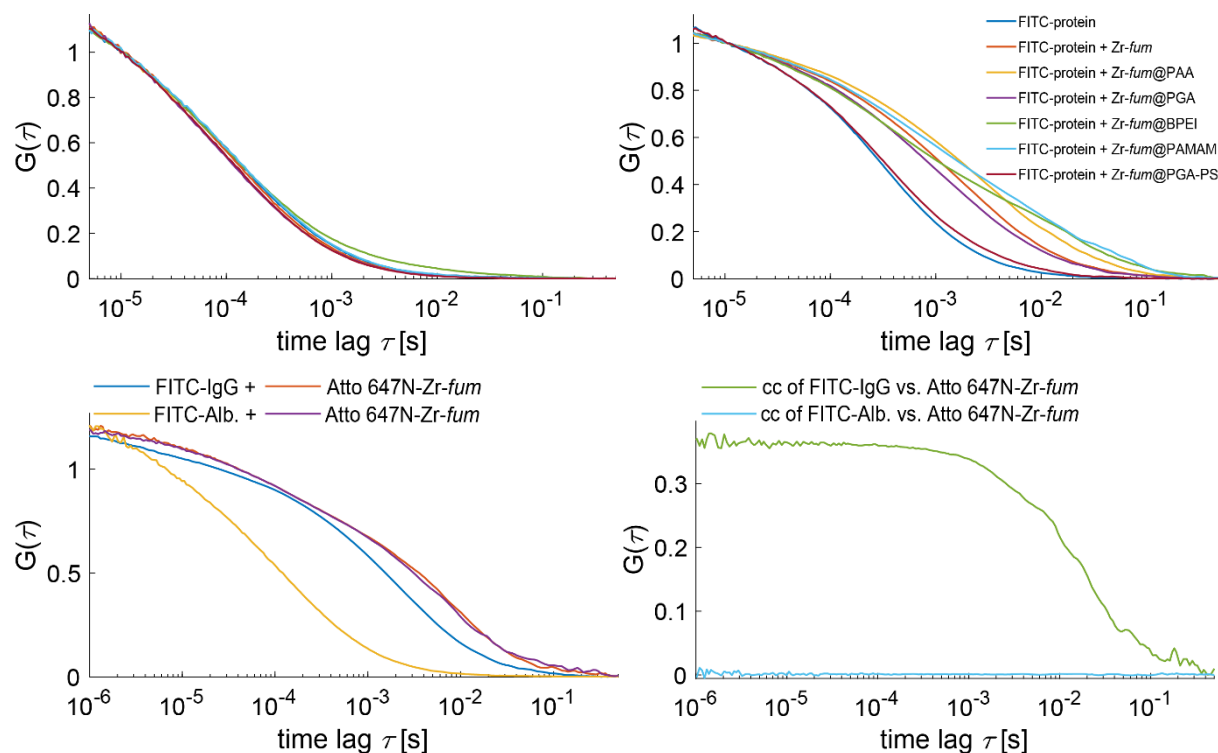
Figure 4-6. FCS measurements of 100 nM FITC-alb and FITC-IgG, (top, left and right), respectively. ACFs in the absence (blue trace) and presence of 10 µg Zr-*fum* and Zr-*fum*@polymer NPs. (bottom, left) ACFs in the presence of 10 µg Atto 647N-labeled Zr-*fum* (FITC-IgG and Atto 647N-labeled Zr-*fum* ACFs, blue and orange traces, respectively) and (FITC-alb and Atto 647N-labeled Zr-*fum* ACFs, yellow and purple traces, respectively). (bottom, right) The corresponding FCCS measurements of FITC-IgG and Atto 647N-labeled uncoated Zr-*fum* (green) and of FITC-alb and Atto 647N-labeled Zr-*fum* (cyan), showing the interaction in case of IgG with Zr-*fum* and its absence in case of albumin.

Cell interactions

After evaluating the bio- and physicochemical characteristics of Zr-*fum*@polymer NPs in cell-free models, *in vitro* studies were carried out to investigate interactions between the NPs and cancer cells. First, MTT cell viability assays were performed to identify effects on cellular metabolism and toxic interactions. All formulations were well tolerated and showed no obvious toxicity up to concentrations of 400 µg/mL (see SI, Figure S4-15). Next, the cellular association, aggregation and cell uptake profile of the different coated formulations was investigated by flow cytometry and confocal laser scanning microscopy (CLSM) after 30 minutes of incubation on HeLa cells (Figure 4-7). Flow cytometry data indicated a high degree of interaction between Zr-*fum*@PAMAM as well as Zr-*fum*@BPEI and HeLa cells, a finding most likely attributable to electrostatic adhesion to the cell membrane. In direct comparison, the percentage of fluorescence-positive cells was in the same range in case of all formulations (Figure 4-7b), but median fluorescence intensity was strongly increased in case of (+)-polymer coated Zr-*fum* NPs (Figure 4-7c). CLSM provided information about the exact spatial localization of Zr-*fum* NPs within the cells. Images were in good agreement with the

previously observed high cellular association of (+)-polymer coated Zr-*fum* NPs, however only large aggregates on the cell surface and no intracellular particles were observed. In contrast, the other colloidally more stable formulations all showed cellular internalization and no extracellular aggregation (Figure 4-7d). These findings confirm the expected strong interaction of (+)-polymer coated Zr-*fum* NPs with cellular membranes but also point to unfavorable aggregation under physiological conditions.
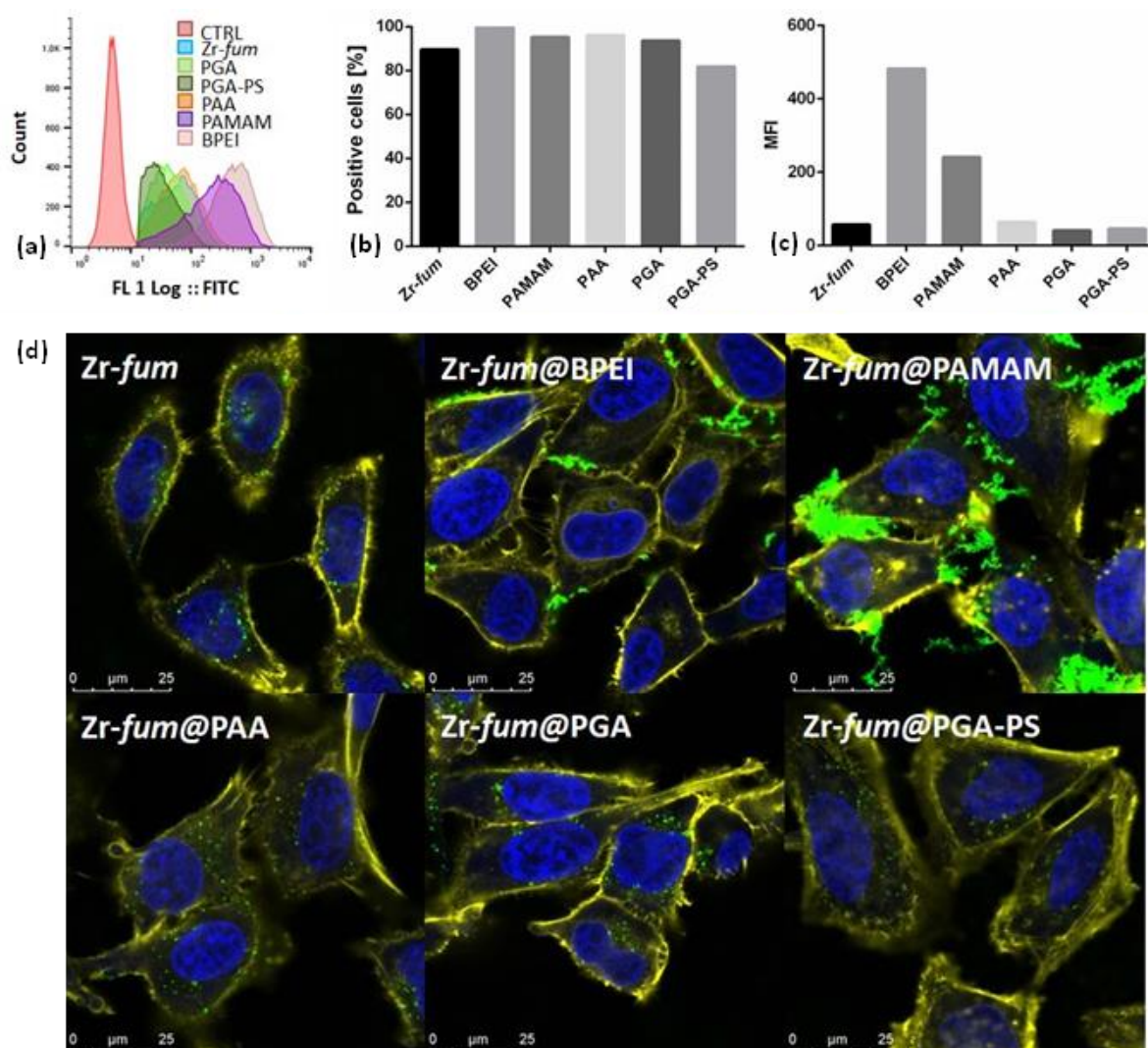

Figure 4-7. Cellular association, aggregation and uptake profile of Zr-*fum*@polymer NPs as determined by flow cytometry (a-c) and confocal laser scanning microscopy (CLSM) (d). Zr-*fum* NPs were labeled with calcein as described in the SI. All differently functionalized NPs were incubated on HeLa cells for 30 minutes at a final concentration of 50 µg/mL. (a) Single parameter histogram of cellular fluorescence, (b) percentage of calcein-positive cells and (c) median fluorescence intensities of calcein-positive cell subpopulation. PAMAM and BPEI-coated Zr-*fum* NPs mediated highest fluorescence intensity of cells indicating strongest cellular association; coating with negatively charged polymers PGA, PGA-PS and PAA resulted in cellular association in a similar range as uncoated Zr-*fum*. (d) Nuclei were stained with DAPI (blue channel), F-Actin was stained with Phalloidin-Rhodamin (yellow channel), calcein-fluorescence (green channel). Images were recorded 30 minutes after NP addition. BPEI-coated and PAMAM-coated Zr-*fum* NPs showed strong extracellular aggregation on the cell surface and low intracellular localization. Uncoated, PAA-coated, PGA-coated and PGA-PS coated Zr-*fum* NPs all showed dispersed NPs in suitable size ranges and were internalized into cells.

4.3. Conclusion

In this paper, we report a straightforward functionalization approach for MOF NPs based on self-assembly. Different polymers could be attached onto the external surface by an entropically preferred exchange of the modulator (formic acid) by the coordinating groups of the polymers. This process can be described as self-assembly modulator replacement. The released formic acid could be detected in the supernatant after the coating process, which supports the proposed mechanism. Exploiting this efficient self-assembly approach, different MOF@polymer NP formulations were prepared, fully characterized and tested for their behavior and interactions in a biologically relevant environment. The investigations revealed great colloidal stability of Zr-*fum* NPs by coating them with the block copolymer PGA-PS. These Zr-*fum*@PGA-PS NPs retained their monodispersity independent of pH in aqueous solutions as well as in a broad range of environments, such as protein containing buffer solution and cellular medium. These findings make it a promising candidate for an intravenously injected nanocarrier system due to its expected long time stability in the human bloodstream, which is mandatory for effective passive targeting on tumor tissue by the EPR (Enhanced Permeability and Retention) effect.

Our results suggest that MOF NPs can be easily functionalized with different kinds of polymers via self-assembly. The self-assembly of functional polymers is a powerful approach to "program" the MOF NP surface to i) increase colloidal stability over physiological pH ranges; ii) increase colloidal stability in high ionic-strength buffers; iii) control the protein binding in a biological environment; iv) resist being scavenged by macrophages; v) exhibit low nonspecific binding to healthy tissues; vi) exhibit long circulation times; and vii) influence biodistribution in a favorable way. Due to the easy integration of different functionalities (e.g. shielding, targeting, bioresponsive domains, etc.) into the polymers and their straightforward self-assembly onto MOF NP surfaces, we predict that this functionalization concept will develop into a general functionalization strategy for MOF NPs.

4.4. Materials and Methods

Chemicals: Zirconium (IV) chloride (ZrCl$_4$, Aldrich, $\geq$ 99.0%), fumaric acid (Sigma-Aldrich, $\geq$ 99.9% trace metals basis), 2-[4-(2-hydroxyethyl)piperazine-1-yl]ethanesulfonic acid (HEPES, Biomol GmbH), glucose (Applichem), poly-L-glutamic acid sodium salt (PGA, Sigma-Aldrich, MW 15.000-50.000), polyacrylic acid (PAA, Sigma-Aldrich, average MW ~15.000), branched polyethylene imine (BPEI, Sigma-Aldrich, average MW ~25.000), polyamidoamine dendrimer (PAMAM, Sigma-Aldrich, ethylenediamine core, generation 4.0), poly(ethylene glycol) methyl ether (PEG, Sigma-Aldrich, average M$_n$ ~ 5.000), TWEEN® 20 (Tween, Sigma-Aldrich, MW ~1228), formic acid assay kit (K-Form, Megazyme) were used as received. Cell culture media, antibiotics and fetal bovine serum (FBS) were purchased from Life Technologies or Sigma-Aldrich, respectively.

Synthesis of Zr-fum NPs: Zr-*fum* NPs were synthesized according to a procedure reported by *Zahn et al.*[77]. ZrCl$_4$ (120.5 mg, 0.517 mmol) and fumaric acid (180.0 mg, 1.550 mmol) were dissolved in bi-distilled H$_2$O (10 mL). Formic acid (0.975 mL, 1.190 g, 25.85 mmol) was added and the reaction mixture was sealed in a 25 mL glass autoclave (Schott, Duran®). The mixture was heated to 120 °C for 24 h and was allowed to cool down to RT afterwards. Further, the resulting NPs were transferred into 15 mL Falcon® tubes and centrifuged (7187 rcf / 10 min). After re-dispersion in bi-distilled H$_2$O (6 mL), the Zr-*fum* NPs were transferred to Eppendorf® tubes and centrifuged (16900 rcf / 10 min). The washing steps (dispersion + centrifugation) were repeated twice with EtOH, and Zr-*fum* NPs were stored in an ethanolic stock solution.

Dye labeling of Zr-fum NPs

Calcein-labeling: Zr-*fum* NPs were dispersed in an aqueous calcein solution (0.25 mM) resulting in a 5 mg/mL dispersion. The NPs were shaken for 15 min (600 rpm) at RT, centrifuged and washed with bi-distilled H$_2$O, twice with HBG and stored in an ethanolic stock solution.

Atto647n-labeling: Atto647n-labeling was performed according to a procedure reported in the literature.[78]

Preparation of Polymer stock solutions: Polymers were dissolved in bi-distilled H$_2$O, resulting in aqueous solutions of 10 mg/mL and stored at 7 °C.

Polymer coating of Zr-fum NPs: Polymer solution (10 mg/mL; 20 µL or 400 µL, respectively) was provided in bi-distilled H_2O (280 µL or 5.6 mL, respectively). Zr-*fum* NPs (1,43 mg/mL in EtOH; 0.7 mL or 14 mL, respectively) were added dropwise within two minutes and the dispersion was allowed to stir for three minutes. Ultrasound was applied for one minute and the solution was again stirred for three minutes. The resulting particles were centrifuged (16900 rcf / 10 min) and washed twice with bi-distilled H_2O (see washing step for "Synthesis of Zr-fum NPs"). Zr-*fum*@polymer NPs were stored in an aqueous stock solution.

Detection of formic acid after coating of Zr-fum NPs in supernatant by formic acid assay kit (K-Form, Megazyme): Approx. 900 µL supernatant of the coating reactions (1 mg coating procedure) were aspirated after centrifugation of the NPs (16900 rcf / 10 min), transferred into an Eppendorf® tube and centrifuged again (16900 rcf / 10 min) to remove NPs which might have stayed in dispersion after the first centrifugation step. 300 µL of this supernatant were diluted with 1.8 mL bi-distilled H_2O in a quarz cuvette (QS, SUPRASIL®; Hellma Anlaytics). 200 µL buffer solution ("Bottle 1" from K-Form, Megazyme) and 200 µL NAD+-solution ("Bottle 2" from K-Form, Megazyme) were added and the mixture was allowed to homogenize for approx. 5 minutes. UV-Vis absorption was measured (A1) and 50 µL formate dehydrogenase ("Bottle 3" from K-Form, Megazyme) was added afterwards. The solution was mixed by gentle inversion of the cuvette and the reaction was allowed to run for approx. 12 minutes. The UV-Vis absorption was measured and the absorbance difference was calculated (see Figure 4-2 and Table S4-1). Control experiments were performed according to the same procedure, using 50 µg/mL polymer solutions in an ethanol/water mixture (70:30).

Synthesis of PGA-PS (Synthesis of PSar$_{124}$-b-PGlu$_{33}$): PGA-PS was synthesized according to the procedure published in the literature.[79] For simplification, PSar$_{124}$-*b*-PGlu$_{33}$ was abbreviated as PGA-PS.

Cell Culture: HeLa cells were cultured at 37 °C and 5% CO_2 in Dulbecco's modified Eagle's medium (DMEM), supplemented with 10% FBS, 100 U/mL penicillin and 100 µg/mL streptomycin.

Preparation of HEPES-buffered glucose (HBG): HEPES (2.38 g, 10 mmol) and glucose monohydrate (28.95 g, resulting in 5 % w/v glucose) were dissolved in bi-distilled H_2O (490 mL) and the pH was adjusted to 7.4 by addition of NaOH (approx. 10 mL, 0.5 M).

Metabolic activity assay of Zr-fum NPs and Zr-fum@polymer NPs (MTT assay): HeLa cells were seeded in 96-well plates at a density of 5.000 cells/ well 24 h prior to incubation with the different particle concentrations. Before incubation with the Zr-*fum* NPs, medium was replaced with 100 µL fresh medium. Particles diluted in 20 µL HBG were added to each well and incubated on cells for 24 h at 37 °C and 5% CO_2. 100 µL of MTT solution (3-(4,5-dimethylthia-zol-2-yl)-2,5-diphenyltetrazolium bromide in medium; 0.5 mg/mL) were added after removing the medium. After an incubation time of 2 h, unreacted dye and medium were removed and the 96-well plates were frozen at −80 °C for at least 30 min. The purple formazan product was then dissolved in 100 µL DMSO (dimethyl sulfoxide) per well and quantified measuring absorbance using microplate reader (Tecan SpectraFluor Plus, Tecan, Switzerland) at 590 nm with background correction at 630 nm. All studies were performed in triplicate. The relative cell viability (%) related to control wells treated only with 20 µL HBG was calculated as ([A] test/[A] control) × 100%.

Fluorescence (cross-) correlation spectroscopy (FCS/FCCS): The fluorescence correlation measurements (FCS) and dual-color fluorescence cross-correlation measurements (FCCS) were performed on a home-built microscope as described elsewhere.[80] The following laser lines were used for excitation: 470-nm (LDH-P-C-470) and 635-nm (LDH-P-C-635b) pulsed laser diodes for FITC-dye labeled IgG / Albumin and Atto 647N-dye labeled Zr-*fum* excitation, respectively. The laser power was measured at the sample using a slide power meter (S170C-Thorlabs) to be ~ 4.5 and 17.5 µW for the 470 and 635-nm lasers, respectively. The measurements were performed using a 60x water, NA 1.27 objective (Plan Apo 60 x WI, Nikon). The raw optical data and subsequent correlation analysis were performed with our PIE analysis with Matlab (PAM) software.[81] PAM is a stand-alone program (MATLAB; The MathWorks GmbH) for integrated and robust analysis of fluorescence ensemble, single-molecule, and imaging data.

The FCCS data were acquired by recording the detected photons of two single photon avalanche photodiodes (SPADs) on two separate time correlated single photon counting cards (TCSPC, SPC-150 Becker and Hickl) for a period of 15 minutes. Similarly, the FCS data were acquired by recording the photons with a single APD on a TCSPC card for a period of 15 minutes. Measurements were conducted in HEPES buffered glucose (HBG) for simulating physiological body conditions.

A three-component model assuming a 3D Gaussian focus shape was used for fitting the autocorrelation functions (ACFs) (eq. 4-1).

$$g(\tau) = \frac{\gamma}{(N_1 + N_2 + N_3)^2} \cdot \left[\left(N_1 \left(1 + \frac{4D_1 \cdot \tau}{\omega_r^2}\right)^{-1} \cdot \left(1 + \frac{4D_1 \cdot \tau}{\omega_z^2}\right)^{-\frac{1}{2}} \right) + \left(N_2 \left(1 + \frac{4D_2 \cdot \tau}{\omega_r^2}\right)^{-1} \cdot \left(1 + \frac{4D_2 \cdot \tau}{\omega_z^2}\right)^{-\frac{1}{2}} \right) + \left(N_3 \left(1 + \frac{4D_3 \cdot \tau}{\omega_r^2}\right)^{-1} \cdot \left(1 + \frac{4D_3 \cdot \tau}{\omega_z^2}\right)^{-\frac{1}{2}} \right) \right] \qquad (4\text{-}1)$$

N is the apparent average number of particles in the observation volume. The N_1 fraction refers to freely diffusing FITC, which accounts for the protein labeling efficiency, the N_2 fraction refers to the freely-unbound labeled proteins, and N_3 refers to the proteins bound to the Zr-*fum*. D_1, D_2, and D_3 refer to the respective diffusion coefficients of N_1, N_2, and N_3, respectively. The time delay of the autocorrelation is represented by τ. ω_r and ω_z are the lateral and axial focus sizes, respectively, defined as the distance from the focus center to the point where the signal intensity has decreased to $1/e^2$ of the maximum. The shape factor γ is $2^{-3/2}$ for a 3D Gaussian. The correlation at zero lag time was omitted from analysis due to the contribution of uncorrelated shot noise. The fitting was used to extract the fraction of freely diffusing FITC-dye labeled IgG / Albumin and FITC-dye labeled IgG / Albumin bound to the Zr-*fum*.

Confocal laser scanning microscopy: On the day prior to the experiment, HeLa cells were seeded in 8 well-chamber slides (Thermo Fisher Scientific, 20.000 cells in 300 µL medium per well). Cells were incubated at 37 °C and 5% CO_2. On the next day, the medium was aspirated and 300 µL Zr-*fum*@polymer (50 µg/mL in medium) was added to each respective well. After 30 min of incubation (37 °C, 5% CO_2), each well was washed once with 400 µL PBS and cells were subsequently fixated with 4% paraformaldehyde in PBS (30 min incubation at RT). After fixation, each well was once again washed with 400 µL PBS and cell nuclei were stained with DAPI (2 µg/mL), F-Actin was labeled with phalloidin-rhodamine (1µg/mL). After 30 min of incubation (light protection, RT), the staining mixture was aspirated and replaced with 300 µL PBS per well. Images were recorded utilizing a Leica-TCS-SP8 confocal laser scanning microscope equipped with an HC PL APO 63x 1.4 objective. DAPI emission was recorded at 460 nm, calcein at 530 nm and rhodamine at 580 nm. Afterwards, all images were processed by LAS X software from Leica.

Flow Cytometry: On the day prior to the experiment, HeLa cells were seeded in a 24 well plate (60.000 cells in 1 mL medium per well). Next day, the medium was aspirated and replaced with 475 μL fresh medium. 25 μL of 1 mg/mL Zr-*fum*@polymer solution was added to the wells (2 wells per polymer). After 30 minutes of incubation, medium was aspirated and cells were washed with 1 mL PBS. Cells were then trypsinated with 200 μL trypsin/EDTA (5 min, 37 °C). 400 μL medium was added to each well and the 2 wells per polymer were unified. Cells were centrifuged for 5 min at 1500 rpm and room temperature. The supernatant was removed, cells resuspended in 700 μL FACS-buffer (10 % FCS in PBS) and stored on ice. Shortly before the analysis, 2 μL 1 mg/mL DAPI was added to each vial. Utilizing the FlowJo 7.6.5 flow cytometry analysis software, cells were appropriately gated by forward/sideward scatter and pulse width for exclusion of cell aggregates. DAPI was used to discriminate between viable and dead cells. Only isolated viable cells were taken into evaluation. The threshold level for cellular association of calcein was set based on the fluorescence background of HBG treated negative control cells.

4.5. References

[1]   H. Furukawa, K. E. Cordova, M. O'Keeffe, O. M. Yaghi, *Science* **2013**, *341*.

[2]   P. Z. Moghadam, A. Li, S. B. Wiggin, A. Tao, A. G. P. Maloney, P. A. Wood, S. C. Ward, D. Fairen-Jimenez, *Chemistry of Materials* **2017**, *29*, 2618-2625.

[3]   H. Furukawa, U. Müller, O. M. Yaghi, *Angewandte Chemie International Edition* **2015**, *54*, 3417-3430.

[4]   W. Lu, Z. Wei, Z.-Y. Gu, T.-F. Liu, J. Park, J. Park, J. Tian, M. Zhang, Q. Zhang, T. Gentle Iii, M. Bosch, H.-C. Zhou, *Chemical Society Reviews* **2014**, *43*, 5561-5593.

[5]   M. Rubio-Martinez, C. Avci-Camur, A. W. Thornton, I. Imaz, D. Maspoch, M. R. Hill, *Chemical Society Reviews* **2017**, *46*, 3453-3480.

[6]   S. M. J. Rogge, A. Bavykina, J. Hajek, H. Garcia, A. I. Olivos-Suarez, A. Sepulveda-Escribano, A. Vimont, G. Clet, P. Bazin, F. Kapteijn, M. Daturi, E. V. Ramos-Fernandez, F. X. Llabres i Xamena, V. Van Speybroeck, J. Gascon, *Chemical Society Reviews* **2017**, *46*, 3134-3184.

[7]   L. Zhu, X.-Q. Liu, H.-L. Jiang, L.-B. Sun, *Chemical Reviews* **2017**, *117*, 8129-8176.

[8]   J. Lee, O. K. Farha, J. Roberts, K. A. Scheidt, S. T. Nguyen, J. T. Hupp, *Chemical Society Reviews* **2009**, *38*, 1450-1459.

[9]   A. Corma, H. García, F. X. Llabrés i Xamena, *Chemical Reviews* **2010**, *110*, 4606-4655.

[10]   Y. He, W. Zhou, G. Qian, B. Chen, *Chemical Society Reviews* **2014**, *43*, 5657-5678.

[11]   B. Van de Voorde, B. Bueken, J. Denayer, D. De Vos, *Chemical Society Reviews* **2014**, *43*, 5766-5788.

[12]   K. Adil, Y. Belmabkhout, R. S. Pillai, A. Cadiau, P. M. Bhatt, A. H. Assen, G. Maurin, M. Eddaoudi, *Chemical Society Reviews* **2017**, *46*, 3402-3430.

[13]   P. Falcaro, R. Ricco, C. M. Doherty, K. Liang, A. J. Hill, M. J. Styles, *Chemical Society Reviews* **2014**, *43*, 5513-5560.

[14]   I. Stassen, N. Burtch, A. Talin, P. Falcaro, M. Allendorf, R. Ameloot, *Chemical Society Reviews* **2017**, *46*, 3185-3241.

[15]   L. E. Kreno, K. Leong, O. K. Farha, M. Allendorf, R. P. Van Duyne, J. T. Hupp, *Chemical Reviews* **2012**, *112*, 1105-1125.

[16]   P. Horcajada, R. Gref, T. Baati, P. K. Allan, G. Maurin, P. Couvreur, G. Férey, R. E. Morris, C. Serre, *Chemical Reviews* **2012**, *112*, 1232-1268.

[17]   C. He, D. Liu, W. Lin, *Chemical Reviews* **2015**, *115*, 11079-11108.

[18]   S. Wuttke, M. Lismont, A. Escudero, B. Rungtaweevoranit, W. J. Parak, *Biomaterials* **2017**, *123*, 172-183.

[19]   R. Freund, U. Lächelt, T. Gruber, B. Rühle, S. Wuttke, *ACS Nano* **2018**, *12*, 2094-2105.

[20]   C. Doonan, R. Riccò, K. Liang, D. Bradshaw, P. Falcaro, *Accounts of Chemical Research* **2017**, *50*, 1423-1432.

[21]   M.-X. Wu, Y.-W. Yang, *Advanced Materials* **2017**, *29*, 1606134-n/a.

[22]   W. Chen, C. Wu, *Dalton Transactions* **2018**, *47*, 2114-2133.

[23]   P. Horcajada, T. Chalati, C. Serre, B. Gillet, C. Sebrie, T. Baati, J. F. Eubank, D. Heurtaux, P. Clayette, C. Kreuz, J. S. Chang, Y. K. Hwang, V. Marsaud, P. N. Bories, L. Cynober, S. Gil, G. Ferey, P. Couvreur, R. Gref, *Nat Mater* **2010**, *9*, 172-178.

[24]   T. Simon-Yarza, M. Gimenez-Marques, R. Mrimi, A. Mielcarek, R. Gref, P. Horcajada, C. Serre, P. Couvreur, *Angew Chem Int Ed Engl* **2017**, *56*, 15565-15569.

[25]   J. Zhuang, C.-H. Kuo, L.-Y. Chou, D.-Y. Liu, E. Weerapana, C.-K. Tsung, *ACS Nano* **2014**, *8*, 2812-2819.

[26]   B. Illes, S. Wuttke, H. Engelke, *Nanomaterials (Basel, Switzerland)* **2017**, *7*, 351.

[27]   C. He, K. Lu, D. Liu, W. Lin, *J Am Chem Soc* **2014**, *136*, 5181-5184.

[28]   R. Roder, T. Preiss, P. Hirschle, B. Steinborn, A. Zimpel, M. Hohn, J. O. Radler, T. Bein, E. Wagner, S. Wuttke, U. Lächelt, *J Am Chem Soc* **2017**, *139*, 2359-2368.

[29]   S. K. Alsaiari, S. Patil, M. Alyami, K. O. Alamoudi, F. A. Aleisa, J. S. Merzaban, M. Li, N. M. Khashab, *J Am Chem Soc* **2018**, *140*, 143-146.

[30]   J. D. Rocca, W. Lin, *European Journal of Inorganic Chemistry* **2010**, *2010*, 3725-3734.

[31]   A. Carne-Sanchez, C. S. Bonnet, I. Imaz, J. Lorenzo, E. Toth, D. Maspoch, *J Am Chem Soc* **2013**, *135*, 17711-17714.

[32]   A. Zimpel, T. Preiß, R. Röder, H. Engelke, M. Ingrisch, M. Peller, J. O. Rädler, E. Wagner, T. Bein, U. Lächelt, S. Wuttke, *Chemistry of Materials* **2016**, *28*, 3318-3326.

[33]   M. Peller, K. Boll, A. Zimpel, S. Wuttke, *Inorganic Chemistry Frontiers* **2018**.

[34]   M. Lismont, L. Dreesen, S. Wuttke, *Advanced Functional Materials* **2017**, *27*, 1606314.

[35]   A. E. Nel, L. Madler, D. Velegol, T. Xia, E. M. Hoek, P. Somasundaran, F. Klaessig, V. Castranova, M. Thompson, *Nat Mater* **2009**, *8*, 543-557.

[36]   M. V. Zyuzin, Y. Yan, R. Hartmann, K. T. Gause, M. Nazarenus, J. Cui, F. Caruso, W. J. Parak, *Bioconjug Chem* **2017**, *28*, 2062-2068.

[37]   P. C. Ke, S. Lin, W. J. Parak, T. P. Davis, F. Caruso, *ACS Nano* **2017**, *11*, 11773-11776.

[38]   V. Agostoni, P. Horcajada, M. Noiray, M. Malanga, A. Aykac, L. Jicsinszky, A. Vargas-Berenguel, N. Semiramoth, S. Daoud-Mahammed, V. Nicolas, C. Martineau, F. Taulelle, J. Vigneron, A. Etcheberry, C. Serre, R. Gref, *Sci Rep* **2015**, *5*, 7925.

[39]   T. Hidalgo, M. Gimenez-Marques, E. Bellido, J. Avila, M. C. Asensio, F. Salles, M. V. Lozano, M. Guillevic, R. Simon-Vazquez, A. Gonzalez-Fernandez, C. Serre, M. J. Alonso, P. Horcajada, *Sci Rep* **2017**, *7*, 43099.

[40]   E. Bellido, T. Hidalgo, M. V. Lozano, M. Guillevic, R. Simón-Vázquez, M. J. Santander-Ortega, Á. González-Fernández, C. Serre, M. J. Alonso, P. Horcajada, *Advanced Healthcare Materials* **2015**, *4*, 1246-1257.

[41]   S. Wuttke, S. Braig, T. Preiss, A. Zimpel, J. Sicklinger, C. Bellomo, J. O. Radler, A. M. Vollmar, T. Bein, *Chem Commun (Camb)* **2015**, *51*, 15752-15755.

[42]   D. Liu, C. Poon, K. Lu, C. He, W. Lin, *Nature Communications* **2014**, *5*, 4182.

[43]   B. Illes, P. Hirschle, S. Barnert, V. Cauda, S. Wuttke, H. Engelke, *Chemistry of Materials* **2017**, *29*, 8042-8046.

[44]   H. Hintz, S. Wuttke, *Chem Commun (Camb)* **2014**, *50*, 11472-11475.

[45]   P. Hirschle, Prei, F. Auras, A. Pick, J. Volkner, D. Valdeperez, G. Witte, W. J. Parak, J. O. Radler, S. Wuttke, *CrystEngComm* **2016**, *18*, 4359-4368.

[46]   S. Wuttke, A. Zimpel, T. Bein, S. Braig, K. Stoiber, A. Vollmar, D. Müller, K. Haastert-Talini, J. Schaeske, M. Stiesch, G. Zahn, A. Mohmeyer, P. Behrens, O. Eickelberg, D. A. Bölükbas, S. Meiners, *Advanced Healthcare Materials* **2017**, *6*, 1600818.

[47]   M. Boncheva, G. M. Whitesides, *MRS Bulletin* **2011**, *30*, 736-742.

[48]   T. Xia, M. Kovochich, M. Liong, H. Meng, S. Kabehie, S. George, J. I. Zink, A. E. Nel, *ACS Nano* **2009**, *3*, 3273-3286.

[49]   Y. Shan, T. Luo, C. Peng, R. Sheng, A. Cao, X. Cao, M. Shen, R. Guo, H. Tomas, X. Shi, *Biomaterials* **2012**, *33*, 3025-3035.

[50]   Y. Zhang, A. Satterlee, L. Huang, *Mol Ther* **2012**, *20*, 1298-1304.

[51]   U. Lachelt, E. Wagner, *Chem Rev* **2015**, *115*, 11043-11078.

[52]   J.-P. Behr, *CHIMIA International Journal for Chemistry* **1997**, *51*, 34-36.

[53]   A. Akinc, M. Thomas, A. M. Klibanov, R. Langer, *J Gene Med* **2005**, *7*, 657-663.

[54] I. Conejos-Sanchez, I. Cardoso, M. Oteo-Vives, E. Romero-Sanz, A. Paul, A. R. Sauri, M. A. Morcillo, M. J. Saraiva, M. J. Vicent, *J Control Release* **2015**, *198*, 80-90.

[55] A. Duro-Castano, R. M. England, D. Razola, E. Romero, M. Oteo-Vives, M. A. Morcillo, M. J. Vicent, *Mol Pharm* **2015**, *12*, 3639-3649.

[56] A. Nino-Pariente, A. Arminan, S. Reinhard, C. Scholz, E. Wagner, M. J. Vicent, *Macromol Biosci* **2017**, *17*.

[57] G. Consiglio, P. Di Pietro, L. D'Urso, G. Forte, G. Grasso, C. Sgarlata, D. Cossement, R. Snyders, C. Satriano, *J Colloid Interface Sci* **2017**, *506*, 532-542.

[58] M. G. Simoes, A. Hugo, P. Alves, P. F. Perez, A. Gomez-Zavaglia, P. N. Simoes, *Colloids Surf B Biointerfaces* **2018**, *164*, 50-57.

[59] J. M. Harris, R. B. Chess, *Nature Reviews Drug Discovery* **2003**, *2*, 214.

[60] J. Yoo, A. Birke, J. Kim, Y. Jang, S. Y. Song, S. Ryu, B.-S. Kim, B.-G. Kim, M. Barz, K. Char, *Biomacromolecules* **2018**.

[61] F. Sigmund, F. Wessely, in *Hoppe-Seyler´s Zeitschrift für physiologische Chemie, Vol. 157*, **1926**, p. 91.

[62] A. Birke, J. Ling, M. Barz, *Progress in Polymer Science* **2018**.

[63] D. Huesmann, A. Sevenich, B. Weber, M. Barz, *Polymer* **2015**, *67*, 240-248.

[64] M. Barz, R. Luxenhofer, R. Zentel, M. J. Vicent, *Polymer Chemistry* **2011**, *2*, 1900-1918.

[65] G. Zahn, H. A. Schulze, J. Lippke, S. König, U. Sazama, M. Fröba, P. Behrens, *Microporous and Mesoporous Materials* **2015**, *203*, 186-194.

[66] K. Mio, F. Shuhei, H. Kenji, K. Susumu, *Angewandte Chemie International Edition* **2010**, *49*, 5327-5330.

[67] I. Abánades Lázaro, S. Haddad, J. M. Rodrigo-Muñoz, C. Orellana-Tavra, V. del Pozo, D. Fairen-Jimenez, R. S. Forgan, *ACS Applied Materials & Interfaces* **2018**.

[68] P. Deria, J. E. Mondloch, O. Karagiaridi, W. Bury, J. T. Hupp, O. K. Farha, *Chemical Society Reviews* **2014**, *43*, 5896-5912.

[69] L. Y. T. Chou, K. Ming, W. C. W. Chan, *Chemical Society Reviews* **2011**, *40*, 233-245.

[70] C. Y. Tay, M. I. Setyawati, J. Xie, W. J. Parak, D. T. Leong, *Advanced Functional Materials* **2014**, *24*, 5936-5955.

[71] D. Magde, E. Elson, W. W. Webb, *Physical Review Letters* **1972**, *29*, 705-708.

[72] E. E. L., M. Douglas, *Biopolymers* **1974**, *13*, 1-27.

[73]   C. A. Diebolder, F. J. Beurskens, R. N. de Jong, R. I. Koning, K. Strumane, M. A. Lindorfer, M. Voorhorst, D. Ugurlar, S. Rosati, A. J. Heck, J. G. van de Winkel, I. A. Wilson, A. J. Koster, R. P. Taylor, E. O. Saphire, D. R. Burton, J. Schuurman, P. Gros, P. W. Parren, *Science* **2014**, *343*, 1260-1263.

[74]   M. P. Monopoli, C. Aberg, A. Salvati, K. A. Dawson, *Nat Nanotechnol* **2012**, *7*, 779-786.

[75]   P. Schwille, F. J. Meyer-Almes, R. Rigler, *Biophysical Journal* **1997**, *72*, 1878-1886.

[76]   B. K. Müller, E. Zaychikov, C. Bräuchle, D. C. Lamb, *Biophysical Journal* **2005**, *89*, 3508-3522.

[77]   G. Zahn, H. A. Schulze, J. Lippke, S. König, U. Sazama, M. Fröba, P. Behrens, *Microporous and Mesoporous Materials* **2015**, *203*, 186-194.

[78]   R. Roder, T. Preiss, P. Hirschle, B. Steinborn, A. Zimpel, M. Hohn, J. O. Radler, T. Bein, E. Wagner, S. Wuttke, U. Lachelt, *J Am Chem Soc* **2017**, *139*, 2359-2368.

[79]   J. Yoo, A. Birke, J. Kim, Y. Jang, S. Y. Song, S. Ryu, B.-S. Kim, B.-G. Kim, M. Barz, K. Char, *Biomacromolecules* **2018**.

[80]   J. Hendrix, V. Baumgartel, W. Schrimpf, S. Ivanchenko, M. A. Digman, E. Gratton, H. G. Krausslich, B. Muller, D. C. Lamb, *J Cell Biol* **2015**, *210*, 629-646.

[81]   W. Schrimpf, A. Barth, J. Hendrix, D. C. Lamb, *Biophysical Journal* **2018**, *114*, 1518-1528.

4.6. Appendix
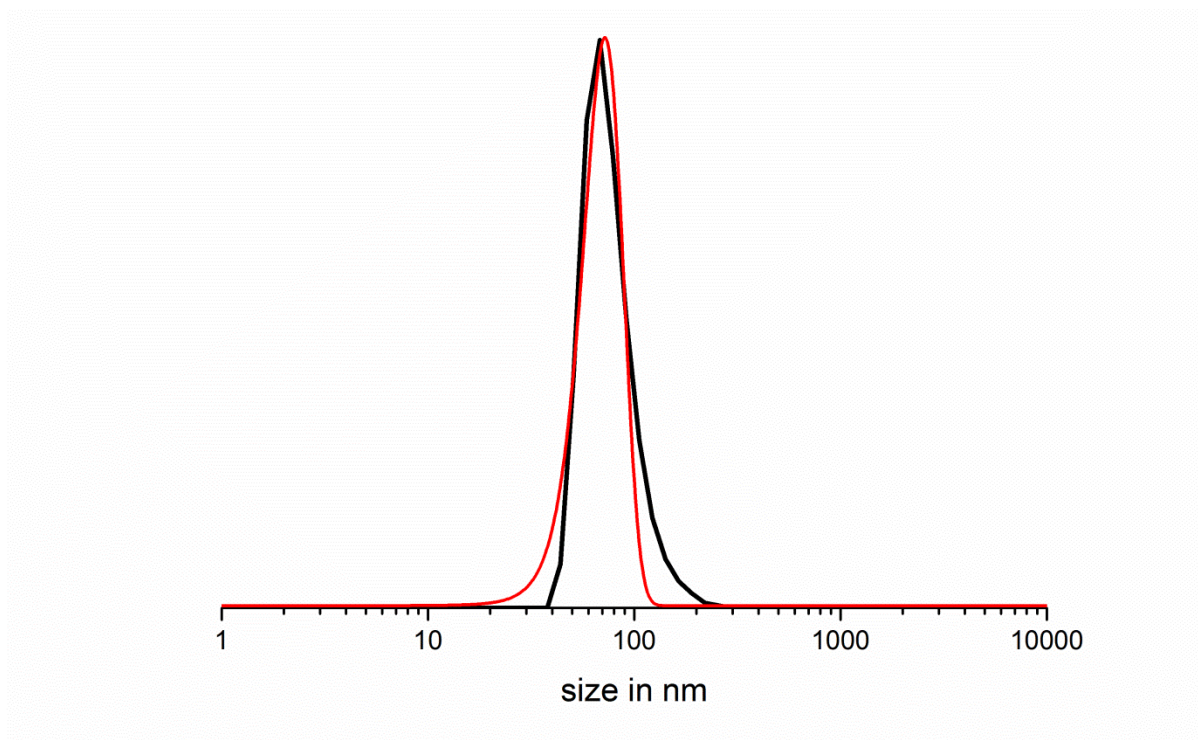
Figure S4-1. DLS size distribution (black) and Gauss-fit (red) of Zr-*fum* NPs in ethanolic dispersion.
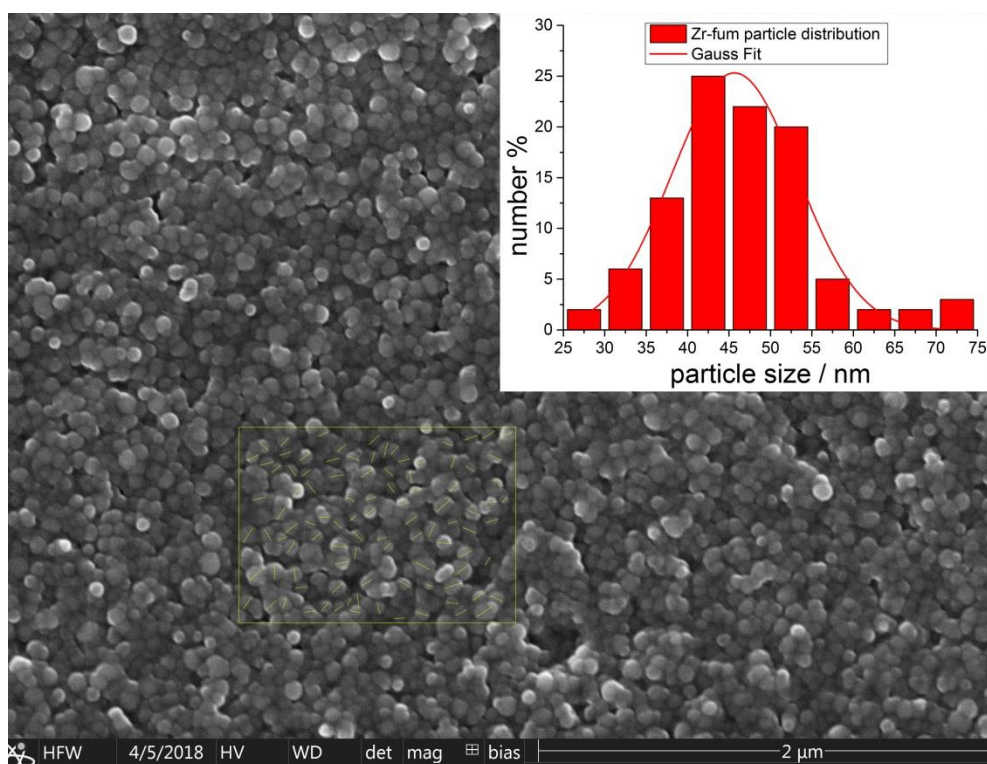
Figure S4-2. SEM overview of Zr-*fum* NPs with size distribution (inset) determined from the region of interest (yellow box).
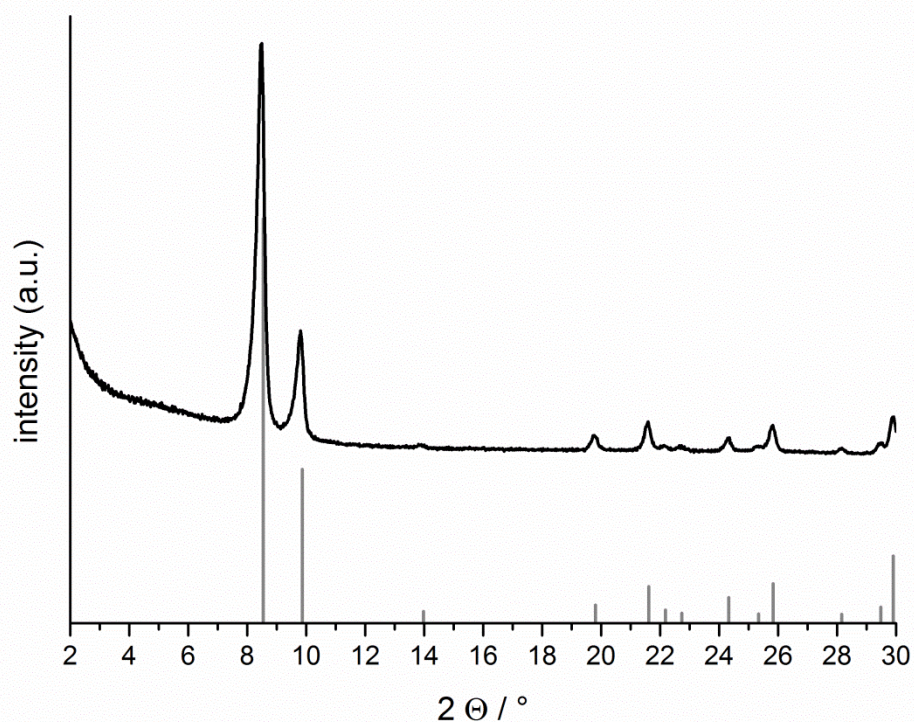
Figure S4-3. XRD pattern of Zr-*fum* NPs compared to calculated Zr-*fum* pattern.
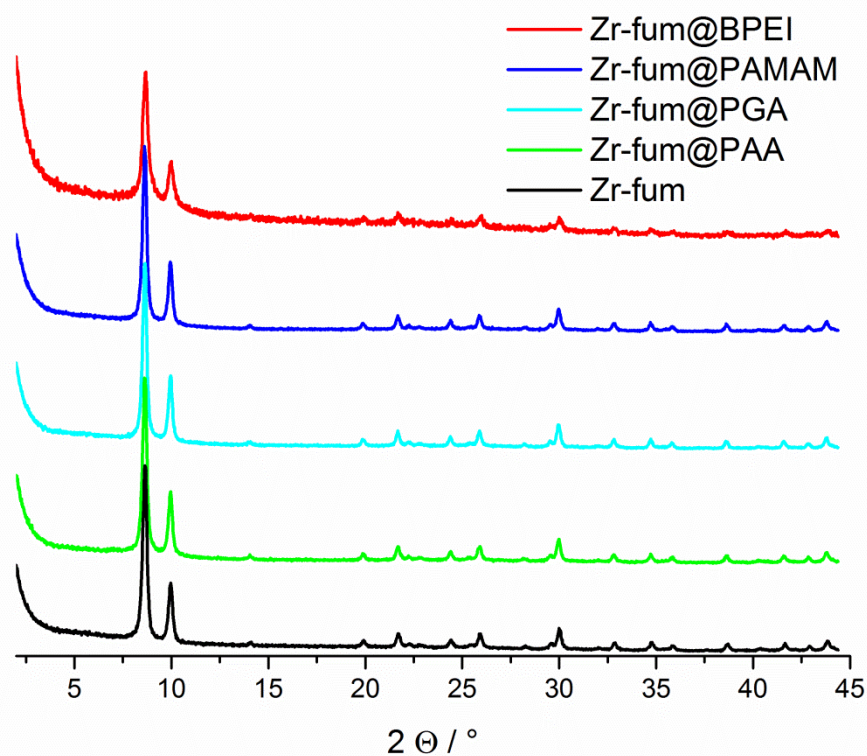
Figure S4-4. PXRD spectra of unfunctionalized Zr-*fum* and Zr-*fum*@polymer.
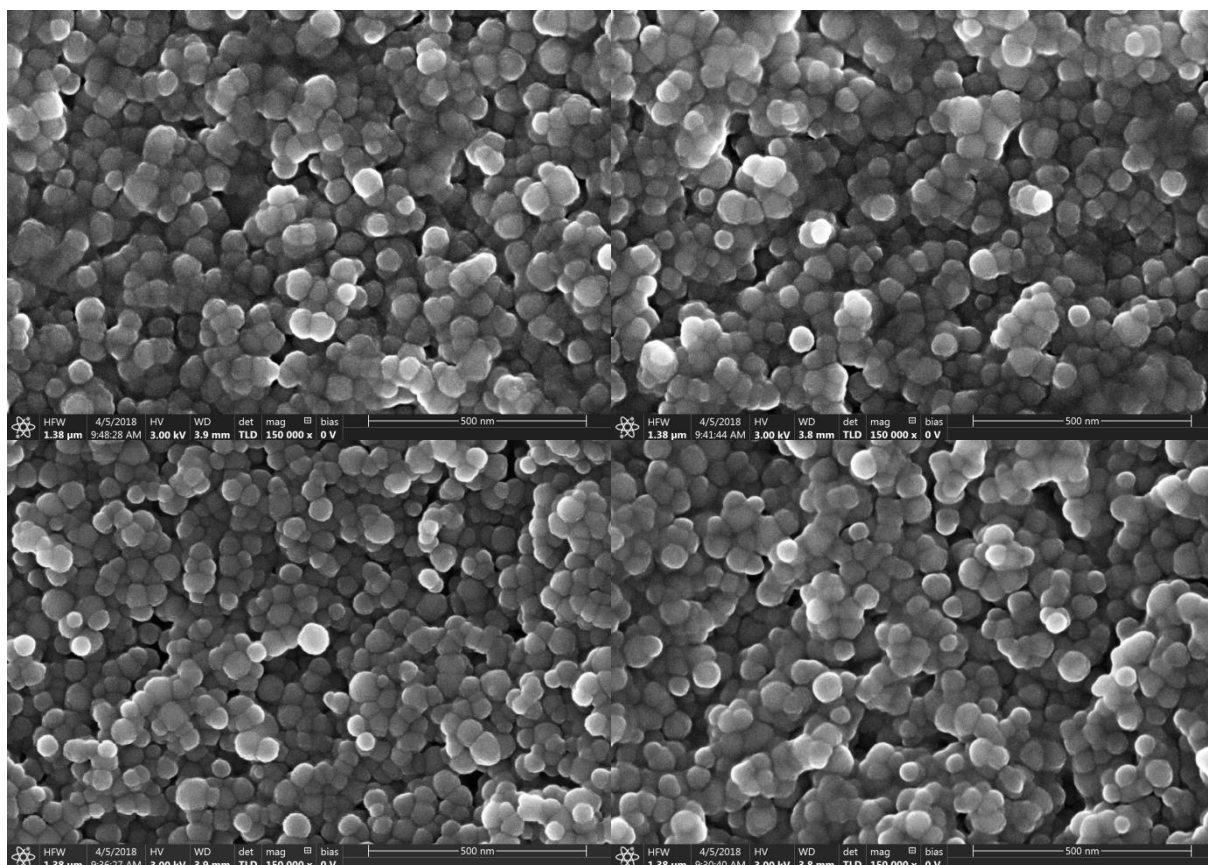
Figure S4-5. SEM comparison between Zr-*fum*@polymer NPs: Zr-*fum*@BPEI (top left); Zr-*fum*@PAMAM (top right); Zr-*fum*@PAA (bottom left); Zr-*fum*@PGA (bottom right).
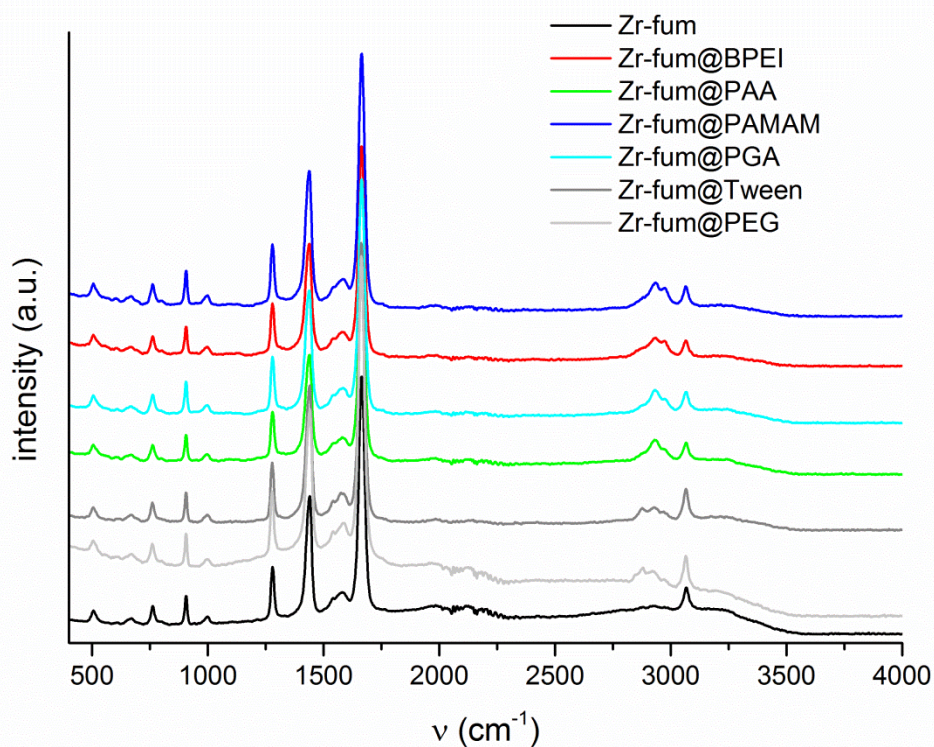
Figure S4-6. Full Raman spectra (as measured) of unfunctionalized Zr-*fum* and Zr-*fum*@polymer.
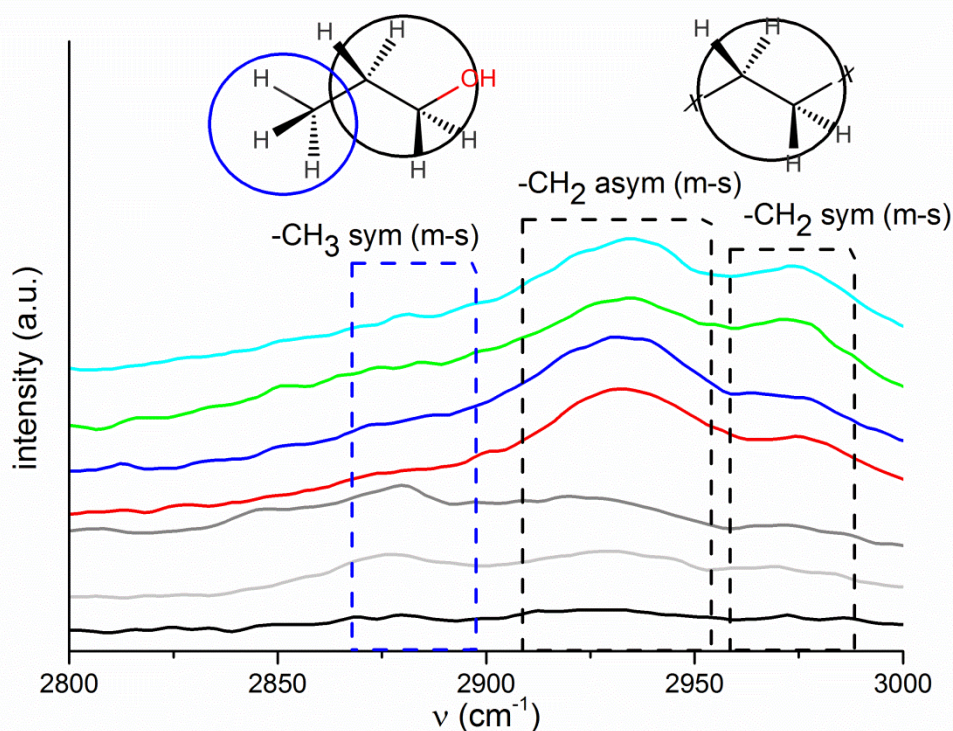
Figure S4-7. Partial region of Raman spectra (normalized to internal standard: fumaric acid C-H vibration at 3064 cm^{-1}) with indications for strongly appearing –CH$_3$ and –CH$_2$ stretching vibrations.[1] Blue box shows more pronounced -CH$_3$ bonds for PEG and Tween® , which results from EtOH residues after drying. For legend, see Figure S4-6.
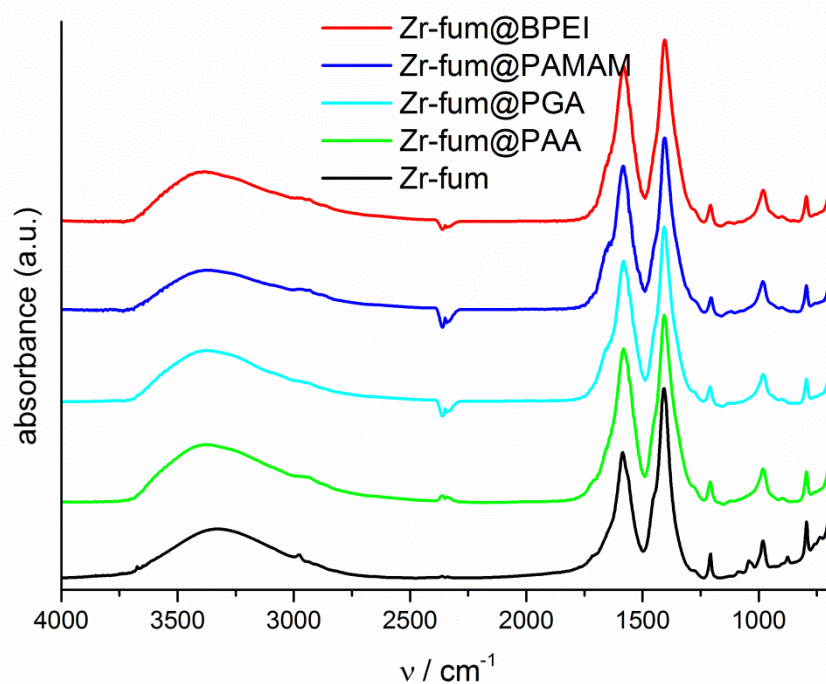
Figure S4-8. FTIR spectra of unfunctionalized Zr-*fum* and Zr-*fum*@polymer.
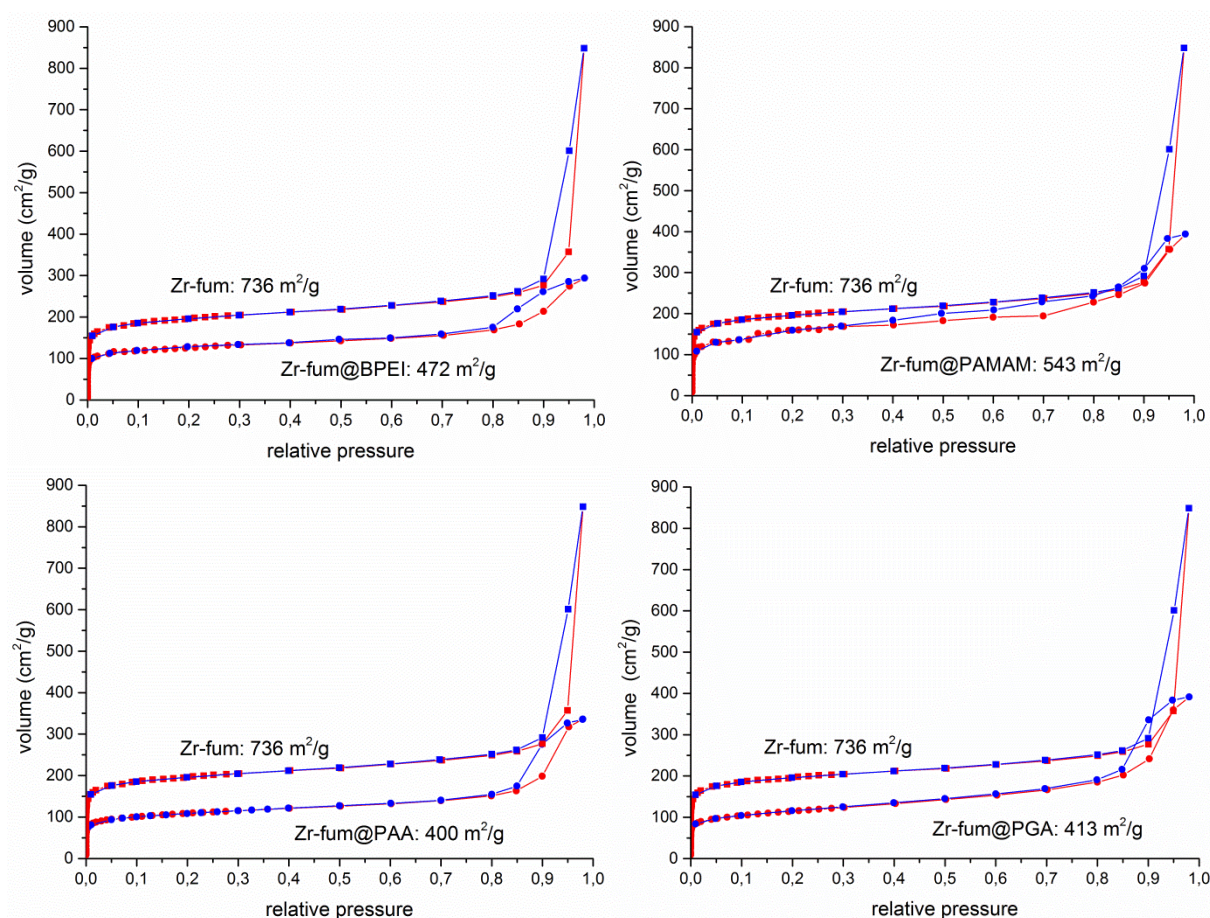
Figure S4-9. Nitrogen sorption isotherms of Zr-*fum* NPs in comparison to Zr-*fum*@polymer NPs.
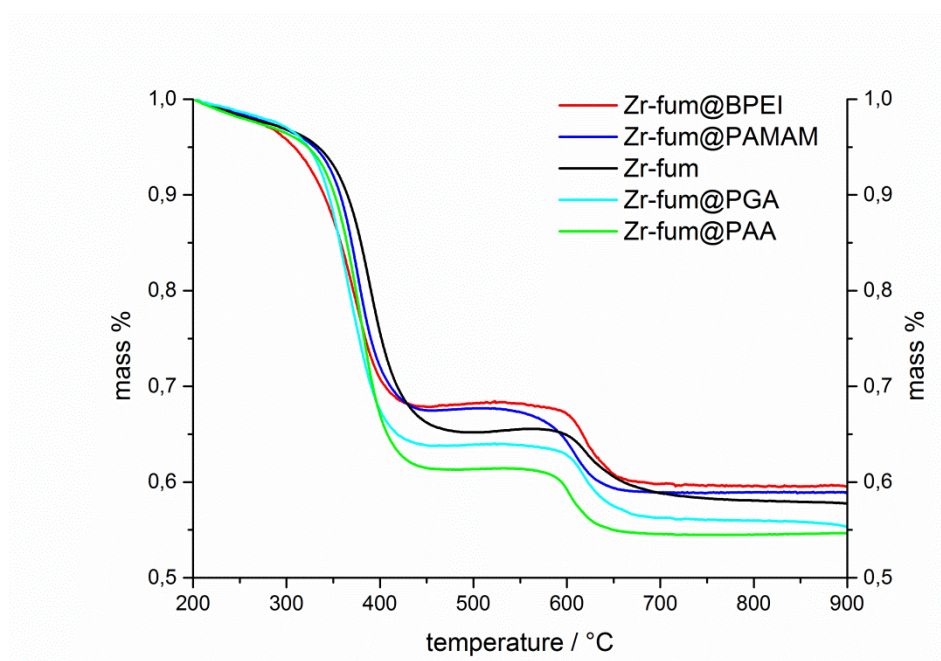
Figure S4-10. TGA comparison of the different Zr-*fum*@polymer fomulations.
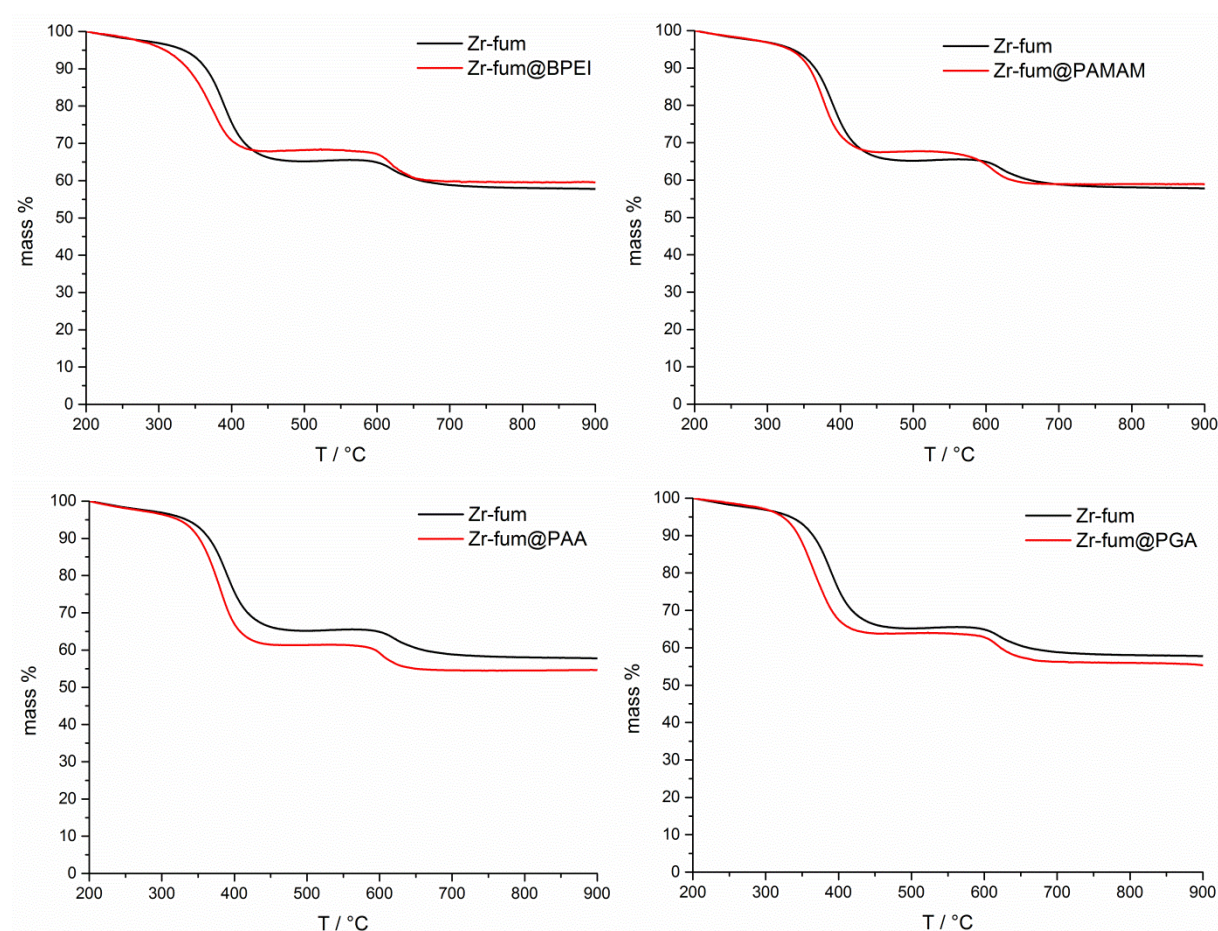
Figure S4-11. TGA of Zr-*fum* NPs in comparison to Zr-*fum*@polymer NPs.

Table S4-1. Determination of formic acid concentration in supernatant of different polymer coating reactions.

The calculations were done using Mega-Calc^{TM} (freeware supplied by Megazyme). A1 represents the absorption value before addition of formate dehydrogenase, A2 represents the absorption value after the completed reaction (approx. 12 min).

Blank absorbance values (EtOH/H2O 70:30)

A1	A2
0,4669	0,7127

Absorbance values (at 340 nm; Reference at 450 nm)			Results	
Sample	A1	A2	Abs (Formic Acid)	Formic Acid (g/L)
Zr-*fum*@PGA	0,4873	1,0151	0,2820	0,018
Zr-*fum*@PAMAM	0,5322	1,0099	0,2319	0,014
Zr-*fum*@BPEI	0,5618	1,0539	0,2463	0,015
Zr-*fum*@PAA	0,5259	1,4079	0,6362	0,040
Zr-*fum*	0,5326	0,8752	0,0969	0,006

Average amount of formic acid after polymer coating of 1 mg MOF (in 1 mL coating supernatant, taking PGA, PAMAM, BPEI into consideration):

(18 µg + 14 µg + 15 µg)/3 = 16 µg

Total amount of coordinatively bound formic acid per mg (after substraction of free formic acid):

16 µg – 6 µg = 10 µg

→ 10 µg formic acid / 1 mg MOF **≈ 1 w%**
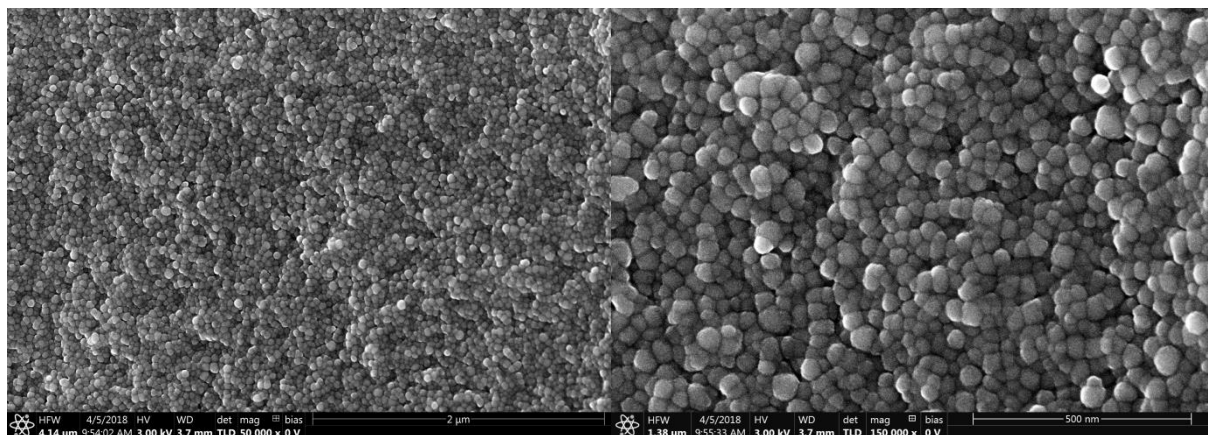
Figure S4-12. SEM images of Zr-*fum*@PGA-PS NPs at two magnifications (left: × 50000; right: × 150000).
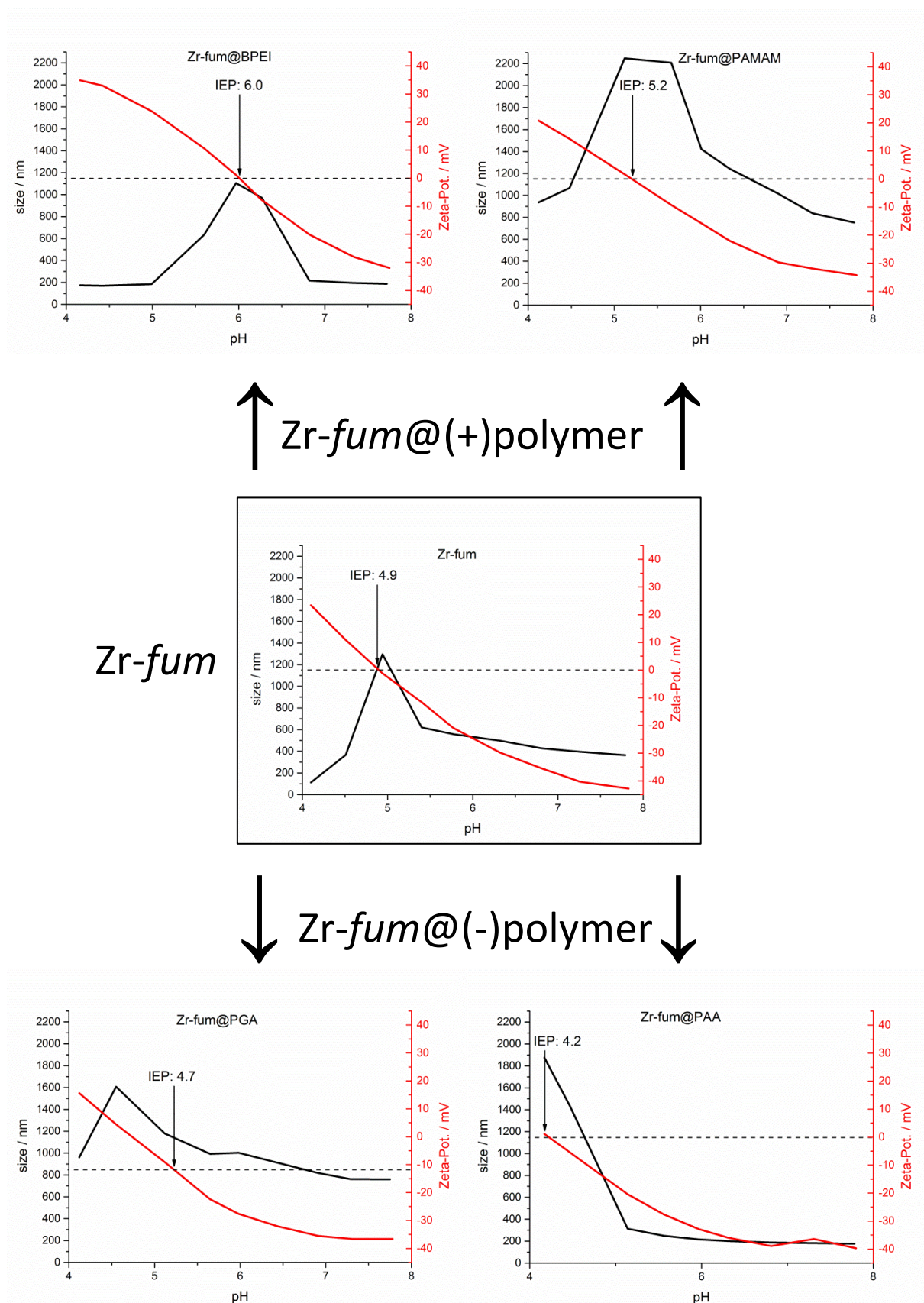
Figure S4-13. Titration curves of unfunctionalized Zr-*fum* and Zr-*fum*@polymer. Size (Z-average) and Zeta-potential is plotted against the pH of the dispersion. Zr-*fum*@(+)polymer NPs are plotted at the top, unfunctionalized Zr-*fum* in the middle and Zr-*fum*@(-)polymer at the bottom of the figure.
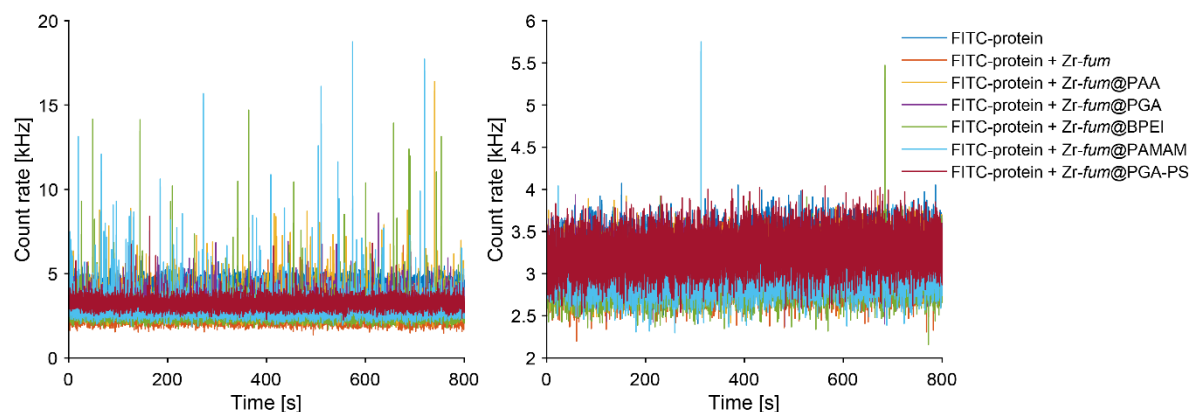
Figure S4-14. The detected photon-macrotime counts of 100 nM FITC-IgG (**left**) and 100 nM FITC-albumin (**right**) in the absence or presence of 10 µg Zr-*fum* and Zr-*fum*@polymer NPs.

Table S4-2. The values obtained from the FCS measurements, applying a 3-component diffusion fit, where N_1 is the fraction of free dye, N_2 is the FITC-IgG fraction, and N_3 is the FITC-IgG fraction interacting with the Zr-*fum* and Zr-*fum*@polymer NPs.

	N_1	N_2	N_3	Ratio = $N_3 / (N_2 + N_3)$
IgG	0.46	1.41	0.01	**0.01**
IgG + Zr-*fum*	0.11	0.18	0.32	**0.64**
IgG + Zr-*fum*@PAA	0.09	0.20	0.36	**0.64**
IgG + Zr-*fum*@PGA	0.17	0.35	0.39	**0.53**
IgG + Zr-*fum*@BPEI	0.14	0.30	0.26	**0.46**
IgG + Zr-*fum*@PAMAM	0.10	0.30	0.33	**0.52**
IgG + Zr-*fum*@PGA-PS	0.32	0.81	0.09	**0.10**
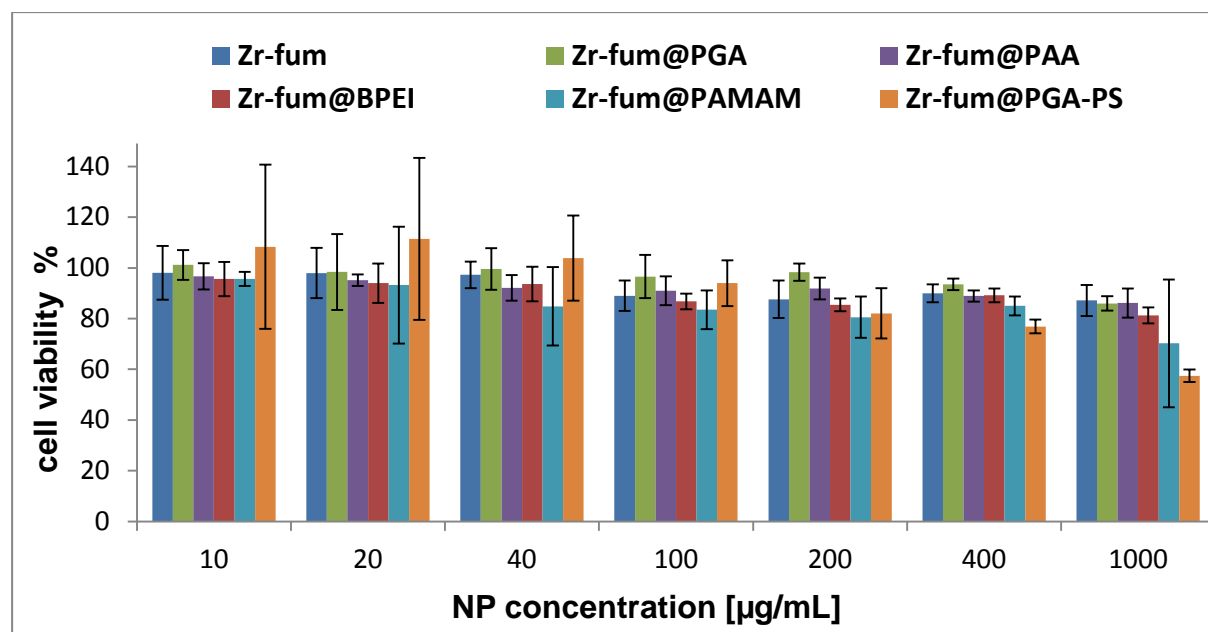
Figure S4-15. MTT cell viability assays of all Zr-*fum*@polymer formulations as well as unfunctionalized Zr-*fum*. No significant toxicity can be observed up to concentrations of 0.4 mg/mL, while at highest concentration of 1 mg/mL effects on metabolic activity become apparent.
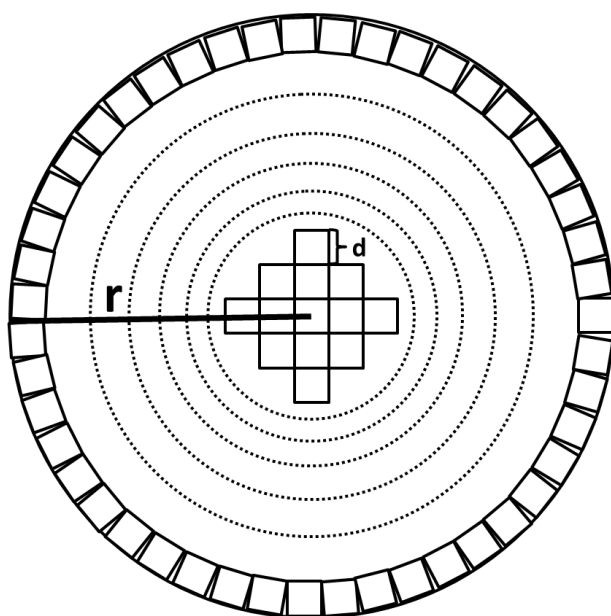
Theoretical Estimate (wt% formic acid per NP)

Figure „Theoretical Estimate": Schematical drawing of spherical Zr-*fum* NPs with radius r = 23 nm, consisting of unit cells with edge length d = 1,79 nm.

Assuming Zr-*fum* NPs to be spherical with an average diameter of 46 nm (from SEM; Figure S4-9), one derives a particle surface and volume of:

$$V_{NP} = \frac{4}{3}r^3\pi = \frac{4}{3}(23\ nm)^3\pi = 5,1 \cdot 10^4\ nm^3$$

$$S_{NP} = 4r^2\pi = 4(23\ nm)^2\pi = 6,65 \cdot 10^3\ nm^2$$

The dimensions of a Zr-*fum* cubic unit cell were taken from Wißmann *et al.*[2] resulting in a volume of:

$$V_{UC} = d^3 = (1,79\ nm)^3 = 5,74 \cdot nm^3$$

This results in a total number of unit cells per particle:

$$N_{total} = \frac{V_{NP}}{V_{UC}} = \frac{5,1 \cdot 10^4\ nm^3}{5,74 \cdot nm^3} = 8885$$

Since the area of one face of cubic unit cell is much smaller than the external particle surface

$$S_{UC} \ll S_{NP}$$

it can be assumed that the planar external cube surfaces sum up to the curved external particle surface. The total number of unit cells on the external surface (which can carry formic acid) can be calculated, assuming the surface of a unit cell on the external surface to be

$$S_{UC} = d^2 = (1,79\ nm)^2 = 3,2\ nm^2$$

resulting in

$$N_{surface} = \frac{S_{NP}}{S_{UC}} = \frac{6,65 \cdot 10^3\ nm^2}{3,2\ nm^2} = 2078$$

Considering 6 cubic faces of the unit cell as well as 6 fumaric acids, one fumaric acid (the one at the external NP surface) will be theoretically replaced by formic acid. This means 2078 UC per NP consist of $[Zr_6O_4(OH)_4(O_2C-(CH)_2-CO_2)_5(HCOO)]$ = ①, while $8885 - 2078 = 6807$ UC contain the usual chemical formula $[Zr_6O_4(OH)_4(O_2C-(CH)_2-CO_2)_6]$[7] = ②.

Taking into account the different atomic masses of internal ($M_{②}$) and external ($M_{①}$) unit cells, the total atomic mass per NP is:

$$M_{total} = M_{①} + M_{②} = 2078 \times 1293\,Da + 6807 \times 1362\,Da = 11,96 \cdot 10^6\,Da$$

The atomic mass of formic acid per particle can be calculated by:

$$M_{formic\,acid} = 2078 \times 45\,Da = 9,4 \cdot 10^4\,Da$$

The weight percent (w%) of formic acid in the material is therefore given by:

$$\frac{M_{formic\,acid}}{M_{total}} = \frac{9,4 \cdot 10^4\,Da}{11,96 \cdot 10^6\,Da} = 0,8\,w\%$$

This estimation is in very good agreement with experimental data, revealing approx. 1 w% of formic acid released by the coating procedure.

References:

[1]   G. Socrates, *Infrared and Raman Characteristic Group Frequencies: Tables and Charts*, 3rd Edition ed., John Wiley and Sons, Ltd., Chichester, **2001**.

[2]   G. Wißmann, A. Schaate, S. Lilienthal, I. Bremer, A. M. Schneider, P. Behrens, *Microporous and Mesoporous Materials* **2012**, *152*, 64-70.

5.   Kinetic analysis of the uptake and release of fluorescein by metal-organic framework nanoparticles

This chapter is based on the following publication:

Tobias Preiß, Andreas Zimpel, Stefan Wuttke, Joachim O. Rädler, *Materials* **2017**, *10*, 216.
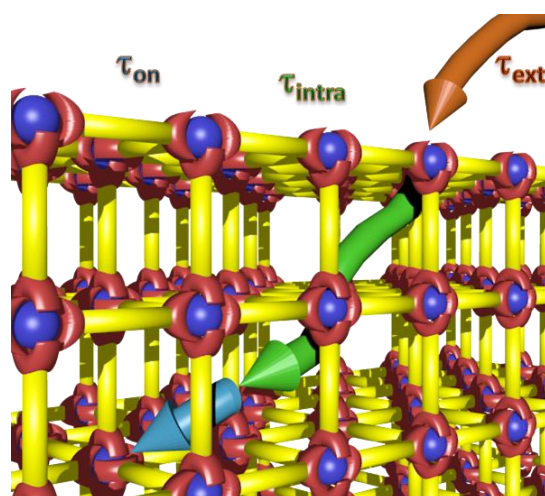
5.1. Introduction

The widespread use of porous materials in the field of separation, storage and catalytic process technologies requires a thorough understanding of the adsorption and desorption of guest molecules within the porous structure. In this context, metal-organic frameworks (MOFs) are an interesting class of materials, as they are crystalline and hence possess a regular porous structure.[1–4] In MOFs, inorganic metal nodes connected by organic linkers create a diverse but well-defined chemical environment, which allows specific interactions with guest molecules. As a matter of fact, MOFs exhibit some of the highest porosities (1000 to 7000 m²/g) of all known porous solids, with pore sizes in the range of 0.3 to 6 nm.[5] Their high porosities and, in particular, the combination of high surface area with tunable pore size render MOFs ideal for applications in gas storage and separation[6,7], catalysis[8–10], sensing[11,12], electronics[13], drug delivery[14–16] and X-ray analysis of the structures of guest molecules within the MOF scaffold[4,17].

Recently, several reports have pointed to the general applicability of MOF nanoparticles (MOF-NPs) for drug delivery, as they have high loading capacities and are functionalizable, and certain structures have been shown to be biocompatible (e.g. MIL-100(Fe); MIL stands for Materials of Institute Lavoisier)[11,15,16,18–21]. MOF-NPs have been loaded with various drugs, including cisplatin[22], 5-fluorouracil[23], ibuprofen[24], doxorubicin and cidofovir[25]. Both MIL-100(Fe) and MIL-101(Cr) represent good model materials for drug delivery, due to their large pores (diameters of 25-29 Å for MIL-100 and 29-34 Å for MIL-101) and window sizes (diameters of 5-9 Å for MIL-100 and 12-17 Å for MIL-101)[26,27]. MIL-100 and 101 show high chemical stability and typically large BET surface areas of up to 6000 m²/g for the bulk material (2000-4000 m^2/g as nanoparticles)[28–31]. Indeed, in many respects, MIL-100(Fe) NPs are the most promising MOF-based vehicles available for drug delivery[25,32].

The ability of NPs made of solid materials to load and then specifically release drug molecules within the human body has been at the forefront of biomedical nanotechnology for more than a decade.[33–39] Yet studies on the loading and release kinetics of drugs in porous nanocarriers are very rare, even for established systems based on polymer, silica or liposome particles[34,40–42]. One basic question that remains open is how pore size affects uptake and offloading. It is known that, within porous materials, diffusion coefficients are reduced by a factor 10^4, as transport becomes an effectively 1D diffusion process[43]. Furthermore, the affinity of the cargo molecules for the internal surface of the porous material (host-guest interaction) is likely to play an important role in determining the kinetics of transport as well as the loading capacity.[44] It is conceivable that molecules undergo repeated cycles of absorption and desorption, and brief spells of free diffusion before an equilibrium situation is reached. In addition, the conditions will change during the course of *in-vivo* delivery. Affinity is likely to depend on the pH value of the environment, owing to the influence of pH on the charge of both cargo and MOF. As the pH varies within the human body, release kinetics will vary with local acidity. With the use of MOF-NPs as reliable and tunable drug carrier systems in mind, characterization of host-guest interaction and release is essential for optimized dosing.

In this work, we study the loading and release kinetics of MIL-100(Fe) and MIL-101(Cr). Our goal is to elucidate -- on the basis of these representative MOF-NPs -- the mechanisms and limiting factors that drive and constrain, respectively, molecular transport in and out of porous NPs, and compare these results with theoretical estimates. To this end, we characterize the MOF-NPs using transmission electron microscopy (TEM), dynamic light scattering (DLS) and X-ray diffraction (XRD), and measure the uptake of fluorescein via fluorescence

spectroscopy at various pH values. We find that MIL-100(Fe) and MIL-101(Cr) NPs have well defined size distributions and crystallinity, and remain crystalline in buffer. DLS and zeta-potential measurements show that NP agglomeration is strongly pH dependent. By performing titration studies we determined the dissociation constants for fluorescein (disodium salt) and find that the NPs have a high payload capacity, which is compatible with the internal area estimated from BET measurements. Kinetic fluorescence studies show fast loading kinetics with high affinity in (unbuffered) distilled water (at low pH) and slower loading kinetics (i.e. lower affinity) at high pH ($7.4 - 8.4$), while release shows the converse behavior: high affinity and slow release at low pH (and in water). We show that loading and release kinetics can be theoretically described by diffusion to target, followed by restricted internal diffusion and equilibrium binding to the internal surface (physisorption). These findings demonstrate that physicochemical studies of MOF-NP loading enable rational, predictive design of release scenarios, particularly with regard to varying pH conditions.

5.2. Results and Discussion

In all following experiments, we study MOF-NPs of types MIL-100(Fe) and MIL-101(Cr), which were synthesized as described in Wuttke *et al.*[45] Prior to the loading and release studies, we characterized the size distribution of the MOF-NPs using DLS, FCS and TEM[46], their major structural features by XRD, and their porosities by measuring nitrogen adsorption and deriving sorption isotherms to confirm the expected regular porosity of MOF-NPs.
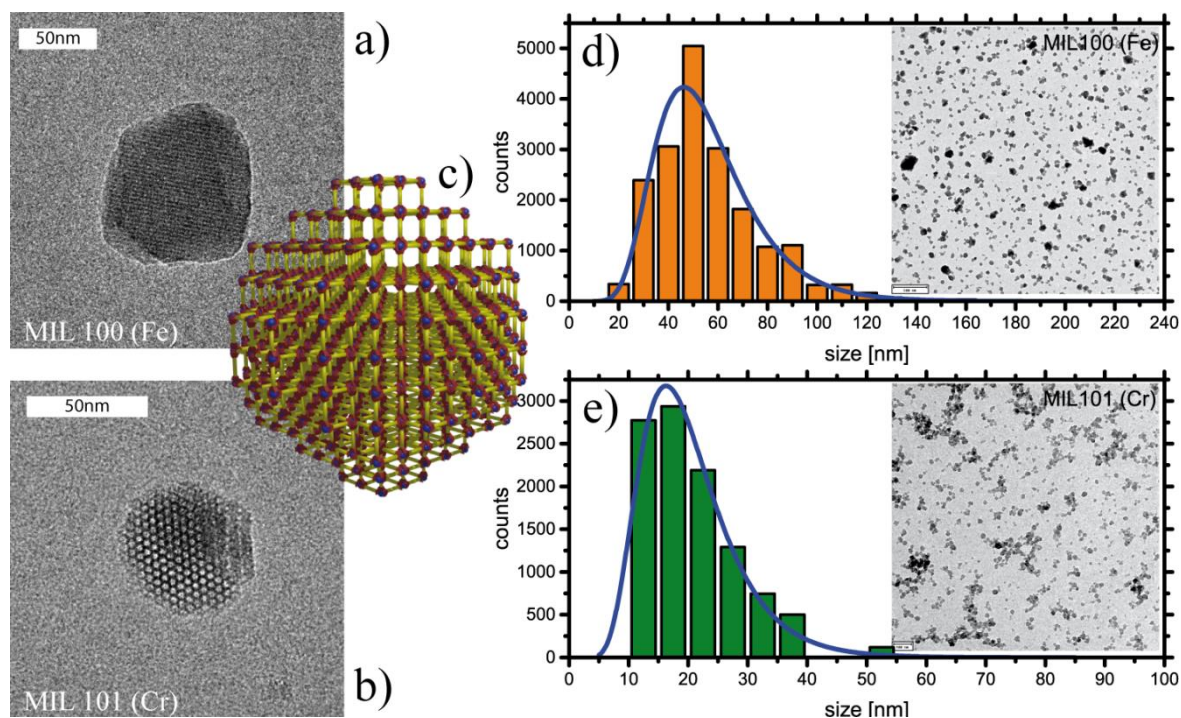

Figure 5-1. a) & b) TEM images of the two MOP-NP types used here show mesoporous structure and shape. c) Simplified depiction of the crystalline structure with hollow pores taking up most of the volume; yellow rods with red ends: organic linker, blue dots: metal centers. d) & e) Size histogram of MOF-NPs based on particle analysis of electron micrographs yields a typical size for MIL-100(Fe)(Fe) of 53nm and for MIL-101(Cr) of 19nm.

TEM images of MIL-100(Fe) and MIL-101(Cr) NPs reveal particles with an approximately spherical shape (Figure 5-1). Moreover, the TEM images indicate high crystallinity of the particles, as evidenced by the presence of electron diffraction fringes. We analyzed the size distribution based on different TEM images of MOF-NPs (see SI)[46]. Over 10,000 particles were examined for their projected size, assuming sphericity and employing image analysis for separation of closely adjacent particles (for details, see SI). The size histograms of both MOF-NPs reveal a slightly polydisperse ($\sigma > 5\%$ [47,48]) distribution (Figure 5-1 d) and e)). MIL-100(Fe) NPs have a mean diameter of 52.4 nm ($\sigma = 32\%$, FWHM 30.9 – 69.5 nm), whereas MIL-101(Cr) NPs have a mean size of 18.9 nm ($\sigma = 35\%$, FWHM 10.3 – 25.7 nm). We utilized this information to estimate numbers of NPs per volume given an estimate of NP

mass based on the crystallographic mass densities[26,27]. For MIL-100(Fe) NPs we used a mean radius of $r_{MIL-100} = 26.5\ nm$ and a mass density of $\rho_{MIL-100} = 0.98\ g/ml$[26]. We obtain a mean mass per NP of $m_{MIL-100} = 76 \cdot 10^{-18}$g and thus a number density of $N_{MIL-100} = 1.31 \cdot 10^{13}$ NPs per mg (for details, see SI). This corresponds to an NP number concentration of $n_{MIL-100} = 21.7\ pmol$. Using the corresponding values $r_{MIL-101} = 9.45\ nm$ and $\rho_{MIL-101} = 0.62\ g/ml$[27], we derived a mean particle mass of $m_{MIL-101} = 2.2 \cdot 10^{-18}g$ and thus $N_{MIL-101} = 4.56 \cdot 10^{14}$ particles per milligram ($n_{MIL-100} = 760\ pmol$). These values were subsequently used to calculate molecular loading per NP.

To complement the information derived from 2D projections of NPs imaged by TEM, DLS-based analysis of MOF-NPs in solution (see SI) provided information on their diffusive behavior and hence on the hydrodynamic radius of the NPs. In accordance with results reported in the literature[45], MIL-100(Fe) and MIL-101(Cr) NPs have hydrodynamic diameters of about 124 nm and 69 (±19) nm respectively. Comparison of these observations with the TEM size distribution results suggests that the NPs tend to form small agglomerations in unbuffered water. XRD measurements (see SI) confirm the crystallinity of the MOF-NPs observed in the TEM images[26,27].

In order to verify the stability of the particles over the time scales employed for loading and release, XRD measurements were performed on NPs that had been incubated in buffer for 1 h. The results (see SI) show no significant change in the diffraction pattern, indicating that there is no structural change in the NPs.

On examining the size distributions of the NPs in the presence of various concentrations of fluorescein with DLS, we noted that the size of MIL-100(Fe) NPs increases slightly with increasing concentrations of fluorescein. This indicates that NPs tend to aggregate under varying fluorescein concentrations. One possible explanation is the alkalinity of fluorescein disodium salt, which will lead to concentration-dependent changes in pH. Electrostatic interactions between charged molecules or "crosslinking" of MOF NPs by fluorescein molecules, as has been found for, e.g., doxorubicin[49] might also contribute to this effect. In order to examine these possibilities more closely, we performed DLS and concurrent zeta-potential experiments on suspensions of MOF-NPs in water. The pH was increased incrementally in steps of 0.5 units (the initial suspension of MOFs in water has a pH of 2) by adding NaOH (see SI), allowing us to study the pH dependency of effective particle size in a well-defined system. DLS analysis yields an initial size of about 200 nm for MIL-100(Fe) and about 50 nm for MIL-101(Cr). With increasing alkalinity the zeta-potential drops, and below a value of about ±25 mV particles tend to agglomerate. This finding is in agreement with the

previous observation that a zeta-potential of greater than 25 mV (absolute value) is required for NPs to be stabilized by electrostatic repulsion.[35,50] In the case of MIL-100(Fe) NPs, the zeta-potential drops to negative values at pH values higher than 5.5. This leads to newly emerging repulsion forces, so that agglomerates tend to separate again. The strong dependence of particle size and zeta-potential on the pH of the local environment is taken into account in our theoretical model (see below), but this could be avoided by appropriate coating of the MOF-NPs[32,45,51].
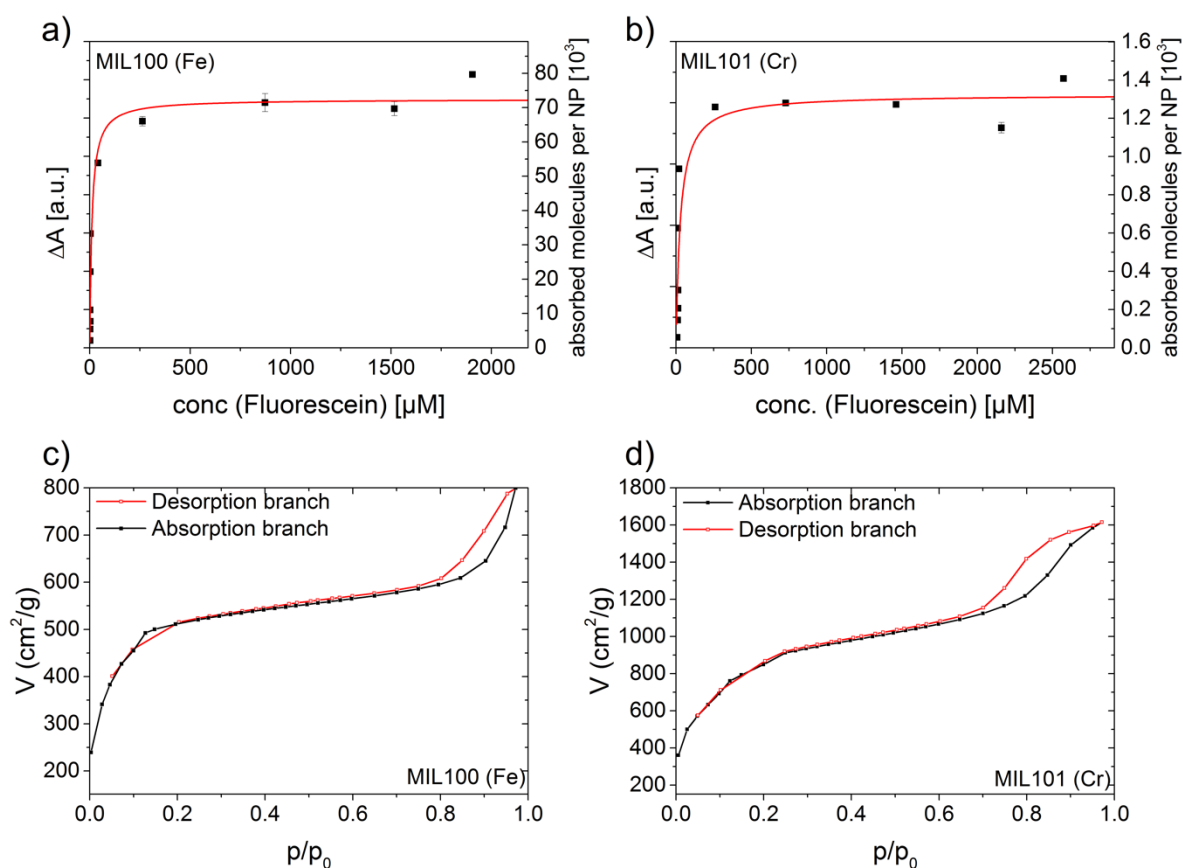
Figure 5-2. a) & b): Amounts of fluorescein loaded into MOF NP (obtained from the difference in absorption between the starting fluorescein solution and the supernatant recovered after loading) as a function of external fluorescein concentration fit to Langmuir-type curves. The calculated dissociation constants and maximum payload capacities per mg of NPs are: $k_D^{MIL100} = 11$ µM, $k_D^{MIL101} = 136$ µM, $P_{max}^{MIL100} = 649.4$ µg, $P_{max}^{MIL101} = 413.5$ µg. c) & d): Measurements of nitrogen gas absorption by the MOF-NPs. The BET surface area obtained for MIL-100(Fe) NPs is 2004 m²/g and for MIL-101(Cr) is 3205 m²/g. Taking both into account yields a mean area occupied by one fluorescein molecule of 2 nm² for MIL-100(Fe) and 5 nm² for MIL-101(Cr).

We then turned to the loading behavior, and determined the dissociation constants and the maximum capacities of MOF-NPs for uptake of fluorescein. For this purpose NP suspensions that had been incubated for a certain time (24 h) in fluorescein solutions of different concentrations were centrifuged, and the fluorescein remaining in the supernatant was

quantified by UV-VIS absorption using a calibration curve based on a fluorescein dilution series (see SI). The difference in absorbance between the starting solutions and the supernatants recovered after centrifugal removal of both types of MOF-NPs is shown in Figure 5-2 a) and b) (for details see SI). We used initial fluorescein concentrations of between 20 µg/ml and 1500 µg/ml. Each data point represents the average of three independently prepared and measured samples. The data were fitted to a Langmuir-type sorption function:

$$P(c) = \frac{P_{Max} \cdot c}{c + K_D}$$

Here c is the concentration of fluorescein, P_{Max} is the saturation value of adsorbed fluorescein and K_D is the dissociation constant (i.e. the concentration at which half of the maximal possible fluorescein is adsorbed). Both MIL-100(Fe) with $K_D^{MIL-100} = 4.4\,µg/ml = 11\,µM$ and MIL-101(Cr) with $K_D^{MIL-101} = 11.7\,µg/ml = 36\,µM$ were found to have low dissociation constants, both compared to that of doxorubicin bound to MIL-100(Fe) as determined by Anand et al. [91 $µM$] and in light of its high maximal capacity for adsorbed fluorescein ($P_{max}^{MIL-100} = 649.4\,µg = 1.6\,µmol$ and $P_{max}^{MIL-101} = 413.5\,µg = 1.0\,µmol$).[49] We convert the adsorbed mass of fluorescein per mass unit of nanomaterial into a molar ratio (number of adsorbed fluorescein molecules per NP) using the molar mass of the NPs obtained from TEM analysis and $M_{FC} = 412.3\,g/mol$ for fluorescein disodium (see SI for further details). The calculated number of adsorbed fluorescein molecules per single NP is shown in Figure 5.2 (right axis). The large numbers (on the order of 10^3 to $>10^4$) indicate the high payload capacity of the MOF NPs. Note that these loading capacities correspond to a weight payload ratio (load weight/carrier weight) of 41% for MIL-101(Cr) and 65% for MIL-100(Fe). The latter is in good agreement with published data for other guest molecules[25,24,49]. We also constructed N_2 isotherms (Figure 5-2) for comparison of the amount of loaded fluorescein molecules with the accessible internal surface area of the MOF-NPs. The corresponding BET surface area is estimated to be $S_{BET} = 2004\,m^2/g$ for MIL-100(Fe) and $S_{BET} = 3205\,m^2/g$ for MIL-101(Cr). By combining the maximum payload capacity per mg NPs with the BET surface results, we calculate the area occupied by one fluorescein molecule (A_{FC}) for both types of MOF-NPs: $A_{FC}^{MIL-100} = S_{BET}^{MIL-100}/P_{max}^{MIL-100} \cdot 1mg = 2\,nm^2$ and $A_{FC}^{MIL-101} = S_{BET}^{MIL-101}/P_{max}^{MIL-101} \cdot 1mg = 5\,nm^2$. For comparison, a single fluorescein molecule has an approximate projection area of about 1.1 nm^2 (see SI). Hence, we can assume that the internal surface of both MOF-NPs is densely packed with fluorescein molecules.

5. Kinetic analysis of the uptake and release of fluorescein by metal-organic framework nanoparticles
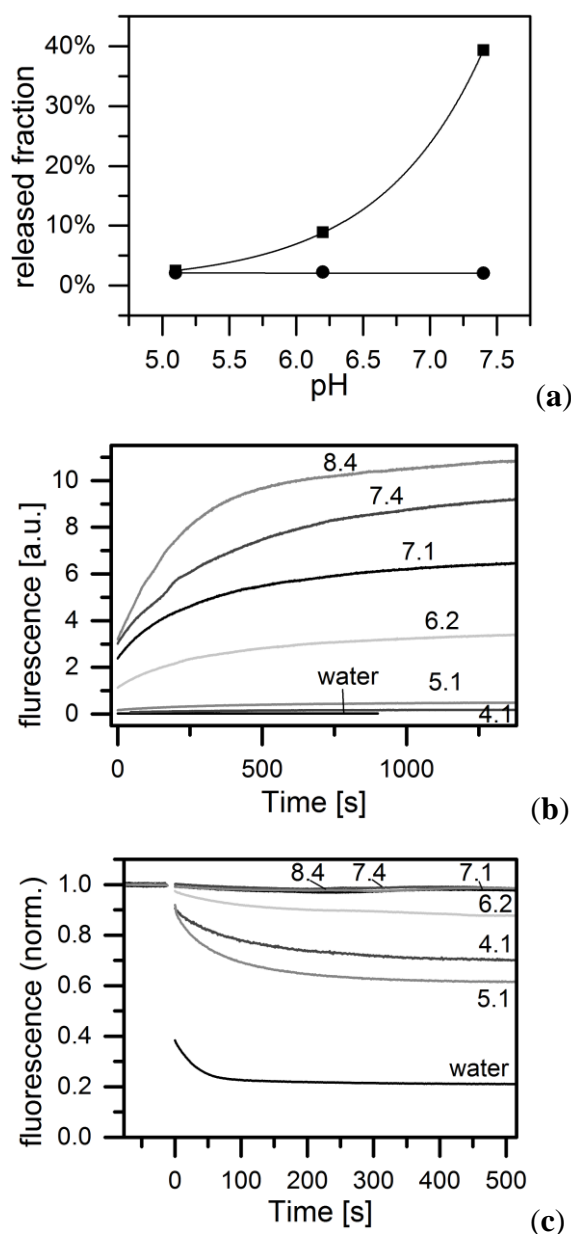

Figure 5-3. a) Fraction of fluorescein released from prefilled MOF-NPs after 90 min in buffer (HBG) at different pH, determined by absorption measurements of supernatant containing free fluorescein. While MIL-101(Cr) (circles) shows almost no (<3%) release of fluorescein at any pH tested, for MIL-100(Fe) (squares) we observed a significant increase in release with rising pH (exponential fit to guide the eye). b) Fluorescence quenching over the time course of release. MIL-100(Fe) nanoparticles filled with fluorescein were suspended in HBG buffered at different pHs. In water there is no increase in fluorescence intensity over time, indicating that there is no release. c) Fluorescence quenching in the time course of loading. Fluorescein solution in HBG buffer at different pH and in water before and after addition of MIL-100(Fe) nanoparticles. In water the loading is the fastest and most efficient. In HBG at pH 4.1 to 6.2 it is slower and less efficient while at pH 7.1 to 8.4 no loading is observed at all.

We next addressed the questions of whether the entire payload can be released by reducing the external concentration of fluorescein, and whether this occurs on a reasonable timescale. To investigate offloading we measure the amounts of fluorescein molecules released by both types of MOF-NPs. To this end, MOF-NPs filled with fluorescein were resuspended in HBG buffer (20 mM HEPES + 5% glucose) at the physiologically relevant pH values of 5.1 (late

endosome) , 6.2 (early endosome) and 7.4 (blood)[52]. After 90 min, particles were removed by centrifugation and the absorbance of the supernatant was measured via UV/VIS (Figure 5-3). As a reference for 100% release the absorbance of fluorescein solutions prepared in HBG at the same pH and concentration as the test solutions were used. In the case of MIL-101(Cr), almost no release (<3%) is observed within 90 min, while for MIL-100(Fe) the amount of released fluorescein increased with rising pH from below 3% at pH 5.1 to about 40% at pH 7.4. Thus it appears that fluorescein binding to MIL-101(Cr) is essentially irreversible under our conditions, or at least exhibits very extremely long off-times.

The pH-dependent release from MIL-100(Fe) deserves further attention. We used time-resolved fluorescence measurements to determine the kinetics of MIL-100(Fe) loading and release, making use of the fluorescence quenching effect observed when fluorescein molecules bind to the porous scaffold of MIL-100(Fe) NPs. Since MIL-101(Cr) does not exhibit this quenching effect, this assay cannot be used on these NPs. Prefilled MIL-100(Fe) NPs were centrifuged and the remaining supernatant was removed. Then the fluorescein-loaded MIL-100(Fe) NPs were re-suspended in HBG buffer at various pH values (pH= 4.1, 5.1, 6.2, 7.1, 7.4 and 8.4). Subsequently, the fluorescence signal originating from the fluorescein released from the MIL-100(Fe) NPs was recorded over time (see Figure 5-3b). The fluorescence signal at late time points increases with increasing pH, although the total amount of fluorescence released is more or less the same at all pHs tested, as can be seen when the fluorescence yield at the respective pH is taken into account. However, no rise in the fluorescence signal is seen in (unbuffered) water, indicating that no release occurs at all at the low pH of the suspension. When the fluorescence intensity after release into buffered medium was compared with that of the supernatant recovered after loading, it emerged that almost all of the fluorescein bound by the NPs is released again. When considering the release time traces in buffer with respect to the *rates* of fluorescein release, it is useful to normalize the data to the final fluorescence signal as shown in SI. Apart from the measurement at pH 8.4, all release curves end up stacked on top of each other, indicating that the temporal characteristics of cargo release are the same for all pH values.

These results require a detailed look at the on-loading kinetic. Loading was monitored by measuring the fluorescence of a 2-ml aliquot of dilute (0.1 µM) fluorescein solution from the moment a small amount (10 µg) of MIL-100(Fe) NPs was mixed into the solution. This was done for fluorescein dissolved in water and in HBG buffered at pH values of 4.1, 5.1, 6.2, 7.1, 7.4 and 8.4. The fluorescence of the solution was measured over time and normalized with respect to the fluorescence signal of the respective starting fluorescein solution without MOF-

NPs (Figure 5-3c). This signal shows a significant decrease over time, which is interpreted as reflecting the decreasing amount of fluorescein remaining in solution due to uptake (and fluorescence quenching) by the MOF-NPs. Inspection of the normalized fluorescence signal after >400 s of loading time reveals a clear trend: In the case of distilled water (MilliQ), the fluorescence drops to $\approx 20\%$ of the signal prior to NP addition. The drop is less obvious when loading is carried out in buffer (at all tested pHs from 4.1 to 8.4). In the latter case, however, a strong pH dependence is found: The initial level of fluorescence declines by about 35% at pH 4.1, the corresponding value at pH 6.1 is 14%, and no detectable change in fluorescence is observed at pH>7. We therefore assume there is no uptake into the NPs under alkaline conditions, and no quenching of fluorescein. Thus we find a clear dependence of the loading rate upon the pH, as revealed by the rate of decay of the fluorescence signal. To quantify this, we fitted an exponential decay to the data for the kinetics of loading (see SI). The resultant loading times are shown in Table 5-1. While loading takes place very rapidly in water, uptake rates in buffer fall with rising pH, and no loading can be quantified at pH 7.1 or higher.

Table 5-1. Results obtained from single exponential decay fitting of loading kinetics in water and HBG buffer at pH 4.1 to 8.4. While the loading process is very fast in water, in buffers with defined pH values rates of loading fall with rising pH, and no loading is detectable at pH 7.1 or higher.

pH	Rates of decay $[10^{-3}\ s^{-1}]$ (from exponential fit)	Characteristic time scales [s]
Water	13 ± 10	$74.5 \pm$
4.1	10 ± 4	$103.6 \pm$
5.1	10 ± 2	$98.5 \pm$
6.2	6 ± 2	$169.9\pm$
7.1	—	
7.4	—	
8.4	—	

5. Kinetic analysis of the uptake and release of fluorescein by metal-organic framework nanoparticles

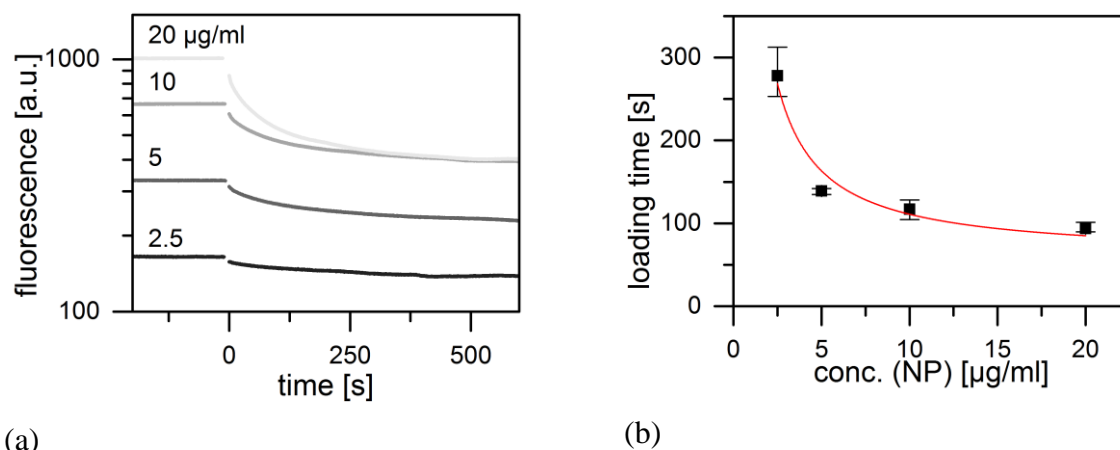(a)   (b)

Figure 5-4. Fluorescence quenching in the time course of loading at various MIL-100(Fe) NP concentrations in HBG (pH 5.1) at fixed fluorescein to NP ratios. (a): Kinetics of the decay of fluorescein fluorescence after addition of NPs at time=0. Time traces were fitted with single exponential decay. (b): The resulting loading times (in black) show a characteristic concentration dependency. This fits well with a model (red) involving a three-step process: free external diffusion, internal diffusion within the lattice and adsorption to the MOF network.

Next we asked whether the observed loading kinetics can be understood as a reaction-limited diffusion process. To this end, we studied the time course of the change in the fluorescein signal during uptake by MIL-100(Fe) at various NP concentrations but constant fluorescein/NP ratio. In this way, the average distance a fluorescein molecule has to diffuse before reaching the NP surface is varied. Experiments were carried out at constant pH of 5.1. The fluorescence time courses decay exponentially for all concentrations, as shown in Figure 5-4a. As before, we assume that fluorescein is quenched during adsorption to the internal MOF surface, and hence that the fluorescence decay is a measure for the rate of loading. Data were fitted by single exponentials and the derived characteristic loading times were plotted as a function of NP concentration (Figure 5-4b). If the loading is dominated by diffusion of molecules from the bulk phase to the MOF surface, we can calculate the on-kinetics and compare the result to the data in Figure 5-4b. The expected time for diffusion to NP surfaces is estimated assuming that, for each NP, molecules are recruited from a spherical volume with a radius equal to half the average NP-NP distance. Diffusion of molecules in a spherical volume with radius R to a spherical absorber with radius r, in the center of that volume is described by the theory of Adam and Delbrück[53]. As further explicated in the SI we derive an estimate for the spherical radius R from the NP concentration. With this we obtain a typical diffusion-limited time for the capture of fluorescein (see also SI):

$$\tau_{diff}(c_{\text{NP}}) \approx \frac{\pi \, r^2 \, \rho}{18 \, c_{NP} \, D}$$

where D is the diffusion coefficient of fluorescein, r the NP radius, ρ the NP mass density in mg/cm^3 and c_{NP} the NP concentration in mg/cm^3. Hence the external diffusion time is predicted to decay in proportion to c_{NP}^{-1}. The experimental loading times follow this prediction, as shown in Figure 5-4. The unbroken curve represents a fit to $A \cdot c_{NP}^{-1} + \tau_0$. The prefactor, A, is in good agreement with the time predicted assuming an effective density of $\rho = 2mg/cm^3$ for the MOF-NPs (see also SI). However, there remains a finite loading time offset, τ_0, even at high NP concentrations, when diffusion time to the target becomes negligible. The latter offset time subsumes all internal processes that occur subsequently to diffusive transport to the NP, including internal (possibly retarded) diffusion through the porous lattice, sorption to the internal surface and possibly surface rearrangements. A schematic representation of the molecular transport processes during loading is depicted in Figure 5-5. If we consider a typical NP diameter to be of the order of 50 nm and assume that internal diffusion rates are 10,000 times slower than in water, we reach an additional delay time of the order of 1 ms. By comparison, the observed offset time, $\tau_0 \approx 60 \ s$, is surprisingly long. A possible explanation is based on the assumption that slow relaxation processes take place in the adsorbed internal monolayer of fluorescein.
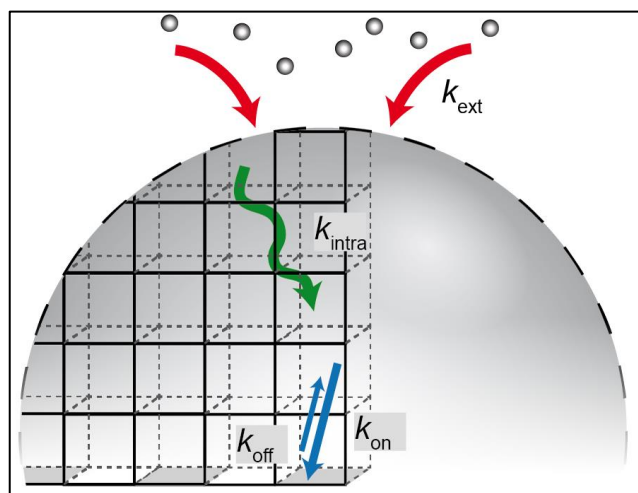

Figure 5-5. Illustration of the loading process: diffusion of external fluorescein molecules into the nanoparticles, as described by the Adam& Delbrück model. This is followed by internal diffusion within the lattice and adsorption to the internal surface of the MOF NP.

5.3. Conclusion

In summary, we have studied the loading (release) of a model guest molecule (fluorescein) into (from) porous MOF-NPs. We found for both studied NP types, MIL-100(Fe) and MIL-101(Cr), that significant amounts of fluorescein can be adsorbed at room temperature. The measured loading capacities, in the range of $>10^3$ molecules per NP, are compatible with the measured internal surface area available. The loading rate in the case of MIL-100(Fe) is found to be dependent on the pH and the solvent (water or HBG). Our studies show that optimal loading of fluorescein is achieved in MilliQ water, and no release from the NPs is detected in this case. Unlike loading, however, the pH dependence of payload release varies between the two types of NPs studied. Virtually no release from MIL-101(Cr) occurs at any of the pH values tested, whereas MIL-100(Fe) NPs release between 3% (at pH 5.1) and about 40% (at pH 7.4) of their adsorbed fluorescein. These findings suggest that the MOF scaffold can confine the guest molecule inside its pores through electrostatic interactions. Considering the versatile MOF chemistry as well as the different ways how to functionalize a MOF scaffold encompass a controlling of the MOF host-guest interactions.

Thus MOF nanocarriers are good candidates for drug delivery and other applications where a high payload is desirable. In addition, MIL-100(Fe) shows release characteristics that can be tuned via pH. The latter result demonstrates that controlled release from MOF-NPs can be detected when loading and offloading of payload molecules by these nanocarriers are characterized. This information is vital for clinical applications as a possible drug delivery system. However, only a small number of relevant drugs exhibit optical fluorescence or optical adsorption changes that can be exploited for time-resolved release studies. Thus, there remains a need for alternative characterization methods to assess loading and release behavior, and to optimize MOF nanocarriers for regulated drug delivery using refined chemical functionalization.

5.4. Materials and Methods

Chemicals: Chromium(III) nitrate nonahydrate (99%, *Aldrich*), terephthalic acid (98%, *Aldrich*), ethanol (99%, *Aldrich*) Iron (III) chloride hexahydrate (Grüssing GmbH), trimesic acid (BTC, Aldrich).

Synthesis of MIL-101(Cr) nanoparticles: The microwave synthesis of MIL-101(Cr) nanoparticles was based on a modified procedure reported in the literature.[1] An amount of 20 mL (1.11 mol) of H_2O was added to 615 mg (3.70 mmol) terephthalic acid and 1.48 g $Cr(NO_3)_3 \cdot 9\,H_2O$ (3.70 mmol). This mixture was put into a Teflon tube, sealed and placed in the microwave reactor (Microwave, Synthos, Anton Paar). Four tubes were filled and inserted into the reactor: one tube contained the reaction mixtures described above; the remaining tubes including the reference tube with the pressure/temperature sensor (PT sensor) were filled with 20 mL H_2O. For the synthesis, a temperature programme was applied with a ramp of 4 min to 180 °C and a holding time of 2 min at 180 °C. After the sample had cooled down to room temperature, it was filtrated and washed with 50 ml EtOH to remove residual e.g. terephthalic acid. For purification, the filtrate was centrifuged and redispersed in 50 ml EtOH three times. The sample was centrifuged at 20000 rpm (47808 rcf) for 60 min.

Synthesis of MIL-100(Fe) nanoparticles: For the microwave synthesis of MIL-100 (Fe) nanoparticles, iron(III) chloride hexahydrate (2.43 g, 9.00 mmol) and trimesic acid (0.84 g, 4.00 mmol) in 30 ml H_2O were put into a Teflon tube, sealed and placed in the microwave reactor (Microwave, Synthos, Anton Paar).[1] The mixture was heated to 130 °C under solvothermal conditions (p = 2.5 bar) within 30 seconds, kept at 130 °C for 4 minutes and 30 seconds and the tube was cooled down to room temperature. For the purification of the solid, the reaction mixture was centrifuged (20000 rpm = 47808 rcf, 20 min), the solvent was removed and the pellet was redispersed in 50 ml EtOH. This cycle was repeated two times and the dispersed solid was allowed to sediment overnight. The supernatant of the sedimented suspension was filtrated (filter discs grade: 391, Sartorius Stedim Biotech) three times, yielding MIL-100(Fe) nanoparticles.

Equilibrium measurements: Payload capacity was measured using an UV/VIS absorption spectrometer (NanoDrop 1000, Thermo Scientific). MOF-NPs (1 mg) in ethanol stock solution were centrifuged (45 min at 14,680 rpm, 20,238×*g*) to remove the supernatant ethanol. The pellet of MOF NPs was then dispersed in an aqueous dilution series of

fluorescein sodium salt (Sigma-Aldrich) by vortexing and sonication (Sonorex) and incubated for 96 h under continuous agitation in a tube rotator. The suspensions were then centrifuged as before to obtain the supernatant fluorescein solution. The absorption spectra of the supernatant, as well as that of the original fluorescein solution, were measured and the area under the curve between 400 to 550 nm, hereinafter denoted as absorbance (see SI), was determined (OriginPro 9 64Bit). This procedure was performed for a concentration series of fluorescein solutions ranging from 5 µg/ml to 1500 µg/ml. A straight line $A = m\,c + t$ was fitted to the integrated absorbance of the original fluorescein solution concentration series, where A is the measured absorbance and c the concentration of the original fluorescein solution (inset in Fig S5-4b).

To determine the amount of fluorescein released, 1 mg of MOF-NPs was first loaded with the compound by suspension in 1 ml of an aqueous solution (100 µg/ml) of fluorescein and incubated for 1 day on a rotary shaker at room temperature. Subsequently the nanoparticles were transferred into 1-ml aliquots of freshly prepared HBG buffer at pH 5.1, 6.2 and 7.4 by centrifugation (15/45 min at 20,238×g), removal of the supernatant and resuspension in buffer. This was followed by 90-min incubation on the rotary shaker at room temperature. After final removal of the nanoparticles by centrifugation for 45 min as before, the absorption spectrum of the supernatant was measured. As a reference for 100% release, the absorption spectra of 100 µg/ml solutions of fluorescein in HBG buffered at pH 5.1, 6.2 and 7.4 were also obtained. The spectra were integrated over the range between 400 and 550 nm (OriginPro 9 64Bit) and the resulting absorbance of the released fluorescein solutions was compared with the reference absorbance at the same pH.

Kinetics of loading/release

Loading: For each measurement, a 2-ml aliquot of fluorescein solution (0.1 µg/ml ≈ 0.24 µmol), made up in water or HBG at pH 4.1, 5.1, 6.2, 7.1, 7.4 or 8.4, was filled into a polystyrene cuvette. The fluorescence signal (divided by the instrument's lamp reference to correct for fluctuations in lamp brightness) emitted upon excitation at 492 nm (slit width, 3 nm) was recorded for at least 60 s in a Fluorolog 3 spectrometer (Horiba, Japan) at 512 nm. Then 2 µl of MIL-100(Fe) suspension (=10 µg) in aqueous ethanol (5 mg/ml) was quickly pipetted into the cuvette and mixed, and the instrument cover was closed again (denoted as t=0s). The fluorescence signal was then monitored over the course of at least 500 s.

Release: For each measurement, 50-µg samples of NPs that had been incubated in 0.5 µg/ml fluorescein were recovered by centrifugation (for 15 min, as above), and the supernatant was

discarded. The pellet was then re-suspended in 10 ml of water or HBG (buffered at one or other of the pH values mentioned above) by sonication (see above), and a 2-ml portion was rapidly transferred to a cuvette and the fluorescence signal was measured for at least 700 s as described above.

Sorption measurements (BET): Nitrogen sorption isotherms were measured at 77°K with a Quantachrome NOVA 4000e. Approximately 20 mg of nanoparticles was degassed at 150°C in high vacuum for at least 12 h prior to measurement. Evaluation of the sorption data was carried out using ASiQwin^{TM} software (Version 2.0, Quantachrome Instruments). BET surface areas were calculated with the linearized form of the BET equation. For all samples the correlation coefficient was higher than 0.999. Adsorption isotherms were used to calculate the pore size distribution by quenched-solid density functional theory (QSDFT, N_2 at 77 K on carbon, cylindrical/spherical pores adsorption branch).

Transmission Electron Microscopy (TEM): For TEM analysis 10 µl aliquots of ethanolic MOF-NP suspension were dried on 300 mesh Formvar/carbon copper grids (Ted Pella USA). Pictures of MOF NPs on grids were obtained on a JEM 1011 (JEOL, Tokyo, Japan) at an acceleration voltage of 80 kV.

X-ray diffraction (XRD): For XRD measurements, approx. 1 mg of the powdered material was distributed homogeneously between two acetate foils (ultraphan) with a thickness of 0.014 mm and fixed in the sample holder. The samples were the measured with the STOE transmission diffractometer system Stadi MP with Cu Kα1 radiation ($\lambda = 1.54060$ Å) and a Ge(111) single-crystal monochromator. Diffraction patterns were recorded with a DECTRIS solid-state strip detector MYTHEN 1K in omega-2-theta scan mode using a step size of 4.71° and a counting time of 80 s per step.

Dynamic light scattering (DLS) and zeta-potential measurements: DLS and zeta-potential measurements of the particles in dispersion (approx. 0.1 mg/mL) were carried out using a Malvern Zetasizer (Nano Series, Nano-ZS). For measurements of the pH dependence of the zeta-potential, the instrument was equipped with a Malvern Multi-Purpose Titrator (MPT-2). A 10-mL aqueous suspension of nanoparticles (0.1 mg/mL) was set to the starting pH with HCl (0.1 M) and titrated in steps of 0.5 pH units with NaOH (0.01 or 0.1 M, respectively) up to the final pH value

5.5. References

[1]   Zhou, H. C.; Long, J. R.; Yaghi, O. M.; *Chem. Rev.* **2012**, *112*, 673–674.

[2]   Zhou, H.-C.; Kitagawa, S.; *Chem. Soc. Rev.* **2014**, *43*, 5415–5418.

[3]   Férey, G.; *Chem. Soc. Rev.* **2008**, *37*, 191–214.

[4]   Inokuma, Y.; Yoshioka, S.; Ariyoshi, J.; Arai, T.; Hitora, Y.; Takada, K.; Matsunaga, S.; Rissanen, K.; Fujita, M.; *Nature* **2013**, *495*, 461–466.

[5]   Furukawa, H.; Cordova, K.; O'Keeffe, M.; Yaghi, O. M.; *Science (80-.).* **2013**, *341*, 974–990.

[6]   He, Y.; Zhou, W.; Qian, G.; Chen, B.; *Chem. Soc. Rev.* **2014**, *43*, 5657–5678.

[7]   Van de Voorde, B.; Bueken, B.; Denayer, J.; De Vos, D.; *Chem. Soc. Rev.* **2014**, *43*, 5766–5788.

[8]   Corma, A.; García, H.; Llabrés i Xamena, F. X.; *Chem. Rev.* **2010**, *110*, 4606–4655.

[9]   Dhakshinamoorthy, A.; Garcia, H.; *Chem. Soc. Rev. Chem. Soc. Rev* **2014**, *5750*, 5750–5765.

[10]   Lee, J.; Farha, O. K.; Roberts, J.; Scheidt, K. A.; Nguyen, S. T.; Hupp, J. T.; *Chem Soc Rev* **2009**, *38*, 1450–1459.

[11]   Kreno, L. E.; Leong, K.; Farha, O. K.; Allendorf, M.; Van Duyne, R. P.; Hupp, J. T.; *Chem. Rev.* **2012**, *112*, 1105–1125.

[12]   Falcaro, P.; Ricco, R.; Doherty, C. M.; Liang, K.; Hill, A. J.; Styles, M. J.; *Chem. Soc. Rev.* **2014**, *43*, 5513–5560.

[13]   Stavila, V.; Talin, A. A.; Allendorf, M. D.; *Chem. Soc. Rev.* **2014**, *43*, 5994–6010.

[14]   Horcajada, P.; Gref, R.; Baati, T.; Allan, P. K.; Maurin, G.; Couvreur, P.; Férey, G.; Morris, R. E.; Serre, C.; *Chem. Rev.* **2012**, *112*, 1232–1268.

[15]   Giménez-Marqués, M.; Hidalgo, T.; Serre, C.; Horcajada, P.; *Coordination Chemistry Reviews*, 2015, *307*, 342–360.

[16]   He, C.; Liu, D.; Lin, W.; *Chem. Rev.* **2015**, *115*, 11079–11108.

[17]   Lee, S.; Kapustin, E. A.; Yaghi, O. M.; *Science (80-.).* **2016**, *353*.

[18]   Rungtaweevoranit, B.; Zhao, Y.; Choi, K. M.; Yaghi, O. M.; *Nano Res.* **2016**, *9*, 47–58.

[19]   Furukawa, S.; Reboul, J.; Diring, S.; Sumida, K.; Kitagawa, S.; *Chem. Soc. Rev.* **2014**, *43*, 5700–5734.

[20]   McGuire, C. V.; Forgan, R. S.; *Chem. Commun.* **2015**, *51*, 5199–5217.

[21]   Kundu, T.; Mitra, S.; Patra, P.; Goswami, A.; Díaz Díaz, D.; Banerjee, R.; *Chem. - A Eur. J.* **2014**, *20*, 10514–10518.

[22]   Huxford, R. C.; Della Rocca, J.; Lin, W.; *Curr. Opin. Chem. Biol.* **2010**, *14*, 262–268.

[23]   Wang, J.; Jin, J.; Li, F.; Li, B.; Liu, J.; Jin, J.; Wang, C.; Zeng, Y.; Wang, Y.; *RCS Adv.* **2015**, *5*, 85606–85612.

[24]   Bernini, M. C.; Fairen-Jimenez, D.; Pasinetti, M.; Ramirez-Pastor, A. J.; Snurr, R. Q.; *J. Mater. Chem. B* **2014**, *2*, 766–774.

[25]   Horcajada, P.; Chalati, T.; Serre, C.; Gillet, B.; Sebrie, C.; Baati, T.; Eubank, J. F.; Heurtaux, D.; Clayette, P.; Kreuz, C.; Chang, J.-S.; Hwang, Y. K.; Marsaud, V.; Bories, P.-N.; Cynober, L.; Gil, S.; Ferey, G.; Couvreur, P.; Gref, R.; *Nat. Mater.* **2010**, *9*, 172–178.

[26]   Horcajada, P.; Surblé, S.; Serre, C.; Hong, D.-Y.; Seo, Y.-K.; Chang, J.-S.; Grenèche, J.-M.; Margiolaki, I.; Férey, G.; *Chem. Commun.* **2007**, *100*, 2820–2822.

[27]   Férey, G.; Mellot-Draznieks, C.; Serre, C.; Millange, F.; Dutour, J.; Surblé, S.; Margiolaki, I.; *Science (80-.).* **2005**, *309*, 2040–2042.

[28]   Llewellyn, P. L.; Bourrelly, S.; Serre, C.; Vimont, A.; Daturi, M.; Hamon, L.; De Weireld, G.; Chang, J. S.; Hong, D.-Y.; Hwang, Y. K.; *et al.*; *Langmuir* **2008**, *24*, 7245–7250.

[29]   Walton, K. S.; Snurr, R. Q.; *J. Am. Chem. Soc.* **2007**, *129*, 8552–8556.

[30]   Jhung, S. H.; Lee, J. H.; Yoon, J. W.; Serre, C.; Férey, G.; Chang, J. S.; *Adv. Mater.* **2007**, *19*, 121–124.

[31]   García Márquez, A.; Demessence, A.; Platero-Prats, A. E.; Heurtaux, D.; Horcajada, P.; Serre, C.; Chang, J. S.; Férey, G.; De La Peña-O'Shea, V. A.; Boissière, C.; *et al.*; *Eur. J. Inorg. Chem.* **2012**, *100*, 5165–5174.

[32]   Zimpel, A.; Preiß, T.; Röder, R.; Engelke, H.; Ingrisch, M.; Peller, M.; Rädler, J. O.; Wagner, E.; Bein, T.; Lächelt, U.; Wuttke, S.; *Chem. Mater.* **2016**, *28*, 3318–3326.

[33]   Kim, B.; Han, G.; Toley, B. J.; Kim, C.; Rotello, V. M.; Forbes, N. S.; *Nat. Nanotechnol.* **2010**, *5*, 465–472.

[34]   Andersson, J.; Rosenholm, J.; Areva, S.; Lindén, M.; *Chem. Mater.* **2004**, *16*, 4160–4167.

[35]   Goesmann, H.; Feldmann, C.; *Angew. Chemie* **2010**, *49*, 1362–1395.

[36]   Mura, S.; Nicolas, J.; Couvreur, P.; *Nat. Mater.* **2013**, *12*, 991–1003.

[37]   Farokhzad, O. C.; Langer, R.; *ACS Nano* **2009**, *3*, 16–20.

[38]   Li, Z.; Barnes, J. C.; Bosoy, A.; Stoddart, J. F. F.; Zink, J. I.; *Chem. Soc. Rev.* **2012**, *41*, 2590–2605.

[39]   Chou, L. Y. T.; Ming, K.; Chan, W. C. W.; Smith, A. M.; Nie, S. M.; Eustis, S.; El-Sayed, M. A.; Lu, A. H.; Salabas, E. L.; Schuth, F.; *et al.*; *Chem. Soc. Rev.* **2011**, *40*, 233–245.

[40]   Zhao, Y.; Ren, W.; Zhong, T.; Zhang, S.; Huang, D.; Guo, Y.; Yao, X.; Wang, C.; Zhang, W.-Q.; Zhang, X.; *et al.*; *J. Control. Release* **2016**, *222*, 56–66.

[41]   Kamarudin, N. H. N.; Jalil, A. A.; Triwahyono, S.; Artika, V.; Salleh, N. F. M.; Karim, A. H.; Jaafar, N. F.; Sazegar, M. R.; Mukti, R. R.; Hameed, B. H.; *et al.*; *J. Colloid Interface Sci.* **2014**, *421*, 6–13.

[42]   Xiao, X.; Liu, Y.; Guo, M.; Fei, W.; Zheng, H.; Zhang, R.; Zhang, Y.; Wei, Y.; Zheng, G.; Li, F.; *J. Biomater. Appl.* **2016**, *0*, 1–13.

[43]   Zürner, A.; Kirstein, J.; Döblinger, M.; Bräuchle, C.; Bein, T.; *Nature* **2007**, *450*, 705–708.

[44]   Medved, I.; Cerny, R.; *Microporous Mesoporous Mater.* **2011**, *142*, 405–422.

[45]   Wuttke, S.; Braig, S.; Preiß, T.; Zimpel, A.; Sicklinger, J.; Bellomo, C.; Rädler, J. O.; Vollmar, A. M.; Bein, T.; *Chem. Commun.* **2015**, *51*, 15752–15755.

[46]   Hirschle, P.; Preiß, T.; Auras, F.; Pick, A.; Völkner, J.; Valdepérez, D.; Witte, G.; Parak, W. J.; Rädler, J. O.; Wuttke, S.; *CrystEngComm* **2016**, *18*, 4359–4368.

[47]   Sun, S.; *Science (80-.).* **2000**, *287*, 1989–1992.

[48]   Park, J.; Lee, E.; Hwang, N.-M.; Kang, M.; Kim, S. C.; Hwang, Y.; Park, J.-G.; Noh, H.-J.; Kim, J.-Y.; Park, J.-H.; *et al.*; *Angew. Chemie* **2005**, *44*, 2873–2877.

[49]   Anand, R.; Borghi, F.; Manoli, F.; Manet, I.; Agostoni, V.; Reschiglian, P.; Gref, R.; Monti, S.; *J. Phys. Chem. B* **2014**, *118*, 8532–8539.

[50]   Tay, C. Y.; Setyawati, M. I.; Xie, J.; Parak, W. J.; Leong, D. T.; *Adv. Funct. Mater.* **2014**, *24*, 5936–5955.

[51]   Agostoni, V.; Horcajada, P.; Noiray, M.; Malanga, M.; Aykaç, A.; Jicsinszky, L.; Vargas-Berenguel, A.; Semiramoth, N.; Daoud-Mahammed, S.; Nicolas, V.; *et al.*; *Sci. Rep.* **2015**, *5*, 7925-1–5.

[52]   Geisow, M. J.; Evans, W. H.; *Exp. Cell Res.* **1984**, *150*, 36–46.

[53]   Adam, G.; Delbrueck, M.; Reduction of Dimensionality in Biological Diffusive Processes. In *Structural Chemistry and Molecular Biology*; Rich, A.; Davidson, N., Eds.; Freeman, San Francisco, **1968**; pp. 198–215.

5.6. Appendix
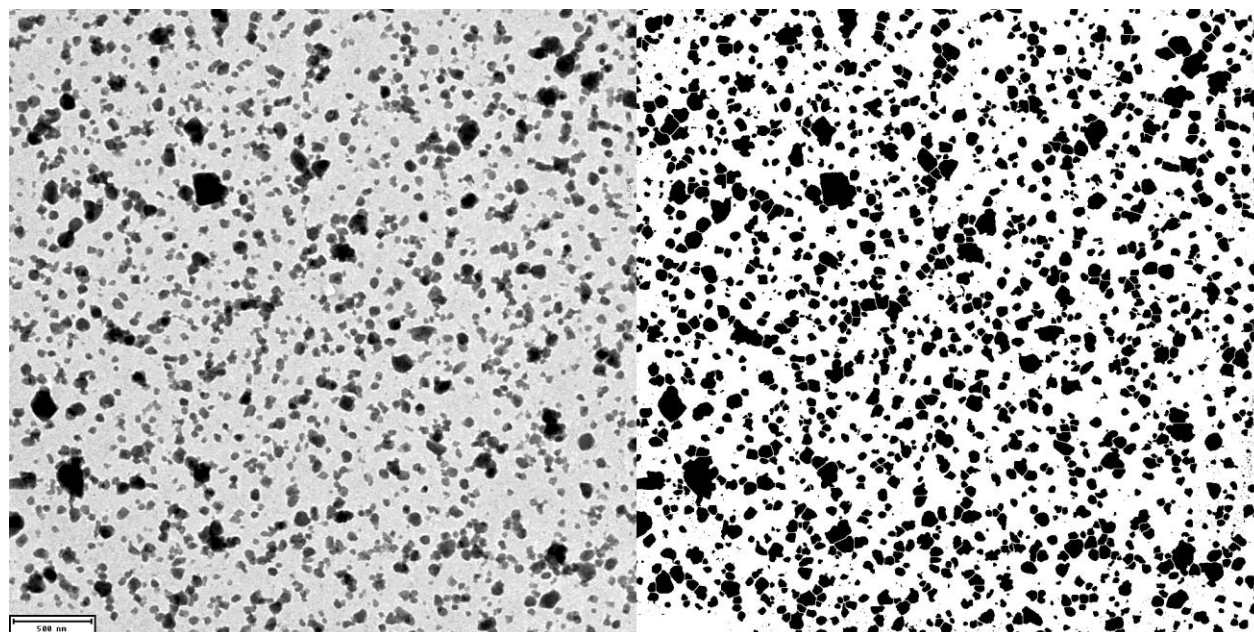
MIL-100(Fe)
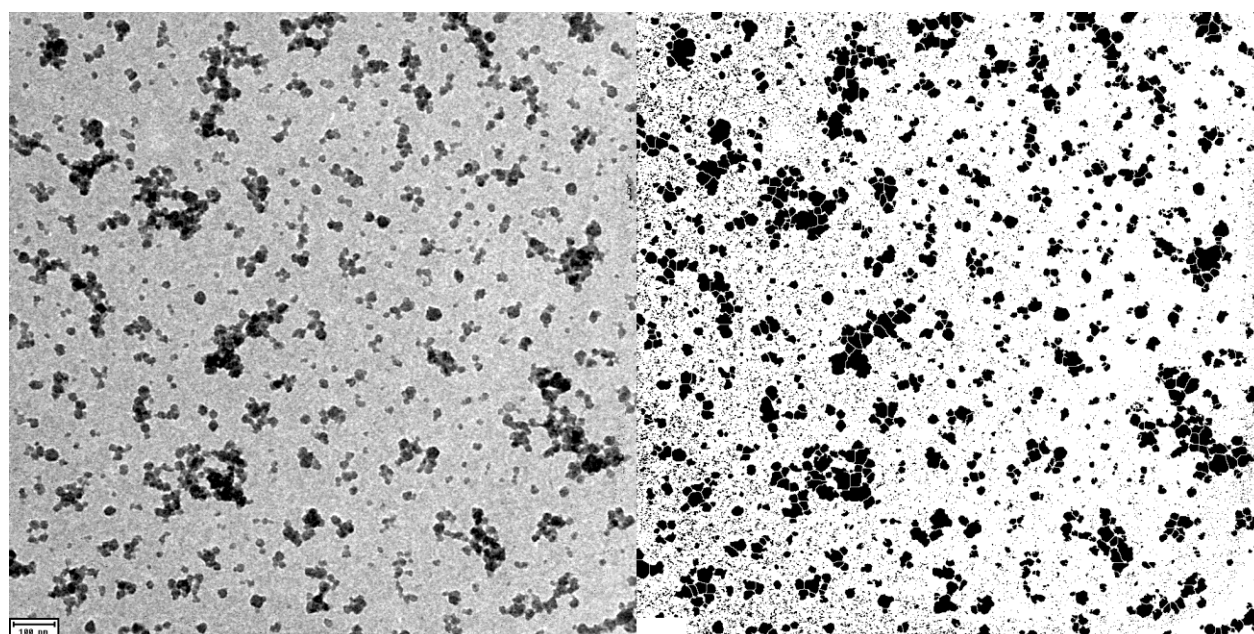
MIL-101(Cr)

Figure S5-1. Juxtaposition of exemplary original TEM image (left) and processed image used for particle analysis (right). Original TEM image was converted to binary image. By applying watershed filter, NP that are close together are separated by a thin white line for the subsequent particle analysis. The "analyse particles" function of ImageJ was used to determine the area of all particles larger than 5nm² (to get rid of background sparkles).
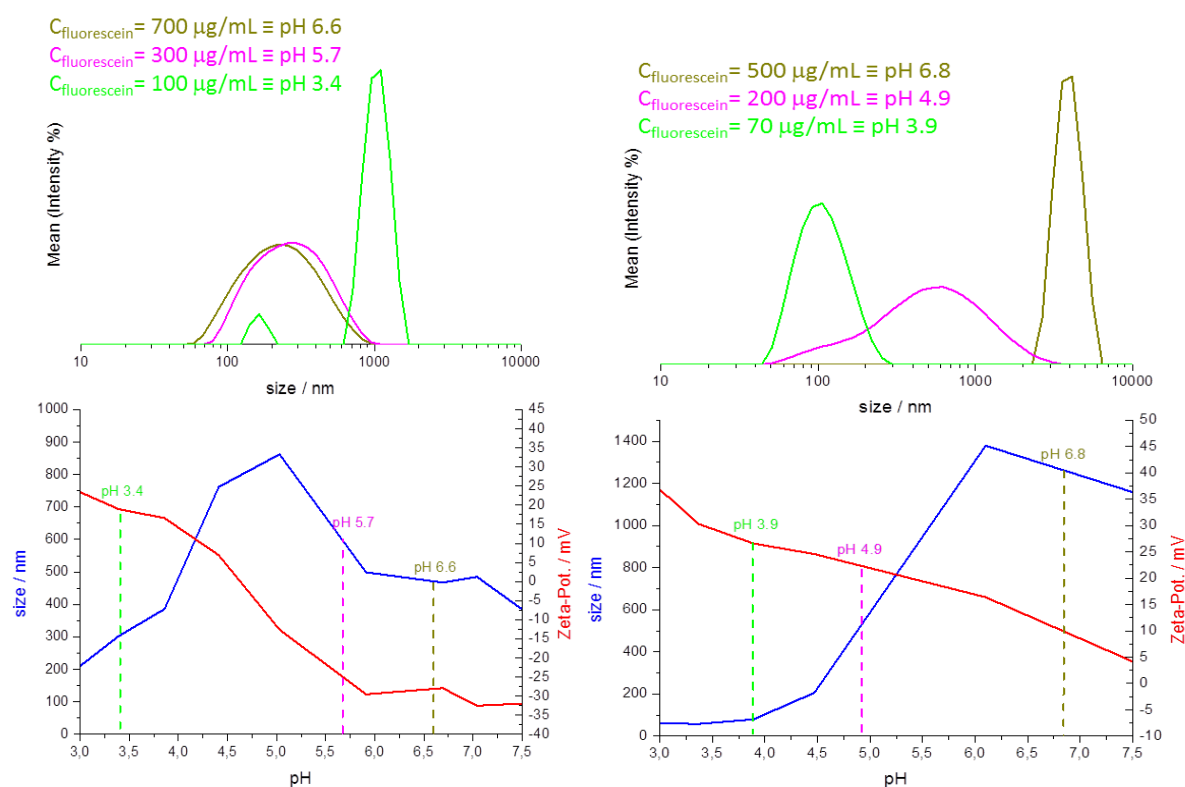
Figure S5-2. DLS (black) and Zeta-Potential (red) measurements at different pH in water.
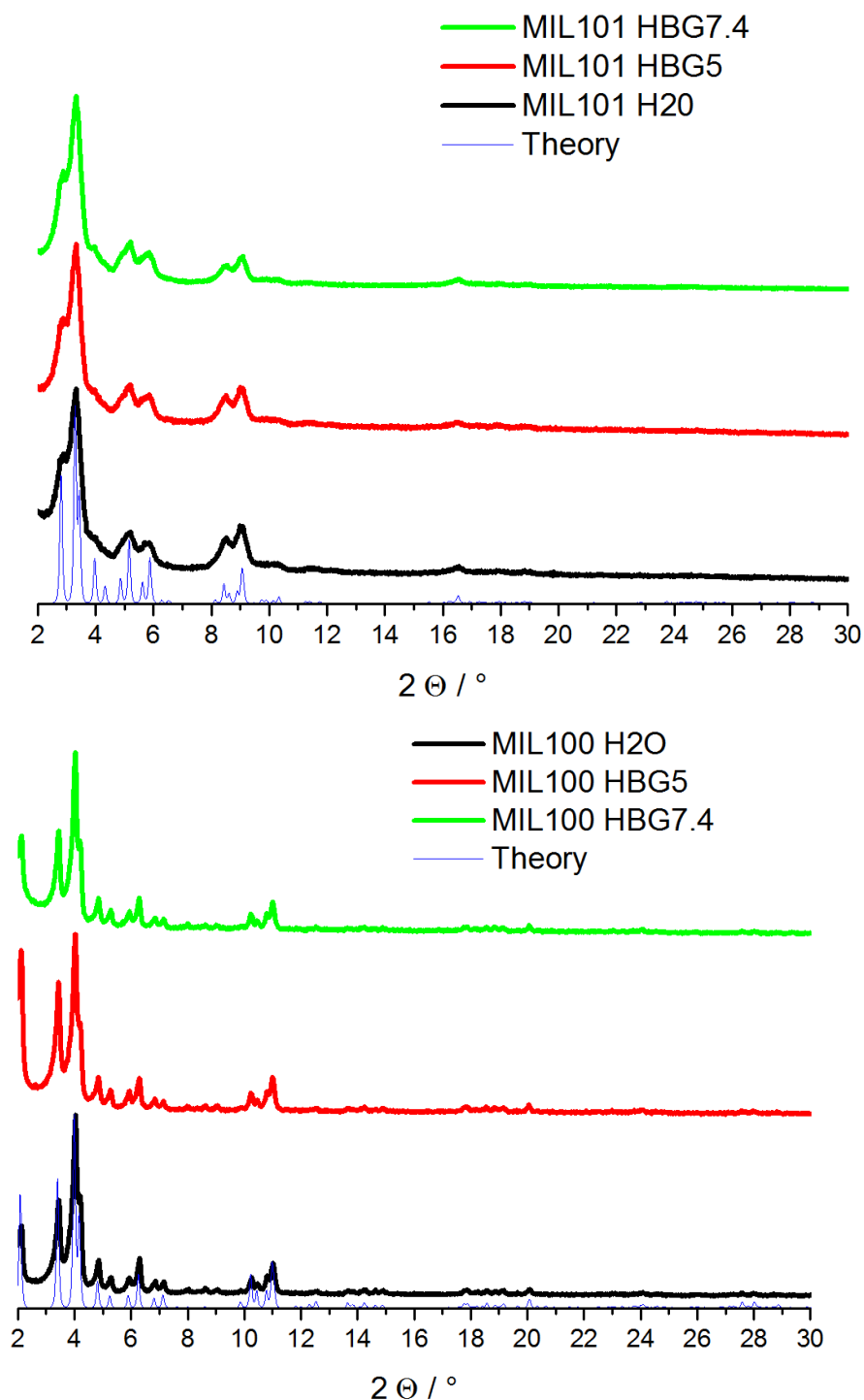
Figure S5-3. XRD measurements of NPs before (black) and after incubation in buffer (red: in HBG pH=5.0, green: in HBG pH=7.4) certifies crystallinity and stability of MOF structure.
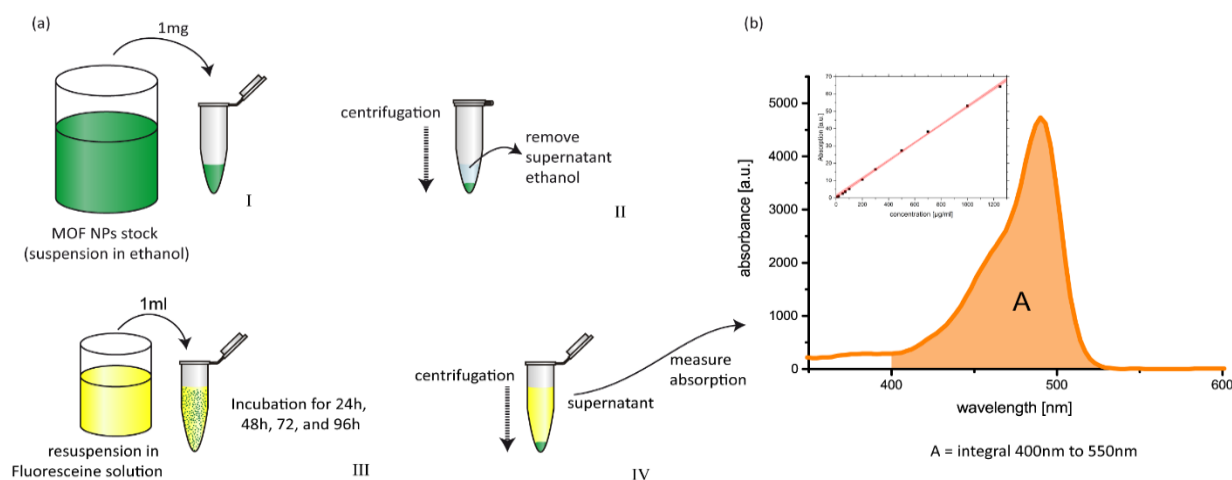
Figure S5-1. Assay for measuring the Payload capacity established, using UV/VIS absorption. Fluorescein solutions were used as calibration standard. a) Preparation and loading process: 1mg MOF NPs (I) were separated from ethanol (II), resuspended in fluorescein solutions of different concentrations and incubated for a certain time (III). For UV/VIS measurement the MOF NPs were separated from incubation solution (IV). b) The absorption spectra of the supernatant solution as well as the original fluorescein solution were measured and integrated within the limits of 400nm to 550nm to determine the remaining amount of fluorescein in the supernatant. Inset: Fluorescein calibration curve with linear fit.
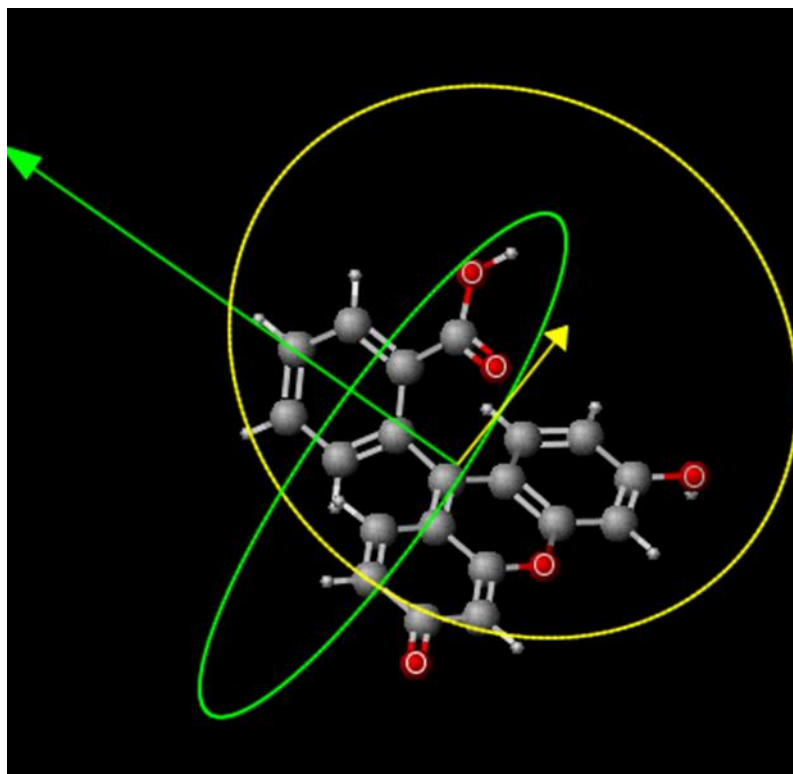
Figure S5-5. Structure of fluorescein molecule and its minimal and maximal projection area (MarvinSketch) max: radius = 6,27Å; min: radius =6,15Å. Arrows indicate surface normal.

5. Kinetic analysis of the uptake and release of fluorescein by metal-organic framework nanoparticles

Release kinetics in HBG Buffer:
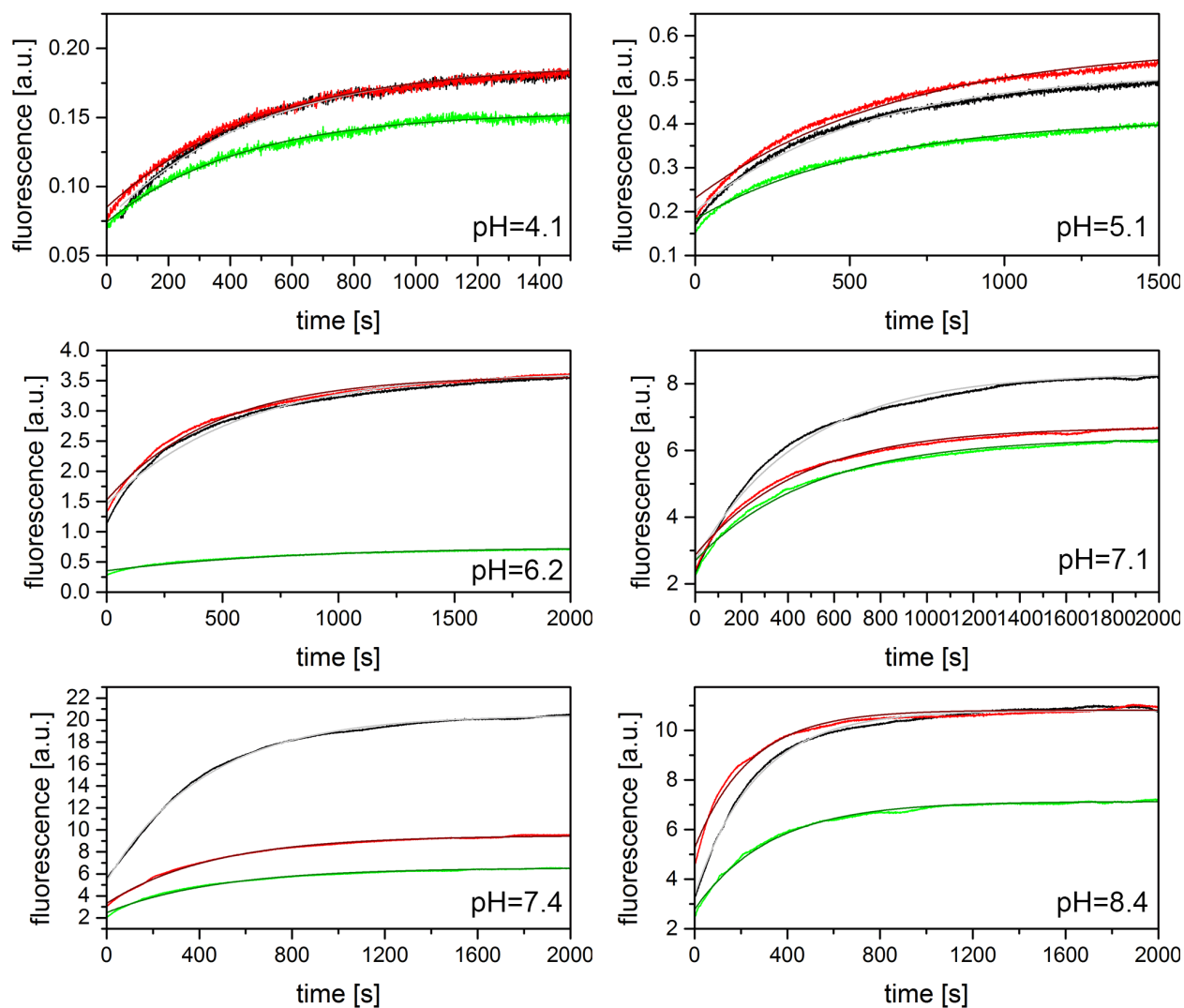
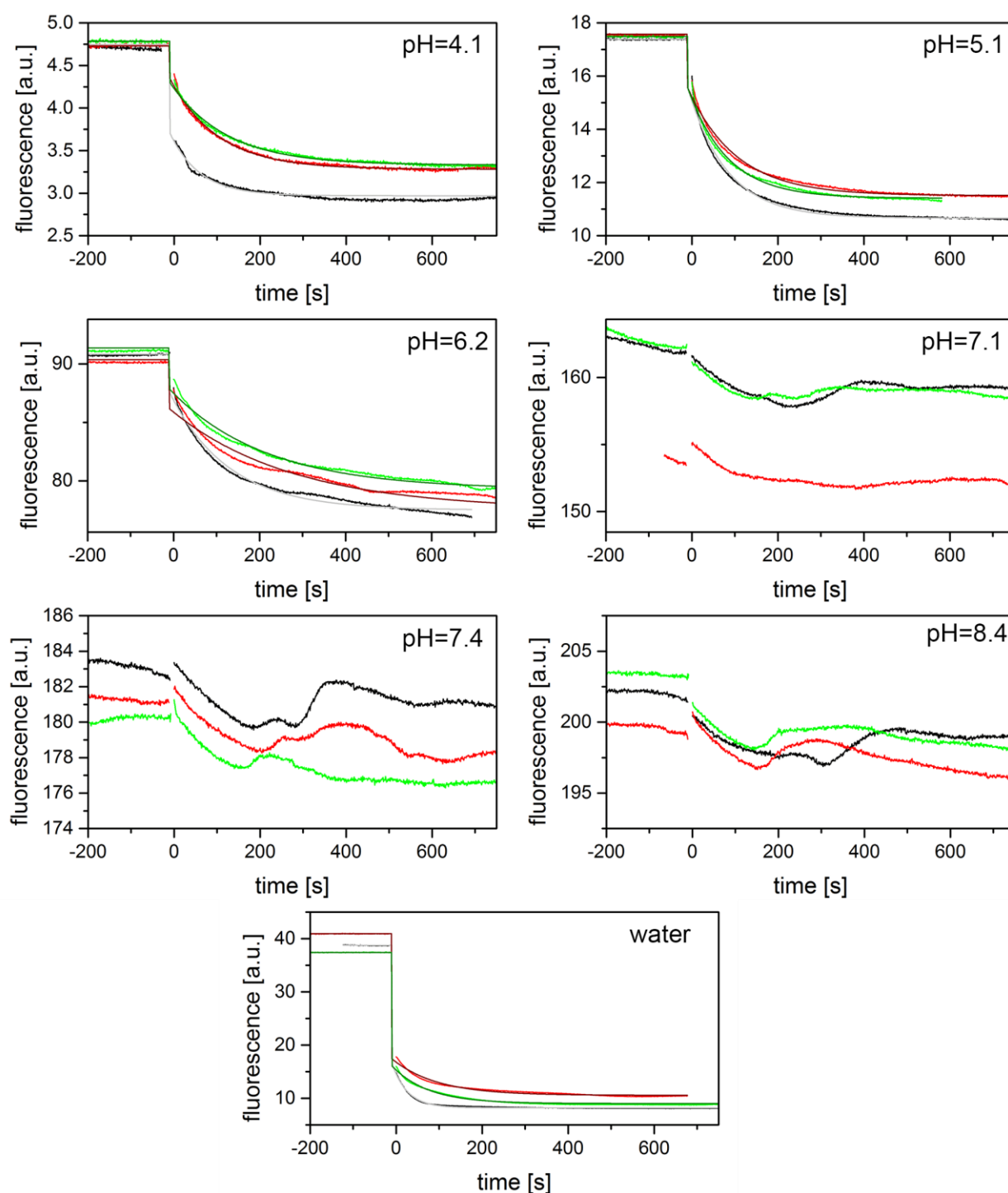**Figure S5-6.** Release kinetics of fluorescein in MIL-100(Fe) NPs in HBG at depicted pH.
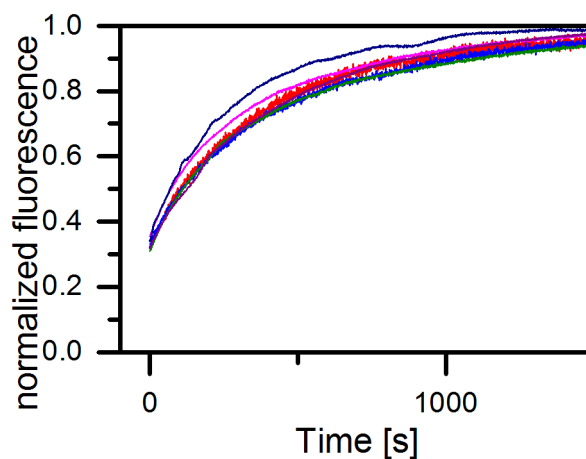
Figure S5-2. Release kinetic measurements normalized to its final signal

Loading kinetics:

Figure S5-8. Loading kinetics of fluorescein into MIL-100(Fe) NPs in HBG at depicted pH and in water.

Calculations

Particle density

To calculate the number of particles per mg we assume spherical particles (Volume $V = \frac{4}{3}\pi r^3$, with NP Radius r). The mass of one NP m_{NP} is then $m_{NP} = V \cdot \rho$ with the mass density ρ of the NP material. The number of particles N in 1mg is then $N = \frac{1\text{mg}}{m_{NP}}$. For MIL-100(Fe) nanoparticles we used a mean radius of $r_{MIL-100} = 26.5\ nm$ (obtained from TEM analysis) and a mass density of $\rho_{MIL100} = 0.98\ g/ml^2$. As a result we arrive at a mean mass per particle of $m_{MIL100} = 0.076$ fg and thus the number of $N_{MIL100} = 1.31 \cdot 10^{13}$ particles per milligramm of material. This corresponds to $n_{MIL100} = 21.7\ pmol$. Respectively for MIL-101(Cr) nanoparticles with $r_{MIL101} = 9.45\ nm$ and $\rho_{MIL101} = 0.62\ g/ml^3$ we derived a mean particle mass of $m_{MIL101} = 2.2\ ag$ and thus $N_{MIL101} = 4.56 \cdot 10^{14}$ particles per milligram ($n_{MIL100} = 0.76\ nmol$).

On-kinetics

To calculate the calculate the on-kinetics in a diffusion dominated process we adapt the theory of Adam and Delbrück[4]: The original formula for the mean time τ a molecule within a Volume with radius r needs to hit a sphere with radius R is $\tau = \frac{\left(1 - \frac{r}{R}\right)^2}{3\, r\, D} R^3$ with D, the diffusion coefficient of the diffusing molecules. This function was adapted to the system at hand: for r we used the particles radius we derived from DLS measurements at used pH 5.1 of 400nm, the diffusion coefficient for fluorescein was found to be 390µm²/s (FCS measurement), the radius R of the volume was determined by calculating the mean solution volume per particle from the overall Volume V and the containing number of nanoparticles N: $R^3 = \frac{V}{N} = \frac{M}{c\,N_A}$. where M is the molar mass of the nanoparticle, c the mass concentration and the Avogadro constant N_A. The molar Mass is derived by the volume of a sphere with the radius of one particle, its mass density ρ and the Avogadro constant: $M = \frac{4}{3}\pi r^3 \rho N_A$. This results in the following formula:

$$\tau(c_{NP}) = \frac{A \cdot 4\pi r^2 \rho}{72\, c_{NP}\, D}\left(1 - \frac{2}{\sqrt[3]{\frac{4\pi\rho}{c_{NP}}}}\right)^2 + \tau_0 \approx \frac{A \cdot \pi r^2 \rho}{18\, c_{NP}\, D} + \tau_0$$

.

Whereas an offset τ_0 was added to compensate for the internal diffusion through the lattice and sorbtion that is represented in Figure 5-5 by the sum of τ_{intra} and τ_{on}. Here we used the mass density $\rho = 2mg/cm^3$ that respects the filling of the nanoparticles with water (mass density of empty MOFs: 0.98mg/cm³ [2] + pore volume 1.030cm³/g [5] filled with water at 0.997mg/cm³ results in 2 mg/ml).

References

[1]   Wuttke, S.; Braig, S.; Preiß, T.; Zimpel, A.; Sicklinger, J.; Bellomo, C.; Rädler, J. O.; Vollmar, A. M.; Bein, T.; *Chem. Commun.* **2015**, *51*, 15752–15755.

[2]   Horcajada, P.; Surblé, S.; Serre, C.; Hong, D.-Y.; Seo, Y.-K.; Chang, J.-S.; Grenèche, J.-M.; Margiolaki, I.; Férey, G.; *Chem. Commun.* **2007**, *100*, 2820–2822.

[3]   Férey, G.; Mellot-Draznieks, C.; Serre, C.; Millange, F.; Dutour, J.; Surblé, S.; Margiolaki, I. A.; *Science (80-.).* **2005**, *309*, 2040–2042.

[4]   Adam, G.; Delbrueck, M. Reduction of Dimensionality in Biological Diffusive Processes. In *Structural Chemistry and Molecular Biology*; Rich, A.; Davidson, N., Eds.; Freeman, San Francisco, 1968; pp. 198–215.

[5]   Bernini, M. C.; Fairen-Jimenez, D.; Pasinetti, M.; Ramirez-Pastor, A. J.; Snurr, R. Q.; *J. Mater. Chem. B* **2014**, *2*, 766–774.

6.   MOF nanoparticles coated by lipid bilayers and their uptake by cancer cells

This chapter is based on the following publication:

Stefan Wuttke, Simone Braig*, Tobias Preiß*, Andreas Zimpel, Johannes Sicklinger, Claudia Bellomo, Joachim O. Rädler, Angelika M. Vollmar, and Thomas Bein, *Chemical Communications*, **2015**, *51*, 15752

* These authors contributed equally to this work

Lipid coated MOF   Cell uptake
nanoparticle   of the nanoparticle
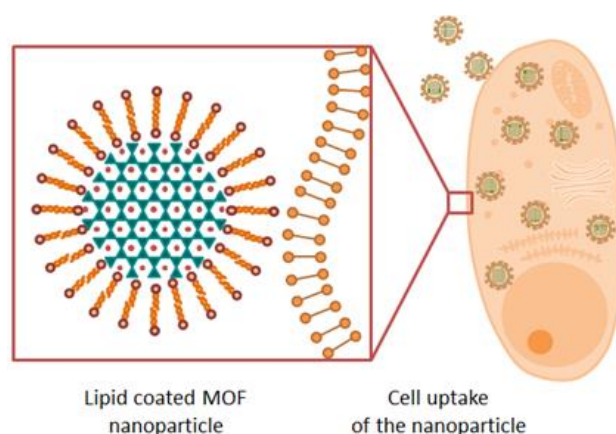
6.1. Introduction

The chemical synthesis of well-defined functional nano-objects is one of the intriguing challenges of nanoscience. In this context metal-organic frameworks (MOFs) offer the ability to generate crystallographically defined, functionalized, porous nanocrystals. MOFs consist of inorganic clusters acting as nodes connected by organic linker molecules. Together, these building blocks create three-dimensional porous crystalline networks with very high pore volume and surface area. The large range of possible compositions (metals, linkers), the structural diversity (pore size, structure, etc.) and the numerous options to functionalize these porous crystalline hybrid inorganic-organic solids make them attractive for different fields of applications such as small molecule storage (H_2, CH_4, CO_2, etc.), catalysis, separation, luminescence, magnetism and other applications.[1-4] In addition, MOFs can be scaled down to nanometer size, which makes them potentially useful as nanocarriers in medical applications.[5]

Incorporating drug molecules into nanocarriers offers exciting opportunities to redefine the pharmacokinetic behavior of the drug, improving its therapeutic efficiency and reducing side effects.[6-8] Several types of drug delivery nanocarriers based on organic platforms such as liposomes, polymers, and dendrimers have been used as "smart" systems that can release therapeutic agents under physiological conditions. Recent research has also addressed the potential of inorganic nanoparticles such as gold, iron oxide or mesoporous silica in this context.[9] The high loading capacity of MOFs for bioactive molecules and their applications for drug delivery and imaging purposes have recently been demonstrated.[5] However, the controlled retention of cargo inside the MOF nanoparticles (NPs) and its controlled release is a challenge that still needs to be addressed.[5, 10-15]

Here we report on the synthesis of MOF nanoparticle-supported lipid bilayers - MOF@Lipid - that synergistically combine properties of liposomes and porous particles. Our aim was to develop a novel route for the flexible, non-covalent encapsulation of biologically active molecules into porous MOF networks that can ultimately serve as functional MOF@Lipid nanocarriers for controlled drug delivery or imaging purposes. Conceptually, a MOF@Lipid nanoparticle may offer three key advantages in comparison to a liposome. First, surface modifications (e.g. modifying the size or the hydrophilic/hydrophobic nature of the pores) of the MOF nanoparticle can control the uptake and release kinetics of the drug.[5, 16] In addition, a MOF@Lipid nanoparticle is expected to be significantly more stable than a liposome, which has an aqueous core instead of a porous MOF core. Finally, due to their high porosity MOF nanoparticles have been shown to offer exceptionally high loading capacities compared to other nanocarrier systems.[5, 11]

6.2. Results and Discussion

To demonstrate our new strategy, we chose the mesoporous iron(III) carboxylate MIL-100(Fe) [16] and the mesoporous chromium(III) carboxylate MIL-101(Cr).[18] MIL-100(Fe) is built up from octahedral trimers connected by trimesate (benzene-1,3,5-tricarboxylate) resulting in a MOF scaffold with large pores (diameter 2.4-2.9 nm) and window sizes (0.6-0.9 nm). MIL-101(Cr) is built up from octahedral trimers connected by terephthalate (benzene-1,4-dicarboxylate), also resulting in a MOF scaffold with large pores (diameter 2.9-3.4 nm) and window sizes (1.2-1.7 nm). Moreover, nanoparticle synthesis is already established for both structures.[11, 19]

Both MOF nanoparticles (NPs) were synthesized in a microwave oven from *Anton Paar* (Synthos 3000). MIL-100(Fe) NPs were obtained by reacting $FeCl_3 \cdot 6H_2O$ and trimesic acid in a 9:4 molar ratio in H_2O, using a temperature controlled microwave program (heating to 130 °C in 30 s and holding at that temperature for 2 min). MIL-101(Cr) nanoparticles were synthesized from an equimolar mixture of terephthalic acid and $Cr(NO_3)_3 \cdot 9H_2O$ in H_2O, using a temperature controlled microwave program (heating to 180 °C in 4 min and holding at that temperature for 2 min). The resulting nanoparticles show the characteristic XRD reflections of the MOFs, with line broadening due to the small particle size (Fig. S6-1 and S6-2).[18, 19] The estimated size distribution of MIL-100(Fe) obtained transmission electron microscopy (TEM) is in the range of 54±24 nm (Fig. S6-6). For MIL-101(Cr), it is in the range of 49±20 nm (Fig. S6-5). In addition, TEM images (Fig. S6-7 and S6-8) confirm the high crystalline quality of the nanocrystals. The calculation of the BET specific surface area based on nitrogen sorption isotherms gave a value of 2004 m²/g for nanoscale MIL-100(Fe) (Fig. S6-9) and 3205 m²/g for nanoscale MIL-101(Cr) (Fig. S6-10), which is similar to reported data.[18, 19]

In the next step, MIL-100(Fe) and MIL-101(Cr) nanoparticles were coated with a lipid bilayer using the lipid DOPC (1,2-dioleoyl-sn-glycero-3-phosphocholine). The principle of the coating procedure is a controlled solvent-exchange deposition of the lipid onto the MOF surface.[20] For this purpose the lipid and the MOF nanoparticles are dispersed in an $EtOH/H_2O$ mixture, where the lipids exist as monomers.[21] When the water concentration is drastically increased, the lipids precipitate on the nanoparticle surface and form a lipid bilayer (Figure 6-1). The successful coating of the MOF nanoparticles with lipid was confirmed by different techniques.
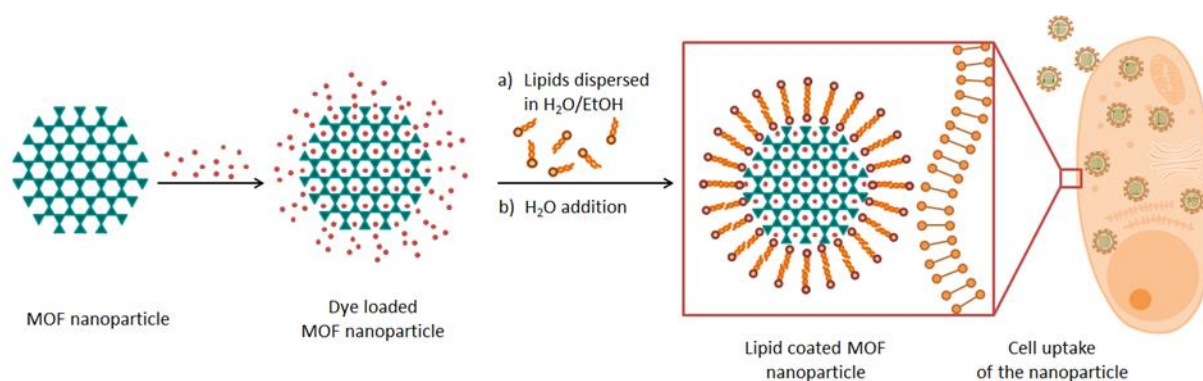
Figure 6-1. Schematic description of the synthesis of lipid bilayer-coated MOF nanoparticles loaded with dye molecules and their uptake in cancer cells.

The diffraction pattern of the two DOPC-coated nanoparticles shows the same reflections as the uncoated nanoparticles (Fig. S6-1 and S6-2). Hence, the MOF structures were stable during the procedure of lipid layer coating. Dynamic light scattering (DLS) data of the MIL-101(Cr)@DOPC nanoparticles showed an increased diameter of 78 ± 22 nm (vs. 69 ± 19 nm for the pure MIL-101(Cr) nanoparticles, Fig. S6-11). This shift of the hydrodynamic diameter of about 10 nm is close to the expected value.[19] Time series of DLS measurements of MIL-100(Fe) and MIL-100(Fe)@DOPC nanoparticles reveal the colloidal stability of the lipid-coated versions whereas the pure nanoparticles agglomerate in a matter of hours (Fig. S6-13 and S6-14). Therefore, the supported lipid can serve not only as a cap system to store molecules inside the MOF nanoparticles but also to increase their colloidal stability, which is of great importance for biomedical applications.

In order to confirm the localization of the lipids on the MOF nanoparticles in solution, both components were labelled and fluorescence cross-correlation analysis (FCCS) was performed. FCCS provides evidence for correlated movement of two differently labelled species within the confocal detection volume, by cross-correlating the fluorescence fluctuation signal of both species.[22-23] Figure 6-2 shows the auto-correlation curves of the Atto633-labeled MIL-101(Cr) and BODIPY-FL-DHPE-labelled DOPC lipids as well as the cross-correlation. The analysis of the cross-correlation shows a high ratio of co-localization of lipids and MOF particles and hence proves the successful lipid coating of the MOF nanoparticle. For the MIL-100(Fe) we found that the fluorescence of different fluorescence dyes is completely quenched. Therefore, FCCS measurements for the MIL-100(Fe)@DOPC system are not applicable. However, we performed fluorescence correlation spectroscopy (FCS) measurements with BODIPY FL DHPE-labelled DOPC lipids alone and with unlabelled MIL-100(Fe) NPs. Juxtaposition of both sample results shows both a completely different count rate and correlation curve, respectively. This strongly indicates an interaction of MIL-100(Fe) NPs with lipids.
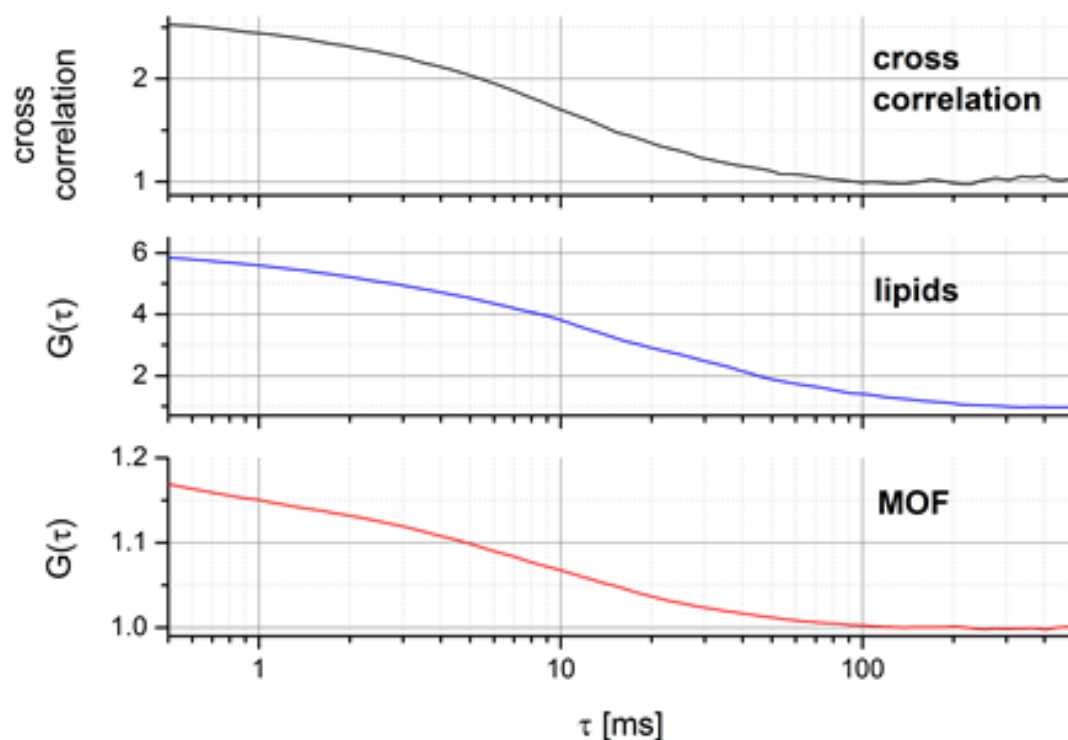
Figure 6-2. FCCS of DOPC lipids (BODIPY labeled) on MIL-101(Cr) nanoparticles (Atto633 labeled). The high cross-correlation amplitude indicates the co-localization of lipids and MOF nanoparticles.

To confirm the successful lipid coating of the porous nanoparticles with another technique, and more importantly, to investigate the sealing properties of the lipid bilayer, we carried out fluorescence release experiments. For this purpose MIL-101(Cr) and MIL-100(Fe) nanoparticles were loaded with fluorescein dye and the dye was encapsulated in the nanoparticles through the formation of the lipid bilayer (Figure 6-1). These dye-loaded nanoparticles were transferred into the cap of a fluorescence cuvette that was subsequently sealed with a dialysis membrane. Only free dye molecules, but not nanoparticles, can pass the membrane into the cuvette volume filled with water where the fluorescence measurement is recorded. Consequently, only dye molecules released from the pores of the particles contribute to the fluorescence intensity measured in the cuvette (detailed information is reported in the SI). Figure 6-3 shows the result of a typical fluorescence release experiment with MIL-101(Cr); the corresponding experiment with MIL-100(Fe) can be found in the supporting information (Fig. S6-15).
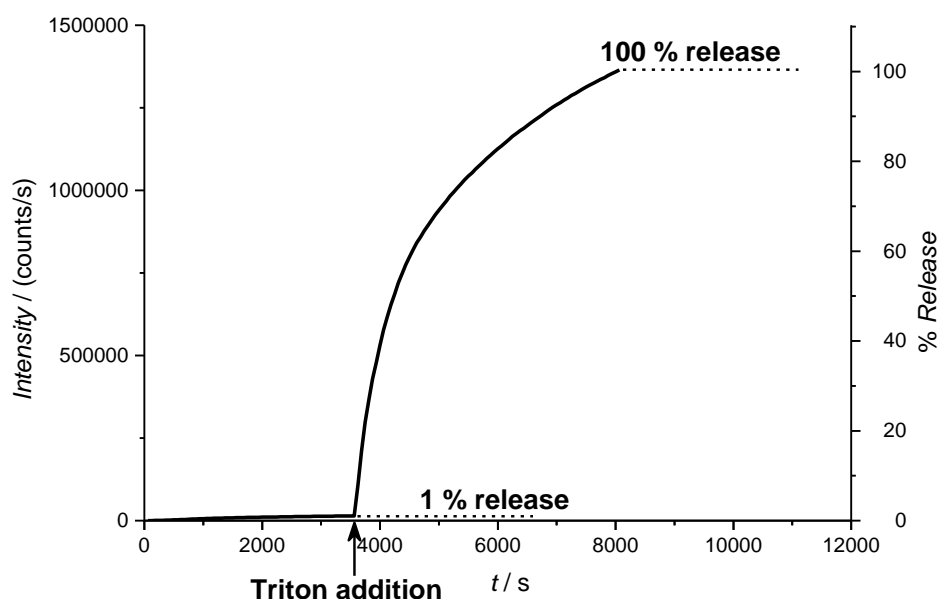
Figure 6-3. Fluorescence release experiments of encapsulated fluorescein in MIL-101(Cr)@DOPC nanoparticles (the data points correspond to the intensities at the peak maxima at 512 nm for fluorescein). After 1 hour of measuring time with no significant increase of the fluorescence intensity, triton was added to the cap system. The destabilization of the lipid bilayer can be observed in the release of the fluorescein dye. The measurement took place at 37 °C and was stopped after 2 h of fluorescein dye release due to an oversaturation of the detector (intensity maximum of the detector 2 million counts per second).

The fluorescence intensity released from DOPC-coated MIL-101(Cr) nanoparticles reached only very low values after 1 h. Hence, we conclude that the dye is retained in the nanoparticles and that the dye molecules do not permeate through the DOPC bilayer. After one hour of monitoring without any significant increase of the fluorescence intensity, the nonionic surfactant triton X-100 was added into the cap. After a short induction period, the fluorescence intensity showed a rapid increase, which subsequently slowed over time. Release kinetics of the dye show a burst release within the first 30 min, which is relatively small in comparison with other nanocarriers,[9, 21] and afterwards a release that is mainly governed by diffusion processes combined with dye-host interactions. Such behaviour can be advantageous for later applications as a drug carrier, because the drug release rate can be controlled by tuning the pore size and shape as well as the functionality of the MOF nanocarrier, and at the same time high burst release effects can be avoided, ensuring a fairly constant drug release. Therefore, the structural features of MOFs including crystalline porosity and widely tunable functionality are advantageous for controlling host-guest interactions.

The above results demonstrate the successful creation of a lipid bilayer around MOF nanoparticles that enables encapsulation of a dye or other molecules inside the MOF scaffold.

For future applications of MOF@Lipid systems in biomedicine, the cellular uptake of these constructs is of particular interest. Due to the quenching effect of the MIL-100(Fe) nanoparticles, corresponding fluorescence tracking experiments can be only done with the MIL-101(Cr)@DOPC nanoparticles. For this purpose, 20.000 T24 bladder carcinoma cells per well with 250 µl medium were incubated with 20 µl of a suspension of Atto-633 labelled MIL-101(Cr)@DOPC NPs (c = 1 mg/ml). Co-staining with PKH26, a red fluorescent dye that stains cellular membranes incorporating biolipid structures, revealed enrichment of MOF nanoparticles in cellular vesicles over time as demonstrated by confocal laser scanning microscopy. As shown in Figure 6-4, strong accumulation of the MOF particles in cellular vesicles is detectable within 6 h and persists for at least 48 h. To investigate whether the MOF@Lipid nanoparticles alter the cellular behaviour and/or condition, an impedance-based real time monitoring (xCELLigence System) approach was used. Importantly, xCELLigence analysis showed that both MOF@Lipid nanoparticle systems themselves have no cytotoxic or anti-proliferative effect on the cancer cells (Figure S6-16 and S6-17).
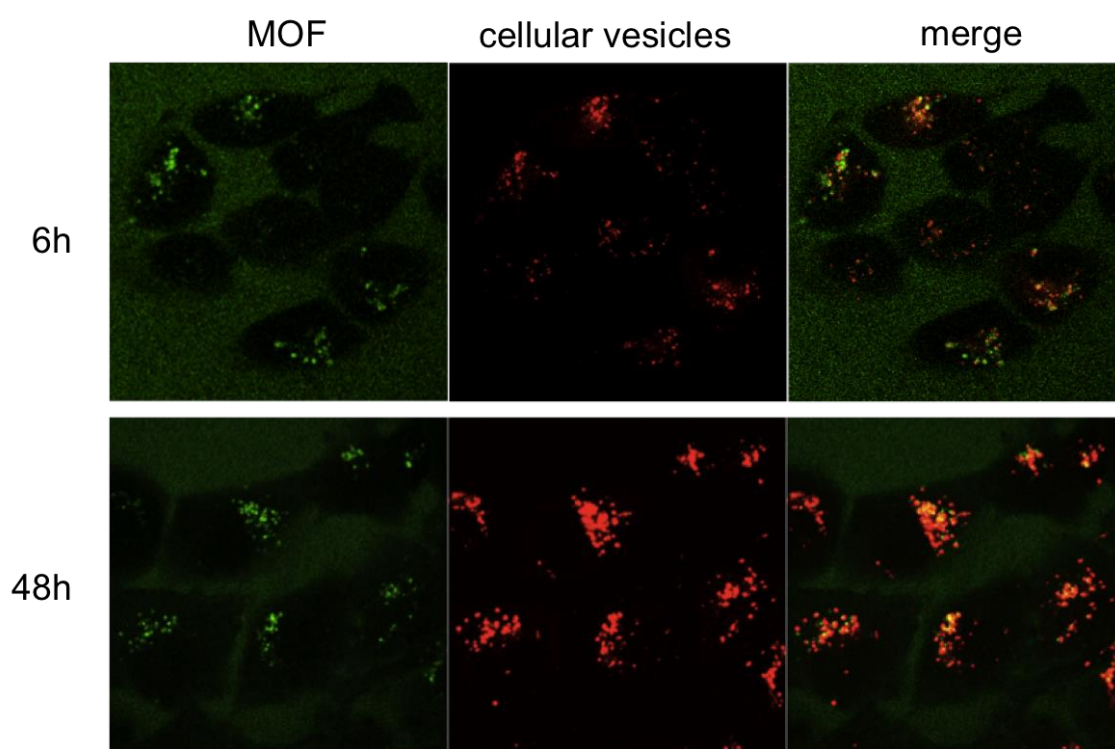
Figure 6-4. Cellular uptake of MOF nanoparticles in cancer cells as monitored by confocal laser scanning microscopy. Bladder cancer cells were incubated with fluorescently-labelled MOF particles for 6 h and 48 h and co-stained with the membrane marker PKH26 to confirm enrichment of MOF in cellular vesicles.

6.3. Conclusion

In summary, we have developed novel metal-organic framework nanoparticles encapsulated by a lipid membrane. We have demonstrated that the MOF@Lipid system can effectively store dye molecules inside the porous scaffold of the MOF while the lipid bilayer prevents their premature release. Moreover, for MIL-100(Fe) the lipid bilayer drastically increases the colloidal stability of the nanoparticles. Employing fluorescence microscopy, we were able to demonstrate the high uptake of lipid-coated nanoparticles by cancer cells. Considering the various ways to synthesize different functionalized MOF nanoparticles as well as the richness of lipids with diverse functions (cap system, triggered release, incorporation of shielding ligand for long circulation times and targeting functions),[24, 25] MOF@Lipid nanoparticles have great potential as a novel hybrid nanocarrier system. On the one hand, the MOF core could store different active species such as imaging, diagnostic or drug molecules, and on the other hand the lipid shell could be used for the incorporation of targeting or shielding ligands (e.g. PEG) as well as for the creation of triggered release mechanisms. Based on the above results with lipid layers serving as model systems, we anticipate further progress in the synthesis of well-defined multifunctional MOF@Lipid nanoparticles for drug delivery and diagnostic purposes and the clinical implementation of this nanotechnology.

6.4. Materials and Methods

Chemicals

Chromium(III) nitrate nonahydrate (99%, *Aldrich*), terephthalic acid (98%, *Aldrich*), ethanol (99%, *Aldrich*) 1,2-dioleoyl-sn-glycero-3-phosphocholine (DOPC, *Avanti Polar Lipids*), fluorescein sodium salt suitable for fluorescence (*Fluka*), triton X-100 (*Aldrich*), N-(4,4-difluoro-5,7-dimethyl-4-bora-3a,4a-diaza-s-indacene-3-propionyl)-1,2-dihexadecanoyl-sn-glycero-3-phosphoethanolamine, triethylammonium salt (BODIPY® FL DHPE, *Invitrogen*).

Synthesis of MIL-101(Cr) nanoparticles

The microwave synthesis of MIL-101(Cr) nanoparticles was based on a modified procedure reported in the literature.[19] An amount of 20 mL (1.11 mol) of H_2O was added to 615 mg (3.70 mmol) terephthalic acid and 1.48 g $Cr(NO_3)_3 \cdot 9\,H_2O$ (3.70 mmol). This mixture was put into a Teflon tube, sealed and placed in the microwave reactor (Microwave, Synthos, *Anton Paar*). Four tubes were filled and inserted into the reactor: one tube contained the reaction mixtures described above; the remaining tubes including the reference tube with the pressure/temperature sensor (PT sensor) were filled with 20 mL H_2O. For the synthesis, a temperature programme was applied with a ramp of 4 min to 180 °C and a holding time of 2 min at 180 °C. After the sample had cooled down to room temperature, it was filtrated and washed with 50 ml EtOH to remove residual e.g. terephthalic acid. For purification, the filtrate was centrifuged and redispersed in 50 ml EtOH three times. The sample was centrifuged at 20000 rpm (47808 rcf) for 60 min. Afterwards the sample was characterized by DLS, XRD, IR, TGA, BET, REM and TEM measurements.

Synthesis of MIL-100(Fe) nanoparticles

For the microwave synthesis of MIL-100 (Fe) nanoparticles, iron(III) chloride hexahydrate (2.43 g, 9.00 mmol) and trimesic acid (0.84 g, 4.00 mmol) in 30 ml H_2O were put into a Teflon tube, sealed and placed in the microwave reactor (Microwave, Synthos, *Anton Paar*).[11] The mixture was heated to 130 °C under solvothermal conditions (p = 2.5 bar) within 30 seconds, kept at 130 °C for 4 minutes and 30 seconds and the tube was cooled down to room temperature. For the purification of the solid, the reaction mixture was centrifuged (20000 rpm = 47808 rcf, 20 min), the solvent was removed and the pellet was redispersed in 50 ml EtOH. This cycle was repeated two times and the dispersed solid was allowed to sediment overnight. The supernatant of the sedimented suspension was filtrated (filter discs

grade: 391, *Sartorius Stedim Biotech*) three times, yielding MIL-100(Fe) nanoparticles. Afterwards the sample was characterized by DLS, XRD, IR, TGA, BET, REM and TEM measurements.

Synthesis of MIL-101(Cr)@DOPC and MIL-100(Fe)@DOPC nanoparticles with encapsulated dyes for fluorescence release and for in vitro experiments

The amount of 1 mg MIL-101(Cr) or MIL-100(Fe) nanoparticles was dispersed in 1 mL of a 1 mM aqueous solution of fluorescein (sodium salt). 24 h later the samples were centrifuged for 5 min at 14000 rpm (16873 rcf). For the application of the lipid layer, the sample was redispersed in 100 µL of a 3.6 mM DOPC (1,2-dioleoyl-sn-glycero-3-phosphocholine) solution in a 60/40 (v/v) H_2O/EtOH mixture. 900 µL H_2O was added and mixed as quickly as possible. By increasing the water concentration, the lipid molecules precipitate and are expected to cover the nanoparticle surface with a lipid layer. For purification, the suspension was centrifuged (5 min, 14000 rpm = 16873 rcf), redispersed in 1 mL H_2O and again centrifuged. Finally the nanoparticles were redispersed in 200 µL H_2O.
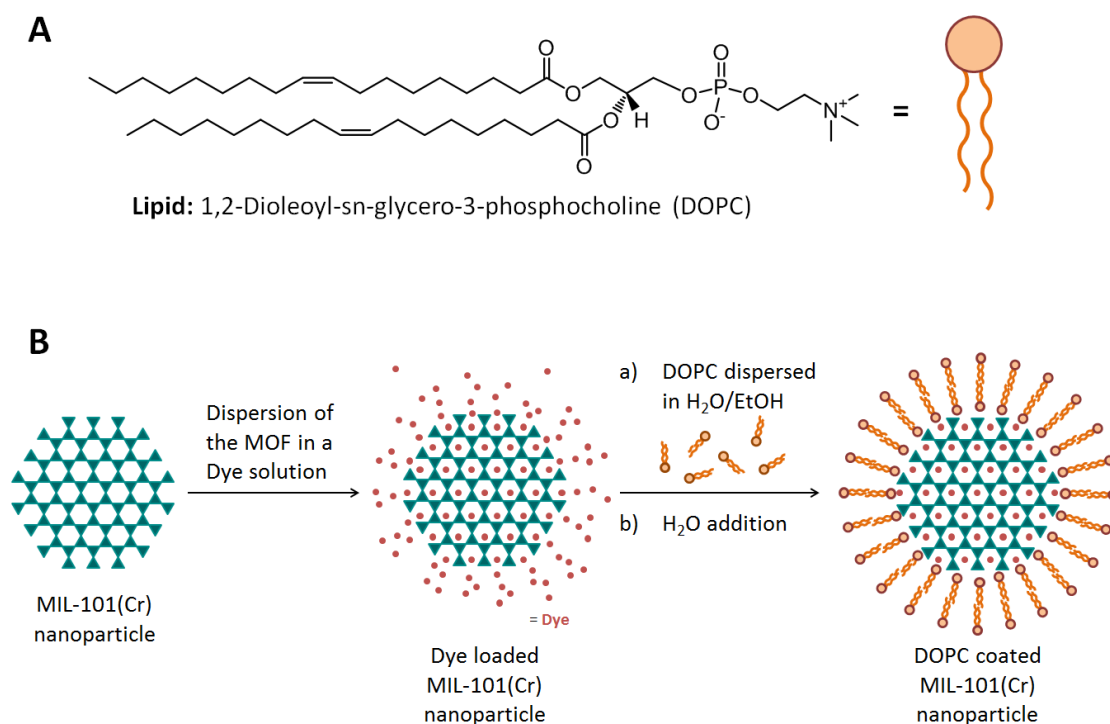
Figure 6-5. (A) Illustration of the lipid DOPC. (B) Schematic depiction of MIL-101(Cr) nanoparticles which are loaded with a dye in the first step, and coated with a lipid bilayer on the MOF nanoparticle surface in the second step.

Synthesis of labeled MIL-101(Cr)@DOPC nanoparticles for FCCS measurements

Loading of MOFs with dye. The amount of 1 µL ATTO 633 NHS (ATTOTec) stock solution (c = 1 mg/ml) was mixed with 100 µL MilliQ water (bi-distilled water from a Millipore system (Milli-Q Academic A10)) just before adding 25µL of this solution to 250 µL of a 10 mg/mL aqueous MOF suspension. This labeling solution was then stirred at room temperature for 48 hours. The nanoparticles were separated from free ATTO 633 molecules by centrifugation (19.000rpm = 20138 rcf, 45min) and resuspending with 1mL MilliQ water, and repeating this cycle 5 times.

Lipid preparation. The amount of 2.5 mg DOPC lipid (1,2-dioleoyl-sn-glycero-3-phosphocholine, Avanti Polar Lipids) was mixed with 0.2 µg BODIPY FL DOPE lipid (N-(4,4-difluoro-5,7-dimethyl-4-bora-3a,4a-diaza-s-indacene-3-propionyl)-1,2-dihexadecanoyl-sn-glycero-3-phosphoethanolamine, Invitrogen) in chloroform (99.995 mol% DOPC and 0.005 mol% BODIPY FL DHPE). After evaporating the chloroform with nitrogen gas, the lipids were further dried in a vacuum overnight. The lipids were then dissolved in 1 mL of a 40 % ethanol/60 % water (v/v) solution to a final concentration of 2.5 mg/mL.

Lipid coating of the MOFs. The amount of 2.5mg labeled MOFs (labeling solution) were centrifuged (19.000 rpm = 20138 rcf, 45min). Afterwards 100 µL of the DOPC/BODIPY FL DHPE lipid in ethanol/water mixture was added. To induce the formation of lipid bilayer on the MOF surface, we quickly added 900 µL of MilliQ water. Afterwards the sample was ready to use for the FCCS measurements.
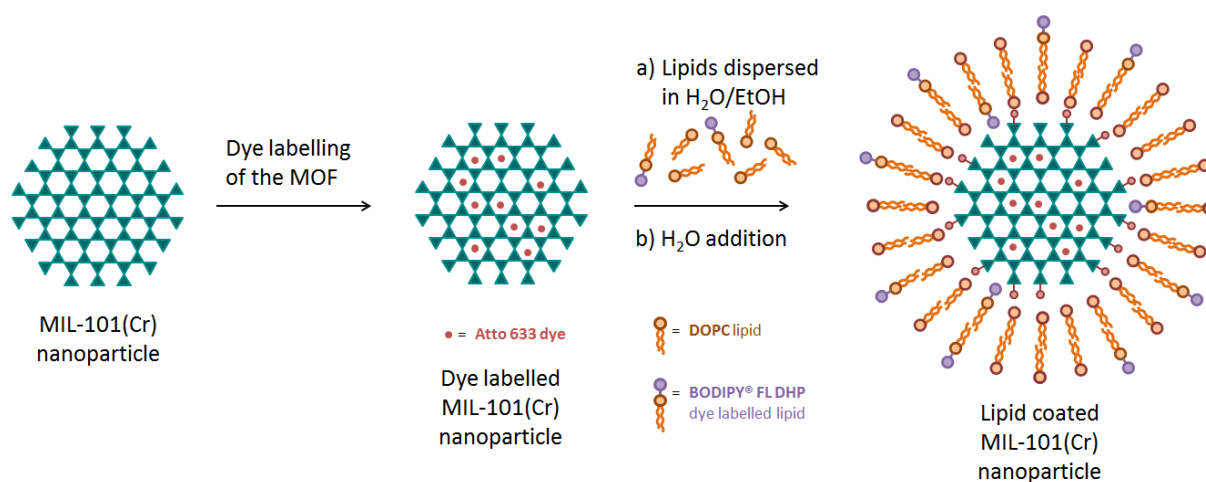
Figure 6-6. Schematic illustration of the dye labelling of MIL-101(Cr) nanoparticles in the first step and the formation of a labeld lipid bilayer on the MOF surface in the second step.

Fluorescence release experiments. An amount of 200 μL of the aqueous suspension containing MIL-101(Cr)@DOPC or MIL-100(Fe)@DOPC loaded with fluorescein was transferred into the cap of a quartz cuvette. The cap was sealed with a dialysis membrane and put on top of a cuvette that was filled with 3 ml H_2O. Only dye molecules can pass the membrane, but no nanoparticles. Consequently, dye molecules that were released from the pores of the particles are responsible for the measured fluorescence intensity. During fluorescence measurement, the water inside the cuvette was stirred and was heated to 37 °C. For the fluorescence measurement with a PTI spectrofluorometer (model 810/814, Photon Technology International), the monochromator slit was set to 1.25 mm, all other slits to 1.00 mm. The excitation wavelength of fluorescein (sodium salt) is 490 nm, the emission wavelength 512 nm. The measurement was run for 1 h with 1 point/min. After the addition of 20 μL of absolute Triton X-100 into the cap-system, the lysis of the lipid bilayer on the MOF nanoparticles allows the diffusion of the dye molecules from the pores and their detection in the cuvette.
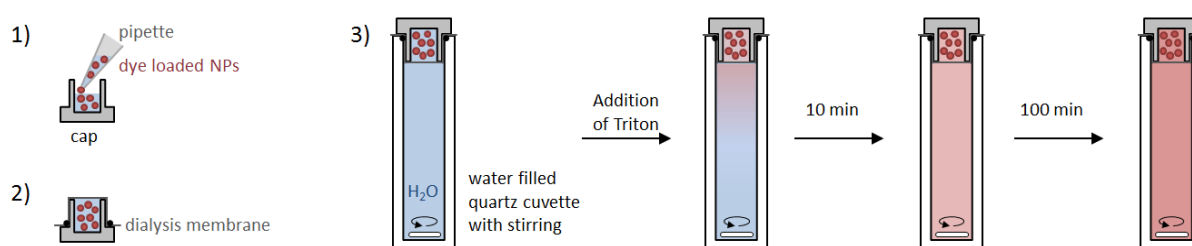
Figure 6-7. Schematic illustration of a fluorescence release experiment.

Confocal laser scanning microscopy and *in vitro* uptake of the nanoparticles. Membranes of bladder carcinoma cells were stained with the red fluorescence dye PKH26 (Sigma-Aldrich, St. Louis, MO, USA) according to manufacturer's instructions. In brief, adhered cells were detached, washed and incubated for 2 min with PKH26 dye solution. After further washing steps, cells were seeded on ibidi μ-slides (Ibidi, Munich, Germany) The next day, cells were treated with 20μl Atto-633 labelled MOF nanoparticles for indicated time points and fluorescence intensities were assessed using a Zeiss LSM 510 Meta microscope.

Impedance-based real-time cell monitoring. Cellular behaviour of MOF treated cells was analysed by utilizing the xCELLigence System (ACEA Biosciences, San Diego, CA, USA), which monitors cellular growth in real-time by measuring the electrical impedance across interdigitated microelectrodes covering the bottom of E-plates. Impedance is displayed as cell

index values. T24 bladder carcinoma cells were seeded at a density of 5000 cells per well in E-plates and different charges of MOF nanoparticles (MOF#1 and #2) and amounts (4µl MOF/100µl medium and 8µl MOF/100µl medium) were added directly to the wells after about 18 h. Cell index tracings were normalized shortly after addition of the particles.

6.5. References

[1] Theme Issue: Metal-Organic Frameworks, H.-C. Zhou, J. R. Long, O. M. Yaghi, *Chem. Rev.*, **2012**, *112*, 673.

[2] Theme Issue: Metal-Organic Frameworks, H.-C. J. Zhou, S. Kitagawa, *Chem. Soc. Rev.*, **2014**, *43*, 5415.

[3] G. Férey, *Chem. Soc. Rev.*, **2008**, *37*, 191.

[4] H. Furukawa, K. E. Cordova, M. O'Keeffe, O. M. Yaghi, *Science*, **2013**, *341*, 974.

[5] P. Horcajada, R. Gref, T. Baati, P. K. Allan, G. Maurin, P. Couvreur, G. Férey, R. E. Morris, C. Serre, *Chem. Rev.*, **2012**, *112*, 1232.

[6] D. Peer, J. M. Karp, S. Hong, O. C. Farokhazad, R. Margalit, R. Langer, *Nature Nanotech.*, **2007**, *2*, 751.

[7] M. E. Davis, Z. Chen, D. M. Shin, *Nature Rev.*, **2008**, *7*, 771.

[8] K. K. Cati, M. E. Belowich, M. Liong, M. W. Ambrogio, Y. A. Lau, H. A. Khativ, J. I. Zink, N. M. Khashab, J. F. Stoddart, *Nanoscale*, **2009**, *1*, 16.

[9] Z. Li, J. C. Barnes, A. Bosoy, J. F. Stoddart, J. I. Zink, *Chem. Soc. Rev.*, **2012**, *41*, 2590.

[10] V. Agostoni, P. Horcajada, M. Noiray, M. Malanga, A. Akykac, L. Jicsinszky, A. Vargas-Berenguel, N. Semiramoth, S. Daoud-Mahammed, V. Nicolas, C. Martineau, F. Taulelle, J. Vigneron, A. Etcheberry, C. Serre, R. Gref, *Sci. Rep.*, **2014**, *5*, 7925.

[11] P. Horcajada, T. Chalati, C. Serre, B. Gillet, C. Sebrie, T. Baati, J. F. Eubank, D. Heurtaux, P. Clayette, C. Kreuz, J.-S. Chang, Y. K. Hwang, V. Marsaud, P.-N. Bories, L. Cynober, S. Gil, G. Férey, P. Couvreur, R. Gref, *Nature Mat.*, **2010**, *9*, 172.

[12] K. Khaletskaya, J. Reboul, M. Meilikhov, M. Nakahama, S. Diring, M. Tsujimoto, S. Isoda, F. Kim, K. Kamei, R. A. Fischer, S. Kitagawa, S. Furukawa, *J. Am. Chem. Soc.*, **2013**, *135*, 10998.

[13] S. Diring, D. O. Wang, C. Kim, M. Kondo, Y. Chen, S. Kitagawa, K. Kamei, S. Furukawa, *Nat. Commun.*, **2013**, *4*, 2684.

[14] C. He, K. Lu, D. Liu, W. Lin, *J. Am. Chem. Soc.*, **2014**, *136*, 5181.

[15] A. C. McKinlay, P. K. Allan, C. L. Renouf, M. J. Duncan, P. S. Wheatley, S. J. Warrender, D. Dawson, S. E. Ashbrook, B. Gil, B. Marszalek, T. Düren, J. J. Williams, C. Charrier, D. K. Mercer, S. J. Teat, Russell E. Morris, *APL Mater.*, **2014**, *2*, 124108.

[16] D. Cunha, M. B. Yahia, S. Hall, S. R. Miller, H. Chevreau, E. Elkaim, G. Maurin, P. Horcajada, C. Serre, *Chem. Mater.*, **2013**, *25*, 2767.

[17] P. Horcajada, S. Surblé, C. Serre, D.-Y. Hong, Y.-K. Seo, J.-S. Chang, J.-M. Grenèche, I. Margiolaki, G, Férey, *Chem. Commun.*, **2007**, *27,* 2820.

[18] G. Férey, C. Mellot-Draznieks, C. Serre, F. Millange, J. Dutour, S. Surblé, I. Margiolaki, *Science*, **2005**, *309*, 2040.

[19] A. Demessence, P. Horcajada, C. Serre, C. Boissière, D. Grosso, C. Sanchez, G. Férey, *Chem. Comm.*, **2009**, 7149.

[20] A. O. Hohner, M. P. David, J. O. Rädler, *Biointerphases*, **2010**, *5*, 1.

[21] V. Cauda, H. Engelke, A. Sauer, D. Arcizet, C. Bräuchle, J. Rädler, T. Bein, *Nano Letters*, **2010**, *107*, 2484.

[22] Rigler, *J. Biotechnol.*, **1995**, *41*, 177.

[23] S. Maiti, U. Haupts, W. W. Webb, *Biophysical J.*, **1997**, *72*, 1878.

[24] T. M. Allen, P. R. Cullis, *Adv. Drug Deliv. Rev.*, **2013**, *65*, 36.

[25] B. Kneidl, M. Peller, G. Winter, L. H. Lindner, M. Hossann, *J. Nanomed.*, **2014**, *4*, 4387.

6.6. Appendix
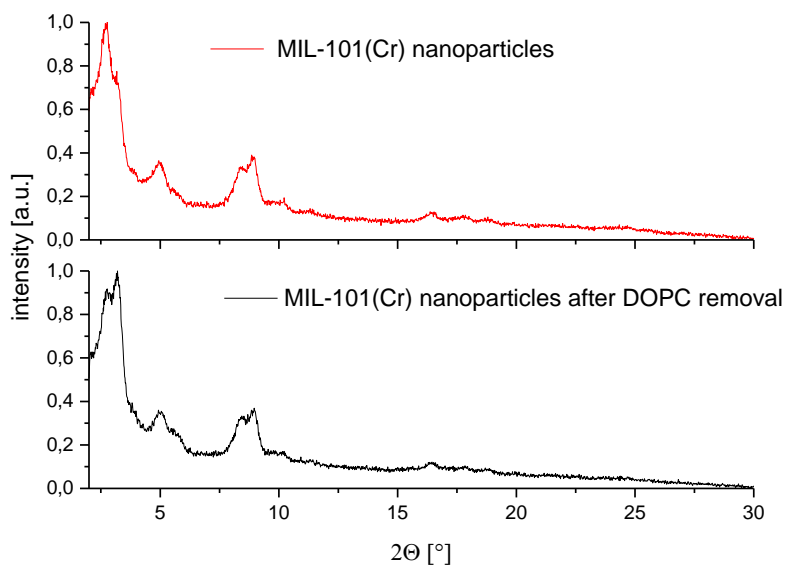
Figure S6-1. X-ray powder diffraction patterns of uncoated MIL-101(Cr) nanoparticles (top) and DOPC coated MIL-101(Cr) nanoparticles after removal of the lipid (bottom).
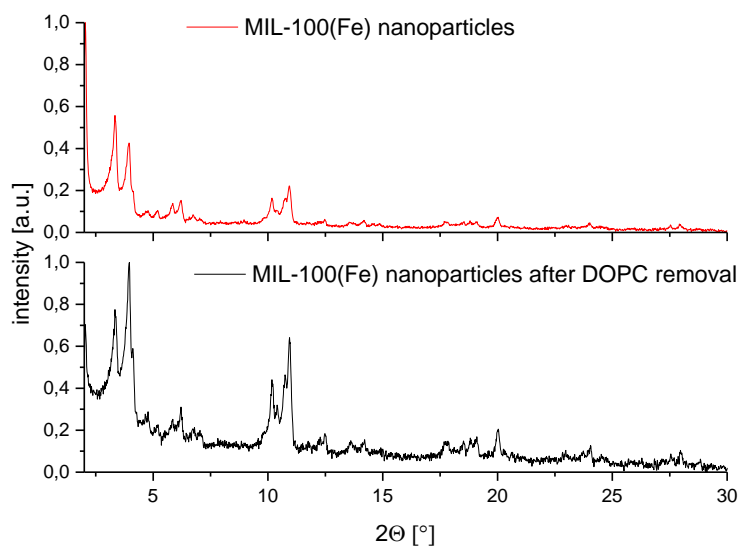
Figure S6-2. X-ray powder diffraction patterns of uncoated MIL-100(Fe) nanoparticles (top) and DOPC coated MIL-100(Fe) nanoparticles after removal of the lipid (bottom).
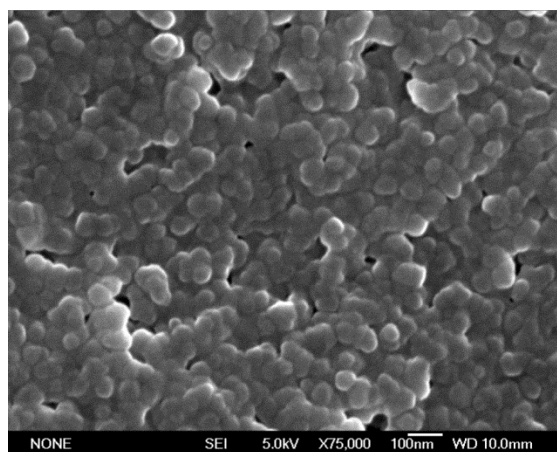
Figure S6-3. Scanning electron micrograph of MIL-101(Cr) nanoparticles.
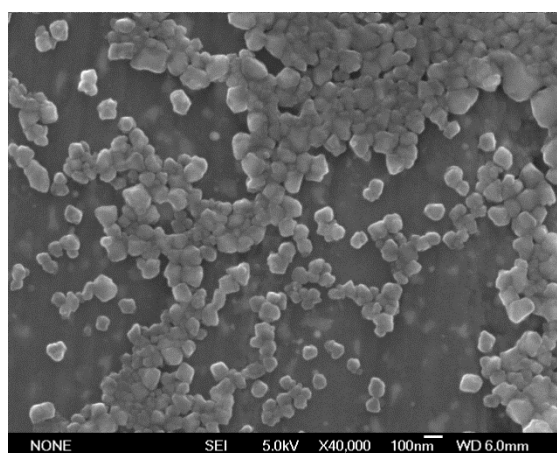
Figure S6-4. Scanning electron micrograph of MIL-100(Fe) nanoparticles.
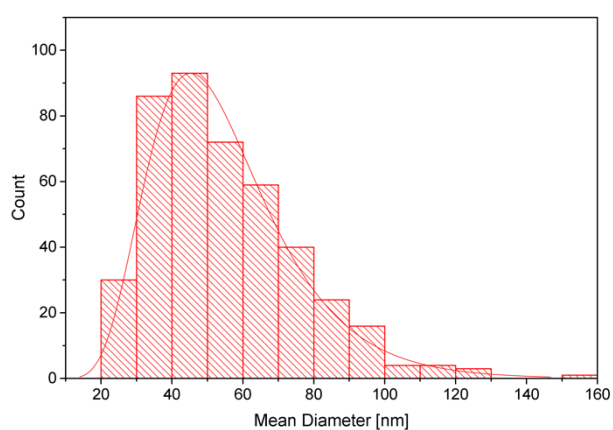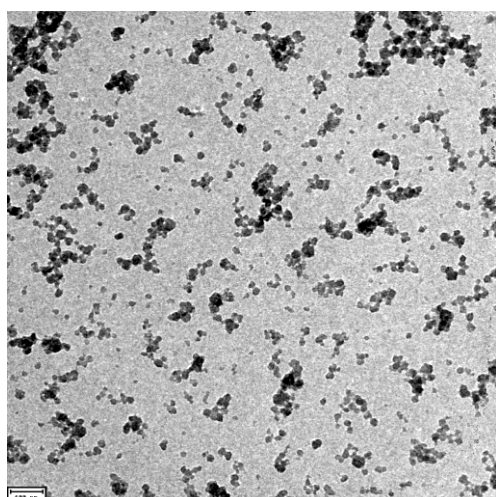
Figure S6-5. Transmission electron micrograph of MIL-101(Cr) nanoparticles (left). Size distribution of MIL-101(Cr) nanoparticles from the TEM picture (right).
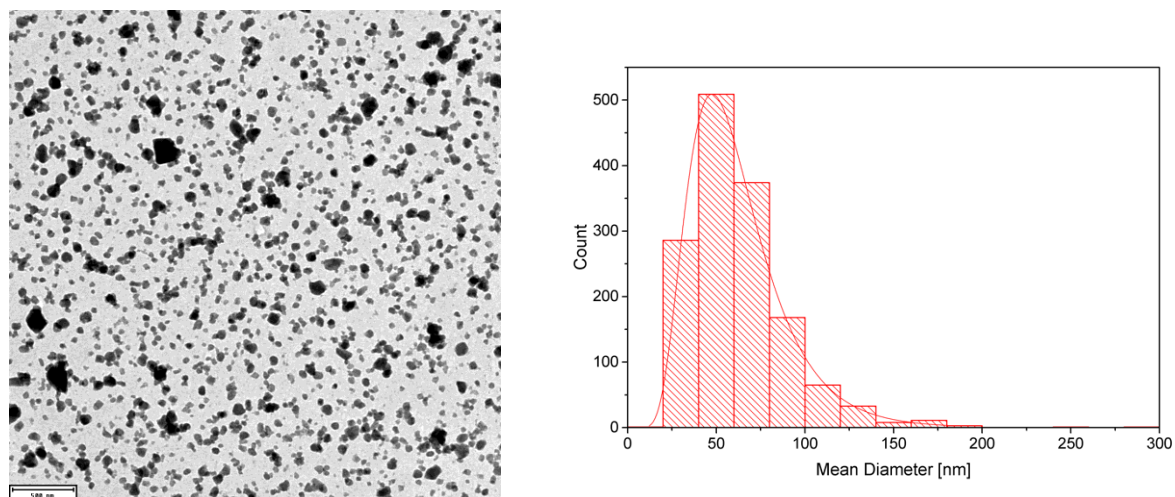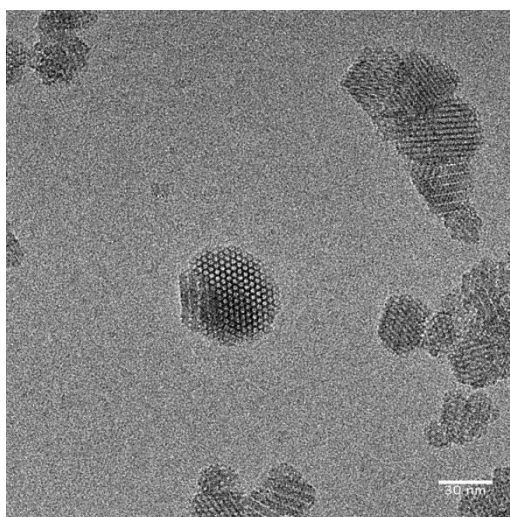
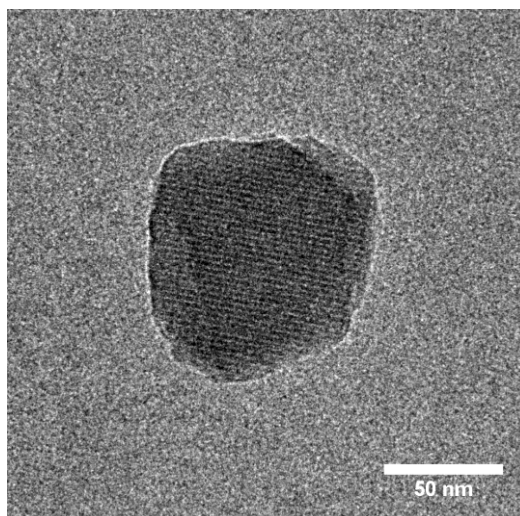**Figure S6-6.** Transmission electron micrograph of MIL-100(Fe) nanoparticles (left). Size distribution of MIL-100(Fe) nanoparticles from the TEM picture (right).

Figure S6-7. Transmission electron micrograph of MIL-101(Cr) nanoparticles – detailed image.

Figure S6-8. Transmission electron micrograph of MIL-100(Fe) nanoparticle – detailed image.
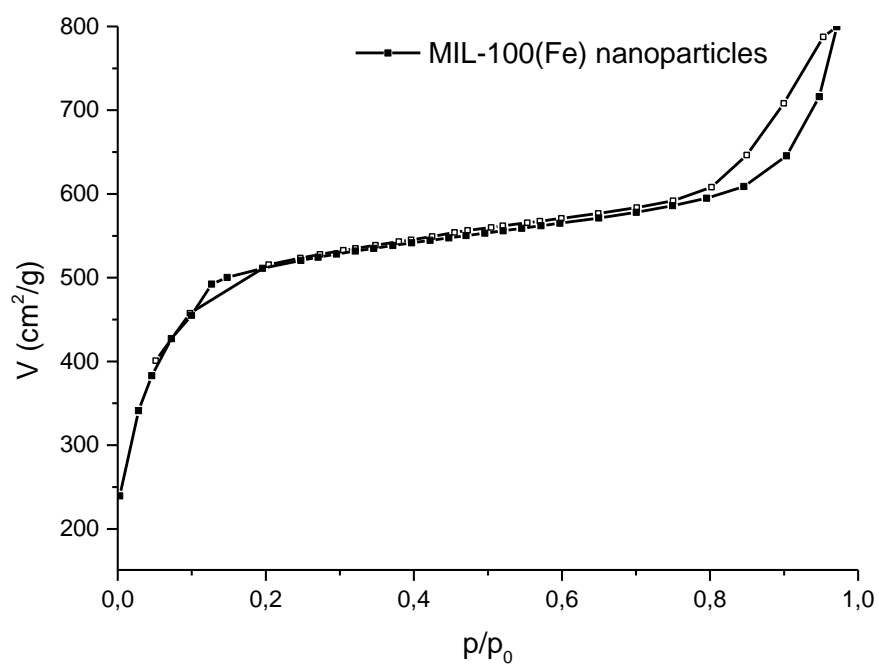
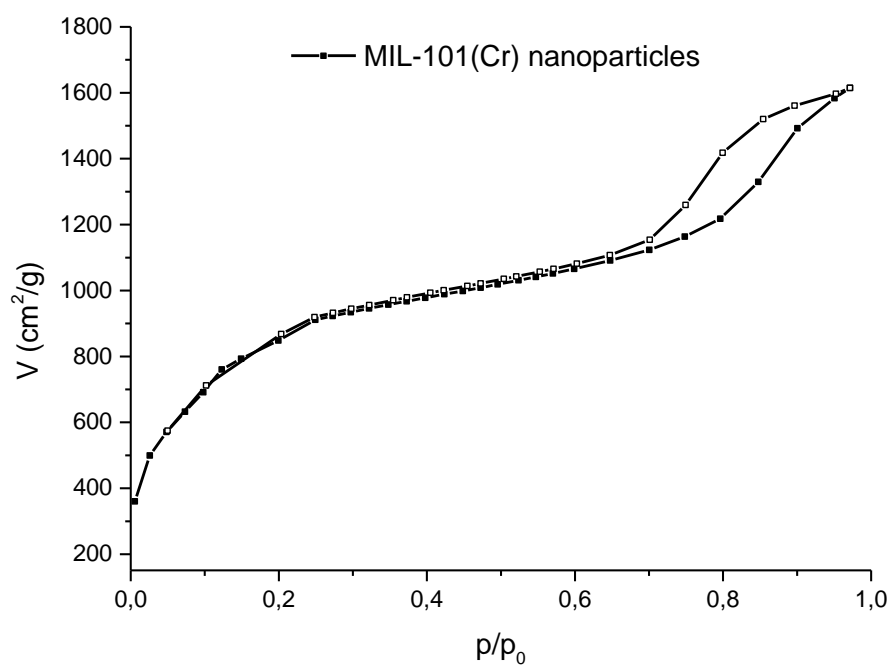**Figure S6-9** Nitrogen sorption isotherm of MIL-100(Fe) nanoparticles. Calculated BET surface: 2004 m^2/g.

Figure S6-10. Nitrogen sorption isotherm of MIL-101(Cr) nanoparticles. Calculated BET surface: 3205 m^2/g.
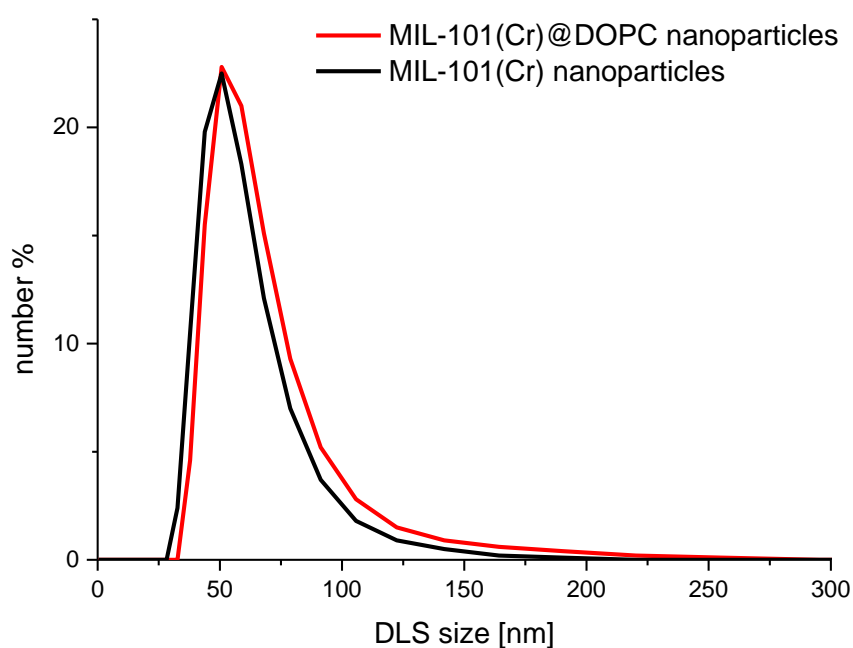
Figure S6-11. DLS size distribution (measured in water) by number comparing uncoated and DOPC-coated MIL-101(Cr) nanoparticles.
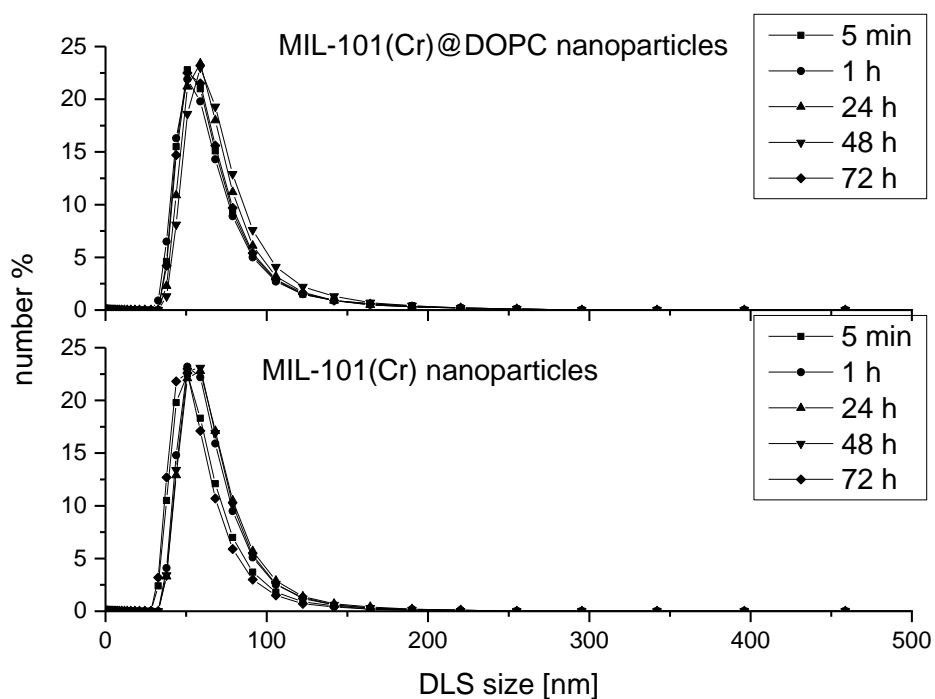

Figure S6-1.2 DLS size distributions by number comparing uncoated and DOPC-coated MIL-101(Cr) nanoparticles over a time period of 72 h.
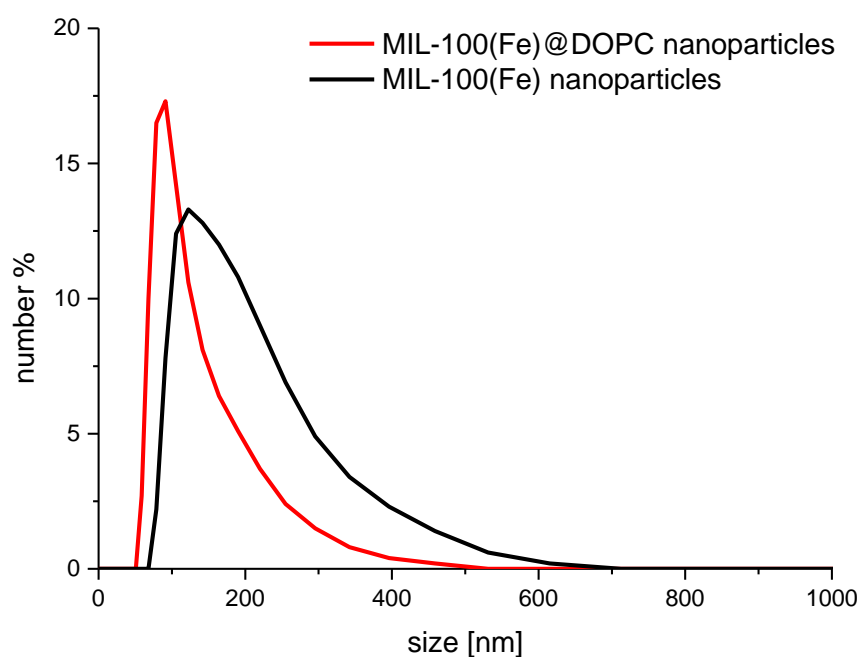
Figure S6-13. DLS size distribution by number (measured in water) comparing uncoated and DOPC-coated MIL-100(Fe) nanoparticles.
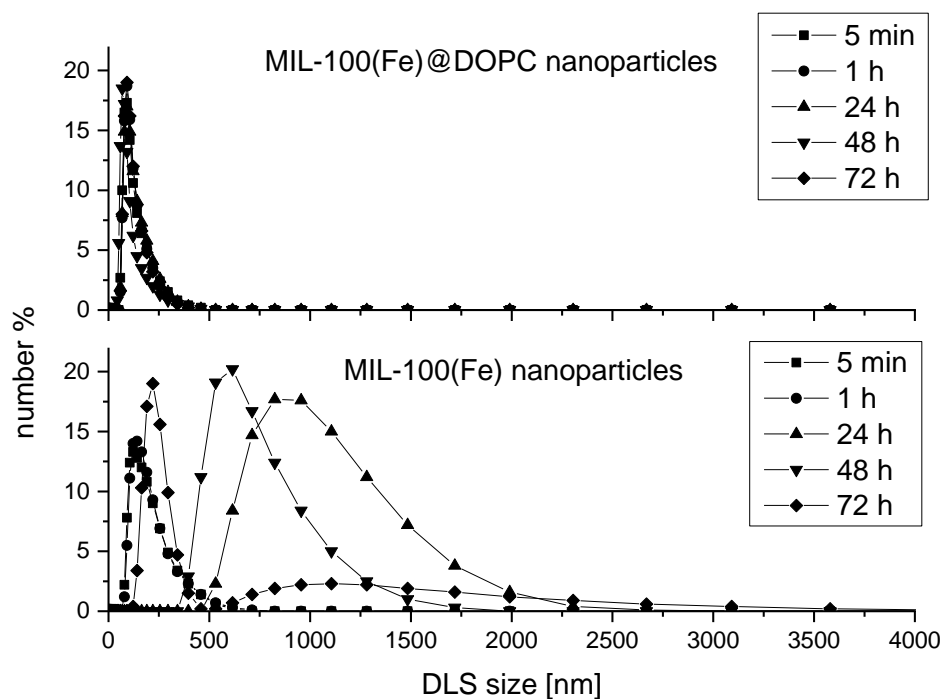

Figure S6-14. DLS size distribution by number, comparing uncoated and DOPC-coated MIL-100(Fe) nanoparticles over a time period of 72 h.
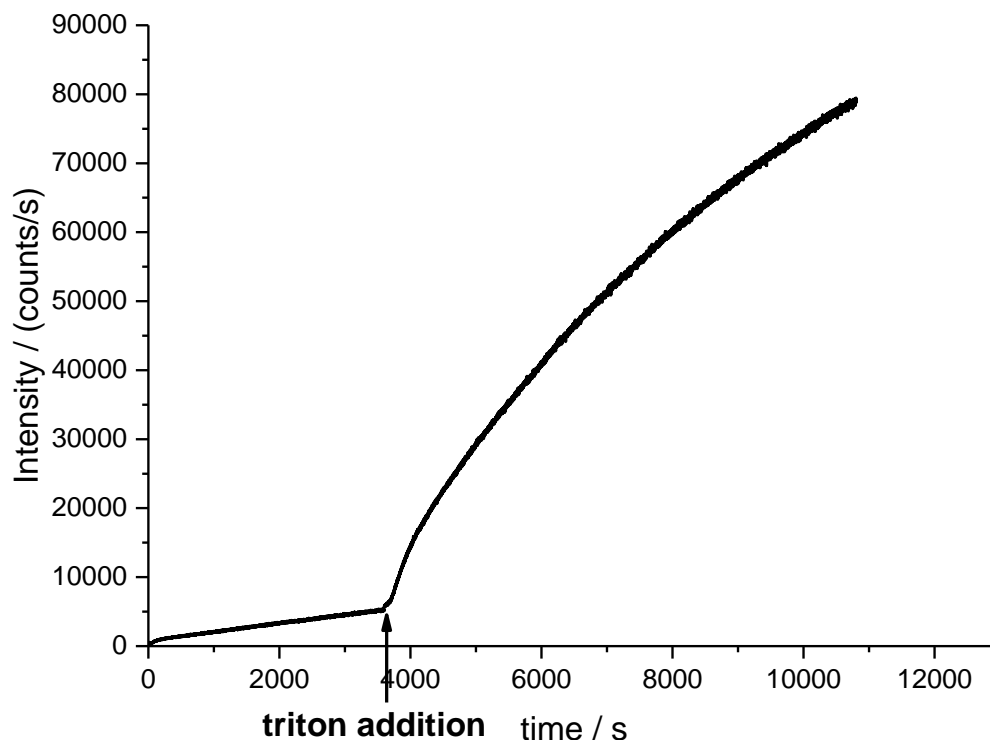
Figure S6-15. Fluorescein release from DOPC-coated MIL-100(Fe) nanoparticles before and after addition of Triton X-100.

Figure S6-16. Impedance measurements of cell cultures. Bladder carcinoma cells were seeded on xCELLigence E-plates and treated at indicated time points with different charges (MOF#1 and MOF#2) and amounts of 6,4 µl and 12,8 µl of MIL-101(Cr)@DOPC nanoparticles (c = 1 mg/ml) per 200 µl medium. Similar cell index values indicate that cells incubated with MOF nanoparticles show a behaviour very similar to PBS-treated control cells.
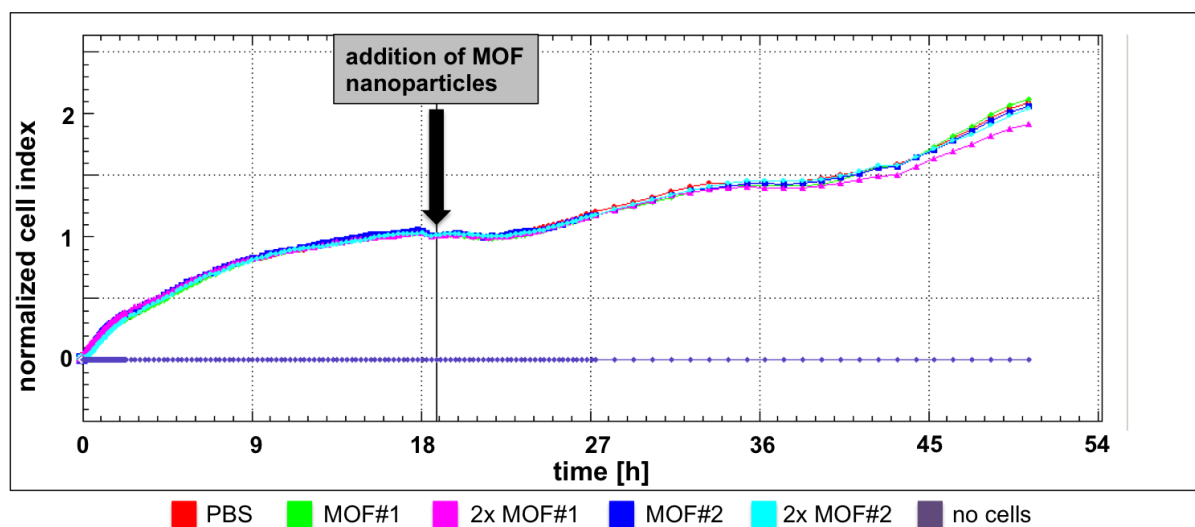
Figure S6-17. Impedance measurements of cell cultures. Bladder carcinoma cells were seeded on xCELLigence E-plates and treated at indicated time points with different charges (MOF#1 and MOF#2) and amounts of 6,4 µl and 12,8 µl of MIL-100(Fe)@DOPC nanoparticles (c = 1 mg/ml) per 200 µl medium. Similar cell index values indicate that cells incubated with MOF nanoparticles show a behaviour similar to PBS-treated control cells.
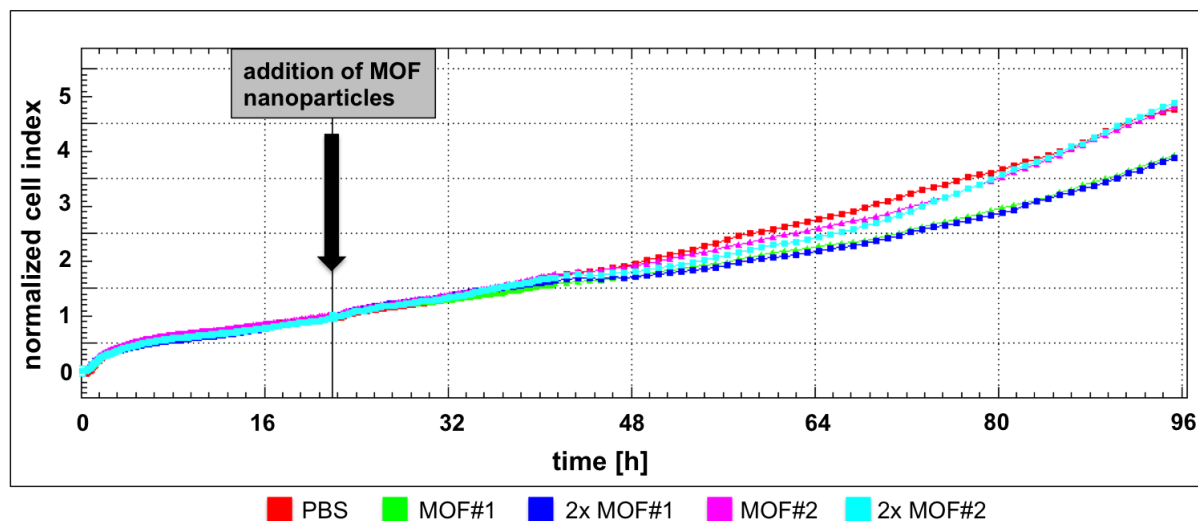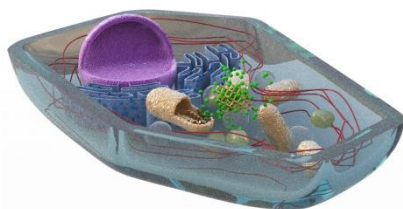
7. Validating metal-organic framework nanoparticles for their nanosafety in diverse biomedical applications

This chapter is based on the following publication:

7.1. Introduction

Nanosized materials have been used for various biomedical applications to improve human disease diagnosis and treatment. These nanomedicines can offer various advantages in applications such as their use as imaging agents for early and minimally-invasive diagnosis, increased drug concentration at a local site, minimized drug degradation and clearance, the possibility of specific cell targeting, and the ease of creating drug-delivery formulations.[1-3] Metal-organic framework (MOF) materials offer the combination of both organic and inorganic design principles and are considered to be a promising new class of nanocarriers with improved biocompatibility. Generally, the MOF construct is based on the principle of connecting metal ions or metal-oxo clusters with organic linkers resulting in crystalline and porous materials.[4-8] The flexibility with which metal clusters and organic linkers can be varied as well as the different possibilities to functionalize MOFs on their inner and outer surface provide a vast number of possibilities for creating tailored porous MOF nanoparticles (MOF NPs) adjusted for the specific purposes.[9-11] MOF NPs have already been loaded with different drugs or with gasotransmitter gases, and the *in vitro* and to some degree the *in vivo* efficacy was demonstrated.[12-20] Key parameters for biomedical applications of nanoparticles include

their size, morphology, surface properties and chemical composition.[21-25] These properties also determine the potential fields of application for MOFs, ranging from diagnosis and sensing to therapeutic drug delivery and multifunctional surface modification of medical implants (Figure 7-1).
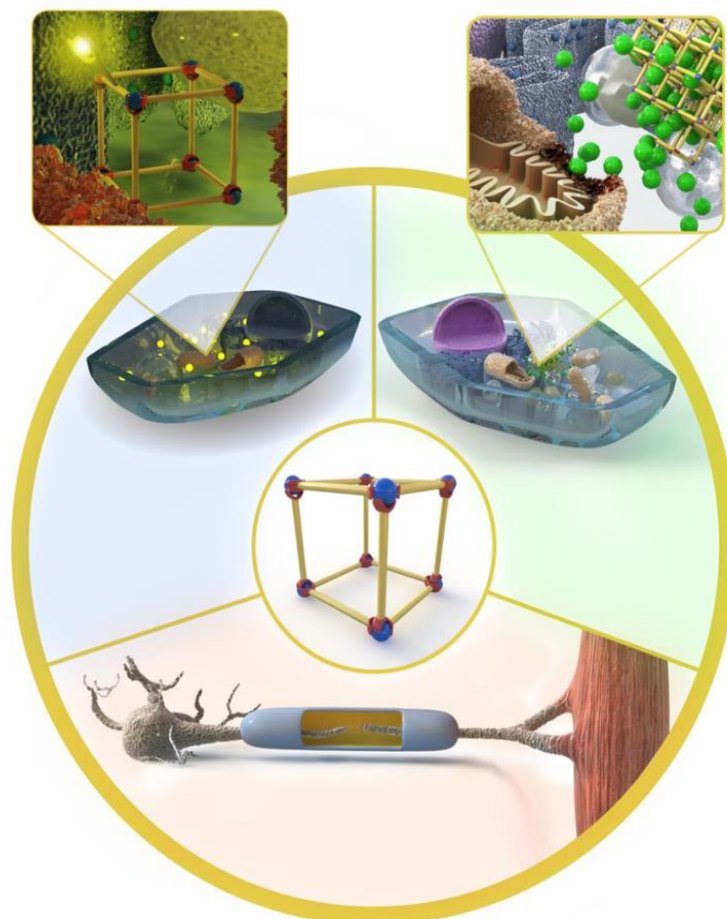
Figure 7-1. Schematic representation of the different possible applications of MOF NPs for diagnosis, therapy and for the creation of smart surfaces.

The same nanomaterials that have been developed for improving diagnosis and therapy, however, may impose health risks to the patient very similar to those known from occupational or environmental particle exposures.[26-28] As such, the application of any novel nanomaterial in the medical context calls for thorough and comprehensive analysis of its cellular biocompatibility and thus nanosafety. In particular, NPs are required to only minimally interfere with the function of their primary effector cells, which are defined as those cells that directly interact with NPs when these are introduced into the biological system. Most surprisingly, so far MOF NPs have not been comprehensively analyzed for their adverse effects on primary effector cells, but have mainly been studied for their *in vitro*

toxicity in cancer cells.[10, 29] Here, we intend to fill this gap by determining and discussing the adverse effects of different MOF NPs for various medical applications ranging from drug delivery to surface coating of medical implants. We here investigated different types of MOF NPs that have distinct properties. All NPs tested in this study have a spherical morphology in common because studies suggested that this particular shape causes least cytotoxicity.[21, 22] For chemical composition and surface charge diversity we choose a Zr-fumarate (Zr-*fum*) MOF, a Fe-trimesate (MIL-100, MIL standing for Material of Institute Lavoisier) and a Cr-terephthalic MOF (MIL-101). The Zr-fumarate MOF[30] features microporosity of 5-8 Å whereas MIL-100(Fe)[31] and MIL-101(Cr)[32] exhibit mesoporosity of 25-28 Å and 30-34 Å, respectively. A characteristic feature of the Zr-fumarate MOF is the fumaric acid linker which is an intermediate in the citric acid cycle and hence a biocompatible molecule. Such microporous MOFs as well as the MIL-100(Fe) and MIL-101(Cr) are particularly well suited for external surface functionalization and transport of large biomolecules such as RNA.[18] The mesoporosity of MIL-100(Fe) and MIL-101(Cr) allows for the storage of drug molecules inside the nanoparticles and at the same time features chemical stability.[32, 33] These particles are particularly promising for drug delivery applications.[34] For systemic delivery of any type of functionalized MOF NP by intravenous injections, the endothelium is the first site of particle contact and uptake. It tightly seals the vessel wall to the surrounding tissue and maintains blood barrier integrity as well as controls local inflammatory responses. In contrast to blood cells, which also encounter nanoparticles upon systemic delivery, endothelial cells are less easily replenished upon damage. Any cytotoxic effects by NPs will thus have a profound effect on endothelial barrier function. We thus assayed survival, apoptotic cell death and inflammatory activation of human primary endothelial cells in response to treatment with our MOF-NPs.

An additional way of NP delivery is their inhalation via the lung. In fact, inhalation of NPs is a natural route of entry to the body as evidenced by the sometimes detrimental uptake of environmental nanoparticles.[35] Hence, the lung is a unique organ particularly suitable for local drug delivery via inhalation. Its large surface area, thin epithelium layer, and rich blood supply allow for rapid uptake of inhalatively applied nanoparticles.[3] To assess the biocompatibility of our MOF NPs for inhalative applications into the lung, we investigated the cellular responses of murine alveolar epithelial cells that constitute the main cell type of the air/blood barrier. In addition, we analyzed activation of the main immune cell type of the lung, the alveolar macrophages. These cells are of key importance for clearing particles and

toxins from the lung and thus control the initial inflammatory response of the lung to foreign material.

Moreover, we envision the use of MOF NPs for coatings as a promising field of application (Figure 1), as already proposed in the literature.[36, 37] Medical implants are mainly artificial structures that are widely applied in the clinic to facilitate cellular regeneration of substitute body functions. Activatable coatings on medical implants allow for the control of adverse inflammatory reactions after implantation and progressive implant and tissue destruction.[38-41] To study the general applicability of MOF NPs in this field, we assayed the cytotoxicity of chemically stable MIL-100(Fe), MIL-101(Cr) and Zr-*fum* MOF NPs of different sizes on primary gingiva fibroblasts as effector cells for dental implants.

A different type of medical implants is represented by nerve guidance tubes that are used to bridge transected peripheral nerves in reconstruction surgeries (Figure 7-1). Currently autologous nerve tissue is used for transplantation to the site of injury. Entubulation strategies with synthetic hollow nerve guidance conduits represent a promising alternative to autologous nerve tissue transplantation to facilitate peripheral nerve regeneration.[42] Functionalization of biosynthetic nerve guidance tubes may be applied in order to deliver regeneration promoting molecules facilitating attraction of Schwann cells.[43-46] To address these issues, we investigated our MOF NPs regarding their biocompatibility with primary adult human Schwann cell cultures as well as in organotypic cultures of rat dorsal root ganglia that contain sensory neurons.

All in all, the aim of our study was to comprehensively investigate the nanosafety and hence the general applicability of different MOF NPs for distinct fields of medical applications. For this purpose, the different experimental setups were designed to be as close as possible to the later applications by the use of the primary effector cells, i.e. endothelial, lung, gingiva and nerve cells, of the respective application field.

7.2. Results and Discussion

Synthesis and characterization of the MOF nanoparticles

Validation of biocompatibility was performed with different MOFs that provide promising properties for the use as drug nanocarrier as well as for the multifunctional surface coating of implants. The structure and phase purity of the nanoparticles were characterized by powder x-ray diffraction (PXRD; Suppl. Figures S7-1, S7-5, S7-9; in general: Figures S7-1 to S7-4 corresponds to MIL-101(Cr), Figures S7-5 to S7-8 corresponds to MIL-100(Fe), Figures S7-9 to S7-12 corresponds to Zr-*fum*) and transmission electron microscopy (TEM) with high-resolution images (Suppl. Figures S7-2, S7-6, S7-10). The expected crystallinity was demonstrated. The calculated Brunauer-Emmett-Teller (BET) surface areas extracted from the nitrogen sorption isotherms (Suppl. Figures S7-3, S7-7, S7-11) are in good agreement with reported data.[30, 34] The hydrodynamic diameters of the different nanoparticles determined with dynamic light scattering (DLS) range from about 40 to 250 nm (Suppl. Figures S7-4, S7-8, S7-12; Table S7-1). The formation of a supported lipid bilayer around the MIL-100(Fe) and MIL-101(Cr) nanoparticles, i.e. 1,2-dioleoyl-sn-glycero-3-phosphocholine (DOPC), enhances their biocompatibility and prevents incorporated cargo from premature release.[34] The smaller hydrodynamic diameter of the MIL-100(Fe)@DOPC in comparison with pure MIL-100(Fe) nanoparticles can be explained by the agglomeration behavior of the latter. This tendency to form agglomerates is prevented by a lipid bilayer.[34] Zeta potential measurements were used to determine the effective charge of the nanoparticles and range from 3 to -43 mV for the nanoparticles investigated (Suppl. Table S7-1).

Evaluation of nanosafety of MOF nanoparticles designed for drug delivery

For the delivery of mesoporous NPs either by intravenous or inhalative routes, the endothelial and alveolar cell barriers need to be overcome without causing cell damage and activation of inappropriate immune responses. We thus examined the cellular response towards MIL-101(Cr) and MIL-100(Fe) MOF NPs with and without supported lipid bilayers in endothelial cells, alveolar epithelial cells and alveolar macrophages and compared it to the response towards non-lipid-coated control particles.

Human endothelial cells, namely primary human umbilical cord vein cells (HUVEC) and human microvascular endothelial cells (HMEC) were cultured to confluency, exposed for up to 72 hours to DOPC-coated iron or chromium MOFs at a dose range of 25 to 200 μg/ml and assayed for cytotoxic and inflammatory responses compared to non-treated and non-coated particle controls. Staining of HMECs for the cytoskeletal actin protein did not reveal any

stress-related rearrangement of actin fibres in response to 24 hours of exposure to MOF nanoparticles (Figure 7-2A and Suppl. Figure S7-13). We further analyzed for early signs of apoptotic cell death using Fluorescence Activated Cell Sorting (FACS)-based analysis of the DNA content. This technique allows for separation of cells according to their DNA content in the different phases of the cell cycle with dividing S and G2 phase cells containing the doubled amount of DNA compared to cells in the resting G1 phase (Suppl. Figure S7-14). Apoptotic cells contain fragmented DNA and can thus be quantified by counting the cells in a sub G1 peak.[47] MIL-101(Cr)@DOPC and also uncoated MIL-101(Cr) did not induce any signs of apoptotic cell death for the full dose range when applied to HMECs for 72 hours. MIL-100(Fe)@DOPC treated HMECs had an increased sub-G1 peak only at the highest particle dose of 200 µg/ml, revealing significant induction of apoptosis with high doses of lipid coated MIL-100(Fe) particles (Figure 7-2B). This was also observed for the non-coated control particles and indicated that Fe-containing MOFs induce apoptotic cell death in endothelial cells at higher doses. Endothelial cells are easily activated upon cell damage by noxious stimuli and particles to express pro-inflammatory surface receptors such as the intercellular adhesion molecule (ICAM). These surface molecules serve as binding sites to capture patrolling immune cells in the blood for activation of local inflammatory responses. Expression of ICAM1, however, was not affected in HUVECs by any of the particles tested as shown by FACS-based quantification of ICAM1 expression after 24 hours of particle treatment in Figure 7-2C. We here used tumor necrosis factor α (TNFα) as a positive control to obtain maximal induction of ICAM surface expression upon inflammatory signaling via TNFα.[48]
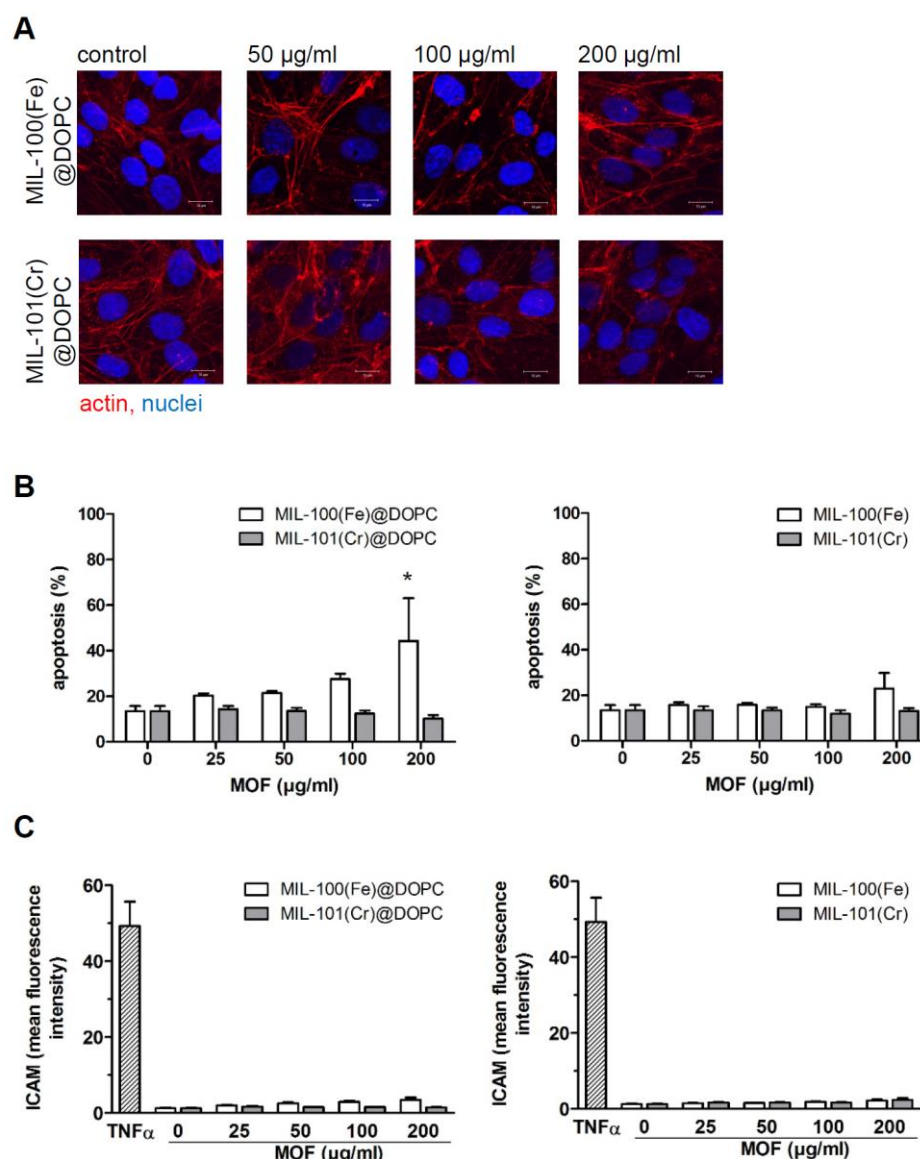
Figure 7-2. Cytotoxic and inflammatory response of human endothelial cells to MIL nanoparticles. (A) Actin staining of MIL-101(Cr)@DOPC and MIL-100(Fe)@DOPC treated HMEC cells. HMEC cells were treated with the respective DOPC coated Fe- and Cr-MOFs particle doses for 24 h. Cells were fixed, actin and nuclei were stained and analyzed by confocal microscopy. (B) Determination of apoptosis rate in HMEC cells after treatment with MIL-101(Cr)@DOPC, MIL-100(Fe)@DOPC, MIL-101(Cr) and MIL-100(Fe). HMEC cells were treated without (0) or with the respective MOF NP concentrations for 72 h, harvested and the percentage of apoptotic cells was measured by FACS analysis. (C) Determination of the inflammatory response in HUVEC cells after treatment with DOPC coated and uncoated Fe- and Cr-MOFs. HUVEC cells were treated without (0) or with the respective nanoparticle concentrations for 24 h, harvested and the level of the inflammatory marker ICAM was determined by FACS analysis. Treatment with TNFα served as a positive control to induce maximal proinflammatory activation of ICAM. Values given are mean of three independent experiments ± SEM. * indicates a significant change compared to the respective controls ($p < 0.05$) using Two-Way ANOVA tests.

In a next step, we studied the cytotoxic effects of the MOF nanoparticles for lung cells, namely murine alveolar epithelial cells (MLE12) and mouse alveolar macrophages (MH-S). Viability of the cells was quantified after 24 hours of particle exposure using the MTT assay which uses conversion of a stable tetrazolium salt into soluble formazan by metabolically

active and thus viable cells. In addition, we measured the amount of lactate dehydrogenase (LDH) in the medium which is released by necrotic cells with disrupted plasma membranes. Viability of MLE12 cells was affected by exposure to higher doses of MIL-101(Cr)@DOPC (200 µg/ml), which corresponded to an increased release of LDH (Figure 7-3A). Exposure to MIL-100(Fe)@DOPC particles had an even more pronounced effect on metabolic activity and was cytotoxic from doses of 100 µg/ml on (Figure 7-3A). These cytotoxic effects were even stronger with uncoated particles (Figure 7-3A) showing that lipid-functionalization improves biocompatibility of both the MIL-100(Fe) and MIL-101(Cr) nanoparticles in lung epithelial cells, respectively. Biocompatibility of Fe-containing MOFs was, however, strikingly different from Cr-MOFs in the alveolar macrophage cell line MH-S. Both DOPC coated and uncoated Fe-MOFs, showed drastically reduced cell viability in MTT and LDH assays (Figure 7-3B), while Cr-MOFs were well tolerated and only induced cell death at the highest dose of 200 µg/ml (Figure 7-3B). To investigate the inflammatory response of these particles in the alveolar macrophages, we determined RNA expression levels of well-known pro-inflammatory mediators such as the cytokine interleukin 6 (IL6), TNFα, and of the enzyme nitrite oxide synthase 2 (Nos2) which generates high levels of nitric oxide (NO) as part of the phagocytotic response of macrophages towards microorganisms, toxins and particles.[49] In addition, we measured expression of heme oxygenase 1 (HO1) and metallothionein 2 (MT2) that are activated as part of the cellular stress response to metals such as iron.[50, 51] As a positive control for efficient induction of these genes, we stimulated MH-S cells with the lipopolysaccharide (LPS), a bacterial wall component that is a strong and well known trigger for inflammatory gene expression (Figure 7-3C).[52] While LPS strongly induced expression of IL6, TNFα, and Nos2, we did not observe any obvious inflammatory gene activation for the tested MOF nanoparticles (Figure 7-3C). In contrast, Fe-containing MOFs induced distinct and dose-dependent upregulation of HO1 and MT2 suggesting pronounced activation of an anti-iron-stress response in alveolar macrophages. Cr-containing MOFs, however, were inert (Figure 7-3C).
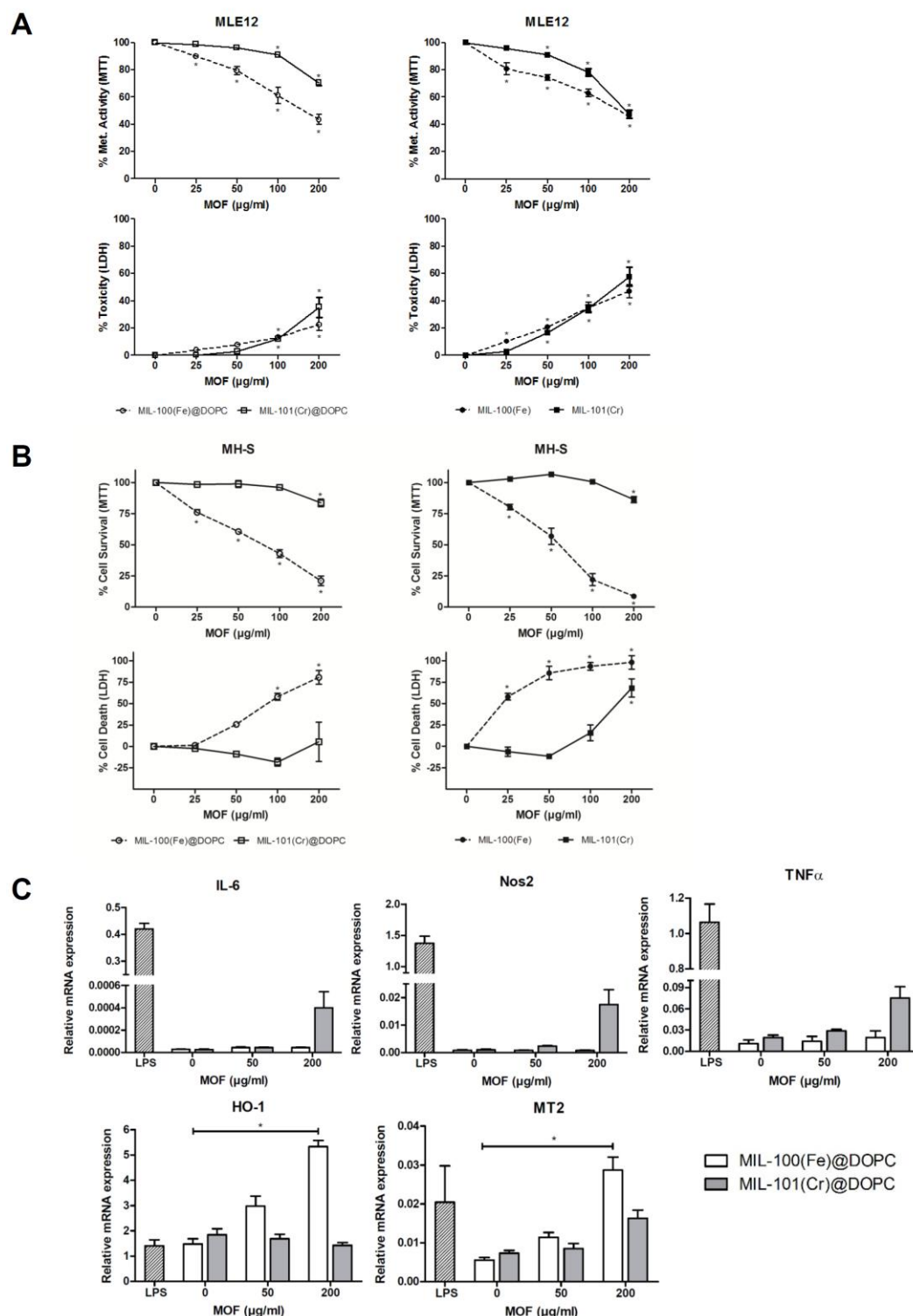
Figure 7-3. Biocompatibility of MIL nanoparticles with the murine alveolar epithelial cell line MLE-12 and the murine alveolar macrophage MH-S cells.

(A) Metabolic activity and toxicity after 24 h of MIL-100(Fe)@DOPC, MIL-101(Cr)@DOPC, MIL-100(Fe), or MIL-101(Cr) exposure to MLE 12 and MH-S cells (B) as analyzed by MTT (upper row) and LDH (lower row) assays, respectively. Untreated cells were set to 100 % survival for the MTT test and 0 % death for the LDH assay. (C) Inflammatory response induced by 4 h exposure to the respective MOFs in MH-S cells as determined by RT-qPCR analysis. 1 µg/mL LPS was used as a positive control to induce pronounced pro-inflammatory gene expression. Values given are mean of three independent experiments ± SEM. * indicates a significant change compared to the respective controls ($p < 0.05$).

Taken together, these data indicate that both Fe and Cr-containing MOFs are well tolerated by endothelial cells whereas the MIL-100(Fe)@DOPC NPs caused some apoptotic cell death from a minimum dose of 100 µg/ml onwards. In contrast, alveolar epithelial cells are generally more sensitive and tolerate only lipid-coated Fe and Cr-containing MOFs at lower doses of up to 50 -100 µg/ml, respectively. Alveolar macrophages appear to be particularly sensitive to iron-containing MOF particles, which cause pronounced induction of a cellular stress response. In contrast, Cr-containing MOFs are well tolerated by these immune cells.

Evaluation of nanosafety of MOF nanoparticles designed for implant coatings

While NPs have been primarily used as mobile nanocarriers in medical applications, they can also be used to modify solid surfaces such as dental implants or cellular guidance structures.[44, 46, 53] In order to evaluate the influence of particle size, chemical composition and surface charge we examined Zr-*fum* MOF, MIL-100(Fe) and MIL-101(Cr) MOF NPs (Suppl. Table S7-1). In proof-of-concept experiments, we investigated the biological effect of the different MOF NPs on gingival fibroblasts, adult human Schwann cells as well as rat neonatal organotypic dorsal root ganglion (DRG) cultures as effector cell systems for dental implants and nerve guidance tubes, respectively.

We first tested primary human gingival fibroblasts for their cytotoxic response towards the above mentioned MOF NPs (Figure 7-4).
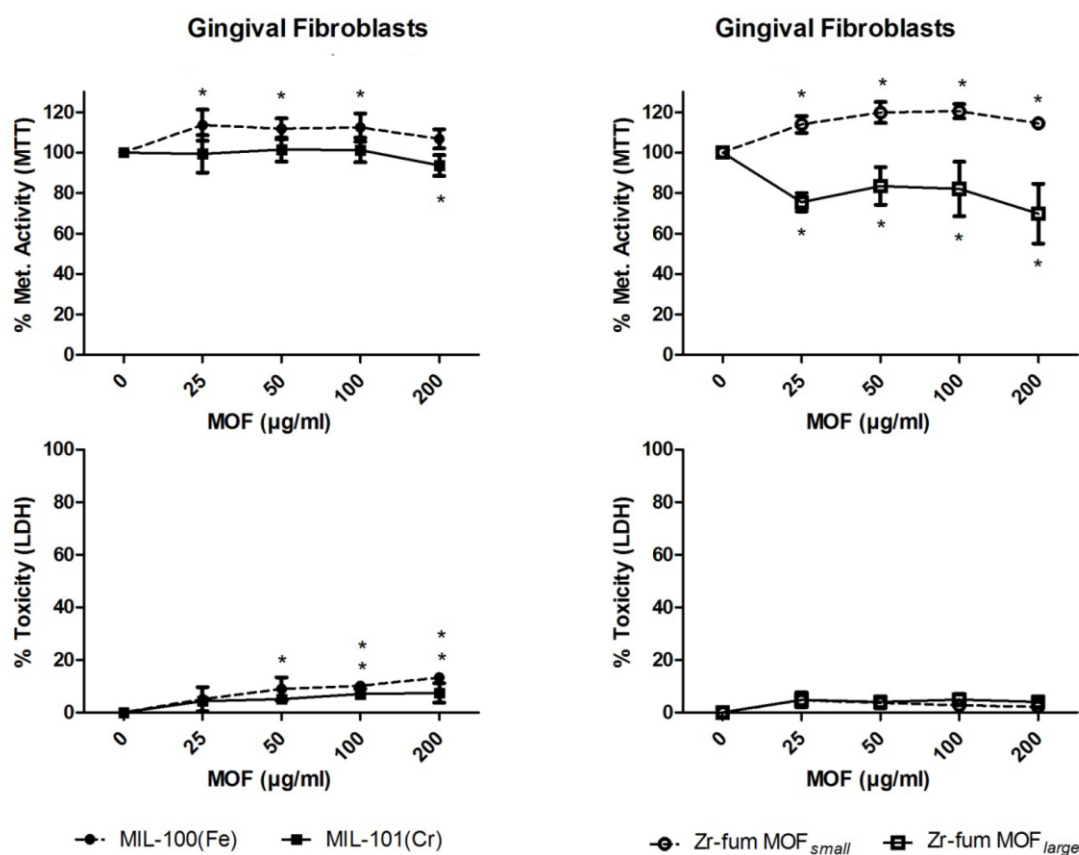
Figure 7-4. Biocompatibility of MOFs with human primary gingival fibroblasts.

Metabolic activity (MTT test) and toxicity (LDH-assay) after 24 h of exposure of gingival fibroblasts to Zr-*fum* MOF$_{small}$, Zr-*fum* MOF$_{large}$, MIL-100(Fe) or MIL-101(Cr) particles, respectively. Untreated cells were set to 100 % metabolic activity for the MTT test and to 0 % toxicity for the LDH assay. Values given are mean of three independent experiments ± SEM. * indicates a significant change compared to the respective controls (p < 0.05).

Remarkably, all of the tested MOF NPs showed only minor signs of cytotoxicity on gingiva fibroblasts: while Zr-*fum* MOFs were well tolerated even at higher doses as revealed by LDH release assays and Zr-*fum* MOF$_{large}$ NP only responded with some decrease in metabolic activity, MIL-100(Fe) or MIL-101(Cr) particles showed some significant increase in LDH release with doses of 50 mg/ml and higher but no significant decrease in metabolic activity indicating that they are well tolerated (Figure 7-4). Scanning electron microscopy (SEM) analysis did not reveal any obvious morphological signs of cell death after incubation with Zr-*fum* MOF NPs (Suppl Figures S7-15A-D).

With regard to NP coating of nerve guidance channels, we used human primary adult Schwann cells as they are the leading supporting cells for peripheral nerve regeneration.[54] Moreover, Schwann cells are in direct contact with the NP coating on the inner surface of nerve guidance channels (Figure 7-1). We first analyzed the morphology and metabolic

activity of adult human Schwann cells cultures after 72 h in response to different doses of the MOF NPs (Figures 7-5A, 7-5B). We detected a pronounced formation of cell clusters when cultures were treated with doses of 200 µg/ml of the different MOF NPs, except for Zr-*fum* MOF$_{large}$ (Figure 7-5A). In contrast, lower doses of MOF NPs ranging from 12.5 to 50 µg/ml did not induce any obvious morphological alterations in the growth behavior of adult human Schwann cells (Figure 7-5A). This corresponded well to the preserved metabolic activity in the presence of most of the MOF NPs at doses up to 50 µg/ml (Figure 7-5B). For the adult human Schwann cells, we used the WST assay to determine metabolic activities. This test is based on the same principle as the MTT test, but easier to use in difficult cell culture systems due to water-solubility and storage conditions. MIL-100(Fe) as well as MIL-101(Cr) nanoparticles reduced metabolic activity of adult human Schwann cell at doses of 50 µg/ml. This did not, however, reach statistical significance and is probably not be related to cell death – as indicated by maintenance of cellular morphology - but may reflect an altered metabolic state of the cells in response to treatment. Metabolic activity was reduced up to approximately 50% of untreated cultures at the highest dose of 200 µg/ml. In presence of Zr-*fum* MOF NPs, the metabolic activity of the cells was almost not affected in a dose range up to 50 µg/ml while the highest concentration of 200 µg/ml of Zr-*fum* MOF$_{large}$ did significantly reduce metabolic activity up to approximately 65% of un-treated controls (Figure 7-5B). In contrast, Zr-*fum* MOF$_{small}$ did not affect the metabolic activity of adult human Schwann cells in culture at any concentration tested. These data indicate that MOF NPs are generally well tolerated by human adult Schwann cells irrespective of the organic components, metal ion content, and size at low doses.

In addition to Schwann cells, we monitored the biological response of sensory neurons to the MOF NPs using rat neonatal organotypic dorsal root ganglion (DRG) cultures. The particular feature of these DRGs cultures is that they contain sensory neurons that extend their axons (neurites) into the peripheral space thus mimicking axonal outgrowth to the periphery. Therefore, these cultures provide a unique opportunity to study the response of the main effector cell type for nerve guidance tubes, i.e. neurite outgrowth behavior of sensory neuronal cells, to novel types of nanomaterial.[44, 55] In this assay, the neurite outgrowth from neonatal rat DRG cultures is quantified by counting the numbers of neurites crossing a circle drawn at 600 µm distance from the center of each DRG (Figure 7-5C). Figure 7-5C shows representative photomicrographs of untreated control DRG and of cultures that have reduced neurite outgrowth upon treatment with the different MOF-NPs added in two concentrations.
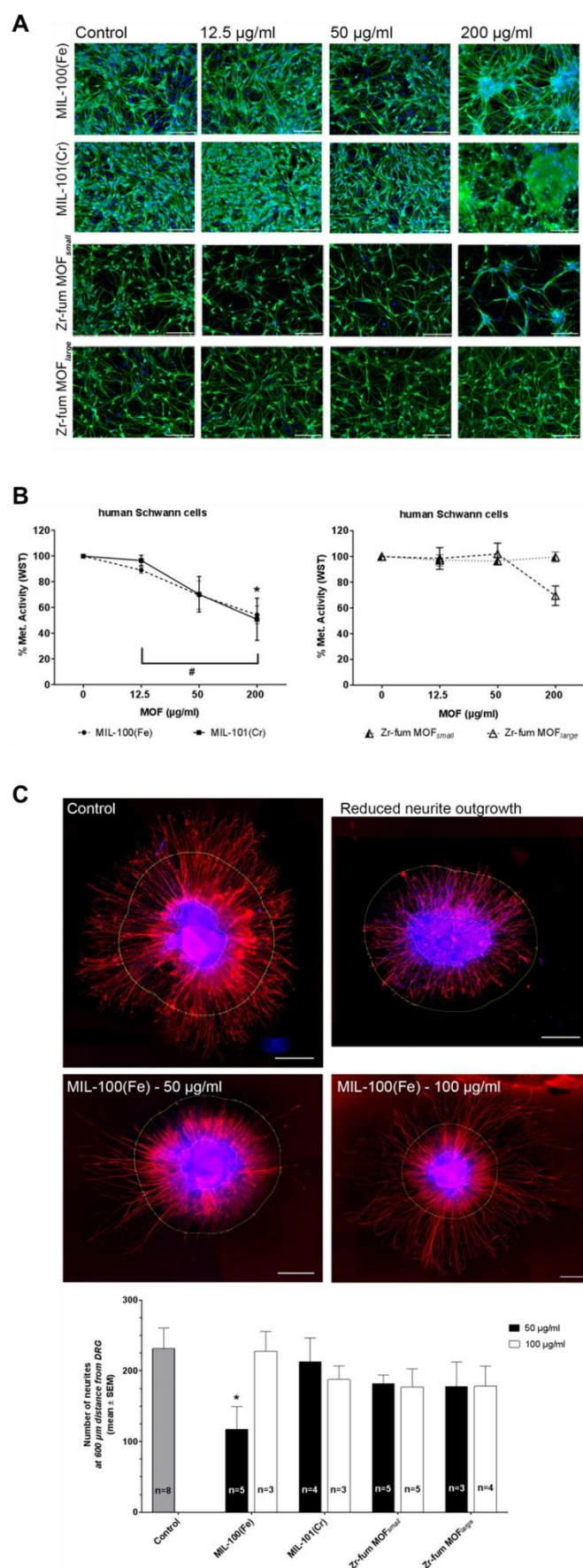
Figure 7-5. Biocompatibility of MOFs on adult human Schwann cells and rat organotypic DRG cultures.

(A) Representative photomicrographs demonstrating the morphology of adult human Schwann cell cultures treated for 72 h with the different MOFs. The typical Schwann ell morphology is demonstrated by bi- and tripolar cells that are organized in a fish swarm-like way. Negatively affected Schwann cell cultures demonstrate cell clustering. Schwann cells are stained in green (anti-S100 antibody) and the nuclei counterstained in blue (DAPI). Scale bars: 200 µm. (B) Line graphs depicting changes in metabolic activity of adult human Schwann cell cultures treated for 72 h with the different MOFs. Values given are mean ± SEM. Significant differences ($p < 0.05$) to control levels (100 %) are marked with *, differences between different doses of MOFs are marked with #. (C) Representative photomicrographs demonstrating the neurite outgrowth from organotypic DRG cultures. Neurites have been quantified at a distance of 600 µm from the center of the DRG (green circle). Neurites are stained in red (anti-beta-III-tubulin antibody) and cell nuclei are counterstained in blue (DAPI). Upper left: example of an untreated control culture with unaffected (regular) neurite outgrowth. Upper right: example of a culture with clearly reduced neurite outgrowth (outliner from cultures treated with Zr-*fum* MOF$_{small}$). Lower left: example of a culture demonstrating slightly reduced neurite outgrowth in the presence of 50 µg/ml MIL-100(Fe). Lower right: example of a culture demonstrating rescued neurite outgrowth in presence of 100 µg/ml MIL-100(Fe). Scale bars: 500 µm. The bar graph depicts changes in neurite outgrowth from organotypic DRG cultures treated for 48 h with the different MOFs. Values given are mean ± SEM. Significant difference ($p < 0.05$) with respect to control levels is marked with *.

As an example for a treatment that showed a dose-dependent effect on neurite outgrowth, representative pictures from the MIL-100(Fe) treated cultures are shown: surprisingly, the low concentration of 50 µg/ml MIL-100(Fe) significantly reduced sensory neurite outgrowth while the doubled concentration rescued it to control levels. For Zr-*fum* MOF$_{small}$ and $_{large}$, we did not observe any loss in neurite outgrowth capacity at both doses tested (Figure 7-5C).

In conclusion, these data demonstrate the principal feasibility of using MIL-100 (Fe) and MIL-101(Cr) as well as Zr-*fum* MOF NPs for coating of dental implants as they were well tolerated by human gingiva fibroblast. For coating of nerve guidance tubes, however, Zr-*fum* MOF$_{large}$ NPs appear to be the most suitable choice as they were best tolerated in both adult human Schwann cells and rat dorsal root ganglia up to doses of 50 µg/ml, respectively.

Discussion

In this study we comprehensively analyzed the nanosafety of different MOF NPs with regard to distinct biomedical applications, ranging from systemic blood and local lung-specific drug delivery to coatings of dental implants and nerve guidance tubes (Table 7-1).

During systemic nanoparticle-mediated drug delivery via the blood, nanomaterials get in contact with the endothelium of the vessels. We show that primary human endothelial cells are not affected by the tested MOF NPs, i.e. MIL-100(Fe) and MIL-101(Cr) and their DOPC-coated derivatives up to high doses of 200 µg/ml toward with regard to apoptotic cell death or inflammatory responses. Similar results have been shown previously for the hepatocarcinoma cell line Hep3B.[29]

7. Validating metal-organic framework nanoparticles for their nanosafety in diverse biomedical applications

Table 7-1. Nanosafety of the different MOF NPs for the respective application.

Nanosafety	MIL-100(Fe)	MIL-100(Fe) @ DOPC	MIL-101(Cr)	MIL-101(Cr) @ DOPC	Zr-*fum* MOF*small*	Zr-*fum* MOF*large*
Systemic drug delivery via endothelial barrier (25-200µg/ml)	✓	✗	✓	✓	nd	nd
Local delivery via the lung (25-100 µg/ml)	✗	✗	✗	✓	nd	nd
Coating of dental implants (25-200µg/ml)	✓	nd	✓	nd	✓	✓
Coating of neural guidance tubes (12.5-200µg/ml)	✗	nd	✗	nd	✗	✓

nd: not determined, ✗: adverse effects, ✓: biocompatible

This identifies these MOF NPs to be potentially suitable nanomaterials for systemic delivery via the blood. Although pharmacokinetics, such as trans-endothelial migration, absorption, bio-distribution and elimination of the MOF NPs needs to be investigated in further studies, the fact that these NPs do not destroy the endothelium forms a mandatory prerequisite for potential intravenous (i.v.) application in the future.

Our data on the lung-specific applications of MOFs demonstrate that differences in the composition of the MOF NPs reflect directly on the bio-response of the cells. In general, both lung epithelial and alveolar macrophage cell lines were clearly more sensitive to the lipid-coated and non-coated MIL-100(Fe) and MIL-101(Cr) NPs compared to the primary human endothelial cells. This might be related to the differential cell culture conditions, as endothelial cells were cultured as a confluent and tight cell monolayer, while the lung cells were grown at subconfluent conditions. However, subconfluent dental fibroblasts were not sensitive to non-coated MIL-100(Fe) and MIL-101(Cr) nanoparticles. Thus, these differential sensitivities most probably reflect the intrinsic differences between the different cell types as also indicated by the differential sensitivity of lung epithelial and lung immune cells to the MOF NPs. Alveolar macrophages showed a striking sensitivity towards iron-containing MOF NPs. MIL-100(Fe)- and MIL-100(Fe)@DOPC-induced toxicity was accompanied by early upregulation of anti-iron stress-response genes. Of note, the iron-containing MOF NPs did not induce upregulation of early inflammatory marker genes such as IL-6, TNFα and Nos2 which are well known mediators of an acute inflammatory response in the lung to foreign material.[56] This is well in line with the previously observed differential response of alveolar macrophages to diverse nanomaterials.[56] Alveolar epithelial cells tolerated these particles well up to doses of 100 µg/ml. In contrast, Cr-containing MOF NPs were well tolerated by both

alveolar epithelial cells and alveolar macrophages at doses up to 100 µg/ml. We tentatively attribute this different behavior to the high chemical stability of the Cr-containing MOF NPs. Only high and slightly toxic doses of 200 µg/ml induced inflammatory gene expression in the alveolar macrophages. A second important observation from our study on the pulmonary effector cells is that lipid-coated MOF NPs were better tolerated by alveolar epithelial cells than their non-coated counterparts. This may be due to improved cellular uptake as previously shown by some of us.[34] The lipid layer might also act as a stealth coating, thus preventing certain cellular response mechanisms from being activated. In conclusion, lung epithelial and immune cells are less sensitive to Cr-based MOF NPs and induce no adverse cytotoxic effects at the low and middle dose-range. These particles can therefore be envisioned as biocompatible nanocarriers for inhalative lung-specific drug delivery, whereas the Fe-based MOF NPs do not seem to be suitable for pulmonary applications. Nanoparticle-mediated drug delivery into the lung via inhalation represents a novel concept for treatment of lung diseases.[57, 58] It is hampered, however, by the fact that the applied nanocarriers have detrimental side-effects for the lung which may either result from acute inflammation and cytotoxicity or upon their accumulation in lung tissue over time causing chronic lung inflammation as shown previously.[59] The here studied MOFs represent a novel type of biodegradable nanomaterial which may possibly overcome these limitations.

Nanosafety of MOF NPs for surface coating of dental implants was tested in primary human gingiva fibroblasts, which are the effector cells that are in direct contact with nanoparticle-coated grafts. Notably, these cells showed no obvious toxic response towards the tested MOF NPs, i.e. MIL-100(Fe) and MIL-101(Cr) and Zr-*fum* MOF$_{small}$ and $_{large}$. In both assays applied, i.e. measurement of metabolic activity and release of LDH, gingival fibroblasts did not reveal a significant toxic response. Moreover, maintenance of the fibroblastoid morphology of the cells indicated good biocompatibility. The lack of toxicity of the MOF NPs in a wide dose-range supports a possible application for coatings of dental implants. Regarding a future application of MOF NPs as coating and nanocarrier for nerve guidance tubes, our data demonstrate the biocompatibility of the MIL-100(Fe) and MIL-101(Cr) as well as Zr-*fum* MOF$_{small}$ and $_{large}$ MOF NPs with adult Schwann cells in the low dose-range. MOF NPs were also generally well tolerated by cultures of dorsal root ganglia and did not notably interfere with the outgrowth of neuronal axons with the prominent exception of Fe-containing MOFs. In particular the low cytotoxic response of adult Schwann cells as well as the inert behavior of sensory neurons towards Zr-*fum* MOF$_{large}$ particles makes those MOF NPs a promising formulation for surface coating of nerve guidance tubes as suggested previously for polysialic

acid and its mimetics.[60, 61, 62] Recently we were able to demonstrate that iron oxide nanoparticles potentially provide a biocompatible tool to delivery of neurotrophic factors in peripheral nerve reconstruction approaches.[44, 63] Our data on the MOF NPs provide now evidence for their potential as delivery system of regeneration promoting peptides within nerve guidance channels.

In conclusion, our data on the biocompatibility of the MIL-100(Fe) and MIL-101(Cr) and the Zr-*fum* MOF NPs are well in line with published studies on cellular uptake.[12, 13, 18, 19, 25, 34] The most important finding of our comprehensive validation is that there are striking differences in the bio-response of the diverse effector cell types to the distinct MOF-NPs (Table 7-1). For the MIL-100(Fe) and MIL-101(Cr) particles, differential responsiveness appears to be directly related to intrinsic differences of the cell types as colloidal stability of these MOFs has been shown to be preserved in different cell culture media for at least 24 hours.[29]

Lipid coated MIL-101(Cr) MOF NPs can be envisioned so far as safe nanoagents for intravenous systemic drug delivery. We have previously shown that the lipid coated MIL-100(Fe) and MIL-101(Cr) MOF NPs are taken up and well tolerated by the T24 bladder carcinoma cell line suggesting that lipid-coated MOF NPs might be feasible nanocarriers for delivery of cytotoxic drugs to tumor cells.[34] In addition, MIL-100(Fe) and MIL-101(Cr) together with Zr-*fum* MOF NPs might be suitable nanoparticles for surface coating of dental grafts. Zr-*fum* MOF$_{large}$ NPs appear to be promising nanomaterial for inner surface modification of nerve guidance tubes. Of note, the lung is particularly sensitive to any nanomaterial but lipid-coated MIL-101(Cr) MOF NPs might be appropriate nanoagents for inhalative drug delivery at a low to middle dose ranges. The particular sensitivity of the lung to nanomaterial is well known and constitutes the basis for the hazardous effects of inhalatively taken up environmental NPs.[28] These results unambiguously demonstrate the requirement for thorough testing of nanomaterials for their respective nanosafety in specific biomedical applications as suggested recently.[26, 58]

7.3. Conclusion

MOF chemistry offers a unique platform to create functional NPs for different biomedical applications with improved biocompatibility. However, NPs have been shown to bear potential risks for human health. Therefore, we validated various MOF NPs for specific medical fields of application. To the best of our knowledge, this is the first time that such NPs have been systematically evaluated for their biocompatibility with their primary effector cells. We demonstrate that the tested MOF NPs show differential toxicity and bio-response in different effector cells tested. Thus, this work defines a novel strategy that, in addition to highlighting the potential important risks of using MOF NPs for specific medical purposes, also demonstrates their differential suitability for applications in drug delivery and for implant coating. Importantly, for the first time we envision the use of MOF NP coatings for dental implants or cellular guidance tubes and show their nanosafety regarding the respective effector cells, such as gingiva fibroblasts and peripheral nerve cells.

Our results thus clearly demonstrate the requirement for thorough testing of nanomaterials regarding their nanosafety in specific biomedical applications as suggested recently, and illustrate the impact of the molecular interface of the MOF NPs for their respective use for systemic drug delivery and surface modification of implants.[26, 56]

7.4. Materials and Methods

Chemicals and cells:

Chromium(III) nitrate nonahydrate (99%, *Aldrich*), terephthalic acid (98%, *Aldrich*), ethanol (99%, *Aldrich*) 1,2-dioleoyl-sn-glycero-3-phosphocholine (DOPC, *Avanti Polar Lipids*), iron (III) chloride hexahydrate (Grüssing GmbH), trimesic acid (BTC, Aldrich), zirconium tetrachloride (Sigma Aldrich), fumaric acid (Sigma Aldrich), formic acid (Sigma Aldrich), propionic acid (Sigma Aldrich).

The solvent ethanol (EtOH, Aldrich, absolute) was used without further purification.

Murine alveolar epithelial cell line, MLE 12, and murine alveolar macrophage cell line, MH-S, were purchased from American Type Culture Collection. MLE 12 cells were grown in complete RPMI-1640 medium (Life Sciences) supplemented with 10% fetal bovine serum (BioChrom) and 1% Penicillin/Streptomycin (Life Technologies), and in the case of MH-S cells, further supplemented with 1 mM Na-Pyruvate, 10 mM HEPES, and 50 µM 2-ME (all AppliChem) at 37 °C in a humidified atmosphere containing 5 % CO_2.

Adult human Schwann cells were harvested from donor nerve samples and highly enriched in selective medium and by cold jet washing as described before.[64] Purified human Schwann cell cultures were cultivated on P-ORN-laminin (1 mg/ml P-ORN, 6 µl/ml laminin, both Sigma-Aldrich, Germany) coated 24-well plates in specific medium: melanocyte growth medium plus supplement (PromoCell, Germany) supplemented with 2 mM forskolin (Calbiochem, Germany), 10 ng/ml fibroblast growth factor 2 (Peprotech, Germany), 5 µg/ml bovine pituitary extract (BPE-26, PromoCell, Germany), 10 nM human recombinant heregulin-beta1 (R&D Systems, Germany) and 1% penicillin/streptomycin (pen/strep, PAA Laboratories, Germany). For biocompatibility testing a density of 4-6x10⁴ Schwann cells/ ml was seeded and cultured for 24 h prior to adding 12.5 µg/ml, 50 µg/ml or 200 µg/ml of MOFs to the medium for 72 h. Each condition was analysed in pairs of 2 sister cultures for WST-1 assay and immunocytochemistry.

Primary human umbilical vein endothelial cells (HUVECs) were isolated by collagenase treatment of umbilical cords. Human microvascular endothelial cells (HMEC) were obtained from the Centers for Disease Control and Prevention (CDC, Atlanta, GA, WA). Cells were cultured in endothelial growth medium (Provitro, Berlin, Germany) supplemented with 10%

heat-inactivated fetal calf serum (FCS) and growth factors (basic fibroblast growth factor 10 ng/ml, Heparin 0.004 ml/ml and epidermal growth factor 0.1 ng/ml) on 0.001% Collagen G.

Human primary gingival fibroblasts were purchased from Provitro (Berlin, Germany). Cells were grown in Dulbecco's Modified Eagle Medium (DMEM) (Biochrom) supplemented with 10% fetal bovine serum (PAN Biotech) and 1% Penicillin/Streptomycin (Biochrom) at 37 °C in a humidified atmosphere containing 5% CO_2. After thawing, cells were subcultured two to three times prior to cell testing.

Preparation and cultivation of primary dissociated rat dorsal root ganglia (DRGs): DRGs were dissected from neonatal Hannover Wistar rats (P1-P3; Janvier, France) and collected in HBSS medium (Hanks balanced salt solution without magnesium and calcium) supplemented with 1% pen/strep (all PAA Laboratories, Germany). After isolation, ganglia were incubated in dissociation solution (HBSS, trypsin EDTA (1x)- 0.25% [Gibco, Germany], 0.1% DNase [0.5% stock, Roche Diagnostics, Germany]) for 15 min at 37 °C. Then collagenase IV (160 U/mg, PAA Laboratories, Germany) was added for another 20 min. Digestion of DRGs was stopped by adding N2 medium with 3% fetal calf serum (DMEM-F12 [PAA Laboratories, Germany], 1% N2-supplement [100x, Gibco, Germany], 0.25% bovine serum albumine [fraction V, 25% stock, Sigma-Aldrich Chemie GmbH, Germany)], 200 mM L-glutamine, 1% pen/strep, 100 mM sodium pyruvate [PAA Laboratories, Germany]). After centrifugation, the supernatant was discarded and fresh N2-medium added to the DRGs. Prior to seeding of single DRGs in the center of wells of a 24-well plate, 150μl of growth factor reduced BD Matrigel^{TM} (BD Biosciences, Germany) were plated into each well. After placing a single DRG in the center of each well, the plate was incubated for 5 min at 37 °C. Then 50 μl of N2-medium were carefully added followed by 60 min incubation prior to finally adding 100 μl of N2-medium for 24 h. Medium was then carefully replaced by regular N2-medium or N2-medium supplemented with 50 μg/ml or 100 μg/ml of each MOF investigated. Each condition was tested in pairs of 2 sister cultures and cultured for an additional 48 h prior to fixation and immunocytochemistry.

RNA preparation and qRT-PCR: MH-S cells were treated with either 50 or 200 μg/mL MIL-100(Fe), MIL-101(Cr), MIL-100(Fe)@DOPC, or MIL-101(Cr)@DOPC for 4 h on 24 well plates. 1 μg/mL LPS (Sigma-Aldrich) was used as a positive control. Total RNA from cells was isolated using Roti®-Quick-Kit (Carl Roth, Karlsruhe, Germany). 100 - 1,000 ng per

sample of total RNA were reverse-transcribed using random hexamers (Life Technologies, Carlsbad, CA, USA) and M-MLV reverse transcriptase (Sigma-Aldrich). Quantitative PCR was performed using the SYBR Green LC480 System (Roche Diagnostics, Mannheim, Germany).

Synthesis of MIL-101(Cr) nanoparticles: For the microwave synthesis of MIL-101(Cr) nanoparticles according to literature,[65] chromium(III) nitrate nonahydrate (1.48 g, 3.70 mmol) and terephthalic acid (615 mg, 3.70 mmol) were heated in 20 mL H_2O bidest. to 220 °C under solvothermal conditions (Microwave, Synthos, *Anton Paar*, p = 18 bar) within four minutes. The mixture was kept at 210 °C for two minutes and the resulting suspension was cooled down to room temperature. The nanoparticles were separated from the occurring bulk material by filtration. For purification, the filtrate was washed four times by centrifugation (1st: 20000 rpm, 60 min; 2nd-4th: 20000 rpm, 45 min) and redispersion in EtOH. Afterwards the sample was characterized by DLS, zeta-Potential XRD, BET and TEM measurements.

Synthesis of MIL-100(Fe) nanoparticles: MIL-100(Fe) nanoparticles were synthesized according to literature.[66] Iron (III) chloride hexahydrate (2.43 g, 9.00 mmol) and trimesic acid (0.84 g, 4.00 mmol) were heated in 30 mL H_2O bidest. was put into a Teflon tube, sealed and placed in the microwave reactor (Microwave: Synthos3000, *Anton Paar*). The mixture was heated to 130 °C under solvothermal conditions (p = 2.5 bar) within 30 seconds, kept at 130 °C for 4 minutes and 30 seconds and the resulting suspension was cooled down to room temperature. For purification of the solid, the reaction mixture was centrifuged (20000 rpm, 45 min) and the pellet was redispersed in EtOH. This cycle was repeated two times and the dispersed solid was allowed to sediment overnight. Afterwards the supernatant was filtrated three times, yielding MIL-100(Fe) nanoparticles in a well dispersed suspension. Afterwards the sample was characterized by DLS, zeta-potential XRD, BET and TEM measurements.

Synthesis of MOF@DOPC nanoparticles: MIL-101(Cr)@DOPC and MIL-100(Fe)@DOPC nanoparticles were synthesized according to literature.[34] The amount of 1 mg MIL-101(Cr) or MIL-100(Fe) nanoparticles was centrifuged for 5 min at 14000 rpm (16873 rcf). For the application of the lipid layer, the sample was redispersed in 100 µL of a 3.6 mM DOPC (1,2-dioleoyl-sn-glycero-3-phosphocholine) solution in a 60/40 (v/v)

H_2O/EtOH mixture. 900 µL H_2O was added and mixed as quickly as possible. By increasing the water concentration, the lipid molecules precipitate and are expected to cover the nanoparticle surface with a lipid layer. For purification, the suspension was centrifuged (5 min, 14000 rpm = 16873 rcf), redispersed in 1 mL H_2O and again centrifuged. Finally the nanoparticles were redispersed in 200 µL H_2O.

Synthesis of Zr-*fum* MOF nanoparticles: Zr-fumarate MOF nanoparticles were synthesized according to a published procedure.[30] $ZrCl_4$ (0.517 mmol, 1 eq) was dissolved in 10 mL water and fumaric acid (1.550 mmol, 3 eq) was added. For the production of the small nanoparticles (sample Zr-*fum* MOF*small*), 50 eq of propionic acid were added as modulator; for the preparation of large nanoparticles (sample Zr-*fum* MOF*large*), 70 eq of formic acid were used. The mixture was then transferred into Teflon-capped glass vials that were put into an oven and heated to 120 °C for 24 h. The white precipitate was collected by centrifugation (10000 rpm, 60 min) and washed with 10 mL water and 10 mL ethanol, respectively. The white powders were dried at room temperature.

Apoptosis assay: The apoptosis rate was determined according to Nicoletti et al. 1991.[47] Briefly, cells were treated with the respective MOF particles for 72 h, trypsinized, washed and incubated with a hypertonic solution containing Triton-X100 and 50 µg/ml propidium iodide. Subdiploid DNA content was determined by flow cytometry (Becton Dickinson, Heidelberg, Germany).

Flow cytometric determination of membrane ICAM level: HUVEC cells were treated with the respective MOF particles and cultured for 24 h. As a positive control, 1 ng/ml TNFα was applied. After stimulation, cells were trypsinized and fixed for 10 min with 4 % methanol-free formaldehyde. Next, cells were washed with PBS and labeled with a FITC-conjugated mouse anti human ICAM antibody (CD54-FITC # 15.2, Biozol, Eching, Germany) for 45 min. After another washing step the ICAM-level was determined by flow cytometry (Becton Dickinson, Heidelberg, Germany).

Immunocytochemistry: HMEC cells were grown on a Collagen G coated (0.001%) 8-well ibidi µ-slide (ibidi, Martinsried, Germany) and treated for 24 h with the respective MOF particles. Cells were fixed with 4% paraformaldehyde, and permeabilized with 0.2 % Triton

X-100 in PBS. After blocking the unspecific binding sites with 1 % BSA, 0.1 %Triton in PBS, Hoechst22358® and rhodamine-conjugated phalloidin (Invitrogen, Eugene, OR, USA) were diluted 1:400 in the blocking solution to stain nuclei and F-actin, respectively, for 2 h at room temperature. Next, cells were washed three times with PBS and once with distilled water and then mounted in PermaFluorTMmounting medium (Beckman Coulter, Krefeld, Germany).

To evaluate Schwann cell morphologies and neurite outgrowth from DGR cultures, immunocytochemistry was performed. For this purpose, cell cultures were gently washed with phosphate buffered salt solution (PBS, Sigma-Aldrich, Germany) and fixed for 20 min with 4% paraformaldehyde (PFA, Merck, Germany). Human Schwann cell cultures were then incubated for 24 h (4 °C) with Schwann cell specific α-S100 antibody (polyclonal, 1:200, DAKO, Denmark) in PBS/0.3% Triton-X-100/5% BSA solution. After washing with PBS, incubation with Alexa 488 goat α-rabbit secondary antibody (1:500, Invitrogen, Germany) for ~1.5 h at room temperature (RT) followed. For detection of neurite outgrowth from DRG cultures, blocking of unspecific antibody binding was induced by incubation with PBS/0.3 Triton-X-100 containing 3% normal goat serum (NGS, GIBCO, Germany) for 1 hr at RT. DRG cultures were incubated overnight (4 °C) with neuron specific α-β-III-tubulin antibody (monoclonal, 1:500, Upstate Biotechnology, USA) in PBS/0.3%Triton-X-100 containing 1% NGS. After washing with PBS, incubation with Cy 3 conjugated goat α-mouse secondary antibody (1:500, Jackson Immunoresearch, USA) for ~1.5 h (RT) followed.

Cell nuclei were counterstained with DAPI (1:1000, Sigma-Aldrich, Germany). After final washing, the plates were subjected to fluorescence microscopy (BX61, Olympus, Germany). For quantification of neurite outgrowth from DRGs, 6-8 images per condition were captured at 20x magnification using Cell P® (Olympus, Germany) and Image J software (Wayne Rasband) and merged to a complete picture. Neurites extending from the DRGs were quantified at a distance of 600 μm from their neuronal nuclei-containing centres.

MTT assay: MTT assay was performed to assess cellular viability upon MOF exposure. Briefly, 3×10^3 gingival fibroblasts were seeded in a 96 well plate, whereas 8×10^4 cells/well MLE 12 or MH-S were seeded in 24 well plates. 24 h after seeding, cells were exposed to 25, 50, 100, or 200 μg/mL MOF suspensions in fresh media for 24 h. After treatment, cells were incubated with Thiazolyl Blue Tetrazolium Bromide solution for determination of metabolic activity (Roche for gingival fibroblasts, Sigma for MLE 12 and MH-S). Absorbances were

measured at 570-580 nm (650 nm reference) using the plate readers Infinite F200 (Tecan) for gingival fibroblasts and Tecan Sunrise for MLE 12 and MH-S cells.

WST-1 assay – human Schwann cells: Because primary adult Schwann cells do not proliferate as fast as the other cell lines used here in this study, their metabolic activity was measured after 72 h of culture time with the WST-1 assay. After 72 h of cultivation in the presence of different MOF concentrations the culture medium was removed and the wells washed with PBS in order to remove all nanoparticles. Then 350 µl/well of culture medium containing the WST-1 compound (1:10) were added. Cells were incubated for ~3.5 h at 37 °C in humidified atmosphere with 5 % (v/v) CO_2. Afterwards triplicates of 100 µl from each sample were transferred to 96-well plates and the optical density (OD) was measured at 450 nm using a multiwell plate reader (EL_x800 BioTek Instruments).

LDH assay: Cell death upon exposure to MOFs of gingival fibroblast, MLE12, HUVEC, and MH-S cells was assessed by the LDH Cytotoxicity Detection Kit (Roche). Cells were seeded and treated with MOFs as described above for the MTT assay. Positive controls were generated by lysing the cells with 1% Triton X-100 (Fluka BioChemika for gingival fibroblasts, AppliChem for MLE 12 and MH-S). After MOF treatments for 24 h, supernatants were used for the LDH reaction. Absorbances were measured at 492 nm (650 nm reference) using the plate readers Infinite F200 (Tecan) for gingival fibroblasts and Tecan Sunrise for MLE 12 and MH-S cells.

Statistics: Data from adult human Schwann cell cultures and human endothelial cells were analyzed using Two-Way ANOVA (Tukey's multiple comparison test), and data from DRG neurite outgrowth assays with the Mann-Whitney-Test using the Graph Pad Prism 6.0 software (Graph Pad, USA). MTT and LDH assay data from gingiva fibroblast, MLE 12 and MH-S cells were analyzed by Two-Way ANOVA using GraphPad Prism 6.0. RT-qPCR data from MH-S cells were analyzed with the Kruskal-Wallis-Test with Dunn's comparison post-hoc test using GraphPad Prism 5.0.

7.5. References

[1]   C. A. Schutz, L. Juillerat-Jeanneret, H. Mueller, I. Lynch, M. Riediker, *Nanomedicine (London, U. K.)* **2013**, *8*, 449.

[2]   V. Wagner, A. Dullaart, A.-K. Bock, A. Zweck, *Nat. Biotechnol.* **2006**, *24*, 1211.

[3]   S. H. van Rijt, T. Bein, S. Meiners, *Eur. Respir. J.* **2014**, *44*, 765.

[4]   H. C. Zhou, J. R. Long, O. M. Yaghi, *Chem. Rev.* **2012**, *112*, 673.

[5]   H.-C. J. Zhou, S. Kitagawa, *Chem. Soc. Rev.* **2014**, *43*, 5415.

[6]   G. Ferey, *Chem. Soc. Rev.* **2008**, *37*, 191.

[7]   H. Furukawa, K. E. Cordova, M. O'Keeffe, O. M. Yaghi, *Science* **2013**, *341*, 974.

[8]   S. Kitagawa, R. Kitaura, S. Noro, *Angew. Chem. Int. Ed. Engl.* **2004**, *43*, 2334.

[9]   A. Carne, C. Carbonell, I. Imaz, D. Maspoch, *Chem. Soc. Rev.* **2011**, *40*, 291.

[10]   P. Horcajada, R. Gref, T. Baati, P. K. Allan, G. Maurin, P. Couvreur, G. Férey, R. E. Morris, C. Serre, *Chem. Rev.* **2012**, *112*, 1232.

[11]   S. Furukawa, J. Reboul, S. Diring, K. Sumida, S. Kitagawa, *Chem. Soc. Rev.* **2014**, *43*, 5700.

[12]   V. Agostoni, P. Horcajada, M. Noiray, M. Malanga, A. Aykaç, L. Jicsinszky, A. Vargas-Berenguel, N. Semiramoth, S. Daoud-Mahammed, V. Nicolas, C. Martineau, F. Taulelle, J. Vigneron, A. Etcheberry, C. Serre, R. Gref, *Sci. Rep.* **2015**, 5: 7925.

[13]   P. Horcajada, T. Chalati, C. Serre, B. Gillet, C. Sebrie, T. Baati, J. F. Eubank, D. Heurtaux, P. Clayette, C. Kreuz, J.-S. Chang, Y. K. Hwang, V. Marsaud, P.-N. Bories, L. Cynober, S. Gil, G. Ferey, P. Couvreur, R. Gref, *Nat. Mater.* **2010**, *9*, 172.

[14]   K. Khaletskaya, J. Reboul, M. Meilikhov, M. Nakahama, S. Diring, M. Tsujimoto, S. Isoda, F. Kim, K.-i. Kamei, R. A. Fischer, S. Kitagawa, S. Furukawa, *J. Am. Chem. Soc.* **2013**, *135*, 10998.

[15]   S. Diring, D. O. Wang, C. Kim, M. Kondo, Y. Chen, S. Kitagawa, K.-i. Kamei, S. Furukawa, *Nat. Commun.* **2013**, 4: 2684

[16]   A. C. McKinlay, P. K. Allan, C. L. Renouf, M. J. Duncan, P. S. Wheatley, S. J. Warrender, D. Dawson, S. E. Ashbrook, B. Gil, B. Marszalek, T. Düren, J. J. Williams, C. Charrier, D. K. Mercer, S. J. Teat, R. E. Morris, *APL Mater.* **2014**, *2*, 124108.

[17]   J. W. Brown, B. L. Henderson, M. D. Kiesz, A. C. Whalley, W. Morris, S. Grunder, H. Deng, H. Furukawa, J. I. Zink, J. F. Stoddart, O. M. Yaghi, *Chem. Sci.* **2013**, *4*, 2858.

[18]   C. He, K. Lu, D. Liu, W. Lin, *J. Am. Chem. Soc.* **2014**, *136*, 5181.

[19] T. Baati, L. Njim, F. Neffati, A. Kerkeni, M. Bouttemi, R. Gref, M. F. Najjar, A. Zakhama, P. Couvreur, C. Serre, P. Horcajada, *Chem. Sci.* **2013**, *4*, 1597.

[20] A. Carné-Sánchez, I. Imaz, M. Cano-Sarabia, D. Maspoch, *Nat. Chem.* **2013**, *5*, 203.

[21] A. Nel, T. Xia, L. Madler, N. Li, *Science* **2006**, *311*, 622.

[22] P. Rivera-Gil, D. Jimenez De Aberasturi, V. Wulf, B. Pelaz, P. Del Pino, Y. Zhao, J. M. De La Fuente, I. Ruiz De Larramendi, T. Rojo, X.-J. Liang, W. J. Parak, *Acc. Chem. Res.* **2013**, *46*, 743.

[23] C. Y. Tay, M. I. Setyawati, J. Xie, W. J. Parak, D. T. Leong, *Adv. Funct. Mater.* **2014**, *24*, 5936.

[24] P. Hirschle, T. Preiß, F. Auras, A. Pick, J. Völkner, D. Valdepérez, G. Witte, W. J. Parak, J. O. Rädler, and S. Wuttke, *CrystEngComm* **2016**, *18*, 4359-4368.

[25] A. Zimpel, T. Preiß, R. Röder, H. Engelke, M. Ingrisch, M. Peller, J. O. Rädler, E. Wagner, T. Bein, U. Lächelt and S. Wuttke, *Chem. Mater.* **2016**, *28*, 3318-3326.

[26] A. E. Nel, W. J. Parak, W. C. Chan, T. Xia, M. C. Hersam, C. J. Brinker, J. I. Zink, K. E. Pinkerton, D. R. Baer, P. S. Weiss, *ACS Nano* **2015**, *9*, 5627.

[27] H. F. Krug, *Angew. Chem. Int. Ed. Engl.* **2014**, *53*, 12304.

[28] G. Oberdorster, E. Oberdorster, J. Oberdorster, *Environ. Health Perspect.* **2005**, *113*, 823.

[29] R. Grall, T. Hidalgo, J. Delic, A. Garcia-Marquez, S. Chevillard, P. Horcajada, *J. Mater. Chem. B* **2015**, *3*, 8279.

[30] G. Zahn, H. A. Schulze, J. Lippke, S. König, U. Sazama, M. Fröba, P. Behrens, *Microporous Mesoporous Mater.* **2015**, *203*, 186.

[31] P. Horcajada, S. Surble, C. Serre, D.-Y. Hong, Y.-K. Seo, J.-S. Chang, J.-M. Greneche, I. Margiolaki, G. Ferey, *Chem. Commun.* **2007**, 2820.

[32] G. Férey, C. Mellot-Draznieks, C. Serre, F. Millange, J. Dutour, S. Surblé, I. Margiolaki, *Science* **2005**, *309*, 2040.

[33] D. Cunha, M. Ben Yahia, S. Hall, S. R. Miller, H. Chevreau, E. Elkaïm, G. Maurin, P. Horcajada, C. Serre, *Chem. Mater.* **2013**, *25*, 2767.

[34] S. Wuttke, S. Braig, T. Preiß, A. Zimpel, J. Sicklinger, C. Bellomo, J. O. Radler, A. M. Vollmar, T. Bein, *Chem. Commun.* **2015**, *51*, 15752.

[35] A. Peters, H. E. Wichmann, T. Tuch, J. Heinrich, J. Heyder, *Am. J. Respir. Crit. Care Med.* **1997**, *155*, 1376.

[36] Fromm, K. M., Silver coordination compounds with antimicrobial properties. *Appl. Organomet. Chem.* **2013**, 27, 683-687.

[37]   Keskin, S.; Kızılel, S., Biomedical Applications of Metal Organic Frameworks. *Ind. Eng. Chem. Res.* **2011,** 50, (4), 1799-1812.

[38]   N. Ehlert, P. P. Mueller, M. Stieve, T. Lenarz, P. Behrens, *Chem. Soc. Rev.* **2013**, *42*, 3847.

[39]   N. Ehlert, M. Badar, A. Christel, S. J. Lohmeier, T. Luessenhop, M. Stieve, T. Lenarz, P. P. Mueller, P. Behrens, *J. Mater. Chem.* **2011**, *21*, 752.

[40]   N. Ehlert, A. Hoffmann, T. Luessenhop, G. Gross, P. P. Mueller, M. Stieve, T. Lenarz, P. Behrens, *Acta biomater.* **2011**, *7*, 1772.

[41]   R. Lensing, A. Bleich, A. Smoczek, S. Glage, N. Ehlert, T. Luessenhop, P. Behrens, P. P. Muller, M. Kietzmann, M. Stieve, *Acta biomater.* **2013**, *9*, 4815.

[42]   R. Deumens, A. Bozkurt, M. F. Meek, M. A. Marcus, E. A. Joosten, J. Weis, G. A. Brook, *Progress in neurobiology* **2010**, *92*, 245.

[43] C. Meyer, S. Wrobel, S. Raimondo, S. Rochkind, C. Heimann, A. Shahar, O. Ziv-Polat, S. Geuna, C. Grothe, K. Haastert-Talini, *Cell transplant.* **2016**, *25*, 159.

[44]   M. Morano, S. Wrobel, F. Fregnan, O. Ziv-Polat, A. Shahar, A. Ratzka, C. Grothe, S. Geuna, K. Haastert-Talini, *Int. J. Nanomed.* **2014**, *9*, 5289.

[45]   C. Meyer, L. Stenberg, F. Gonzalez-Perez, S. Wrobel, G. Ronchi, E. Udina, S. Suganuma, S. Geuna, X. Navarro, L. B. Dahlin, C. Grothe, K. Haastert-Talini, *Biomaterials* **2016**, *76*, 33.

[46]   X. Gu, F. Ding, D. F. Williams, *Biomaterials* **2014**, *35*, 6143.

[47]   I. Nicoletti, G. Migliorati, M. C. Pagliacci, F. Grignani, C. Riccardi, *J. Immunol. Methods* **1991**, *139*, 271.

[48]   F. Mackay, H. Loetscher, D. Stueber, G. Gehr, W. Lesslauer, *J. Exp. Med.* **1993**, *177*, 1277-1286.

[49] T. Lawrence, G. Natoli, *Nat. Rev. Immunol.* **2011**, *11*, 750.

[50]   S. W. Ryter, A. M. Choi, *Antioxid. Redox Signaling* **2002**, *4*, 625.

[51]   M. A. Lynes, J. Hidalgo, Y. Manso, L. Devisscher, D. Laukens, D. A. Lawrence, *Cell stress chaperones* **2014**, *19*, 605.

[52]   S. Gordon, F. O. Martinez, *Immunity* **2010**, *32*, 593.

[53]   N. J. Wood, H. F. Jenkinson, S. A. Davis, S. Mann, D. J. O'Sullivan, M. E. Barbour, *J. Mater. Sci.: Mater. Med.* **2015**, *26*, 201.

[54]   H. Millesi, *Acta neurochir. Supplement* **2007**, *100*, 37.

[55]   S. Wrobel, S. C. Serra, S. Ribeiro-Samy, N. Sousa, C. Heimann, C. Barwig, C. Grothe, A. J. Salgado, K. Haastert-Talini, *Tissue Eng., Part A* **2014**, *20*, 2339.

[56] A. Beyerle, A. Braun, A. Banerjee, N. Ercal, O. Eickelberg, T. H. Kissel, T. Stoeger, *Biomaterials* **2011**, *32*, 8694.

[57] P. Zarogoulidis, E. Chatzaki, K. Porpodis, K. Domvri, W. Hohenforst-Schmidt, E. P. Goldberg, N. Karamanos, K. Zarogoulidis, *Int. J. Nanomed.* **2012**, *7*, 1551-1572.

[58] D. A. Bolukbas, S. Meiners, *Nanomedicine (London, U. K.)* **2015**, *10*, 3203.

[59] R. You, W. Lu, M. Shan, J. M. Berlin, E. L. G. Samuel, D. C. Marcano, Z. Sun, W. K. A. Sikkema, X. Yuan, L. Song, A. Y. Hendrix, J. M. Tour, D. B. Corry, F. Kheradmand, *eLife* **2015**, *4*, e09623.

[60] J. Bushman, B. Mishra, M. Ezra, S. Gul, C. Schulze, S. Chaudhury, D. Ripoll, A. Wallqvist, J. Kohn, M. Schachner, G. Loers, *Neuropharmacology* **2014**, *79*, 456.

[61] K. Haastert-Talini, J. Schaper-Rinkel, R. Schmitte, R. Bastian, M. Muhlenhoff, D. Schwarzer, G. Draeger, Y. Su, T. Scheper, R. Gerardy-Schahn, C. Grothe, *Tissue Eng., Part A* **2010**, *16*, 3085.

[62] A. Mehanna, B. Mishra, N. Kurschat, C. Schulze, S. Bian, G. Loers, A. Irintchev, M. Schachner, *Brain* **2009**, *132*, 1449-1462.

[63] O. Ziv-Polat, A. Shahar, I. Levy, H. Skaat, S. Neuman, F. Fregnan, S. Geuna, C. Grothe, K. Haastert-Talini, S. Margel, *BioMed Res. Int.*, **2014**.

[64] K. Haastert, C. Mauritz, S. Chaturvedi and C. Grothe, *Nature protocols*, 2007, *2*, 99-104.

[65] A. Demessence, P. Horcajada, C. Serre, C. Boissiere, D. Grosso, C. Sanchez and G. Ferey, *Chemical communications (Cambridge, England)*, 2009, DOI: 10.1039/b915011k, 7149-7151.

[66] A. García Márquez, A. Demessence, A. E. Platero-Prats, D. Heurtaux, P. Horcajada, C. Serre, J.-S. Chang, G. Férey, V. A. de la Peña-O'Shea, C. Boissière, D. Grosso and C. Sanchez, *European Journal of Inorganic Chemistry*, 2012, **2012**, 5165-5174.
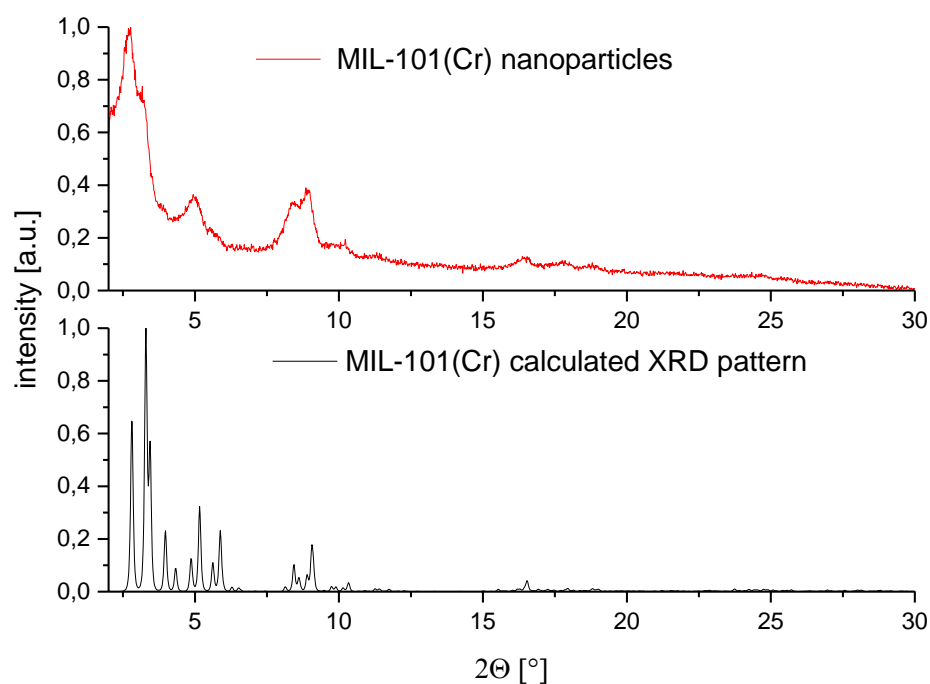
7.6. Appendix

Figure S7-1. X-ray powder diffraction pattern of MIL-101(Cr) nanoparticles (top) and MIL-101(Cr) bulk calculated (bottom).
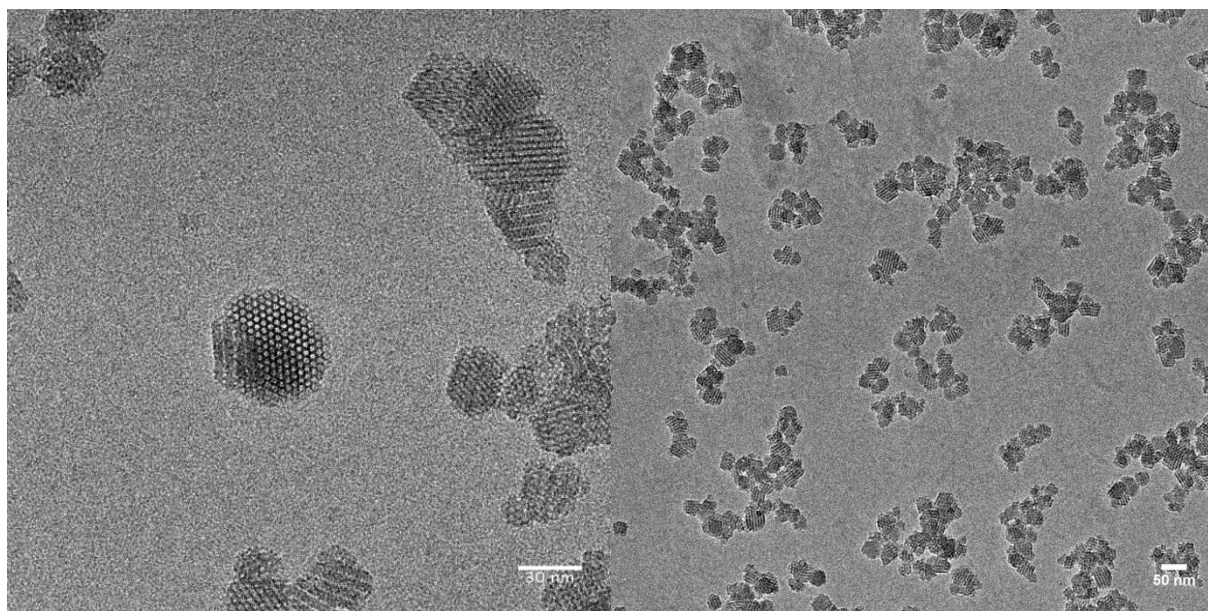

Figure S7-2. Transmission electron micrograph of MIL-101(Cr) nanoparticles – detailed image (left) and overview (right).
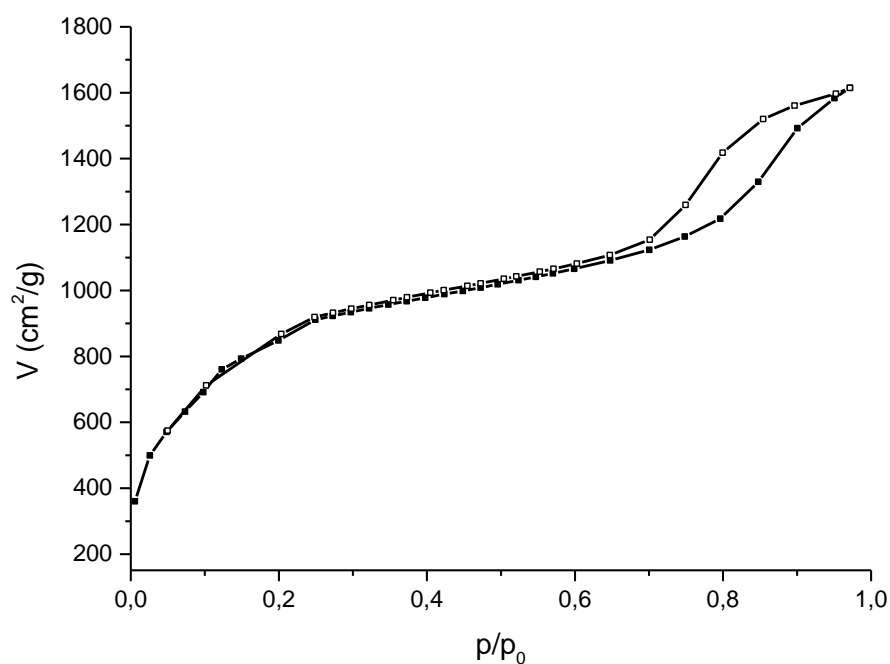
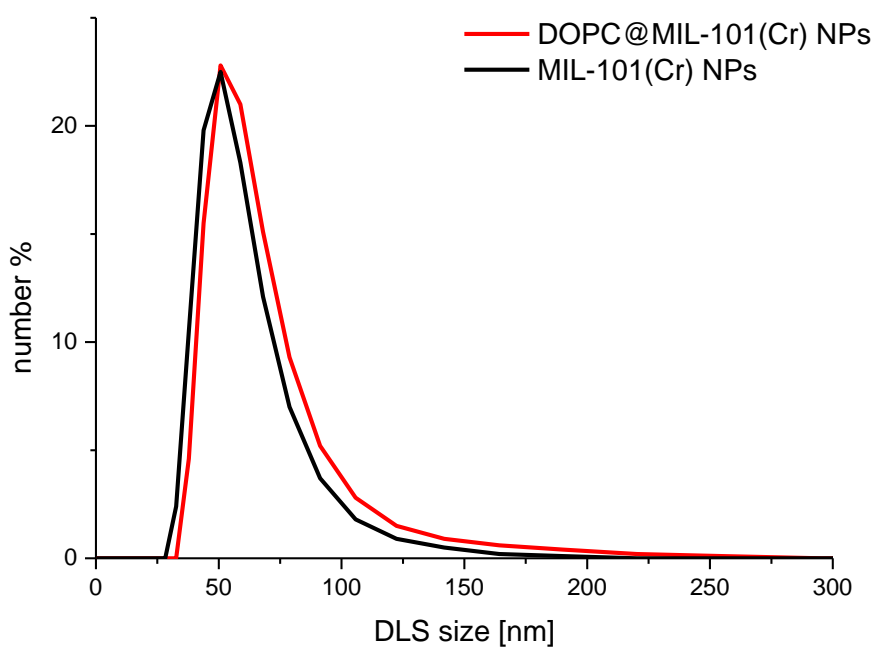**Figure S7-3.** Nitrogen sorption isotherm of MIL-101(Cr) nanoparticles. Calculated BET surface area: 3205 m^2/g.

Figure S7-4. DLS size distribution (measured in water) by number comparing uncoated and DOPC-coated MIL-101(Cr) nanoparticles.
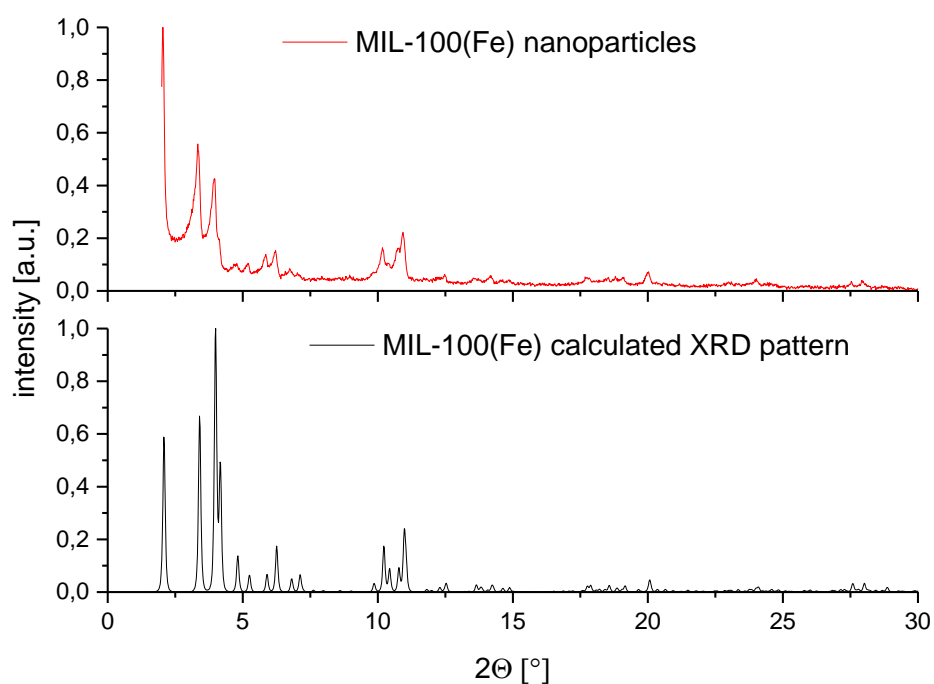
Figure S7-5 X-ray powder diffraction pattern of MIL-100(Fe) nanoparticles (top) and MIL-100(Fe) bulk calculated (bottom).
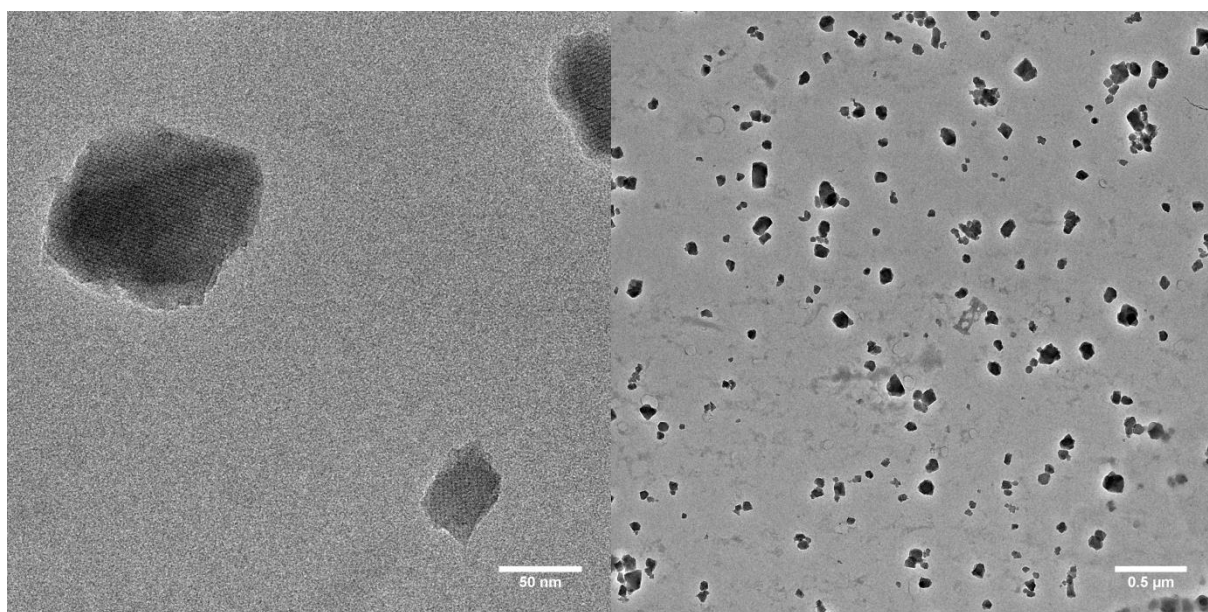

Figure S7-6. Transmission electron micrograph of MIL-100(Fe) nanoparticles - detailed image (right) and overview (left).
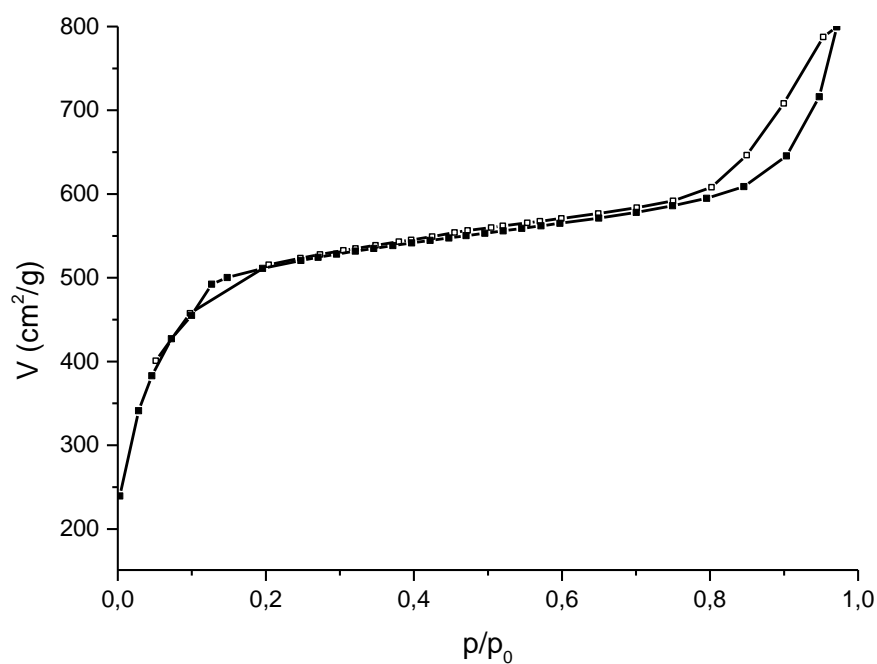
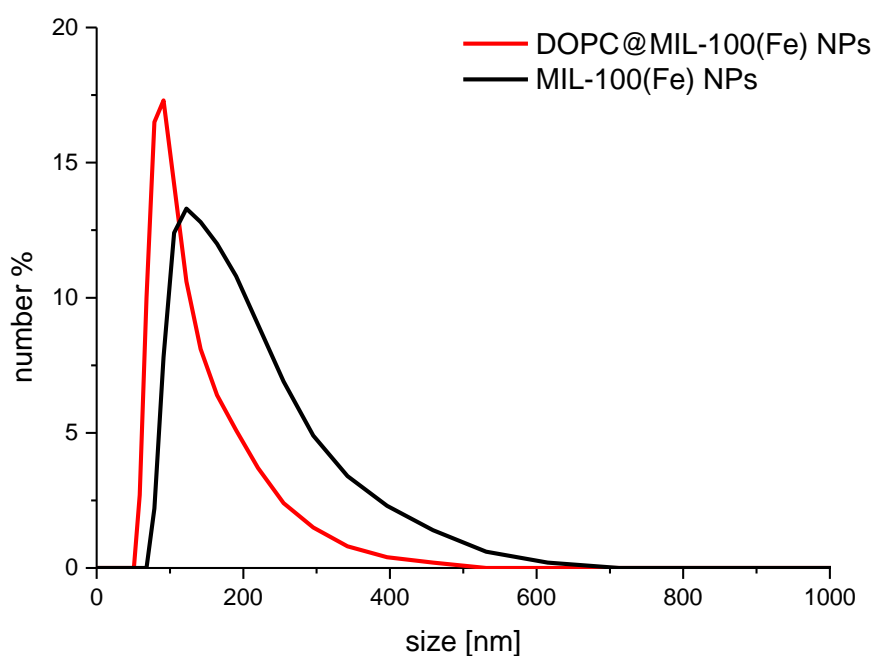**Figure S7-7.** Nitrogen sorption isotherm of MIL-100(Fe) nanoparticles. Calculated BET surface area: 2004 m^2/g.

Figure S7-8. DLS size distribution (measured in water) by number comparing uncoated and DOPC-coated MIL-100(Fe) nanoparticles.
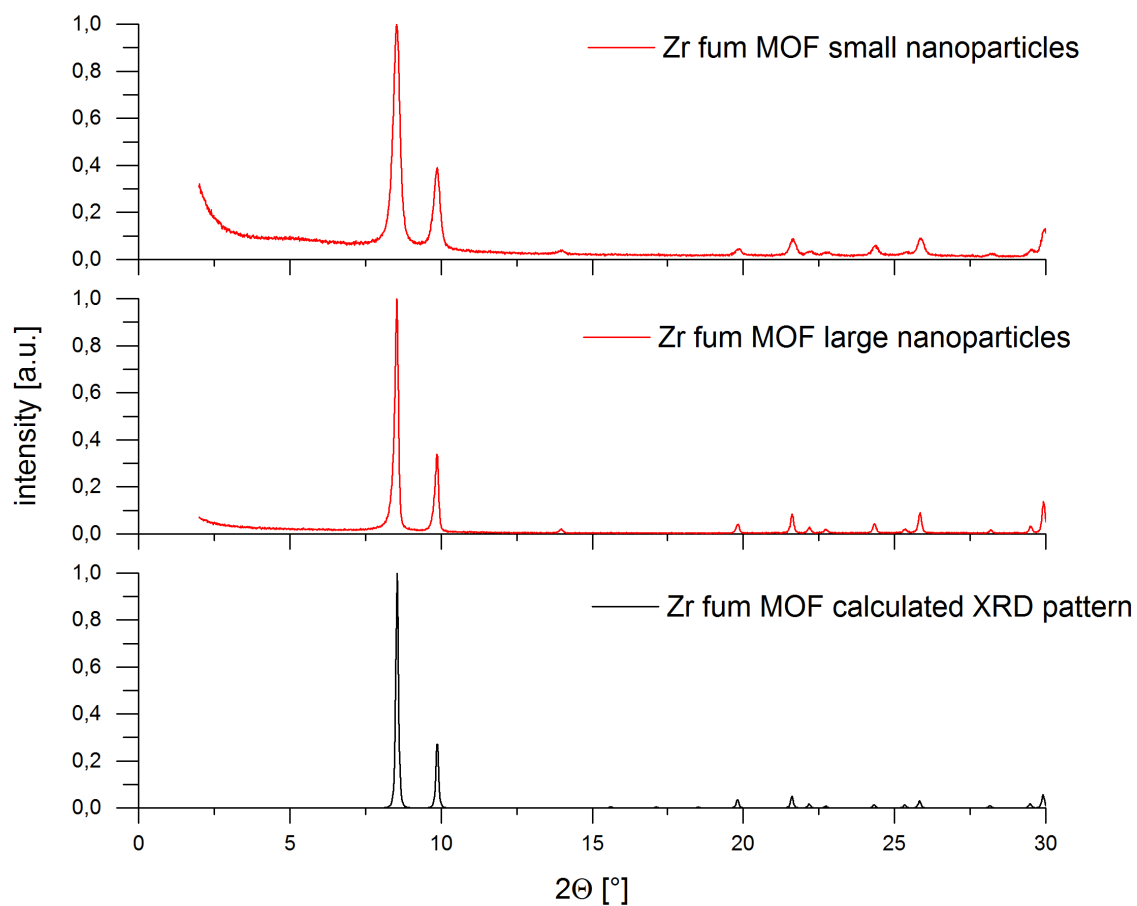
Figure S7-9. X-ray powder diffraction pattern of Zr-*fum* MOF$_{small}$ (top) and Zr-*fum* MOF$_{large}$ (middle) nanoparticles and Zr-*fum* MOF bulk calculated (bottom).
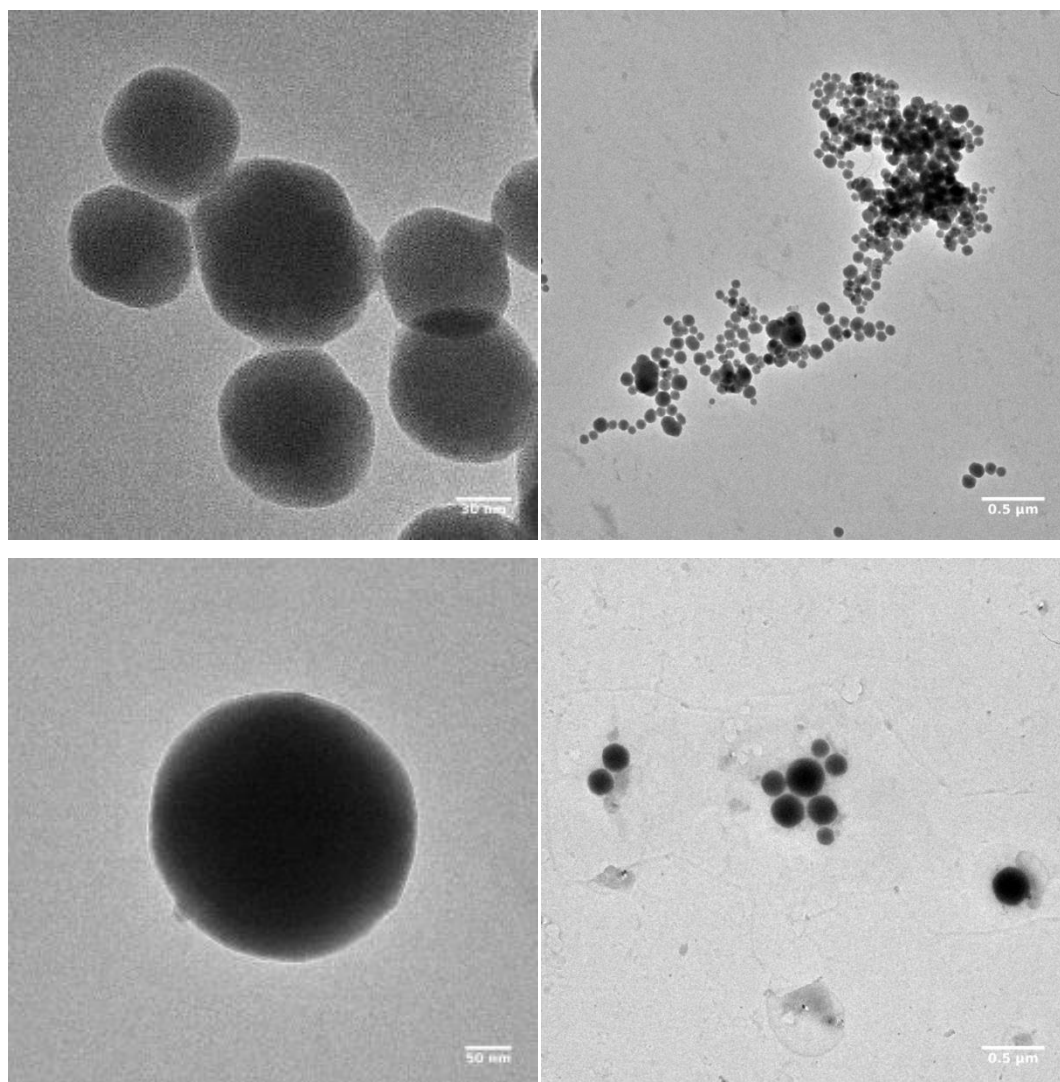
Figure S7-10. Transmission electron micrograph of Zr-*fum* MOF nanoparticles; Zr-*fum* MOF$_{small}$ (top) and Zr-*fum* MOF$_{large}$ (down). Detailed images (left) and overviews (right).
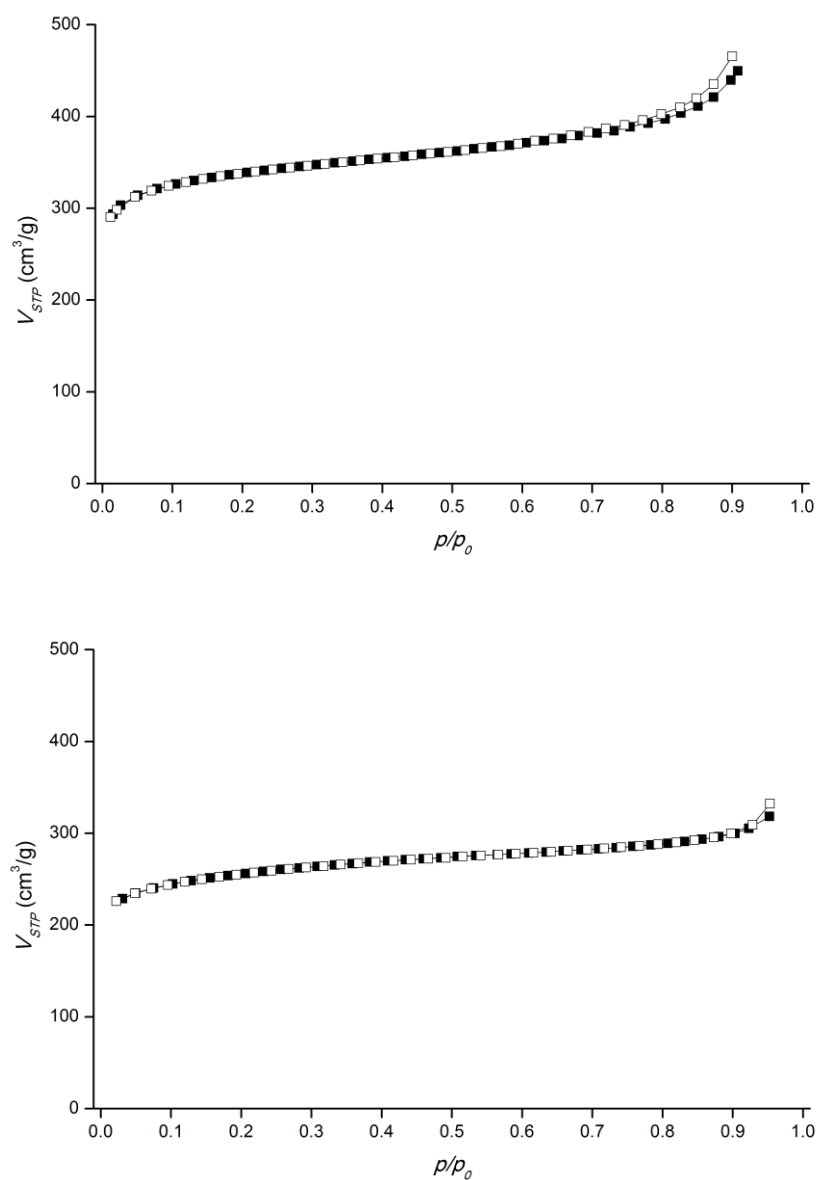
Figure S7-11. Nitrogen sorption isotherm of Zr-*fum* MOF nanoparticles ; Zr-*fum* MOF$_{small}$ (top) and Zr-*fum* MOF$_{large}$ (down). 1250 m²/g and 1000 m²/g Calculated BET surface area of Zr-*fum*-MOF$_{small}$ (top) and Zr-*fum*-MOF$_{large}$: 1250 m²/g and 1000 m²/g, respectively

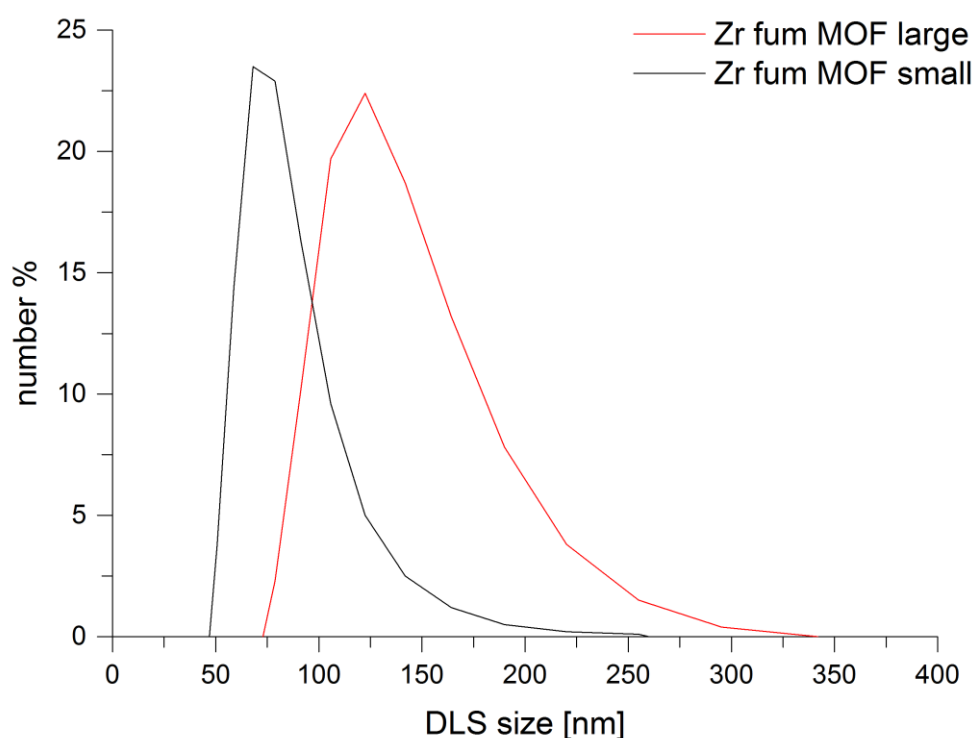**Figure S7-12.** DLS size distribution (measured in water) by number comparing Zr-*fum* MOF$_{small}$ (top) and Zr-*fum* MOF$_{large}$ nanoparticles**.**
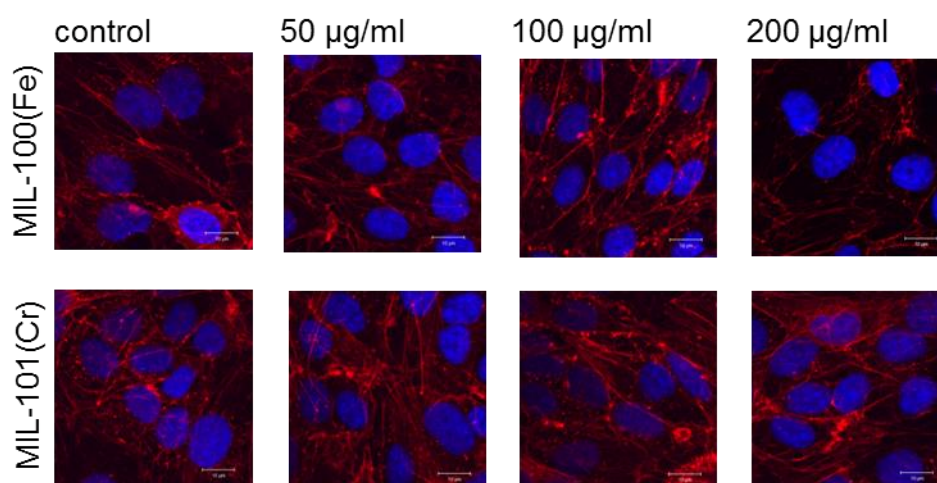

Figure S7-13. Actin staining of MIL-100(Fe) and MIL-101(Cr) treated HMEC cells. HMEC cells were treated with the respective MIL-100(Fe) and MIL-101(Cr) concentration for 24 h. Cells were fixed, actin and nuclei were stained and analysed by confocal microscopy.
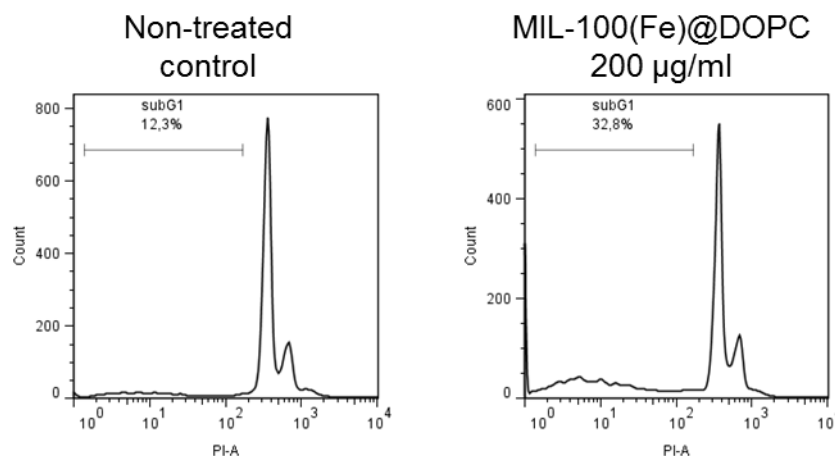
Figure S7-14. Determination of the apoptosis rate by FACS analysis. Apoptotic cells undergo a DNA fragmentation process and are characterized by a reduced DNA content. The DNA content of cells was determined by the DNA intercalating dye propidium iodide (PI). Cells that appear in the subG1 phase have a reduced DNA content and can be identified as apoptotic cells.

Figure S7-15. SEM images of gingival fibroblasts after 24 h incubation with Zr-*fum* MOF$_{small}$ (A, C) and Zr-*fum* MOF$_{large}$ (B, D). 326 fold magnification reveals the cellular morphology (A, B) and 10400 fold magnification reveals the affinity of the NP to the cells (C, D). Cells were fixated with 4% paraformaldehyde and 0.1% glutaraldehyde, dried with ethanol and hexamethyldisilizane and sputtered with 30 nm gold.

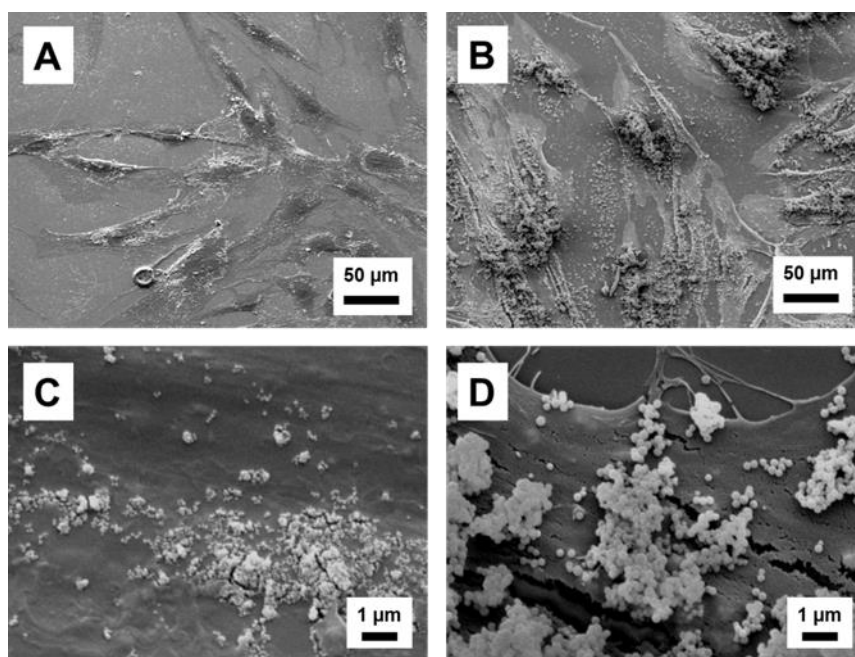# 7. Validating metal-organic framework nanoparticles for their nanosafety in diverse biomedical applications

Table S7-1. Structural properties, hydrodynamic diameter and zeta potential of the different nanoparticles.

MOF	Empirical formula	Metal	Linker	Size (DLS)	PDI (DLS)	Zeta (HBG)
MIL-100(Fe)	$Fe_3O(H_2O)_2OH \cdot \{C_6H_3(CO_2)_3\}_2$	Fe	trimesic acid	180 ± 59 nm	0,278	-42,8 mV
MIL-100(Fe)@DOPC	$Fe_3O(H_2O)_2OH \cdot \{C_6H_3(CO_2)_3\}_2$	Fe	trimesic acid	121 ± 27 nm	0,117	-31,0 mV
MIL-101(Cr)	$Cr_3O(H_2O)_2OH \cdot \{C_6H_4(CO_2)_2\}_3$	Cr	terephthalic acid	57 ± 12 nm	0,162	-0,1 mV
MIL-101(Cr)@ DOPC	$Cr_3O(H_2O)_2OH \cdot \{C_6H_4(CO_2)_2\}_3$	Cr	terephthalic acid	63 ± 13 nm	0,151	2,7 mV
Zr-*fum* MOF$_{small}$	$Zr_6O_4(OH)_4(C_2H_2(CO_2)_2)_6$	Zr	fumaric acid	83 ± 14 nm	0,096	-15 mV
Zr-*fum* MOF$_{large}$	$Zr_6O_4(OH)_4(C_2H_2(CO_2)_2)_6$	Zr	fumaric acid	129 ± 28 nm	0,362	-15 mV

8. pH-selective toxicity of lipid-coated MOF nanoparticles for use as chemotherapeutics

This chapter is based on the following work:

Andreas Zimpel, Sabine Barnert, Stefan Krombholz, Heiko Heerklotz, Valentina Cauda, Stefan Zahler, Angelika M. Vollmar, Stefan Wuttke, and Hanna Engelke; **2018**, *in preparation*
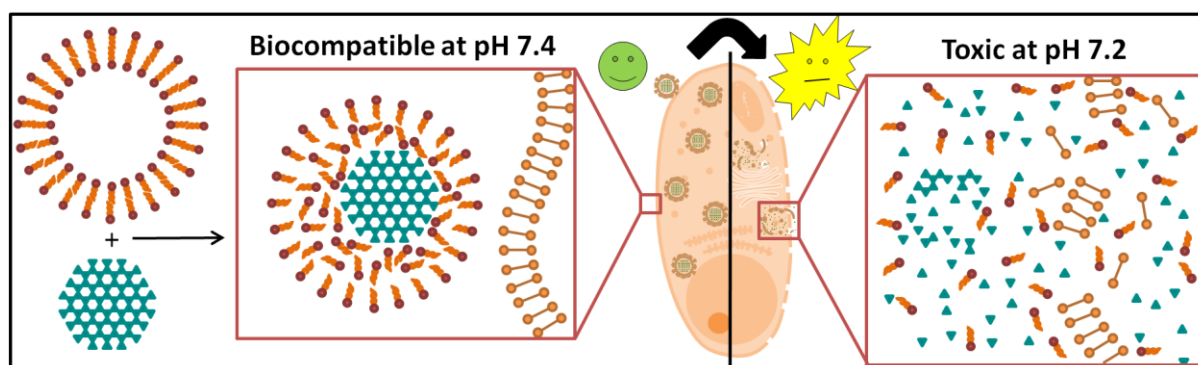
8.1. Introduction

A key challenge in chemotherapy is the selective delivery of drugs to diseased tissue. Any off-target effects of the drugs lead to unwanted side effects.[1] Various kinds of nanoparticles have been designed to overcome this challenge. Usually, these nanoparticles act as nanocarriers encapsulating the drugs and releasing them at the target tissue. However, the employed drugs are usually highly toxic substances and any premature leakage may lead to severe side effects.[2] Even very tight capping mechanisms[3-4] or incorporation of the drug into the structure of the nanocarrier[5] cannot guarantee the absence of premature leakage. Furthermore, after release and action at the target site the drugs may induce side effects in the surrounding tissue before their clearance. An ideal alternative to avoid any off-target effects of these drugs would be to perform chemotherapy without the use of inherently toxic substances as drugs. For example, one such strategy is used in phototherapeutic approaches that generate radical oxygen species locally at a tumor site by irradiation of certain nanosized

materials, such as ZnO-nanoparticles[6-7] that have been injected into the tumor. The radical oxygen species will be toxic to the surrounding cells. They will only be generated by local illumination and are very short-lived. Thus, they shouldn't lead to any systemic side effects. However, the materials constituting these nanoparticles may cause toxic effects, penetration of the irradiation is limited, and patients need to be protected from sunlight.[8] An alternative concept for tumor therapy without inherently toxic substances could be to induce a sudden lysosomal burst that has been shown to lead to cell death.[9] Instead of employing lysosomotropic reagents, such a lysosomal burst could be generated by a sudden increase of the osmotic pressure inside the lysosome. This purely physical effect can be generated by a sudden increase in concentration of almost any molecule and avoids any involvement of inherently toxic substances.

For the generation of such a sudden increase of osmotic pressure inside the lysosome, nanoparticles seem very promising candidates. They have the right size and can be functionalized for cellular internalization into the lysosome. Additionally, they can be designed to decompose under the acidic conditions of the lysosome and their degradation will release the building blocks of the nanoparticles at high concentrations[10] leading to the desired enhanced osmotic pressure.

Specifically, metal-organic framework (MOF) nanoparticles exhibit a range of advantageous properties for this purpose. They can be synthesized from a rich plethora of building blocks and are highly tunable in structure and design.[11-13] Their high porosity allows degrading molecules to readily access the nanoparticle structure enabling a rapid decomposition.[14] Furthermore, their building blocks are linked via coordinative bonds that can be tuned to remain stable during transport, but degrade at the desired kinetics in the presence of competing ions in the lysosome.

Based on the finding that lipid-coated MIL-88A is degraded in the lysosome leading to defects in the lysosomal membrane, yet to an extent that doesn't trigger cell death,[10, 15] we sought to find a similar MOF nanoparticle with different degradation kinetics that might induce a strong lysosomal burst followed by cell death. Here we show that lipid-coated MOF NPs (Lip-MOF NPs) consisting of the biocompatible building blocks iron and trimesic acid (MIL-100(Fe)), is internalized into the lysosome and that slight acidification of the extracellular pH leads to degradation and burst of the lysosome followed by necrosis. Neither the single building blocks of the Lip-MOF NPs nor the nanoparticles at physiological pH affect cell viability. With this dependence on the extracellular pH, the effect of lipid-coated MIL-100(Fe) NPs can be locally restricted, e.g., to the acidic environment of a tumor. This

renders them promising candidates for chemotherapy without the involvement of inherently toxic substances.

8.2. Results and Discussion

Nanoparticle design and characterization. MIL-100(Fe) nanoparticles were synthesized as reported in the literature (characterization and detailed synthesis see SI).[16-18] To facilitate their cellular uptake via endocytosis, the nanoparticles were coated with DOPC (=1,2-dioleoyl-*sn*-glycero-3-phosphocholine)-liposomes (see SI, Figure S8-1) employing lipid fusion as previously described.[10, 15, 19]

The resulting lipid-coated MIL-100(Fe) nanoparticles (DOPC-MIL-100(Fe) NPs) showed additional bands in the infrared spectrum resulting from C-H stretching vibrations of the fatty acid chains, confirming the successful lipid coating (see SI, Figure S8-2). Their zeta potential was enhanced compared to the uncoated particles due to the lipids covering the negatively charged external carboxylic groups of the MOF. BET surface area decreased (from 1576 m^2/g to 846 m^2/g) due to the partial pore clogging induced by the lipids (see SI, Fig. S8-3). Crystallinity of MIL-100(Fe) could be retained during the coating procedure: XRD measurements revealed a decrease in peak intensity after coating due to the high amount of organics, but the intensity could be increased again by washing the particles in ethanol (see SI, Fig. S8-4). TEM of the uncoated nanoparticles shows the typical fringe pattern of a crystalline material. In the TEM images of the Lip-MOFs, the pattern is not visible due to the lipid coating. The hydrodynamic radius of the Lip-MOFs was determined by dynamic light scattering to be 250 nm (see SI, Figure S8-5) – a size that is well suited for cellular internalization via endocytosis. Additionally, agglomerates (> 500 nm) can be detected and these findings could be confirmed by cryo-TEM measurements (see SI, Fig. S8-6). Further, combination of cryo- and high resolution TEM (HRTEM) measurements revealed useful information about the nature of the lipid shell which was created around the MIL-100(Fe) nanoparticles. Figure 8-1 shows images of uncoated and coated MOF NPs taken by cryo-TEM compared to HRTEM.
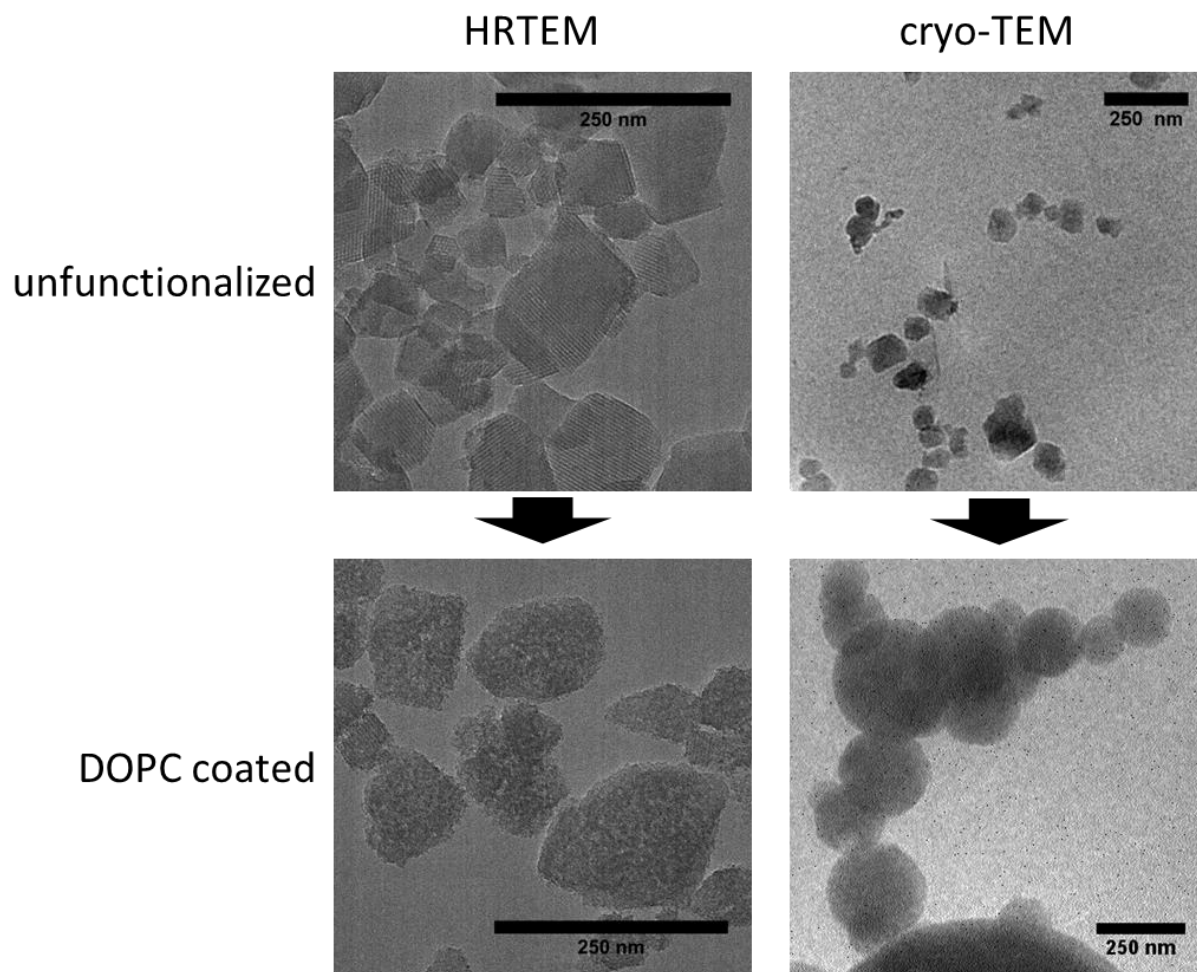
Figure 8-1. TEM images of unfunctionalized (top) and lipid-coated MIL-100(Fe) NPs

HRTEM images show defined edges and lattice planes of the MIL-100(Fe) NPs (top left). The shape of the particles is comparable to cryo-TEM (top right), albeit the resolution of the particles in not as high due to technical properties of the microscopes. Comparing the lipid coated nanoparticles in HRTEM and cryo-TEM (bottom), significant differences can be observed. While HRTEM reveals similar shape and size of the nanoparticles with grainy morphology, cryo-TEM images show roundish nanocomposites with increased size as already indicated by DLS. We attribute these differences in TEM to electron beam sensitivity of the lipid shell which is removed at high voltage in HRTEM but prevented in cryo-TEM due to sample preparation and lower applied voltage. Taking a closer look, cryo-TEM gives further information about the core-shell nature of the nanocomposite (Figure 8-2). Differences between the organic compounds of lipid shell and organic linker containing MOF are hardly visible, as they provide similar contrast (left). Nevertheless, by enhancing the threshold, the MOF nanoparticle within the nanocomposite can be resolved (right), showing again its characteristic edged shape.
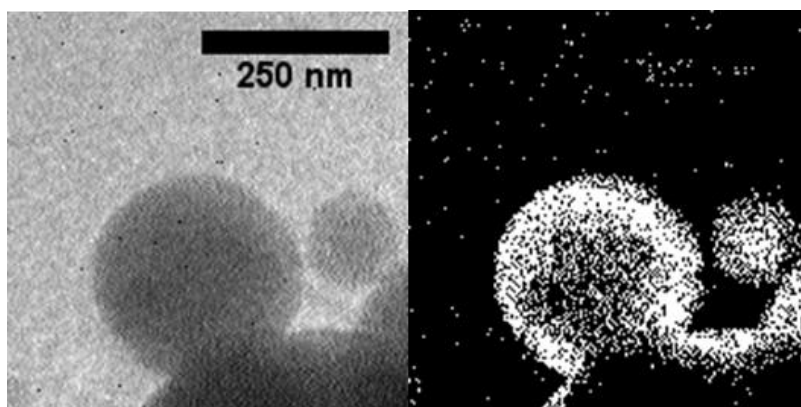
Figure 8-2. cryo-TEM inzoom; original (left) and threshold enhanced (right).

Further, cryo-TEM indicates that DOPC does not form a homogenous lipid bilayer with an aqueous interior but creates a hydrophobic emulsion which completely envelopes the MIL-100(Fe) NPs. These findings are well in accordance with the unexpected high increase in size, as a tight fitting lipid bilayer would only be at the order of a few nanometers.[19]

Effect of DOPC-MIL-100(Fe) NPs on cells. Next, we investigated the effect of Lip-MOFs on cells. We loaded them with the dye calcein prior to liposome coating and incubated them on HeLa cells. Figure 8-3 shows the time course of events after incubation. Directly after incubation the particles are not visible since all calcein is quenched by the nanoparticles. 40 h after incubation calcein was visible in distinct green spots distributed over the cell indicating that it was not encapsulated in the intact Lip-MOF anymore. Shortly after, we observed a sudden spread of the calcein dye all over the cell followed by a burst and deflation of the entire cell.
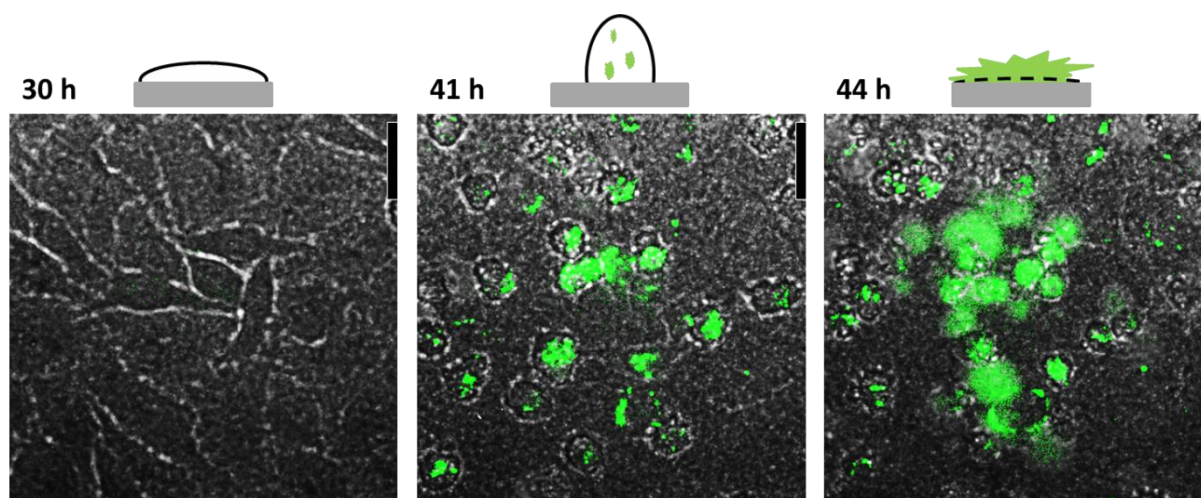

Figure 8-3. CLSM images (overlay of bright-field and fluorescence channel) after 30 h (left), 41 h (middle) and 44 h (right) after incubation. Schematic explanation of the cell shape at the time points (top of each image).

An MTT-test 72h after incubation confirmed the observed toxicity of the Lip-MOF with an IC_{50} of approximatly 9 µg/mL (Figure 8-4A). Strikingly, this toxicity was strongly dependent on the extracellular pH: Metabolizing cells excrete lactic acid leading to a decrease in pH over time. The described cell death was observed in experiments without change of medium resulting in a decrease in pH from 7.4 to 7.2 over time. When the pH was kept constant at pH 7.4 by daily changes of medium, cell viability was not affected significantly (Figure 8-4B). Toxicity of Lip-MOF could be restored by daily changes of medium at pH 7.2 (Figure 8-4C). This toxicity in the absence of any inherently toxic substances renders the Lip-MOF a promising candidate for a new concept of chemotherapeutics avoiding conventional, toxic drugs. Furthermore, the dependence on the acidic extracellular pH provides a means to selectively target the acidic tumor environment in addition to potential targeting ligands that can be attached to the outer lipid surface.[20]
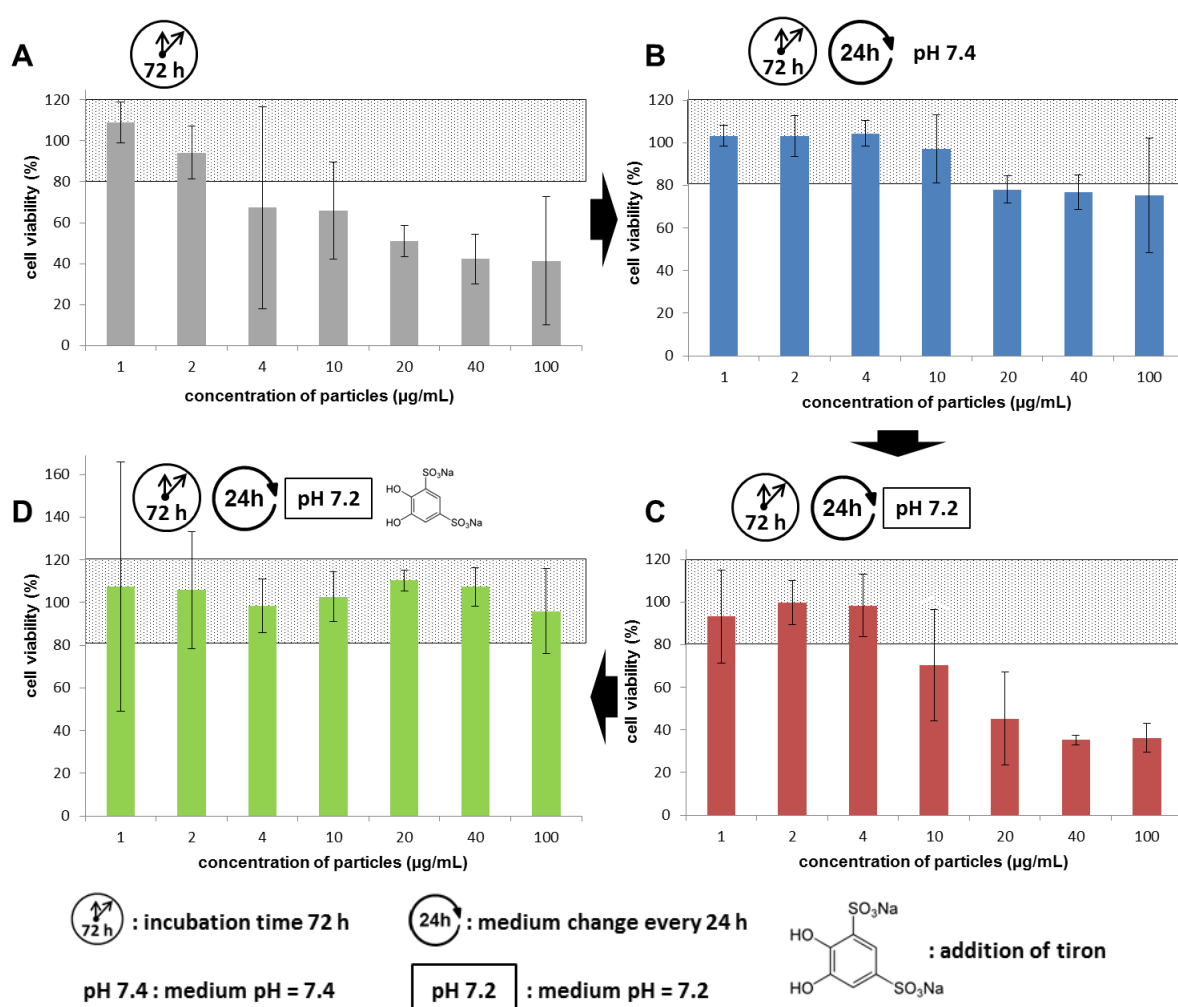

Figure 8-4. MTT plots of DOPC-MIL-100(Fe) NPs after incubation of 72 h (average of 3x3).

Mode of Action. To validate the promise of the Lip-MOF as alternative chemotherapeutic, we sought to investigate its mode of action. First, we studied the cellular internalization mechanism. Cellular uptake of Lip-MOF was quantified 30 min after incubation via inductively coupled plasma optical emission spectrometry (ICP-OES) (Figure 8-5). Comparing the uptake at 37 °C and at 4 °C shows a significant reduction in nanoparticle uptake at reduced temperatures. This reveals energy-dependent endocytosis to be the main uptake pathway for Lip-MOF. Uncoated MIL-100(Fe) on the other hand did not show any toxicity to cells (see SI, Figure S8-7) and its uptake was not significantly reduced at 4°C, i.e. endocytosis was not the main uptake pathway. This suggests that the lipid layer mediates efficient uptake via endocytosis as the first important step for the pH-dependent toxicity of Lip-MOFs.
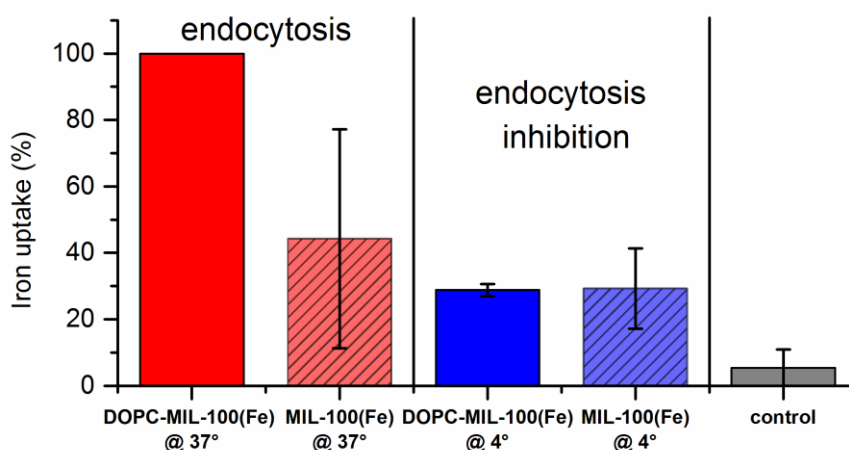
Figure 8-5. Iron uptake of HeLa cells measured by ICP-OES. (Normalized to highest iron uptake for DOPC-MIL-100(Fe) at 37°C).

Further investigation on the uptake mechanism was performed by inhibition of different endocytosis pathways with Dynasore, Cytochalasin D and Filipin, respectively. The results suggest clathrin-mediated endocytosis to be the main uptake pathway as Dynasore showed the strongest reduction in iron uptake measured by ICP-OES (see SI, Figure S8-8).

Lysosomal markers colocalized with the distinct green spots of the dye observed about 40 h after cell incubation with Lip-MOFs (Figure 8-6). Thus, 40 h after incubation via endocytosis the internalized Lip-MOF NPs were in the acidic lysosome, where they were degraded as revealed by the appearance of calcein fluorescence, which is no longer quenched by the nanoparticles.

Figure 8-6. Confocal microscopy images of HeLa cells incubated with DOPC-MIL-100(Fe)-ATTO633 after three days of incubation at lowered extracellular pH.

Lysosomal degradation of the Lip-MOF was also confirmed by immediate decomposition in artificial lysosomal fluid (ALF), which simulates the ly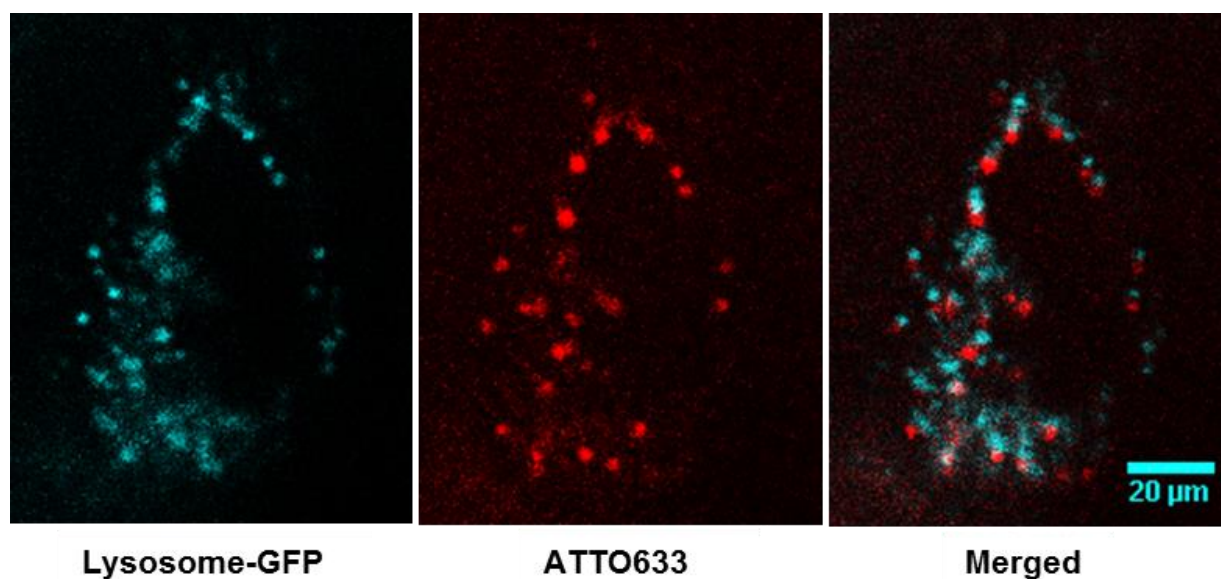sosomal environment. Quantitative UV-Vis measurements of an iron marker revealed within errors a complete decomposition of the Lip-MOF after only one hour in ALF. In simulated body fluid, which simulates the extracellular body environment, no decomposition of the Lip-MOF could be detected. (see SI, Figure S8-9). This decomposition of the Lip-MOF in the lysosome is a crucial part of its toxicity. Accordingly, calcein fluorescence in the lysosome as a reporter of Lip-MOF degradation was observed whenever the necrotic burst of cells followed. Under conditions that do not induce cell death, such as MOF without lipid bilayer or constant extracellular pH 7.4, this calcein fluorescence in the lysosome was not detected. To test the hypothesis that the amount of degradation products generates the lysosomal burst possibly via osmotic pressure, we added tiron to the cells 24 h after MOF incubation. This iron chelator is cell membrane permeable. It will chelate the iron in the lysosome and transport it outside the cell driven by diffusion. This leads to a decrease of iron in the lysosome and should thus decrease the osmotic pressure and inhibit the toxic lysosomal burst. Indeed, we found the addition of tiron to prevent cell burst confirming that the high amount of ions resulting from Lip-MOF degradation leads to the toxic cell death (Figure 8-4D).

Dependence on extracellular pH. Artificial lysosomal fluid contains citric acid, which causes degradation of the Lip-MOF by complexing the iron. Its role in ALF is the simulation of acidic lysosomal enzymes. In order to find the origin of the lysosomal degradation of Lip-MOF we investigated the influence of lysosomal enzymes and side products of their reactions. A direct degradation of the Lip-MOF by enzymes is very unlikely due to their specificity and steric hindrances. Accordingly, none of the tested inhibitors of various lysosomal hydrolases had an effect on the toxicity of Lip-MOF (see SI, Figure S8-10). However, the enzymatic reaction of acidic phosphatases in the lysosome produces phosphoric acid.[21] A test of Lip-MOF stability in the presence of phosphoric acid showed an instantaneous degradation in 1 M phosphoric acid. The degradation in phosphoric acid depended strongly on the concentration of the acid. Time-based dissolution experiments in 0.1 M phosphoric acid revealed a complete dissolution of the nanoparticles within 3 h (see SI, Figure S8-11). Thus, the phosphoric acid produced by acidic phosphatase activity might cause the observed lysosomal degradation of the Lip-MOF. Since we observed degradation of the Lip-MOF only at an extracellular pH of 7.2 or less, we next tested the dependence of phosphatase activity on extracellular pH. Indeed, we found an increase in phosphatase activity at decreased extracellular pH as shown in live-cell images of phosphatase-activity in Figure 8-7.
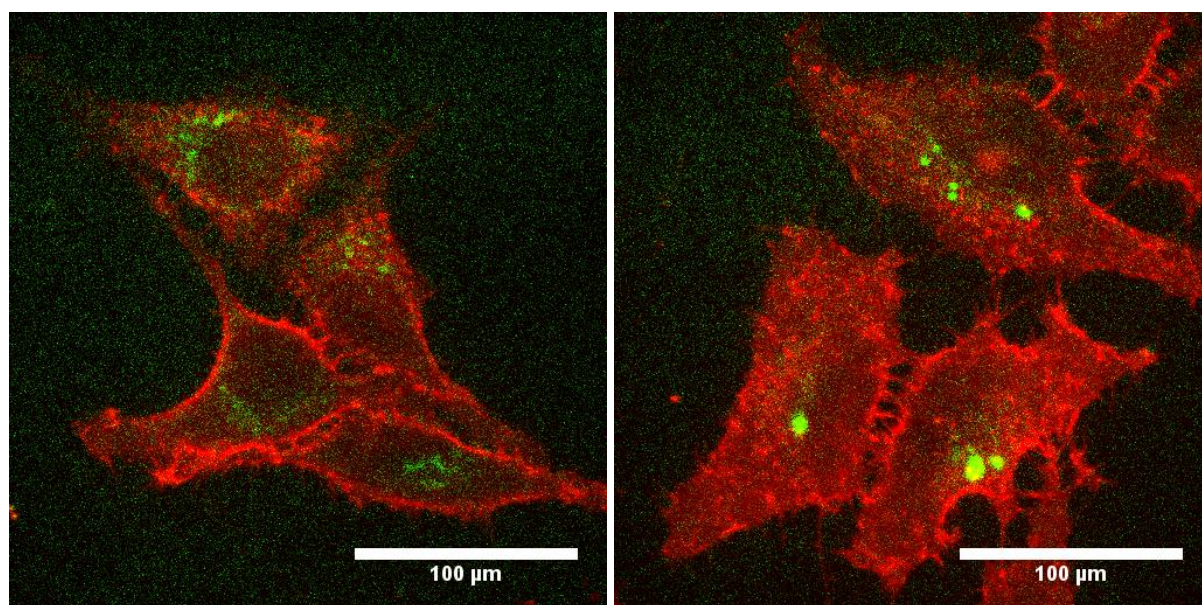
Figure 8-7. Confocal microscopy images of HeLa cells incubated at pH 7.4 (left) and pH 7.2 (right). Green dots show acid phosphatase activity inside the cells being concentrated in the lysosomes and with increased fluorescence intensity for cells incubated at pH 7.2.

This finding is in accordance with changes in lysosomal enzymes with extracellular pH reported in the literature.[22] Given the strong sensitivity of Lip-MOF degradation on the concentration of phosphoric acid, this increase of phosphatase activity at slightly acidic extracellular pH can explain the dependence of Lip-MOF toxicity on the extracellular pH. Beyond an explanation of the pH-dependence, it also suggests phosphatase activity as marker for the efficiency of Lip-MOFs in potential applications.

8.3. Conclusion

Our study demonstrates a novel approach for cancer therapy, using non-toxic components to create a pH-selective chemotherapeutic system. DOPC-liposomes were fused with MIL-100(Fe) NPs, creating so called Lip-MOF NPs in an appropriate size range (approximately 250 nm) for intravenous injection or cellular uptake. The nanocomposites were fully characterized and investigated in a detailed TEM study, comparing HRTEM and cryo-TEM. The images confirmed a successful DOPC-coating of MIL-100(Fe) NPs. Furthermore, the effect on cancer cells was investigated. After 72 h of incubation, HeLa cell viability decreased significantly for Lip-MOF NPs, while HeLa cells incubated with bare MIL-100(Fe) remained unaffected. The observed toxicity of the Lip-MOF NPs was found to be dependent on a slightly acidic external pH of the medium. This is an important feature which makes the system an interesting candidate for treatment of tumor tissue known to provide slightly acidic external pH of its environment. The mechanism of cell death was analyzed by cell uptake and dissolution studies, revealing a high endocytosis mediated cell uptake for the lipid-coated MIL-100(Fe) nanoparticles as well as a very fast dissolution in the lysosome due to increased phosphatase activity by reduced external pH. These results are highly promising for a selective treatment of tumor tissue, which provides lower extracellular pH due to an increased lactic acid fermentation of cancer cells (Warburg effect).

8.4. Materials and Methods

Chemicals: Iron (III) chloride hexahydrate (Grüssing GmbH), trimesic acid (BTC, Aldrich), 1,2-dioleoyl-*sn*-glycero-3-phosphocholine (Avanti Polar Lipids, Inc.; Alabama, USA), Dulbecco's Phosphate-Buffered Saline (DPBS, no calcium, no magnesium; ThermoFisher Scientific), 1-ethyl-3-(3-dimethylaminopropyl)carbodiimide (EDC hydrochloride, Aldrich, crystalline), 2-[4-(2-hydroxyethyl)piperazine-1-yl]ethanesulfonic acid (HEPES, Biomol GmbH), Glucose monohydrate (Applichem), Hanks' balanced salt solution (HBSS), Tiron (4,5-dihydroxybenzene-1,3-disulfonic acid disodium salt, Sigma-Aldrich), LysoLive Lysosomal Phosphatase Assay Kit (Marker Gene, USA)

The solvents ethanol (EtOH, Aldrich, absolute), N-N'-dimethylformamide (DMF, Iris Biotech) and deuterated trichloromethane (CDCl$_3$, Euriso-top, 99.8 % D) were used without further purification. Dichloromethane (DCM) and methyl-tert-butyl ether (MTBE, Brenntag) were distilled before use. Cell culture media, antibiotics and fetal bovine serum (FBS) were purchased from Life Technologies.

Preparation of MIL-100(Fe) nanoparticles: For the microwave synthesis of MIL-100 (Fe) nanoparticles, iron(III) chloride hexahydrate (2.43 g, 9.00 mmol) and trimesic acid (0.84 g, 4.00 mmol) in 30 ml H$_2$O was put into a Teflon tube, sealed and placed in the microwave reactor (Microwave: Synthos3000, *Anton Paar*). The mixture was heated to 130 °C under solvothermal conditions (p = 2.5 bar) within 30 seconds, kept at 130 °C for 4 minutes and 30 seconds, and the resulting solid was cooled down to room temperature. For purification of the solid, the reaction mixture was centrifuged (Sorvall Evolution RC, *Thermo Scientific*, 47808 rcf / 20000 rpm, 20 min), the solvent was removed and the pellet was redispersed in EtOH. This cycle was repeated two times and the dispersed solid was allowed to sediment overnight. The supernatant was filtrated three times (filter discs grade: 391; Sartorius Stedim Biotech), yielding MIL-100(Fe) nanoparticles, which were left in the filtrate. The nanoparticles were characterized as described below.

Labeling of MIL-100(Fe) nanoparticles for fluorescence imaging: For fluorescence measurements MIL-100(Fe) NPs were covalently coupled with ATTO633-NH$_2$ dye via EDC mediated amide-coupling reaction.[18] In general, 5 mg particles were suspended in 1 ml ethanol. After addition of about 1 mg of EDC hydrochloride (5.2 μmol) and 5 μl of dye (0.01 mg; c= 2 mg/ml), the resulting mixture was stirred overnight at room temperature in the dark. Afterwards, the labeled particles were centrifuged (8 min / 16900 rcf) and washed three

times with an EtOH:H$_2$O (1:1) mixture until the supernatant was colorless. The pellet was suspended EtOH and stored in the dark.

Preparation of DOPC liposomes: 10 mg (12.7 μmol) 1,2-dioleoyl-*sn*-glycero-3-phosphocholine were dispersed in 10 mL DPBS. The dispersion was extruded 11 times with a mini-extruder (Avanti Polar Lipids, Alabama, USA) equipped with a polycarbonate membrane (0.1 μm; Whatman, GE Healthcare) which was supported by two polyethylene drain discs (10 mm; Whatman, GE Healthcare). The resulting liposomes were analyzed by DLS and cryo-TEM measurements (see Figure S1).

Preparation of DOPC-coated MIL-100(Fe) nanoparticles: 1 mg MIL-100(Fe) nanoparticles were dispersed in 200 μL DOPC liposome suspension. 200 μL bi-distilled H$_2$O was added and the mixture was shaken for 1.5 h (600 rpm; RT). The particles were centrifuged and the resulting pellet was washed (3x) and stored in DPBS. The resulting material was characterized by DLS, XRD, IR, cryo-TEM, HRTEM, N2 sorption and zeta-potential measurements.

Preparation of HEPES Buffered Glucose (HBG), simulated body fluid (SBF) and artificial lysosomal fluid (ALF): HEPES (2.38 g, 10 mmol) and glucose monohydrate (28.95 g, resulting in 5 w% glucose) were dissolved in bi-distilled H$_2$O (490 mL) and the pH was adjusted to 7.4 by addition of NaOH (approx. 10 mL, 0.5 M). SBF and ALF were prepared according to literature.[23]

Cell culture

HeLa cells were cultured at 37 °C and 5% CO$_2$ in Dulbecco's modified Eagle's medium (DMEM), supplemented with 10% FBS, 100 U/mL penicillin and 100 μg/mL streptomycin.

Metabolic activity assay (MTT)

Standard MTT: HeLa cells were seeded in 96-well plates at a density of 5.000 cells/well 24 h prior to incubation with the different particle concentrations. Particles diluted in 20 μL DPBS were added to each well and incubated on cells for 72 h at 37 °C and 5% CO$_2$. Medium was removed and after washing each well three times with 100 μL Hanks' balanced salt solution (HBSS buffer), 100 μL of MTT solution (3-(4,5-dimethylthia-zol-2-yl)-2,5-diphenyltetrazolium bromide in medium; 0.5 mg/mL) were added. After an incubation time of

2 h, unreacted dye and medium were removed and the 96-well plates were frozen at −80 °C for at least 30 min. The purple formazan product was then dissolved in 100 μL DMSO (dimethyl sulfoxide) per well and quantified measuring absorbance using microplate reader (TecanSpectrafluor Plus, Tecan, Switzerland) at 590 nm with background correction at 630 nm. All studies were performed in triplicate. The relative cell viability (%) related to control wells treated only with 20 μL DPBS was calculated as ([A] test/[A] control) × 100%.

<u>Additional procedures:</u>

- medium was changed every 24 h to maintain controlled medium pH

- medium was adjusted to pH 7.2 by adding 15 μL HCl (1 M) per milliliter medium and incubation over night at 37 °C and 5% CO_2.

- 10 μL of a 1 M Tiron solution was added after medium exchange (after 24 h particle incubation)

Determination of the iron uptake in 24 h: HeLa cells were seeded in 96-well plates (Corning Costar, Sigma-Aldrich, Germany) (5000 cells/well; 100 μL DMEM) and were incubated 24 h post seeding with 10 μL Lip-MOF or MOF dispersion (1 mg/mL in DPBS) per well for 24 h (conditions: 37°C; 5% CO_2). Medium was removed and the cells were washed with DPBS to remove non-internalized particles. By addition of 30 μL trypsin solution (Thermofisher Scientific) and incubation for 10 min at 37°C the cells were detached from the wells. 100 μL DPBS was added and the cells were transferred and combined into a 15 mL conical centrifuge tube. After centrifugation (20 min / 7197 rcf) the supernatant was removed and the cells were analyzed by ICP-OES (12 wells combined).

Determination of uptake mechanisms by thermal endocytosis inhibition: HeLa cells were seeded in 96-well plates (Corning Costar, Sigma-Aldrich, Germany) (5000 cells/well; 100 μL DMEM) and were incubated 24 h post seeding with 10 μL Lip-MOF dispersion (1 mg/mL in DPBS) or 10 μL bare MIL-100(Fe) NPs dispersion (1 mg/mL in DPBS) per well, respectively (conditions: 37 °C; 5% CO_2). After 30 min, medium was removed (12 +12 wells for Lip-MOF and MOF, respectively) and the cells were washed with DPBS to remove non-internalized particles. By addition of 30 μL trypsin-solution and incubation for 10 min at 37 °C the cells were detached from the wells. 100 μL DPBS was added and the cells were transferred into 15 mL conical centrifuge tubes (wells of same particle type were combined). The well plate was afterwards cooled to 4°C for 30 min and the procedure was repeated for 4°C (12 + 12 wells for Lip-MOF and MOF, respectively).

After centrifugation (7197 rcf / 7830 rpm, 20 min) the supernatant was removed and the cells were analyzed by ICP-OES. Experiments were performed in biological triplicates.

Determination of endocytosis mechanism by addition of endocytosis inhibitors: HeLa cells were seeded in 96-well plates (Corning Costar, Sigma-Aldrich, Germany) (5000 cells/well; 100 µL DMEM). 24 h post seeding, medium was replaced by Dynasore (80 µM), Cytochalasin D (10 µM) or Filipin (1 µM) containing medium (12 wells each). The cells were incubated for 30 minutes and 10 µL Lip-MOF dispersion (1 mg/mL in DPBS) per well was added (conditions: 37°C; 5% CO_2). After 30 min, medium was removed and the cells were washed with DPBS to remove non-internalized particles. By addition of 30 µL trypsin solution and incubation for 10 min at 37°C the cells were detached from the wells. 100 µL DPBS was added and the cells were transferred into 15 mL conical centrifuge tubes (wells of same particle type were combined).
After centrifugation (7197 rcf / 7830 rpm, 20 min) the supernatant was removed and the cells were analyzed by ICP-OES. Experiments were performed in biological triplicates.

High resolution transmission electron microscopy (HRTEM): All samples were investigated with an FEI Titan Themis equipped with an extreme field emission gun (X-FEG). A 4k × 4k Ceta 16M^{TM} camera detected bright field and high-resolution TEM images. The samples were prepared by adding a droplet of the diluted ethanolic nanoparticle suspension on a carbon-coated copper grid followed by drying for a few minutes.

Cryogenic electron microscopy (cryo-TEM): All samples were investigated with an Leo 912 Ω-mega TEM (120 keV, Leo Elektronenmikroskopie GmbH, Oberkochen, Germany). The images were detected with a Proscan HSC 2 camera (Oxford Instruments, Abingdon, USA). For sample preparation, a droplet of the corresponding particle suspension (approx. 3 µL) was placed on carbon-sputtered cupper grid (Quantifoil® S7/2 Cu 400 mesh, holey carbon films, Quantifoil Micro Tools GmbH, Jena, Germany), excess of liquid was removed by a filter paper and the grid was shock frosted. It was placed in a cryo sample holder (Model 626-DH, Gatan, Warrendale, USA) and transferred to the TEM. Software iTEM 5.0 (Build 1054, Soft Imaging System GmbH, Münster, Germany) was used to record the images.

Confocal laser scanning microscopy (CLSM): Live-cell microscopy was performed utilizing a spinning disk confocal microscope (Zeiss Observer SD with a Yokogawa CSU-X1

spinning disc unit) and a 63x objective at 37 °C and 5% CO_2. Excitation was with a 488 nm (lysosome-GFP, Calcein in Lip-MOFs) and a 639 nm laser (Atto633/Cy5-labeled MOF). Emission was filtered with a BP 525/50 and a LP 690 filter. Cells were seeded into ibiTreat 8-well slides (ibidi) at a concentration of 5000 cells per well 24-72 h prior to imaging.

For lysosomal staining, CellLight lysosomes-GFP (BacMam 2.0, Thermofisher Scientific) was added to the cells 24 h after cell seeding and at least 24 h before imaging according to the supplier's manual. DOPC-MIL-100(Fe)-ATTO633 NPs (15μL, c_{Stock}= 1 mg/ml) were added 24 h post seeding and after three days of incubation at lowered extracellular pH microscopy was performed. Lysosome-GFP was excited at 100 % of the 488 nm excitation light with an exposure time of 400 ms. ATTO633 was excited at 100 % of the 639 nm excitation light with an exposure time of 100 ms.

For qualitative live cell phosphatase tracking, HeLa cells were seeded into an ibiTreat 8-well microscopy slide (ibidi, Germany) at a density of 5000 cells per well. 24 h after seeding, medium was exchanged to either DMEM at normal pH or at pH 7.2. 24 h later, cells were washed with FBS-free DMEM. 2.5 mL of DMEM was added to one vial of Marker Gene LysoLive Lysosomal Phosphatase Assay Kit according to the manufacturer's instructions. 1 mL of the obtained staining solution was slightly acidified by addition of 15 μL HCl. Subsequently, 300 μL of the staining solution at normal pH and 300 μL of the slightly acidified solution were added to the cells incubated at normal pH and those at pH 7.2 respectively. 18 h after staining, cells were washed twice in PBS, stained with WGA647 (ThermoFisher Scientific) and imaged using the spinning-disk microscope described above. WGA647 was imaged using the 639 nm laser and a 690 LP filter and LysoLive was imaged using a 488 nm laser and a BP 525/50 filter.

Inductively coupled plasma optical emission spectrometry (ICP-OES): Measurements were performed utilizing a radial view simultaneous ICP AES (Vista RL, Varian, Mulgrave, Australia) equipped with a CCD detector. Samples were dissolved in HNO_3 konz. (69% for trace analysis, Aristar®, VWR) and diluted to an appropriate iron concentration.

pH Measurement: All pH measurements were performed by a SevenEasy pH Meter (Mettler Toledo, Ohio, USA) which was calibrated by buffer solutions of pH 4.01, pH 7.00 and pH 9.21. For measurements of the media under cell culture conditions (37 °C, 5% CO_2) the pH Meter was placed in an Galaxy® 14s Incubator (New Brunswick/Eppendorf AG, Germany).

8.5. References

[1]   A. G. Arranja, V. Pathak, T. Lammers, Y. Shi, *Pharmacological Research* **2017**, *115*, 87-95.

[2]   M. W. Tibbitt, J. E. Dahlman, R. Langer, *Journal of the American Chemical Society* **2016**, *138*, 704-717.

[3]   V. Cauda, H. Engelke, A. Sauer, D. Arcizet, C. Bräuchle, J. Rädler, T. Bein, *Nano Letters* **2010**, *10*, 2484-2492.

[4]   C. E. Ashley, E. C. Carnes, G. K. Phillips, D. Padilla, P. N. Durfee, P. A. Brown, T. N. Hanna, J. Liu, B. Phillips, M. B. Carter, N. J. Carroll, X. Jiang, D. R. Dunphy, C. L. Willman, D. N. Petsev, D. G. Evans, A. N. Parikh, B. Chackerian, W. Wharton, D. S. Peabody, C. J. Brinker, *Nature Materials* **2011**, *10*, 389.

[5]   J. G. Heck, J. Napp, S. Simonato, J. Möllmer, M. Lange, H. M. Reichardt, R. Staudt, F. Alves, C. Feldmann, *Journal of the American Chemical Society* **2015**, *137*, 7329-7336.

[6]   S. S. Lucky, K. C. Soo, Y. Zhang, *Chemical Reviews* **2015**, *115*, 1990-2042.

[7]   C. Fu, H. Zhou, L. Tan, Z. Huang, Q. Wu, X. Ren, J. Ren, X. Meng, *ACS Nano* **2018**, *12*, 2201-2210.

[8]   M. Lismont, L. Dreesen, S. Wuttke, *Advanced Functional Materials* **2017**, *27*, 1606314-n/a.

[9]   M. E. Guicciardi, G. J. Gores, *Cell Cycle* **2013**, *12*, 1995-1995.

[10]   B. Illes, P. Hirschle, S. Barnert, V. Cauda, S. Wuttke, H. Engelke, *Chemistry of Materials* **2017**, *29*, 8042-8046.

[11]   H. Furukawa, K. E. Cordova, M. O'Keeffe, O. M. Yaghi, *Science* **2013**, *341*, 1230444.

[12]   M. Rubio-Martinez, C. Avci-Camur, A. W. Thornton, I. Imaz, D. Maspoch, M. R. Hill, *Chemical Society Reviews* **2017**, *46*, 3453-3480.

[13]   H. Furukawa, U. Müller, O. M. Yaghi, *Angewandte Chemie International Edition* **2015**, *54*, 3417-3430.

[14]   H. Furukawa, N. Ko, Y. B. Go, N. Aratani, S. B. Choi, E. Choi, A. Ö. Yazaydin, R. Q. Snurr, M. O'Keeffe, J. Kim, O. M. Yaghi, *Science* **2010**, *329*, 424-428.

[15]   B. Illes, S. Wuttke, H. Engelke, *Nanomaterials (Basel, Switzerland)* **2017**, *7*, 351.

[16]   S. Wuttke, A. Zimpel, T. Bein, S. Braig, K. Stoiber, A. Vollmar, D. Müller, K. Haastert-Talini, J. Schaeske, M. Stiesch, G. Zahn, A. Mohmeyer, P. Behrens, O. Eickelberg, D. A. Bölükbas, S. Meiners, *Advanced Healthcare Materials* **2016**, *6*, 1600818.

[17]   S. Wuttke, S. Braig, T. Preiß, A. Zimpel, J. Sicklinger, C. Bellomo, J. O. Radler, A. M. Vollmar, T. Bein, *Chemical Communications* **2015**, *51*, 15752-15755.

[18]   A. Zimpel, T. Preiß, R. Röder, H. Engelke, M. Ingrisch, M. Peller, J. O. Rädler, E. Wagner, T. Bein, U. Lächelt, S. Wuttke, *Chemistry of Materials* **2016**, *28*, 3318-3326.

[19]   J. Liu, X. Jiang, C. Ashley, C. J. Brinker, *Journal of the American Chemical Society* **2009**, *131*, 7567-7569.

[20]   S. Axel, S. A. M., C. Valentina, S. Alexandra, E. Hanna, R. Ulrich, Z. Kourosh, L. Heinrich, B. Christoph, B. Thomas, *Advanced Healthcare Materials* **2012**, *1*, 360-360.

[21]   H. Bull, P. G. Murray, D. Thomas, A. M. Fraser, P. N. Nelson, *Molecular Pathology* **2002**, *55*, 65-72.

[22]   J. J. Steffan, J. L. Snider, O. Skalli, T. Welbourne, J. A. Cardelli, *Traffic* **2009**, *10*, 737-753.

[23]   M. Marques, R. Löbenberg, M. Almukainzi, *Simulated Biological Fluids with Possible Application in Dissolution Testing, Vol. 18*, **2011**.
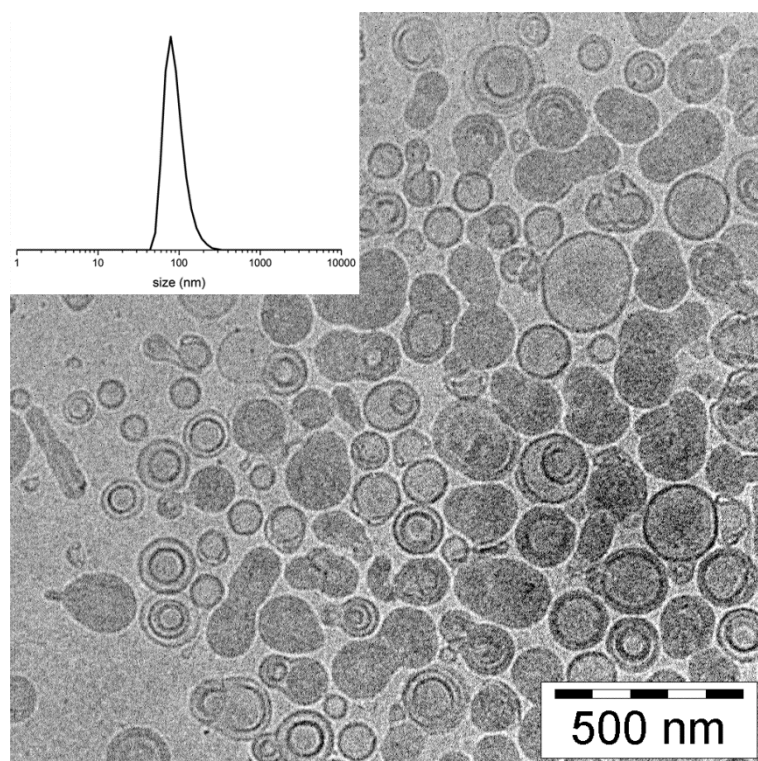
8.6. Appendix

Figure S8-1. Cryo-TEM image of DOPC-liposomes and corresponding DLS measurement (inset) in DPBS buffer solution.

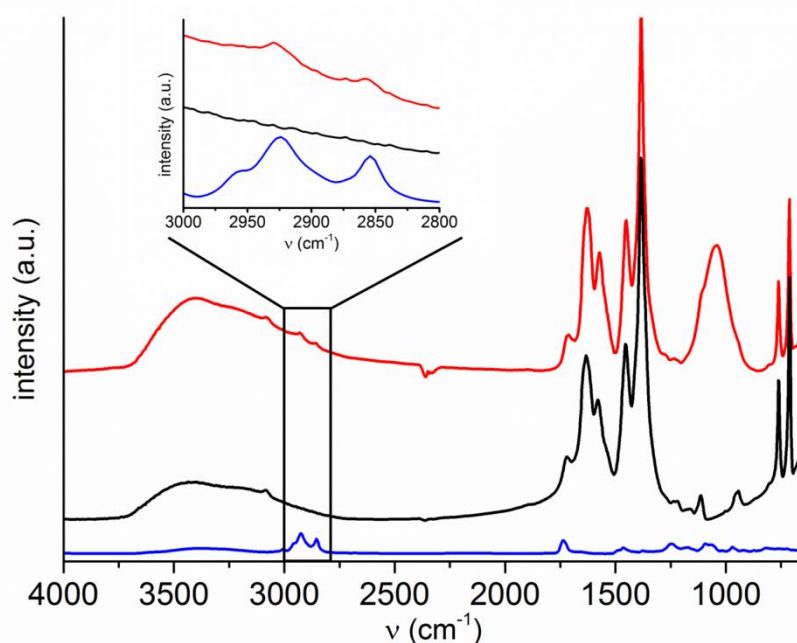**Figure S8-2.** IR spectra of DOPC-MIL-100(Fe) nanoparticles (red) in comparison to unfunctionalized MIL-100(Fe) nanoparticles (black) and pure DOPC (blue). Inset shows a magnification of the significant C-H stretching vibrations present in DOPC and DOPC-MIL-100(Fe).
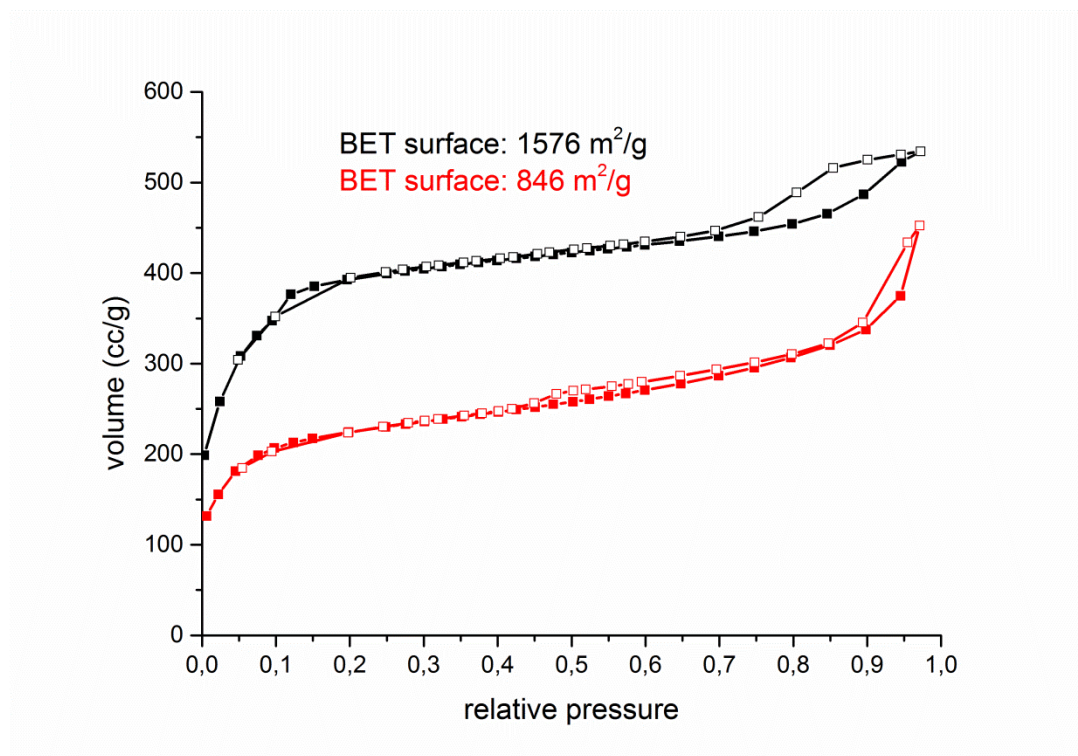
Figure S8-3. N_2-sorption isotherms of unfunctionalized MIL-100(Fe) nanoparticles (**black**) and DOPC-MIL-100(Fe) nanoparticles (**red**).
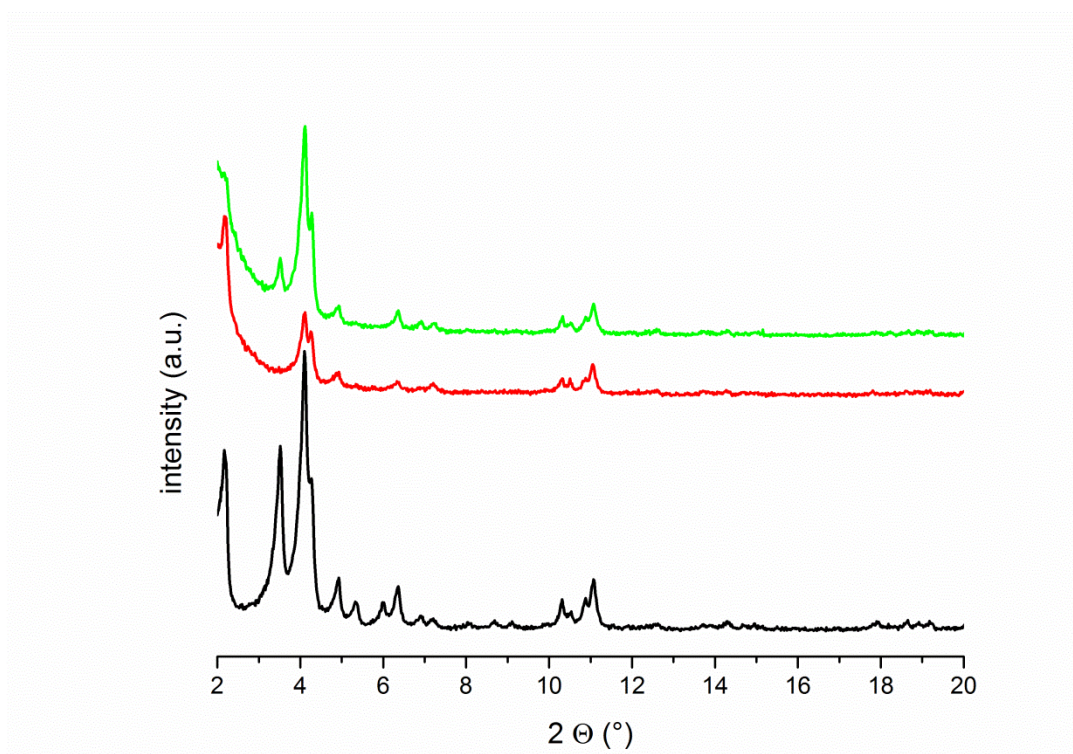

Figure S8-4. X-ray diffraction pattern of MIL-100(Fe) nanoparticles (**black**), DOPC-MIL-100(Fe) nanoparticles (**red**) and ethanol washed DOPC-MIL-100(Fe) nanoparticles (**green**).
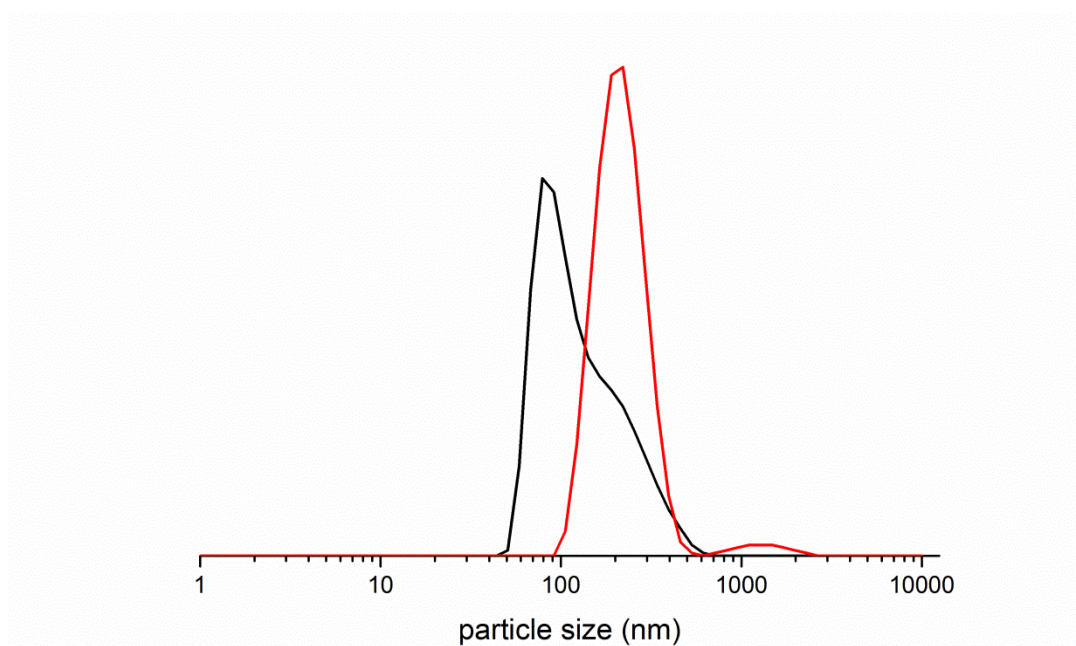
Figure S8-5. DLS plot of unfunctionalized MIL-100(Fe) nanoparticles (**black**) and DOPC-MIL-100(Fe) nanoparticles (**red**).
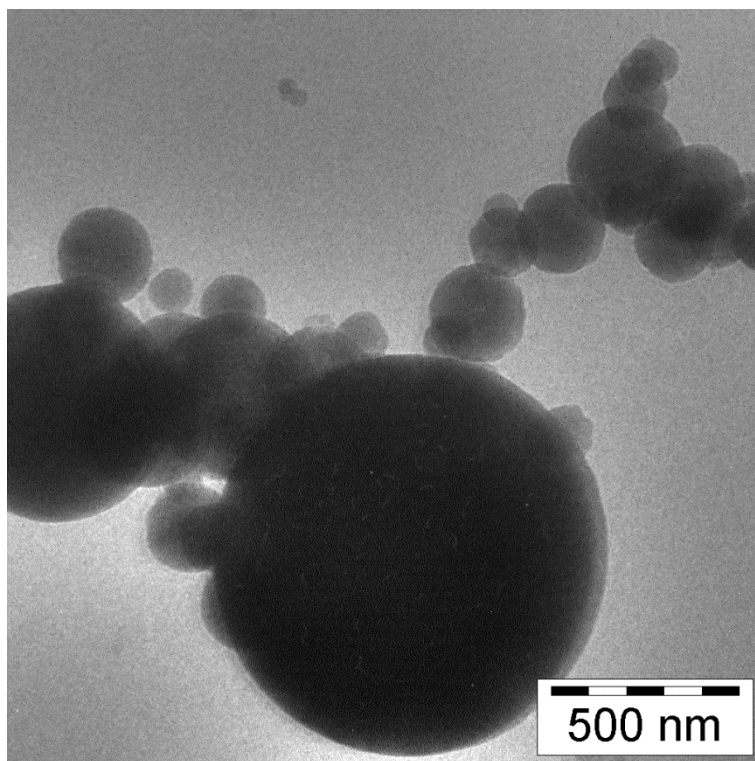

Figure S8-6. Cryo-TEM image of DOPC-MIL-100(Fe) nanoparticles, showing single DOPC-MIL-100(Fe) nanoparticles as well as agglomerates.
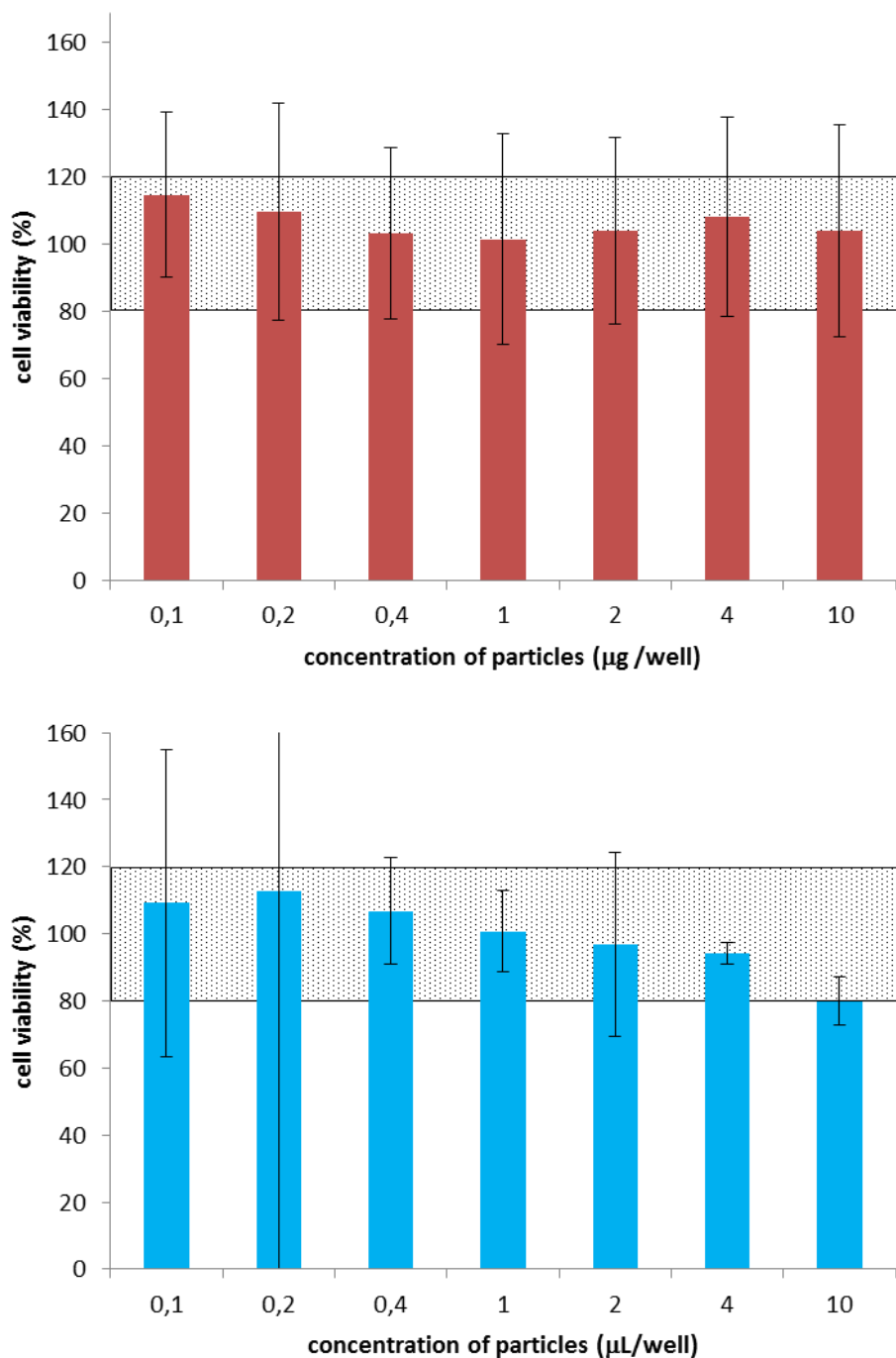
Figure S8-7. MTT cell viability assay of uncoated MIL-100(Fe) NPs (top) and dissolved MIL-100(Fe) (1 mg in 1 mL ALF; bottom) showing both no significant toxicity on HeLa cells.
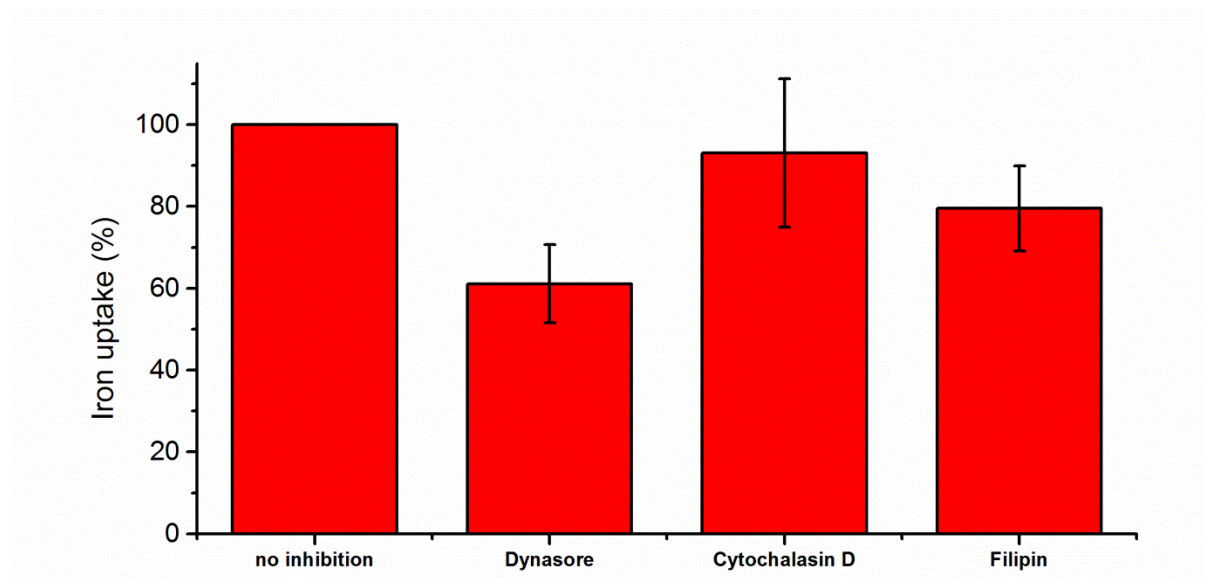
Figure S8-8. Iron uptake of HeLa cells measured by ICP-OES after incubation for 30 min at 37 °C by addition of different endocytosis inhibtors (80 μM Dynasore, 10 μM Cytochalasin D, 1 μM Filipin).
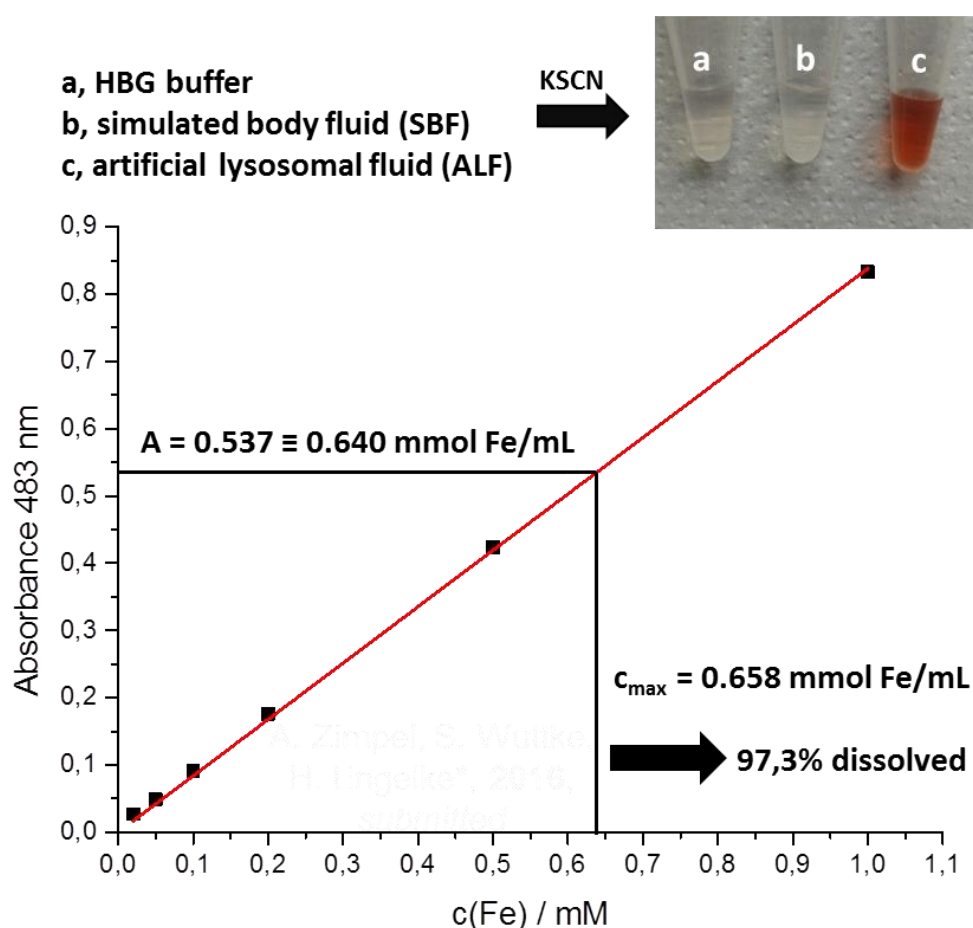
Figure S8-9. Stability of Lip-MOF NPs in different media within 1 h of incubation. A colorimetric assay using rhodamide indicated no dissolution of the nanoparticles in HBG buffer as well as in SBF. For ALF, the evaluated assay showed almost complete and rapid dissolution.
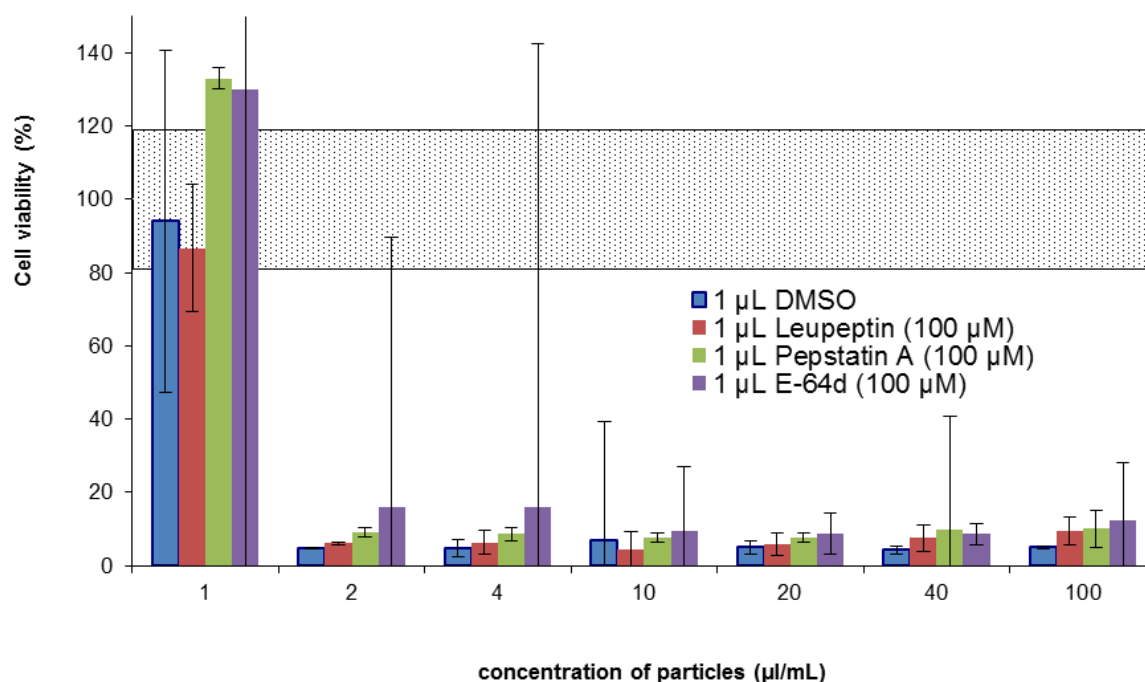
Figure S8-10. MTT cell viability assay of DOPC-MIL-100(Fe) NPs with addition of different protease inhibitors (dissolved in DMSO).
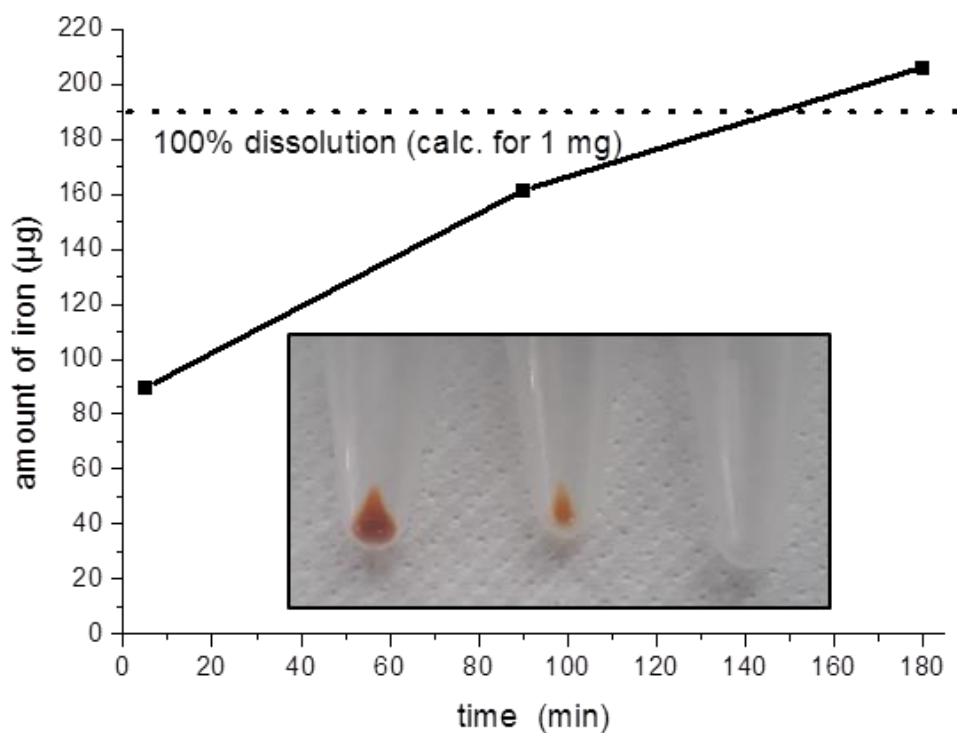
Figure S8-11. Dissolution profile of approx. 1 mg MIL-100(Fe) NPs in 0.1 M phosphoric acid. Iron content was determined by ICP-OES from supernatant. Inset shows the MOF pellet after centrifugation at the selected time points (5 min, 90 min, 180 min).

9.   Conclusion and Outlook

The focus of the presented work was the synthesis and detailed investigation of functional MOF based NP systems for their prospective biomedical applications. To this end, relevant properties such as uptake and release behavior of guest molecules from the nanoparticles as well as their toxicity were studied. Further, using different approaches, MOF NPs were post-synthetically modified on their external particle surface with biocompatible and functional molecules.

In a first project, MIL-100(Fe) NPs were covalently functionalized with two different polymeric structures using peptide coupling chemistry. The covalent nature of the bonding was proven by several techniques and the amount of polymer attachable to the external surface was quantified. The MOF formulations showed good colloidal stability in aqueous media compared to bare MIL-100(Fe) NPs and displayed high uptake by cancer cells but no cytotoxic effects up to rather high nanoparticle concentrations over 24 h. Furthermore, the influence of the polymer shell on the MRI activity of MIL-100(Fe) was investigated and showed only a slight decrease of their longitudinal and transversal relaxivities. This allows for the modification of the coating according to the scientific and clinical needs and, at the same time, *in vivo* investigation of MOF NP distributions such as accumulation in a tumor.

The modification of MOF NPs' external surface with biomedically relevant polymers was the topic of the second experimental chapter. We present a straightforward functionalization approach for Zr-*fum* NPs that can be used to attach different polymers onto the external surface by an entropically preferred exchange of the modulator (formic acid) by the coordinating groups of the polymers. Using the defined block copolymer PGA-PS for external surface functionalization, the resulting NPs retained their monodispersity independent of pH in a broad range of environments, such as aqueous solutions, protein containing buffer solution and cellular medium. These findings make the multifunctional particles promising candidates for an intravenously injected nanocarrier system due to the proposed longtime stability in the human bloodstream which is mandatory for effective passive targeting on tumor tissue by the EPR (Enhanced Permeability and Retention) effect.

In a subsequent project, the loading and release behavior of a model cargo molecule (fluorescein) in and out of mesoporous MOF NPs was tested regarding their potential as drug carrier in ensuing chapters. We found, for both studied NP types MIL-100(Fe) and MIL-101(Cr), that significant amounts of fluorescein can be adsorbed at room temperature ($>10^3$

molecules per NP). These values were evaluated to be compatible with the measured internal surface area. It was found that the loading and release rates are strongly dependent on the pH and the solvent. Considering the results, we conclude that the MOF scaffold can confine the guest molecules inside its pores through electrostatic interactions. As MOF chemistry provides an immense toolbox of different combinations of metal, linker and structure as well as different ways how to functionalize the scaffold, it enables controlling the MOF host-guest interactions. This makes MOF nanocarriers in general good candidates for drug delivery and other applications where a high payload is desirable.

The project in chapter 6 focused on the applicability of MIL-100(Fe) and MIL-101(Cr) as drug delivery vehicles. These MOF NPs were loaded with model drug molecules and were afterwards encapsulated by a lipid membrane to prevent premature cargo release. Moreover, for MIL-100(Fe) the lipid bilayer drastically increased the colloidal stability of the nanoparticles. High uptake of lipid-coated nanoparticles by cancer cells was confirmed by fluorescence microscopy. Considering the various ways to synthesize different functionalized MOF nanoparticles as well as the richness of lipids with diverse functions (cap system, triggered release, incorporation of shielding ligand for long circulation times and targeting functions), we demonstrated that MOF@Lipid NPs have great potential as a novel hybrid nanocarrier system. On the one hand, the MOF core could store different active species such as imaging, diagnostic or drug molecules, and on the other hand the lipid shell could be used for the incorporation of targeting or shielding ligands (e.g. PEG) as well as for the creation of triggered release mechanisms.

After the coating of MOF NPs showed promising results regarding their use in biomedicine, we validated several of the investigated MOF NPs for specific medical fields of application. We demonstrate that the tested MOF NPs (Zr-*fum*, MIL-100(Fe) and MIL-101(Cr) with different sizes and coatings, respectively) showed differential toxicity and bio-response in different effector cells tested. The work highlights the potential important risks of using the tested MOF NPs for specific medical purposes and also demonstrates their differential suitability for applications in drug delivery or for implant coating, respectively. This includes the use of MOF NP coatings for dental implants or cellular guidance tubes and showed their nanosafety regarding the respective effector cells, such as gingiva fibroblasts and peripheral nerve cells.

As lipid coated MIL-100(Fe) NPs were revealed to be toxic under certain conditions in the performed biocompatibility validation described in chapter 7, we further investigated the NP

system for use as chemotherapeutics without addition of drug molecules. In this study, we performed a slightly different coating procedure, where preformed DOPC-liposomes were fused with MIL-100(Fe) NPs, creating MOF core – lipid shell nanoparticles (Lip-MOF NPs) in an appropriate size range (approximately 250 nm) for intravenous injection and cellular uptake. The nanocomposite was fully characterized and investigated in a detailed TEM study. Incubation with cancer cells showed that the toxicity of the Lip-MOF NPs, which is based on an osmotically induced lysosomal burst followed by cell membrane rupture, is dependent on a slightly acidic external pH of the medium. This is an important feature which makes the system an interesting candidate for treatment of tumor tissue known to provide slightly acidic external pH of its environment. Furthermore, the mechanism of cell death was analyzed by cell uptake and dissolution studies, revealing a high endocytosis-mediated cell uptake for the lipid-coated MIL-100(Fe) nanoparticles as well as a very fast dissolution in the lysosome due to increased phosphatase activity by reduced external pH.

In conclusion, this thesis elaborates on the potential for MOF NPs in biomedical applications. The controlled manipulation of the external surface of NPs is of paramount importance as it defines the interface between the NP and its surroundings and determines the overall performance of the NP especially in terms of circulation half-life and targeting efficiency. Different external surface functionalization approaches (covalent, coordinative and lipid-coating) were shown to provide straightforward concepts for the precise modification of the MOF NPs. Using the model cargo fluorescein, loading and release behavior of the mesoporous MOF NPs were investigated to gain information about their capablility for drug delivery. Selected MOF NPs were tested regarding their nanosafety for specific medial purposes, and a lipid-MOF nanocomposite showed promise as pH-selective chemotherapeutic. All in all, the presented work highlights the potential of functionalized MOF NPs as smart drug delivery systems or as drugs by themselves, respectively, to address current challenges in theranostics.

10. Curriculum vitae

Personal Information

Name:	Zimpel, Andreas
Date of birth:	August 14th, 1987
Place of birth:	Rosenheim
Nationality:	German

Education

November 2013 – July 2018	PhD student in the group of Prof. Thomas Bein Under supervision of Dr. Stefan Wuttke Ludwig-Maximilians-University, Munich
April 2011 – September 2013	Master Studies in Chemistry Ludwig-Maximilians-University, Munich Degree: Master of Science (M.Sc., Grade: 1.79)
October 2007 – November 2010	Bachelor Studies in Chemistry and Biochemistry Ludwig-Maximilians-University, Munich Degree: Bachelor of Science (B. Sc., Grade: 2.22)
September 1998 – July 2007	Luitpold-Gymnasium, Wasserburg am Inn General qualification for university entrance (Grade: 2.6)

Research Internship

January 2013 – September 2013	Master thesis (Grade: 1.0) Ludwig-Maximilians-University, Munich Prof. Dr. Thomas Bein **Synthesis and functionalization of MOF nanoparticles intending their use as drug delivery vehicle**

May 2012 – August 2012	Research Internship
	Ludwig-Maximilians-University, Munich
	Prof. Dr. Thomas Bein
	Metal-organic frameworks: Synthesis of novel and functionalized structure as well as nanoparticles
November 2011 – February 2012	Research Internship
	Ludwig-Maximilians-University, Munich
	Prof. Dr. Heinz Langhals
	Darstellung von diamantfixierten Bichromophoren mit orthogonalen Übergangsdipolmomenten und Markierung von MOFs mit Perylenfarbstoffen
April 2011 – July 2011	Research Internship
	Ludwig-Maximilians-University, Munich
	Prof. Dr. Wolfgang Schnick
	Alternative Synthese von $LiCa_3Si_2N_5$ und Synthese von neuartigen Cer-Oxonitridosilicaten
July 2010 – November 2010	Bachelor thesis (Grade: 1.0)
	Ludwig-Maximilians-University, Munich
	Prof. Dr. Thomas M. Klapötke
	Hochenergetische Materialien auf der Basis von Diaminofurazan und Diaminoazoxyfurazan

Awards and Scholarships

CeNS Publication Award 2017; "Best Junior Scientist Publication"

CeNS Travel Award 2016 (1.500 €)

Travel Scholarship of the Gesellschaft Deutscher Chemiker, 2016 (300 €)

1. Place "Hands-on-Experimente-Wettbewerb" at the NIM Nanoday 2014

Work Experience

September - November 2013	"studentische Hilfskraft" at LMU
September/October 2012	"studentische Hilfskraft" at LMU
January 2011 – September 2012	Student Job at Deutsche Post AG
September/October 2009	Student Job at Alpenhain Käsespezialitäten GmbH

Computer Skills

MS Office, ChemDraw, Origin, ImageJ, Blender (basics)

Languages

German: native speaker

English: business fluent

French: basic skills

Other Activities

Since November 2013	Supervision of practical courses in inorganic and physical chemistry, Supervision of interns, master students and exchange students of the Nanosystems Initiative Munich (NIM) Summer Research Program (SRP 2015)

Commitment

private tutor in chemistry, physics and mathematics; soccer youth coach; secretary at "ASV Rott am Inn" soccer

Hobbies

soccer, reading, bavarian culture

11. Publications and Presentations

Journals:

1,) Noncovalent Control of Absorption and Fluorescence Spectra

Langhals, H.; Dietl, C.; Zimpel, A.; Mayer, P.; *J. Org Chem.* **2012**, *77*, 5965-5970.

2,) MOF Nanoparticles Coated by Lipid Bilayers and their Uptake in Cancer Cells

Wuttke, S.; Braig, S.; Preiß, T.; Sicklinger, J.; Zimpel, A.; Bellomo, C.; Rädler, J. O.; Vollmar, A. M.; Bein, T.; *Chem. Commun.* **2015**, *51*, 15752.

3,) Imparting Functionality to MOF Nanoparticles by External Surface Selective Covalent Attachment of Polymers

Zimpel, A.; Preiß, T.; Röder, R.; Engelke, H.; Ingrisch, M.; Peller, M.; Rädler, J. O.; Wagner, E.; Bein, T.; Lächelt, U.; Wuttke, S.; *Chem. Mater.* **2016**, *28*, 3318–3326.

4,) Validating Metal-Organic Framework Nanoparticles for Their Nanosafety in Diverse Biomedical Applications

Wuttke, S.; Zimpel, A.; Bein, T.; Braig, S.; Stoiber, K.; Vollmar, A. M.; Müller, D.; Haastert-Talini, K.; Schaeske, J.; Stiesch, M.; Zahn, G.; Mohmeyer, A.; Behrens, P.; Eickelberg, O.; Bölükbas, D. A.; Meiners, S.; *Adv. Healthcare Mater.* **2016**, *6*, 1600818.

5,) Multifunctional nanoparticles by coordinative self-assembly of His-tagged units with metal-organic frameworks

Röder, R.; Preiß, T.; Hirschle, P.; Steinborn, B.; Zimpel, A.; Hoehn, M.; Rädler, J. O.; Bein, T.; Wagner, E.; Wuttke, S.; Lächelt, U.; *J. Am. Chem. Soc.* **2017**, *139* (6), 2359–2368.

6,) Kinetic analysis of the uptake and release of fluorescein by metal-organic framework nanoparticles

Preiß, T.; Zimpel, A.; Wuttke, S.; Rädler, J. O.; *Materials* **2017**, *10* (2), 216.

7,) Self-assembly of different polymers on MOF nanoparticles for better control of interactions at the biointerface

Zimpel, A.; Danaf, N.; Steinborn, B.; Höhn, M.; Schrimpf, W.; Engelke, H.; Wagner, E.; Bein, T.; Barz, M.; Lamb, D. C.; Lächelt, U.; Wuttke, S.; *manuscript in preparation* **2018**

8,) pH-selective toxicity of lipid-coated MOF nanoparticles for use as chemotherapeutics

Zimpel, A.; Barnert, S.; Krombholz, S.; Heerklotz, H.; Cauda, V.; Zahler, S.; Vollmar, A. M.; Wuttke, S.; Engelke, H.; *manuscript in preparation* **2018**

Review:

Metal-Organic Framework Nanoparticles for Magnetic Resonance Imaging

Peller, M.; Böll, K.; Zimpel, A.; Wuttke, S.; *Inorg. Chem. Front.* **2018**, DOI:10.1039/C8QI00149A.

Bookchapter:

Beetz, M.; Zimpel, A.; Wuttke, S. (August 2016); *Nanoparticles*. In: Kaskel, S. (Ed.); *The Chemistry of Metal-Organic Frameworks: Synthesis, Characterization, and Applications.* Weinheim: Wiley-VCH

Oral Presentations:

1,) 4th MOF Young Investigator Symposium; La Jolla / San Diego, CA, USA, 2016

2,) International Symposium on Composites of Metal and Covalent Organic Frameworks: Fundamental Design & Applications; Granada, Spain, 2017

Poster Presentations:

1,) Deutsche Zeolite Tagung (DZT 2014); Paderborn, Germany

2,) Tagung der deutschen Bunsengesellschaft (Bunsentagung 2014); Hamburg, Germany

3,) 6th International Conference of the Federation of European Zeolite Associations (FEZA 2014); Leipzig, Germany

4,) CeNS Workshop Venice "Channels and Bridges to the Nanoworld", Venice International University (VIU), San Servolo, Venice, Italy

5,) 1st European Conference on Metal Organic Frameworks and Porous Polymers (EuroMOF 2015); Potsdam, Germany

6,) 5th International Conference on Metal-Organic Frameworks & Open Framework Compounds (MOF 2016); Long Beach, CA, USA